DOCTORAL THESIS

Synthesis of Magnetic Nanofibers for Their Potential Applications in Wireless Charging for Energy Efficient EVs

---

Author:
TEHREEMA NAWAZ

Supervisors:
MARTYN P. COLES
GRANT V. M. WILLIAMS
SHEN V. CHONG

A thesis
submitted to the Victoria University of Wellington
in partial fulfilment of the requirements for the
degree of Doctor of Philosophy

2022

Declaration of Authorship

I, TEHREEMA NAWAZ, declare that this thesis titled, Synthesis of Magnetic Nanofibers for Their Potential Applications in Wireless Charging for Energy Efficient EVs and the work presented in it are my own. I confirm that:

- This work was done wholly or mainly while in candidature for a research degree at this University.

- Where any part of this thesis has previously been submitted for a degree or any other qualification at this University or any other institution, this has been clearly stated.

- Where I have consulted the published work of others, this is always clearly attributed.

- Where I have quoted from the work of others, the source is always given. With the exception of such quotations, this thesis is entirely my own work.

- I have acknowledged all main sources of help.

- Where the thesis is based on work done by myself jointly with others, I have made clear exactly what was done by others and what I have contributed myself.

Signed: *Tehreema*

No matter what the circumstances will be, you do not stop growing towards the higher goals

Abstract

There is a growing demand to find new materials for flux guiding applications in the inductive power transfer systems. The inductive power transfer system (IPT) in electric vehicles has gained importance due to advantages including safety, efficiency, flexibility, and user-friendliness. The potential of IPT systems in dynamic flux transfer on-road requires the flux concentrators to maximize flux transfer at minimum power losses. Ferrite materials are the most commonly used materials in the IPT cores for flux-transfer applications due to their reasonable susceptibility, high resistivity, and semi-conducting nature. Their high resistivity is advantageous to minimize eddy-current losses. However, there are certain drawbacks to their use, for example, they can still result in some eddy-current losses as their resistivity is not high enough, they are very brittle in nature and are difficult to be made in thin sheets or in arbitrary shapes, and they are very heavy that increases the vehicle mass and energy consumption. An ideal material for wireless charging applications should be thin, and flexible that can be made in arbitrary shapes with a reasonable susceptibility and high resistivity for wireless charging applications.

This thesis aimed to investigate the preparation of bimetallic $Ni_{1-x}Fe_x$, semi-conducting $MnFe_2O_4$, and Sm^{3+} doped semi-conducting $MnFe_{2-x}Sm_xO_4$ nanofibers made by an electrospinning method for their potential applications in wireless charging. $Ni_{1-x}Fe_x$ was selected because the bulk material shows a high permeability which is useful for flux-guiding, but it has a low resistivity. However, the preparation of thin $Ni_{1-x}Fe_x$ nanofiber sheets can result in high resistivities in nanodimensions. The parameter x was studied by varying its value between 0.1-0.5 as $Ni_{1-x}Fe_x$ show high susceptibility at x∼0.2, and high magnetic moment at x∼0.5. The characterizations showed the presence of $Ni_{1-x}Fe_x$ nanoparticles formation within nanofibers for all the samples which can be advantageous to further increasing the resistivity and to reduce eddy-current losses. A bimodal particle size distribution was observed at x∼0.1, that became less bimodal at x∼0.2 and skewed with predominantly small nanoparticles at x∼0.5. Superparamagnetic behaviour was observed at x∼0.5 due to the formation of smaller nanoparticles. There was a systematic increase in the differential susceptibility with increasing x from 6 at x∼0.1 to 18 at x∼0.5. These results were encouraging for potential applications in wireless charging.

Semiconducting $MnFe_2O_4$ nanofibers were made by electrospinning method because bulk material has high resistivity. The thermal processing of these nanofibers

at 700°C resulted in large polycrystalline nanoparticles whereas, the thermal processing at lower temperature 620°C resulted in a mixture of small nanoparticles within these nanofibers. The presence of some single crystal nanorods was also seen in both samples. The high field magnetization was largest for the sample processed at higher temperature, i.e. 57% of the total magnetization value at 700°C as compared to 46% obtained at low temperatures at 620°C. However, one sample processed at 620°C showed the complete formation of $MnFe_2O_4$ nanorods with a highest saturation magnetization to 76% of the total magnetization. These results are encouraging as the potential of nanorod synthesis can be useful in the flux guiding applications. Electrospun $MnFe_{2-x}Sm_xO_4$ nanofibers with Sm^{3+}(x) doping were also made to observe the change in the structural and magnetic properties at x=0.06-0.25. The results showed the successful incorporation of Sm^{3+} in the crystal structure of $MnFe_2O_4$ at x$\leq$0.2. Polycrystalline nanoparticles were seen at low fractions of x$\leq$0.1 but more smaller nanoparticles were formed at x=0.2 and x=0.25. Superparamagnetic behaviour was observed at high fractions of x (x=0.2 and x=0.25). The saturation magnetization for x$\leq$0.2 was largest for x=0.06. This study has provided a solid foundation for a more in-depth exploration of magnetic electrospun nanofiber sheets for future applications in wireless charging systems.

Acknowledgements

My sincere gratitude goes to Professor Grant Williams, my supervisor, who has always been a mentor in science, an excellent critique in my analytic approach, and an excellent coach in polishing my research communication in various multi-science forum talks. Throughout this journey, I am especially thankful to Professor Martyn Coles, my co-supervisor, for his invaluable discussions, feedback, and most importantly, his morale-boosting encouragement. It is my pleasure to thank Dr. Shen Chong, who has played an integral role in conducting my magnetic measurements, guiding me in analysis, and assisting me in report writing. The support you provided me along this journey could not have been better without it. The assist from Associate Professor, Andy Edgar is another one of the many things I am thankful for about this project. He has been more than helpful in teaching me how to use the equipment and giving me tips in the thermal analysis profiles.

I am thankful to my collaborators and my whole Inductive Power Transfer (IPT) team for giving me the opportunity to work on this project. Despite the diverse nature of this project, I have gained so much knowledge and insight from the other teams working on it. Thanks for inviting me to your annual meetings, which have been highly insightful for clearing my understanding.

It is with a great deal of gratitude that I acknowledge David Flynn, an invaluable asset to this university, for his greater contribution to the field of electron microscopy, including SEM and TEM. The training, guidance, and facilitation that he gave me to learn microscopes and learn so much from his expertise means a lot to me. I have been receiving constant help from him since the very first month of my PhD, and his affectionate personality is a wonderful source of inspiration for many PhD students at Victoria University of Wellington. Likewise, I appreciate Sara Spencer, a kind and very friendly person from Robinson's Research Institute, for her help with electron microscopy imaging. I am thankful to Doctor Mathew Cairns for his guidance, which helped me learn how to use XRD for conducting measurements.

My heartful thanks to my lab mates, including Dr. Vaibhav Bhugra, Dr. Joe Schuyt, and Dr. Fraser Hughson for their valuable assistance and thought-provoking discussions during this project. My journey of learning at SCPS has been filled with meaningful and inspiring moments. I am thankful to my group members, and to

my peers in science at SCPS, for their encouragements and cheerful discussions during lunch that gave me so many memories to cherish for lifetime from this journey. A special and very warm thanks to my office friends and colleague's including Dr. Thathsaranie (Tatt), Lara Browne (Laura), Jessie Siesicki (Jeff), Brenda Luong (Bread), Mathew Brett (Mat-R), and Lucy Druzianic (Lucy) for making my workdays pleasant and enjoyable.

I would like to give a shout-out to all my friends who have had my back through thick and thin during this journey: Ayesha, Shabana, Saima, Saba, Shalini, Fozia, Hellen, Courtney, Mariya, Mehma, Hajira, Huzaifa and Awais. It's been an honor to have you all in my life and have you been such a big part of making it what it is today, as well as being there to help me out when things got rough. I wish to acknowledge my family's support and great love, my aunt, Nagina khala, my sister, Mah-e-neema, and my brother, Arham for always being supportive and being there for me during this journey. I would also like to thank my best friend, life partner, and my love, Salman for his support and appreciation along the way.

The last words are for my parents, Muhammad Nawaz, my father and Samina Mushtaq, my mother, without whom I would not have been able to live this dream. They are my motivation and my inspiration to look-forward to the bigger goals. I cannot express my emotional status of penning down this acknowledgement to my late father, with whom I saw this dream, and who is my role model for reaching where I stand now. He was an inspiration to me throughout my life and truly my hero. In memory of him, I will keep working hard towards achieving my goals with enthusiasm!

Contents

List of Figures

List of Tables

List of Abbreviations

SEM	Scanning electron microscopy
TEM	Transmission electron microscopy
EDS	Energy dispersive X-ray spectroscopy
XRD	Powder X-Ray diffraction
SAED	Selected area electron diffraction
MPMS	Magnetic properties measurements system
TGA	Thermogravimetric analysis
DSC	Differential scanning calorimetry
STEM	Scanning transmission electron microscopy
IPT	Inductive power transfer
EVs	Electric vehicles
OECD	Oraganization for economic co-operation and development
ICEV	Internal combustion engine vehicles
CPT	Capacitance power transfer
DC	Direct current
AC	Accerelarating current
LS method	Light scattering method
BSE	Back scattered electrons
PVP	Polyvinylpyrrolidone
DMF	Dimethylformamide
kV	Kilovolt, SI unit of voltage
MPa	Megapascal, SI unit of pressure
Al	Aluminium
Fe	Iron
Ni	Nickel
Mn	Manganese
Sm	Samarium
HSP	Hansens solubility parameters

SQUID	Superconducting Quantum Interface Device
M_s	Saturation magnetization
μ_B	Bohr magneton
T_f	Spin freezing temperature
$M_{s,c}$	Saturation magnetization of spin-ordered core
$M_{c,d}$	Saturaion magnetization of spin-disordered shell

To my father...
for giving me
vision, and
empowering
me with your
teachings!

Chapter 1

Introduction

1.1 An overview

Inductive power transfer (IPT) is a safe and clean technology that allows contact-less power transfer in various applications. It has been employed in modern electronics including contact-less charging pads for mobile phones and laptops, biomedical devices, and now in the wireless charging of electric vehicles (EVs).[1] This has been advantageous to address the energy scarcity challenges and mitigate emissions for a cleaner environment. The typical operation of IPT technology in EVs includes the power transfer via two strongly coupled coils operating at a high frequency through an air gap between the road and in EV.[2] This requires a soft magnetic material in the cores of inductively coupled coils with high susceptibility and low coercivity for an efficient power transfer without significant power losses. Ferrites are the most commonly used materials for such applications due to their high susceptibility and low coercivity for maximum power transfer. However, there are certain limitations involved with their use, including brittleness, thickness, and low resistivity that cause eddy-current losses.[1] Other materials include Permalloy ($Ni_{1-x}Fe_x$), but the low resistivity makes them unfavorable for high-frequency applications.[3] To address these challenges a material with thin dimensions, high susceptibility, and low coercivity is required.

Recently, one-dimensional nanofibers have gained interest due to their long directions, and high shape anisotropy, which is favorable for flux-guiding applications. Their advantages include a large surface area and very thin diameters for compact magnetic devices.[4, 5] The use of thin sheets of magnetic nanofibers in IPT is advantageous because they can reduce power losses in comparison to their bulk counterpart. If nanofibers contain magnetic nanoparticles, this can further reduce power losses due to higher resistivities from enhanced carrier scattering in non-conducting polymers, as the characteristics of nanoparticles are different from their bulk counterparts. For example, at extremely small dimensions of a nanoparticle, the thermal energy exceeds the magnetocrystalline anisotropy. This leads to super-paramagnetism with no hysteresis, while maintaining reasonable magnetic susceptibility.[6]

This Ph.D. dissertation has focused on the fabrication of polymer nanofibers containing bimetallic $Ni_{1-x}Fe_x$ nanoparticles and semiconductor $MnFe_2O_4$ nanoparticles, as both of these soft magnetic materials show remarkable magnetic properties in bulk. There is no report on the fabrication of bimetallic $Ni_{1-x}Fe_x$ nanofibers, therefore the fabrication of bimetallic $Ni_{1-x}Fe_x$ at various fractions of x is interesting to investigate, for their structural and magnetic properties. There are some reports available in the literature for the synthesis of $MnFe_2O_4$ nanofibers, however, the results on the structural and magnetic properties are questionable at best. The synthesis and detailed characterizations were performed on the $MnFe_2O_4$ nanofibers that focus on their structural and magnetic analysis. The $MnFe_2O_4$ nanofibers have also been doped with rare earth Sm^{3+} (x) for the first time at various fractions of x in $MnSm_xFe_{2-x}O_4$ nanofibers. The motivation behind this study is based on the interesting results obtained in the previous reports when $MnFe_2O_4$ nanomaterials were doped with other trivalent rare earth ions. It is believed that the trivalent $Sm_3{}^+$ doping in $MnFe_2O_4$ can give interesting structural and magnetic properties for $MnFe_{2-x}Sm_xO_4$ nanofibers.

1.2 Key research questions

1. What is a suitable method to prepare $Ni_{1-x}Fe_x$ and $MnFe_2O_4$ nanofibers?

2. How the structural and magnetic properties differ in $Ni_{1-x}Fe_x$ nanofibers when x is varied from x=0.1 to x=0.5?

3. How the structural and magnetic properties differ in $MnFe_2O_4$ nanofibers calcined at two different temperatures?

4. What is the effect of rare earth ion Sm^{3+} doping on the magnetic and structural properties of $MnSm_xFe_{1-x}O_4$ nanofibers at varying fraction of x?

Thesis structure

- **Chapter 2** provides the background knowledge on the existing IPT technology, its working procedure, the existing core materials, and the limitations involved with the use of core materials. It also explains the concepts of magnetism, classification of magnetic materials, the magnetic interactions, and other important concepts to understand the nature of core materials in the IPT cores. The literature supporting the importance of nanodimensions and the motivation for the synthesis of magnetic nanofibers is also explained in this chapter.

- **Chapter 3** explains the experimental procedure used for the preparation of magnetic nanofibers. The solution preparation for electrospinning, parameters on an electrospinning set-up, and thermal treatment profile has been discussed in this chapter. Characterization techniques including, XRD, SEM, TEM, STEM maps, SAED, and SQUID measurements that are used to analyse the structural and magnetic properties also discussed in detail for nanofibers.

- **Chapter 4** discusses the fabrication of $Ni_{1-x}Fe_x$ nanofibers at two different fractions of x from x~0.1 to x~0.2. The differences in structure and magnetic properties for these fractions are compared. The magnetic results are also evaluated to find the details of $Ni_{1-x}Fe_x$ at each fraction.

- **Chapter 5** discusses the fabrication of $Ni_{1-x}Fe_x$ nanofibers with x~0.5. The reasoning behind the modified method for the preparation of x~0.5 nanofibers is discussed in detail. These nanofibers are characterized and the difference in structure as well as in the magnetic properties are discussed in detail.

- **Chapter 6** discusses the fabrication of $MnFe_2O_4$ nanofibers at two different annealing temperatures. The differences in the structure as well as in the magnetic properties at both temperatures are discussed in detail.

- **Chapter 7** discusses the fabrication of Sm^{3+} doped $MnSm_xFe_{1-x}O_4$ nanofibers at x= 0.06, 0.1, 0.2, and 0.25. The effect of varying x on the structural and magnetic properties at each fraction has been analysed. The results are also compared with the undoped $MnFe_2O_4$ nanofibers.

- **Chapter 8** summarises the findings of this research work.

- **Chapter 9** discusses the future prospects of this research work.

Chapter 2

Theory and background

2.1 Energy crisis and emissions in the transportation sector

The world is facing a serious crisis related to the use of unsustainable and non-renewable energy sources to maintain both transportation and industrial sectors. The depletion of the fossil fuel reserves and the growing demand in energy security is a wake up call for the need to explore alternative, sustainable and renewable energy sources. It is also anticipated that the consumption of fossil fuels will increase by 49% in OECD (Organization for Economic Co-operation and Development) countries whereas, the total energy demands of non-OECD countries will continue to increase by 84% until the year 2035 (Figure 2.1). The transport sector utilizes 30% of the total energy consumption, which is projected to increase by 54% until 2035. [7] In addition to this, the cost of fuel is expected to increase substantially in the next two decades. [7]
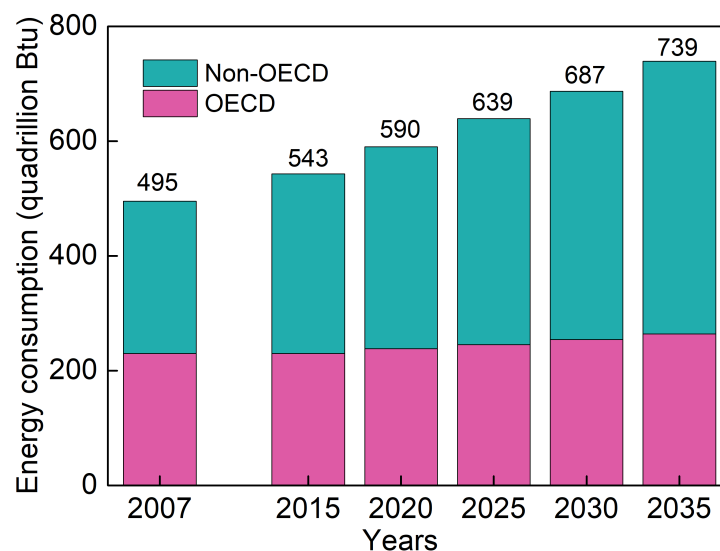
FIGURE 2.1: World marketed energy consumption by EIA (Energy Information Administration)[7]

Energy consumption (in Btu) [1] by fossil fuels has played a significant role in the increased air pollution due to greenhouse gas emissions. There is a constant increase in the earths temperature by 2% each year which is related to the CO_2 emissions in the atmosphere. [8] The transportation sector is one of the main contributors towards greenhouse gas emissions and resource depletion. Therefore, global attention has now been focused towards the deployment of renewable energy sources to mitigate emissions and promote green transportation.

2.2 An era of electric vehicles

Recently, there has been an increased interest towards the replacement of internal combustion engine vehicles (ICEV) with electric vehicles (EVs) in transition towards the green technology. Unlike ICEVs, EVs emits no gases, and are considered to be an eco-friendly alternative. EV transportation sector has additional benefits in the economic growth along with the environmental benefits. Economic growth involves the development of more technological industries that can have a potential to expand the energy sanctuary with renewable energy sources.[9, 10] The electric motors in EVs have greater efficiency (80-95%) than ICEV combustion engines, with only 20% efficiency, this makes EVs a more adaptable alternative.

The growing demand from government, policy makers, industries, and environmentalists has a significant contribution in the growing numbers of EVs on roads. In 2010 there were only few hundred EVs on the roads, which has grown to six million in the first half of 2019, and is expected to rise to 85 million by 2035.[11, 12]

Another report has highlighted the growth in the EV sales in the year 2021 between China, USA, and Europe in Figure 2.2. It can be seen that China is leading with EV adaptability and their EV market growth has increased up to 4-fold by the end of the year.[13]

---

[1]Btu=British thermal unit (1 Btu $\approx$1 kJ)
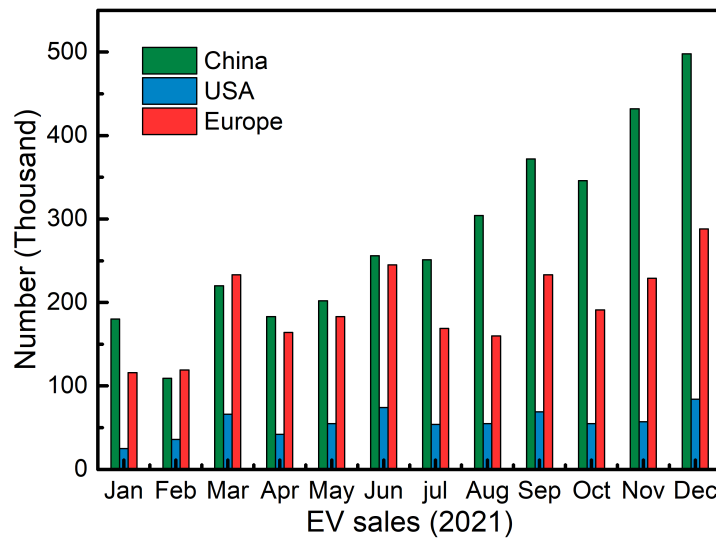
FIGURE 2.2: EV sales in the year 2021

2.2.1 History of EVs

The idea behind today's EVs was pioneered by Robert Anderson, who founded the first electric carriage. Later in 1884, the first electric car was created by Thomas Parker.[14, 15] In 1897, the first electric taxi company was founded, that operated on a battery facility. However, due to long recharging times and lack of a recharging facility, the discharged batteries were replaced.[15] In the early 20th century, thousands of electric taxis, trucks, and buses were produced by the single electric vehicle company. The company later went bankrupt due to several disadvantages including small charging stations, high manufacturing costs, small range, and high prices.[15]

These disadvantages have led to the production of ICEV as they were easier to operate, lightweight, and used low-cost combustion oils. However, EVs regained their importance in 1990 when California introduced regulations regarding low-emissions cars to reduce greenhouse gas emissions. Later in 2008, the first electric car was invented that allowed the user to cover 320 kilometers without charging. After a year, a series of electric cars attracted consumers due to suitable prices and satisfactory battery capacity.[15]

Nowadays, electric car production has improved significantly with a wide range of EVs that are user-friendly, efficient, and low maintenance for better performance. The EV market has grown significantly and is set to replace ICEVs in the near future.

2.2.2 Limitations of existing EVs operation

2.2.2.1 Long charging times

An increased number of EVs on roads requires robust, efficient, and effective charging. This has caused a significant burden on power stations. Most EVs use plug-in

cables for recharging regardless to their location, at home, or on highways. This limits the mobility of EVs on the roads. Moreover, plug-in charging requires long exposure charging times and is not electrically safe. There are currently four types of chargers available on the market including very slow chargers, fast chargers, rapid chargers, and the Tesla supercharger. The power rating for these plug-in chargers is between 3 to 6 kW for slow chargers, 7 to 22 kW for fast chargers and above 42 kW for rapid chargers. The battery recharging duration can also be categorized on this basis, wherein slow chargers can take up to 10 hours for recharging a battery that is suitable for at-home charging. The fast chargers may take up to 4 hours to charge the battery of the car and are typically installed in parking lots and shopping malls. The rapid chargers take around 30 minutes to an hour to charge the battery and are installed at gas stations. The charging time for the fast charger is still high when compared to gasoline refilling, and a high cost is required for the installation of these chargers.[16, 17]

2.2.2.2 Battery life

Another drawback associated with the use of energy storage batteries is the importance of maintaining the operation of EVs on the roads. The state-of-the-art storage material is Li-ion batteries. Although these batteries have a high energy density (200 Wh/kg) when compared with other commercially available batteries or petroleum (1200 Wh/kg) their energy density is still very low. These batteries have high initial costs, a high degradation limit associated with their charging and discharging, and high-cost recyclability.[18] The average life cycle of an EV battery is between 8-10 years, and its efficiency can reduce by up to 80% over time.[19] Plug-in EVs require heavy batteries for energy storage, and it is expected that the Li-ion share will increase to 530 kilotons by the end of 2025. Due to which, there is an increased risk of large volumes of battery waste in the future as recycling methods are very expensive and limited.[16, 20]

2.2.2.3 Cost and affordability

The market price of EVs is very high compared to that of gasoline cars. However, it is expected to reduce with adaptability and market expansion. There is good potential for EVs due to their sustainability and government policies, however, still there is a need for further improvement in this technology for integration into everyday life.

2.3 Wireless technology in EVs

Wireless technology was first developed in the late 19th century by Nicola Tesla, with the invention of the wireless electric bulb. That bulb was powered by the induction between two closely placed metal plates attached in an enclosed circuit. Modern wireless technology is capable of power transfer up to two meters between two strongly coupled coils. Wireless technology is classified into two categories.

1. Capacitance power transfer (CPT)

2. Inductive power transfer (IPT)

CPT is the mode of power transfer through an electric field between two coupled capacitors. The applications of CPT are in low-power energy transfer devices, as it can transfer between two closely placed capacitors with a small air gap. The use of CPT through large air gaps is a potential risk to the environment, as it involves the leakage of electric fields through power losses.

IPT technology is preferred for power transfer at large air gaps with increased output. This technology is beneficial to EVs with optimal air gaps between the road and the vehicle, thereby preventing power losses to the surrounding environment. [21]

2.3.1 Advantages of IPT in EVs

IPT can address the first two challenges of plug-in EVs by automation of the charging process and can remove the range restrictions with potential benefits of mobility, safety, environment, and infrastructure. There are currently three types of wireless technology

1. Stationary power transfer

2. Semi-dynamic power transfer in waiting lanes and parking lots

3. Dynamic power transfer for highways

IPT is more advantageous than plug-in charging, as it provides a comparable reduction in greenhouse gas emissions and performance, but it facilitates the users in various ways. Firstly, it saves the time that one must spend charging traditional EVs. It is user-friendly and can also prevent lost charging opportunities, as, if someone forgets to plug in the vehicle. Wireless technology is also beneficial in saving additional infrastructure space as the whole system is embedded underground. This can also prevent the cluttering of several wires and electrical components that are associated with the plug-in chargers. Thus, there is no need for independent charging units for EVs, and more EVs can be served in charging lots. Semi-dynamic and dynamic wireless charging are greatly beneficial as there is no need to stop the vehicle as it charges whilst moving.[10, 22]

In dynamic power transfer, IPT technology does not require heavy batteries as compared to plugin EVs. As a result, lightweight EVs can be produced with reduced volumes of battery waste. The energy consumption by the IPT EVs is also expected to be less compared to the plugin EVs for equivalent charging efficiency.[22]

2.3.2 Components of an IPT system in EVs

The schematic illustration below in Figure 2.3 shows the basic components of IPT technology in EVs. The whole system is divided into two parts; half embedded in the road and half at the base of an EV.
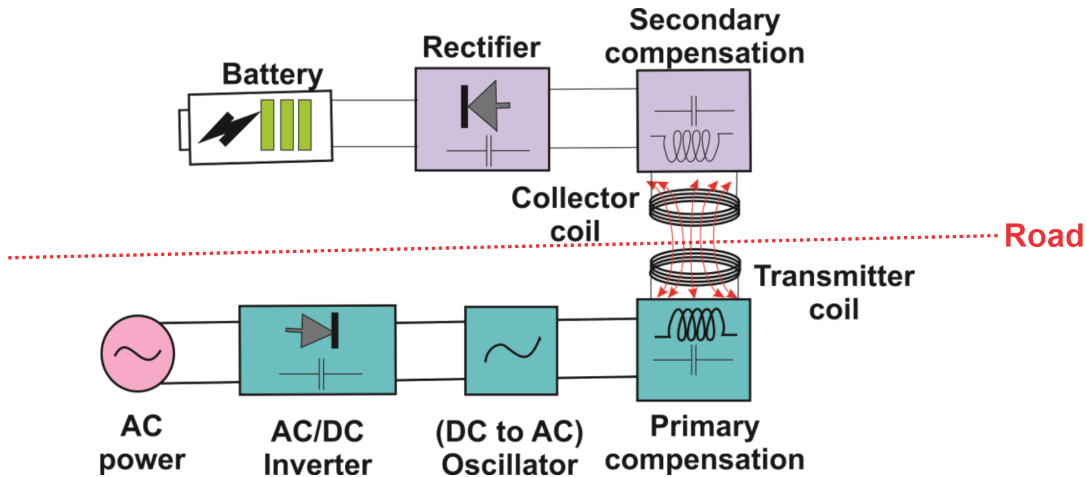
FIGURE 2.3: Schematic illustration of an IPT set-up

The primary source of energy in an IPT system is an accelerating current (AC) source, which provides a low-frequency AC (50-60Hz). This frequency is very low to drive the transmitter coil and consequently transfer energy to the collector coil. Therefore, this incoming AC power is first converted to a single-step or two steps high-frequency AC power. However, most electronic systems use two-step AC/D-C/AC conversion inverters for high-frequency AC output applications. The inverter converts the low-frequency AC power to the direct current (DC) with power factor correction (compensation of the lagging currents with the help of capacitors). This DC power is then converted back to a high-frequency AC (20-100 kHz) to radiate the transmitter coil after passing through the primary compensation network (This primary compensation network is important to safely transfer the high-frequency AC to the transmitter coil and to compensate the electric losses). The high-frequency AC in the transmitter coil generates an electric field, which is responsible for the production of an oscillating magnetic field in the collector coil. The oscillating magnetic field works on the principle of Faraday's law and induces an AC voltage in the collector coil. The produced AC voltage passes through the secondary compensation network and is rectified into a DC power. Finally, the DC power goes through a filter to reduce ripple voltage (Figure 2.4) to charge the battery of an EV.[21, 23–25]
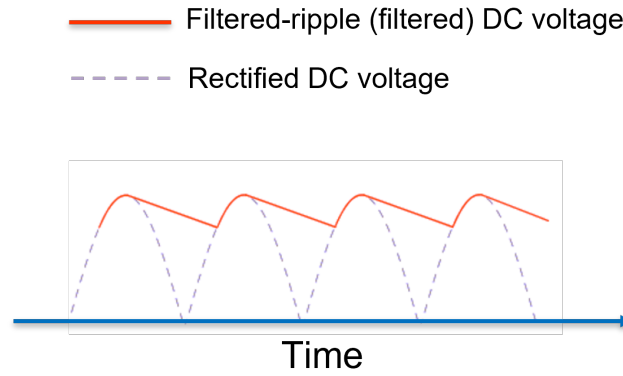
FIGURE 2.4: Ripple free DC voltage after filtration

2.3.3 Core material for inductive power transfer

The role of inductively coupled coils is very significant in determining the power transfer and leakage (power losses) during the wireless transfer between roads and EVs. For example, loosely coupled coils due to misalignment can result in more power losses than strongly coupled coils, and consequently emit hazardous electromagnetic radiation in the surrounding environment.[18] As a result of this, there is not enough power transfer from the transmitter coil to the collector coil. Therefore, to improve the tendency of power transfer and to reduce losses, soft magnetic materials are used in the core of these two coils.[26]

To further understand the types and properties of such magnetic materials, the fundamentals of magnetism are briefly explained below.

2.4 Concept of magnetism and magnetic materials

2.4.1 Magnetic susceptibility and magnetic permeability

The response of a material under an applied magnetic field (H) is determined by a quantity known as magnetic susceptibility (χ). The relationship of magnetic susceptibility to the induced magnetization (M) at an applied magnetic field is given in the equation (2.1).[27]

$$M = \chi H \tag{2.1}$$

or

$$\chi = \frac{dM}{dH} \tag{2.2}$$

M is the magnetization of the material under an applied magnetic field (H). The SI unit for both magnetization (M) and applied magnetic field is Ampere/meter (A/m). (For comparison with the literature, other cgs units (emu/g or emu/cm^3) are also in use for magnetization). Another rearranged equation. (2.2) provides a

more clear understanding of χ, which is the dimensionless proportionality factor at equal units of M and H, and hence provides the degree of induced magnetization in a material under applied magnetic field.

Another important term is the magnetic flux density (B) or magnetic induction which is defined as the magnetic flux per unit area (magnetic flux is the concentration of flux lines at one point). It is the amount of induced magnetic force on a material when placed in an external magnetic field (H). The SI unit for B is Tesla. Both B and H represent the strength of the magnetic field, but H is the extrinsic magnetic force applied on a material, whereas B represents how effectively that material utilizes that magnetic force to induce a magnetic field inside the material. The relationship between magnetization, magnetic induction, and the applied magnetic field is shown by the equation (2.3) below. [27, 28]

$$\vec{B} = \mu_o \vec{H} + \mu_o \vec{M} \tag{2.3}$$

Where $\mu_o \approx 4\pi \times 10^{-7} \, \text{N/A}^2$.

A similar term to magnetic susceptibility (χ) is magnetic permeability (μ), which represents the degree of penetration of the magnetic field inside a material to increase magnetic induction. The SI unit of μ is newton per ampere squared (N/A^2). This is shown by the equation (2.4) given below.[27]

$$B = \mu H \tag{2.4}$$

The proportionality factor μ is called the permeability, which is a scalar quantity for an isotropic material but can be a tensor for an anisotropic material. Another important term is the relative permeability (μ_r), which is given by the ratio between the permeability of a material to the permeability of free space (μ_o). (equation (2.5)[27, 28]

$$\mu_r = \frac{\mu}{\mu_o} \tag{2.5}$$

The relationship between the relative permeability to the magnetic susceptibility can be derived from the equation (2.3). Now if we add the value of M from (2.1) and rearrange the equation, the new equation becomes as (2.6) given below.

$$B = \mu_o H (1 + \chi) \tag{2.6}$$

Adding the value of B from equation (2.4) and rearranging, the equation becomes (2.7).

$$\frac{\mu}{\mu_o} = 1 + \chi \tag{2.7}$$

From (2.5) the relation between the relative permeability to the susceptibility is given as (2.8) or (2.9)

$$\mu_r = 1 + \chi \tag{2.8}$$

or

$$\chi = \mu_r - 1 \tag{2.9}$$

The value of χ increases from 10^{-5} to 10^5 from very weak to strong magnetic materials and is a parameter to classify materials on various types of magnetization.[29]

2.5 Classification of magnetic materials

2.5.1 Diamagnetic materials

Diamagnetic materials show a negative response or a very weak response in the presence of an external applied field. These materials will create an induced magnetic field in the opposite direction to the external field, thus causing a repulsive effect. The applied magnetic field will interact with a diamagnetic material in such a way that it alters the orbital velocity of the electron around the nucleus. Therefore, due to the inner shielding of the material, the induced magnetic dipole moment will be in opposite direction to the applied field. This induced dipole moment will disappear quickly after the removal of an external magnetic field. The diamagnetic materials have paired electrons in their valence shell.[30, 31]

Figure 2.5 (a) shows a diamagnetic material where there is no induced magnetic dipole in the absence of an external magnetic field. When an external field is applied to the system, the induced magnetic dipoles are arranged in the opposite direction to the external field as shown in Figure 2.5 (b). The value of the relative permeability of such materials is less than one or the magnetic susceptibility value will be close to zero as per shown in Figure 2.5 (c). The magnetic susceptibility remains unchanged at varying temperatures for diamagnetic materials as shown in Figure 2.5 (d).
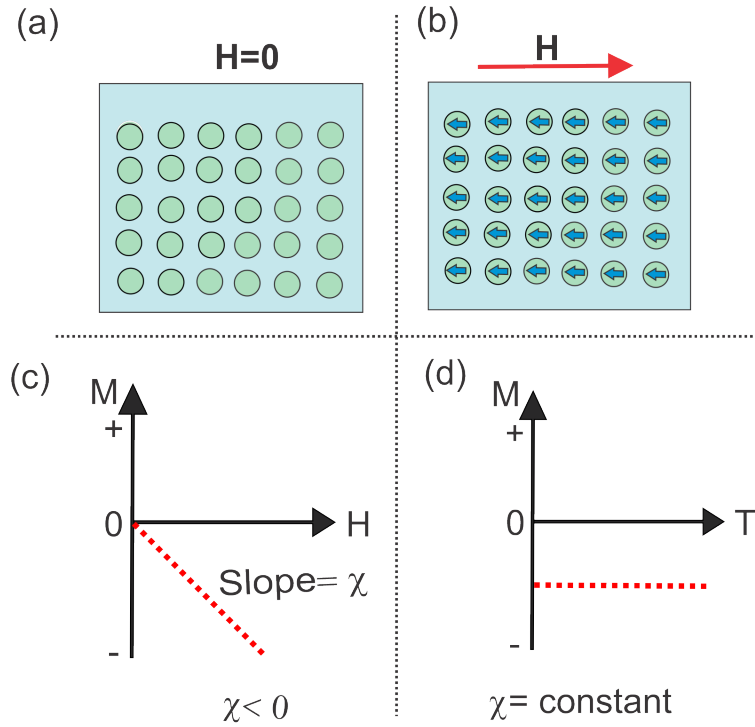
FIGURE 2.5: Diamagnetic material (a) in the absence of magnetic field (H), (b) in the presence of (H), (c) Susceptibility in the presence of (H), and (d) Effect of temperature on the magnetic susceptibility of a diamagnetic material

2.5.2 Paramagnetic materials

Paramagnetic materials are materials that are magnetized easily in the presence of an external magnetic field, however, show no magnetism in the absence of a magnetic field. These materials have unpaired electrons that are influenced by the external magnetic field, resulting in the formation of polarized atomic orbitals and a net positive magnetic moment. Figure 2.6 (a) shows a paramagnetic material at room temperature without an external magnetic field. It can be seen that the magnetic spins (spin of an electron responsible for magnetization in a material) are randomly oriented in the material and net magnetization is zero. When a magnetic field is applied to this system in Figure 2.6 (b), the magnetic spins tend to line up in the direction of the applied field, giving a net magnet moment in the same direction as the applied magnetic field. The relative permeability of these materials is greater than one as per shown in Figure 2.6 (c) and the susceptibility is in inverse relationship with temperature. When the temperature increases, the thermal energy of the magnetic moments increases, this breaks their alignment due to the thermal vibrations of magnetic moments, thus decreasing the overall magnetic dipole moment. This can be explained by the Curie-law for non-interacting magnetic moments or isolated magnetic moments as given below in (2.10), (Figure 2.6 (d)).[32]

$$\chi = \frac{C}{T - \theta} \tag{2.10}$$

Where C is the Curie constant which is directly related to the number of localized electrons and θ is the Curie-Weiss temperature that reflects the strength of the magnetic pathway. When θ is equal to zero, the solid will stay paramagnetic at all the probed temperatures.
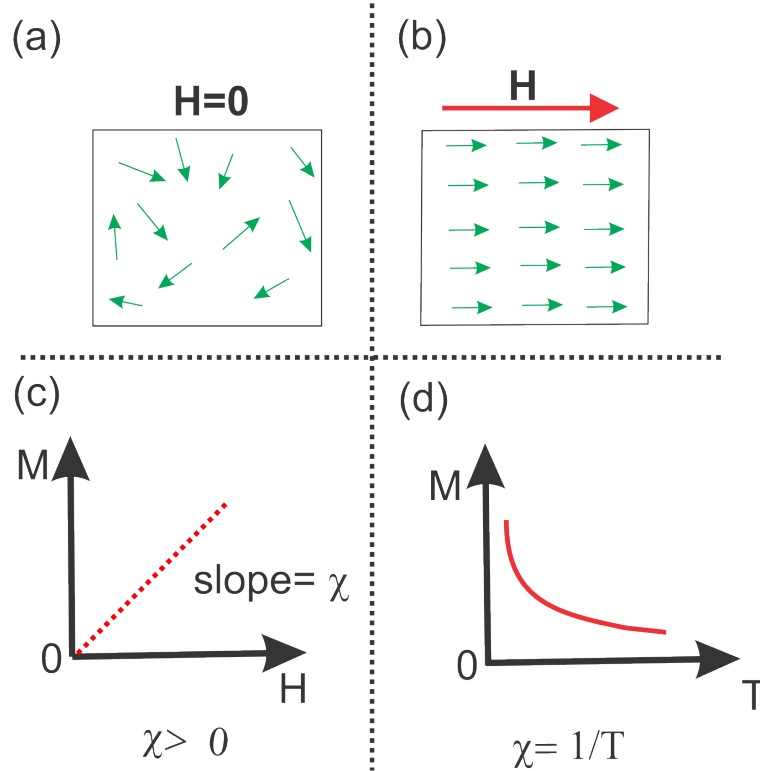
FIGURE 2.6: Paramagnetic materials (a) in the absence of (*H*), (b) in the presence of (*H*) at low temperature, (c) Susceptibility in the presence of *H* at high temperature and (d) Effect of temperature on susceptibility of a paramagnetic material by Curie-law

2.5.3 Ferromagnetic materials

Ferromagnetic materials are strongly influenced by the applied magnetic fields and become polarized in the direction of an applied magnetic field. These materials show spontaneous magnetization as they possess multiple magnetic domains where each domain contains many atoms with individual magnetic moments aligned parallel to each other. This gives a net magnetic moment to that domain. In these materials, the domains are oriented in different directions to each other in the absence of an applied magnetic field. However, when an external magnetic is applied to the material, the domains start moving to arrange their magnetic moments in the direction of the external field. Ferromagnetic materials show high permeability depending on the strength of the applied magnetic field due to exchange interactions in long-range order of magnetic dipoles. These materials are strongly influenced by the temperature and lose their magnetic ordering when Curie temperature (T_c) is reached (Figure 2.7). T_c is intrinsic to different for different ferromagnetic materials, For example, the T_c for iron (Fe) is 1043 K while for nickel (Ni) is 1388 K.
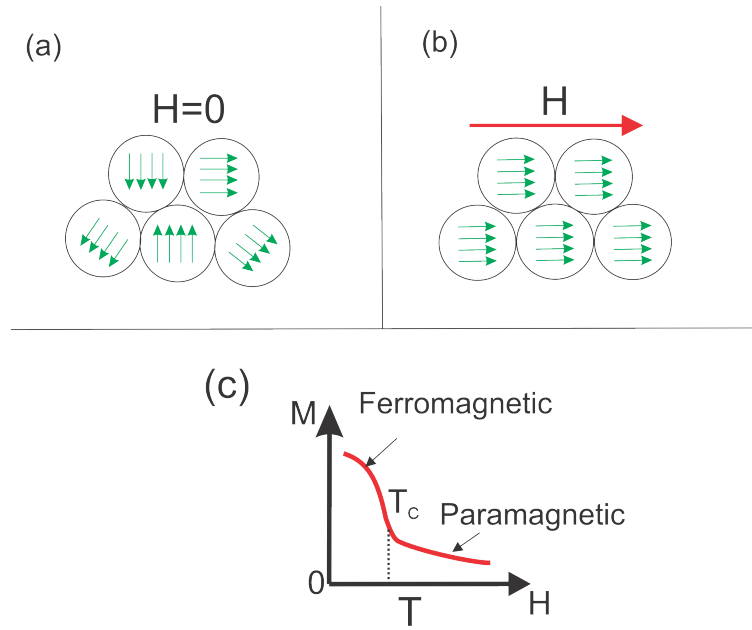
FIGURE 2.7: (a) Ferromagnetic material in absence of magnetic field, (b) in presence of the magnetic field, (c) Effect of temperature on susceptibility by Curie-Weiss law

The susceptibility for ferromagnetic materials above T_c can be calculated by the following expression (equation (2.11)).[33]

$$\chi = \frac{C}{T - T_C} \tag{2.11}$$

The equation (2.11) is known as Curie-Weiss Law, where C is the curie constant and T is the absolute temperature. The susceptibility of ferromagnetic materials is highest as compared to the other classes and it can go up to the order of 10^6 for strong ferromagnets. [34]

Hysteresis curve of a ferromagnetic material

The relationship of magnetic induction in a material in response to the applied magnetic field is studied by plotting magnetic field density against the applied magnetic field. This plot is known as the hysteresis curve or BH loop. A similar curve is obtained where magnetization replaces B and is called the MH loop. However, in both cases, H is increased from zero to a high value as shown in Figure 2.8.

It can be seen from Figure 2.8, that by increasing the applied magnetic field, the magnetization increases linearly to reach the saturation point (where a further increase in the *H* has a small or no effect on magnetization). At this point, almost all the magnetic domains in the materials align with the external magnetic field. When the applied magnetic field is reduced to zero, the original curve is not retraced. This shows that the material has attained the magnetic history where the magnetization does not follow the same path on the initial curve. On a symmetrical MH loop, this extra distance covered by the magnetization from point a to b shown on the MH loop is known as remnant magnetization or remanence (M_r). At this point, an equal

but reverse H is applied to the material to reduce M to zero. In response to this, the curve moves to point c, where the M becomes zero. This is known as coercivity (H_c) or coercive field. (where the strength of the applied magnetic field is enough to flip enough domains in the opposite direction that the total magnetization becomes zero).

As H increases in the negative direction, the material becomes saturated again in the opposite direction (point d). Again when H is reduced to zero, a remnant magnetization or M_r is obtained in a negative direction that becomes zero when the field H is revered back to a positive direction to remove residual magnetization. The MH loop is characteristic of magnetic materials and is used to describe the magnetic response of a material under an applied magnetic field.[35]
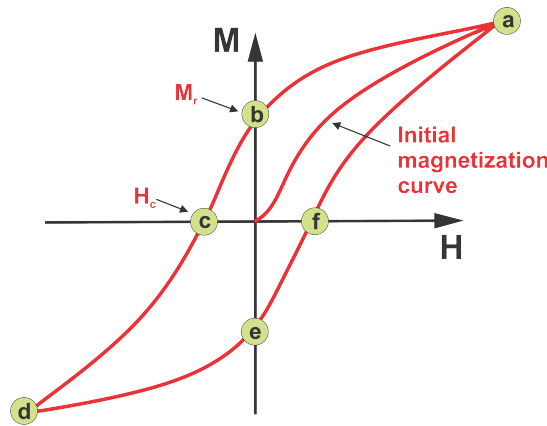
FIGURE 2.8: Hystersis loop (MH loop) showing the initial magnetization curve, remanent magnetization (M_r), and coercivity (H_c) in a ferromagnetic material

2.5.4 Antiferromagnetic materials

Antiferromagnetic materials are materials that have an ordered arrangement of their magnetic spins anti-parallel on different sub-lattices of a material. The magnetic moments arising from the spins will cancel each other out and give an overall zero magnetization at room temperature. These materials have small permeabilities, and, are often classified as paramagnetic materials above Néel temperature (T_N). The value of susceptibility has a unique temperature dependence that increases first by increasing the temperature until a certain limit is reached, known as Néel temperature (T_N). Beyond this temperature, the value of susceptibility decreases as thermal vibrations increase, and the material behaves like a paramagnet. (Figure 2.9)[27]

The susceptibility of an antiferromagnetic material far above the T_N is given by the following expression in equation (2.12),

$$\chi = \frac{C}{(T + T_N)} \tag{2.12}$$
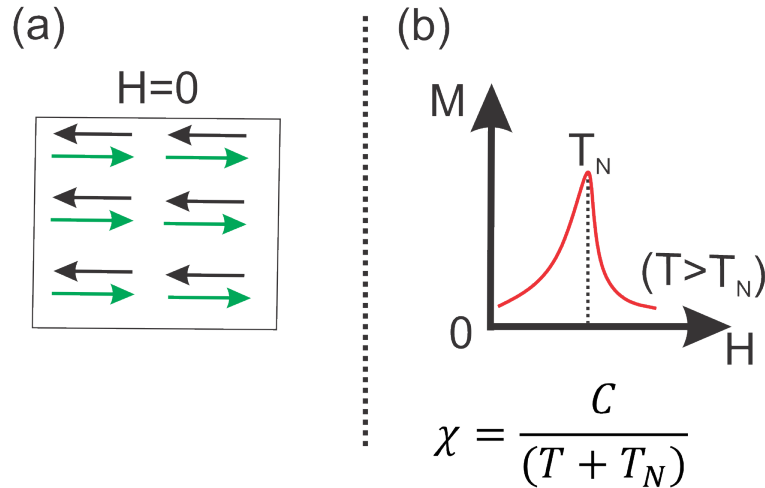
FIGURE 2.9: Antiferromagnetic material in the absence of magnetic field. (b) Effect of temperature on susceptibility far above the T_N

2.5.5 Ferrimagnetic materials

Ferrimagnetic materials are classified between ferromagnetic materials and antiferromagnetic materials. As in antiferromagnetic materials, the magnetic spins in ferrimagnetic materials are placed in parallel directions on different sub-lattices, but the magnitude of magnetization on these sub-lattices is not equal. That makes the net magnetization non-zero for the material (Figure 2.10). Since antiferromagnetic materials are not strongly magnetic and do not give rise to spontaneous magnetization, ferrimagnets are often compared to ferromagnetic materials due to their spontaneous magnetization at room temperature. Their spontaneous magnetization disappears above T_c, after which they become a paramagnet due to thermal disruptions in the magnetic spins. Ferrites are common examples of ferrimagnetic materials. The general formula for these ferrites is $MO.Fe_2O_3$, where M= zinc, cadmium, iron, nickel, manganese, or magnesium. There are generally two sub-lattice sites known as tetrahedral and octahedral sites in the crystal structure of these spinel ferrites or inverse spinel ferrites ($MnFe_2O_4$). In the case of magnetite Fe_3O_4 (inverse spinel), there are two ionic states for iron Fe^{2+} and Fe^{3+}. These ions are arranged in a sub-lattice in a way that out of sixteen, eight octahedral sites are occupied by the Fe^{3+} while the rest are occupied by Fe^{2+}. The other eight tetrahedral sites are occupied by Fe^{3+} ions (2.10 (b)). The opposing magnetic moments at tetrahedral and octahedral sites (Fe^{3+} interact through superexchange interactions, and couple antiferromagnetically that cancels their magnetic moments ($5\mu_B$). It leaves the eight Fe^{2+} ions on the octahedral sites that couple ferromagnetically through double exchange interactions via oxygen atoms with Fe^{3+} ions at octahedral sites.[36] These ions are responsible for the magnetization in magnetite ($4\mu_B$).[33] The magnetic interactions in Fe_3O_4 are shown in Figure 2.11. In Figure 2.10 (c) cubic spinel structure of zinc ferrite $ZnFe_2O_4$ is shown where Fe^{3+} ions couple antiferromagnetically on the octahedral sites via superexchange interactions. Whereas, zinc ions Zn^{2+} are

non-magnetic in nature and arranged on the tetrahedral sites. The value of the Néel temperature (T_N) is ~11K (below which it shows antiferromagnetic ordering).[37–39] The crystal structure of bulk manganese ferrite is partially inverse spinel that can be written as $(Mn_{1-x}Fe_x)_A[Mn_xFe_{2-x}]_BO_4$. Where A and B show the tetrahedral and octahedral sites. The value of the inversion parameter x can be up to 20% which is important to determine the magnetic moment of the $MnFe_2O_4$. It can be between $3\mu_B$-$5\mu_B$ depending on the degree of inversion.[40] Figure. 2.10 shows the complete spinel structure of $MnFe_2O_4$ that can have the highest magnetic moment $5\mu_B$ due to the absence of inversion.
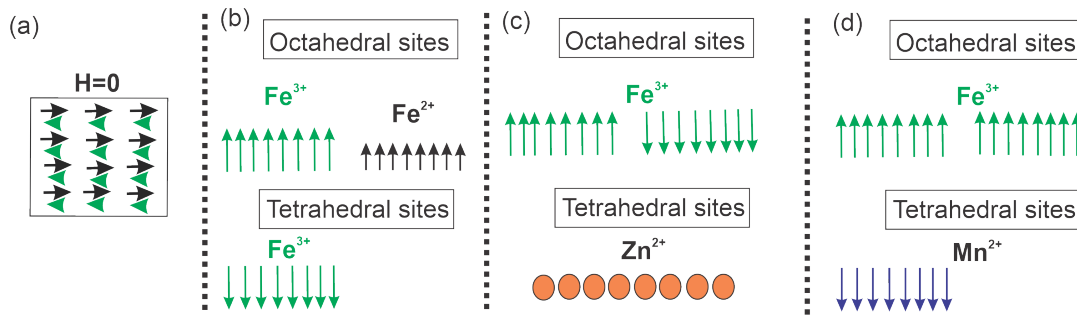
FIGURE 2.10: (a) Ferrimagnetic material in absence of magnetic field, (b) Magnetite sub-lattices showing magnetic moments of both Fe^{3+} and Fe^{2+} ions due to ferrimagnetic coupling in an inverse spinel structure, (c) Zinc ferrite sub-lattices showing antiferromagnetic coupling at octahedral sites and tetrahedral sites containing non-magnetic Zn^{2+} ions, and (d) Manganese ferrite sub-lattices showing ferromagnetic coupling between Fe^{3+} ions at the octahedral sites and antiferromagnetic coupling between Fe^{3+} at octahedral sites and Mn^{2+} ions at the tetrahedral sites in a spinel structure
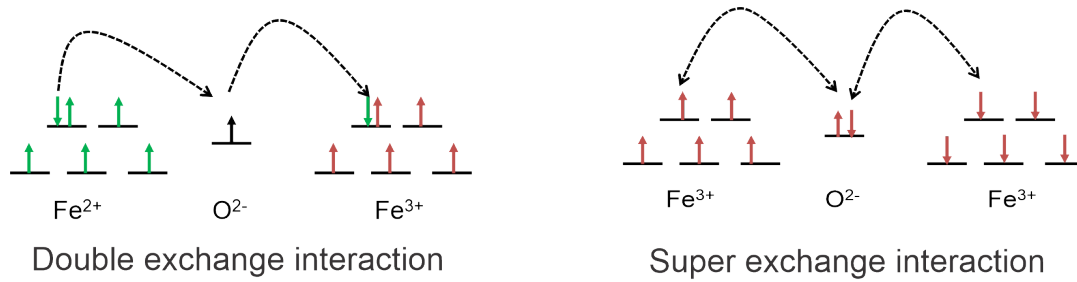
FIGURE 2.11: Magnetic interaction in magnetite

2.5.6 Superparamagnetic materials

Superparamagnetism is observed in small ferro or ferrimagnetic nanoparticles when the size of the nanoparticle is decreased to the single domain range. The magnetization of these nanoparticles is considered to be a single giant magnetic moment or super moment, that comes from the sum of individual moments of atoms within a particle. The magnetic response is characterized above the characteristic temperature known as blocking temperature (T_B) that originates from the magnetic anisotropy of nanoparticles that aligns the moments in the preferred orientation. In a non-interacting spherical nanoparticles system, the magnetic anisotropy energy (E_A) is proportional to the particle volume as shown by the equation (2.13) given below.

$$E_A = KV \tag{2.13}$$

Where K is the magnetic anisotropy of nanoparticles, and V is the volume of the nanoparticles. The whole expression KV represents the magnetic anisotropy barrier for a magnetic superparamagnetic nanoparticle system.

The thermal fluctuations in magnetic moments with increasing temperature play a very important role to understand the magnetic properties of superparamagnetic nanoparticles. At high temperatures, when the thermal energy is larger than the magnetic anisotropy energy ($k_B T \gg E_A$) the magnetic moments can randomly flip their direction showing paramagnetic-like behavior or superparamagnetic behavior. But, if the thermal energy is much lower than the magnetic anisotropy energy ($k_B \ll E_A$), the magnetic moments are believed to be in a block state in their anisotropic axis without switching the orientation. At finite temperature, the magnetic moments flip and reverse their direction and the time observed between two flips is known as Néel relaxation time (τ_N).[41] It follows the Arrhenius law and the expression for τ_N is shown in the following equation (2.14)

$$\tau_N = \tau_0 e^{\frac{E_B}{k_B T}} \tag{2.14}$$

Where τ_0 is the characteristic length of time for a material that varies between 10^{-9} to 10^{-10}s for different materials. Another important term is the measurement time, τ_m which is very important in determining the magnetic state of the material: if τ_m is greater than τ_N ($\tau_m \gg \tau_N$), the magnetic moments will fluctuate freely in a paramagnetic manner, i.e. the superparamagnetic state. If τ_m is much smaller than the τ_N ($\tau_m \ll \tau_N$), then the materials are said to be in a blocked state. The limit at which the $\tau_m \equiv \tau_N$ provides the definition of $_B$ that is shown in the following equation 2.15.[41]

$$T_B = \frac{kV}{k_B ln\frac{\tau_m}{\tau_N}} \tag{2.15}$$

The hysteresis curve for superparamagnetic materials shows negligible coercivity that differentiates it from other paramagnetic, ferro/ferrimagnetic materials.[34,

41]

2.6 Role of angular momentum in magnetism

The magnetic moment of an atom is a fundamental property of unpaired electrons in the partly filled electronic shells, and it depends on both spin angular momentum and orbital angular momentum of an electron. Orbital angular momentum ($\vec{L}$) of an electron is associated with the rotation of an electron in an orbit around the nucleus, whereas spin angular momentum ($\vec{S}$) is associated with the spinning of an electron around its axis. The total angular momentum of an atom is represented by J, and it is the sum of both its orbital angular momentum ($\vec{L}$) and spin angular momentum ($\vec{S}$) ((2.16)).

$$\vec{J} = (\vec{L} + \vec{S}) \tag{2.16}$$

Whereas, the total magnetic moment (m) is the sum of both total orbital magnetic momentum (μ_L) and spin magnetic momentum (μ_S) of electrons within an atom. It is shown by the equation (2.17) given below.

$$m = gJ\mu_B \tag{2.17}$$

Where μ_B is a constant known as Bohr magneton, which is used to describe the magnetic moment of an atom and g is the spectroscopic splitting factor, which is also called the g-factor. The value of the g-factor is given below in equation (2.18).

$$g = 1 + \frac{J(J+1) + S(S+1) - L(L+1)}{2J(J+1)} \tag{2.18}$$

If there is no net orbital contribution in the magnetic moment, then L=0, and J=S. In such a situation the value of g becomes g=2. But when the net spin contribution is zero when the spins gets canceled out, then J=L and g=1.[30]

2.7 Exchange interactions in magnetic materials

The magnetic moments of transition metal elements as well as ferrimagnetic materials are more greatly dependent on the electronic spin than the orbital angular momentum. Therefore, spin interactions are very important in determining the magnetic properties of atoms. For example, the potential energy (U_{ij}) of two neighboring atoms with spins S_i and S_j in a system is given as (equation (2.19)).[29, 42]

$$U_{ij} = -JS_i.S_j \tag{2.19}$$

Where J is the exchange integral that can be positive or negative depending on the spin exchange interaction on the neighboring atoms. If the two spins are arranged parallel with overall minimum energy then the value of J is positive. If the

spins are aligned in antiparallel directions to each other, the J becomes negative. Other exchange interactions are indirect exchange interactions that are explained below.[42]

2.7.1 Indirect exchange interactions

These interactions occur in a system where there is a long separation between the magnetic ions and direct exchange interactions are either absent or the value of their exchange integral is too small to be accepted. The indirect exchange interactions include superexchange interactions and double exchange interactions.

Superexchange interactions are mainly present in the insulators, where non-magnetic atoms are present between the magnetic ions. One such example is the manganese oxide ions, where non-magnetic oxygen atoms are bridged between magnetic manganese ions and are responsible for the magnetic interactions in such material (Figure 2.12).
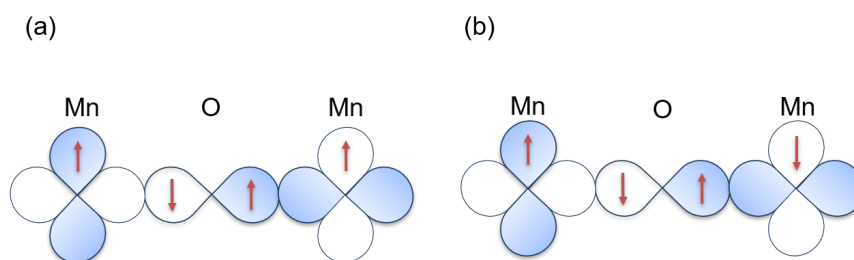
FIGURE 2.12: Superexchange interactions between Mn atoms through an oxygen atom (a) Ferromagnetic coupling (b) Antiferromagnetic coupling

In Figure 2.12, the d-orbitals of Mn atoms overlap with the p-orbitals of non-magnetic oxygen atoms. Due to this, the indirect interactions between two Mn ions give rise to two different types of magnetic ordering. The superexchange interactions are dependent on the magnitude of magnetic moments of interacting atoms, the orbital overlap between the non-magnetic atoms and the metal ions, and on the bond angle. For example, when the bond angle is at $180°$, the superexchange overlap gives rise to strong ferromagnetic interactions between two Mn ions as per shown in Figure 2.12. Whereas, antiferromagnetic ordering is favorable for the parallel orientation of magnetic ions as per shown in Figure 2.12.

Double exchange interactions are present in some oxides, where the ions of the same metal are present in different oxidation states. These interactions happen with the electron transfer between the magnetic ions via non-magnetic atomic orbitals that are bridged between two magnetic ions. There is a simultaneous transfer of two electrons in double exchange interactions and the example is shown in Figure 2.13.

In Figure 2.13, a spin-up electron hops from the bridging oxygen atom to Mn^{4+}, and is simultaneously replaced by another spin-up electron from Mn^{3+} ion without changing the spin direction. This hopping is responsible for the ferromagnetic alignment for such oxides due to double exchange interactions.
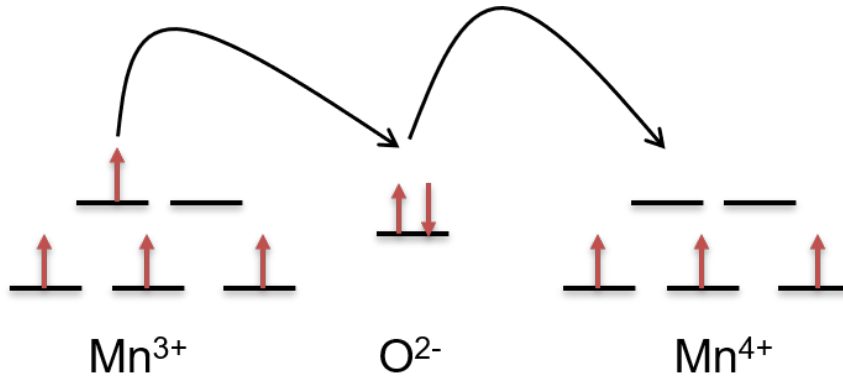
FIGURE 2.13: Double exchange interactions

2.8 Some other important terms

2.8.1 Exchange bias

When ferromagnetic material couples with an antiferromagnetic material through an interface, the exchange interactions cause a shift in the hysteresis along the field axis. This behavior is known as exchange bias ($H_e b$) behavior (Figure 2.14). When a saturating magnetic field is applied above the T_N temperature, it aligns the ferromagnet in the direction of the applied magnetic field. However, when this material is field-cooled, some magnetization remains pinned at small negative fields. This can only be removed when the applied magnetic field is large enough to reverse the direction of the ferromagnet towards the original positive direction. This gives a shift in the magnetization curve and is called exchange bias as per shown in Figure 2.14. Exchange bias can be simply explained by a model given for a ferro/antiferromagnetic interface exchange interaction in a thin film given below in equation (2.20),[43]

$$B_E = -HMt_f cos\theta - Jcos\theta + K_f sin^2\theta \tag{2.20}$$

Where B_E is the exchange energy, H is the applied magnetic field and M is the magnetization in the material. Other terms are t_f related to the thickness of the ferromagnetic film, J is the exchange integral between ferromagnet and antiferromagnet, and K_f is the uniaxial anisotropy of ferromagnet, and θ is the angle between M and K_f.

Exchange bias is always observed in thin magnetic layers, but it can also be present in magnetic nanomaterials, where spin defects are present due to spin disordered shells around a magnetically ordered core. The spin interactions between the magnetically ordered core and spin disordered shell cause the exchange bias for such systems.[43]
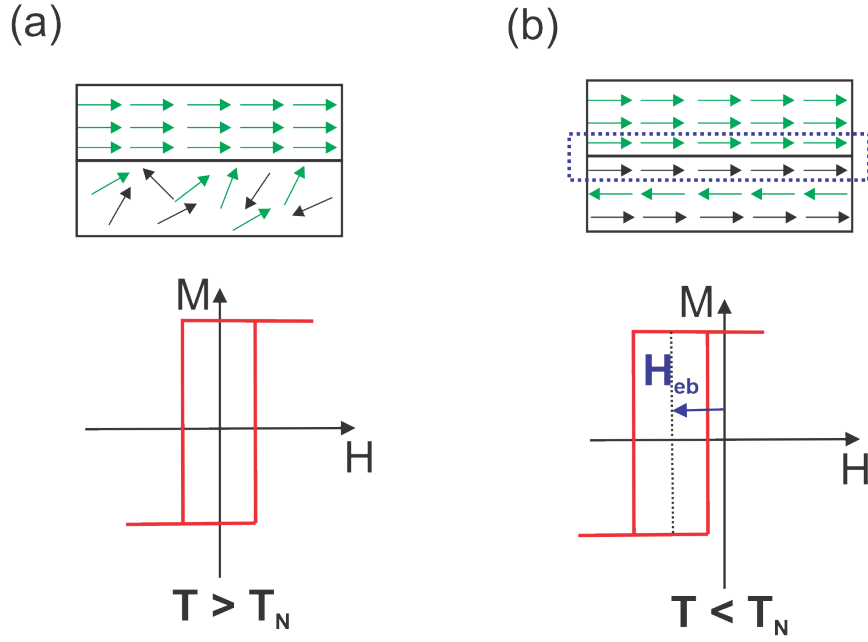
FIGURE 2.14: (a) Hysteresis curve below T_N with no hysteresis shift (b) Hysteresis shift (H_{eb}) towards left due to extra energy required to align material at interface above T_N

2.8.2 Magnetocrystalline anisotropy

The tendency of magnetic spins to align in the preferred direction of the crystallographic axis is known as magnetic crystalline anisotropy. Magnetocrystalline anisotropy is the intrinsic property of a material, which is caused by the interaction of spin magnetic moments with the crystal lattice (spin-orbit coupling). These interactions give rise to easy and hard directions for magnetization in a material.

When an external magnetic field is applied to a material, the magnetic spins tend to rotate in the direction of the applied magnetic field. Similarly, the orbit of the electrons also tends to rotate in the direction of the external field, but the strong coupling between the orbit and crystal lattice resists the rotation of the spin axis. Therefore, the amount of energy required to rotate the spins from their easy axis to the hard axis of rotation for magnetization is known as magnetocrystalline anisotropic energy. The application of a magnetic field at 90 degrees is required to rotate the magnetic spins from their easy axis to the hard axis of magnetization. In cubic systems, the additional energy density due to their magnetocrystalline anisotropy can be written as, (equation (2.21))

$$E = K_0 + K_1(a_x^2 a_y^2 + a_y^2 a_z^2 + a_z^2 a_x^2) + K_2 a_x^2 a_y^2 a_z^2 \qquad (2.21)$$

Where a_i are the directional cosines for magnetization with respect to the axis of thw crystal lattice, K_i is the magnetocrystalline anisotropy constant representing the zero (K_0), first (K_1), and second order (K_2) for magnetocrystalline anisotropy energy. Some materials have a small magnetocrystalline anisotropy and do not require

strong magnetic crystalline energy. Such materials are known as soft magnetic materials. Whereas, other materials with large magnetocrystalline anisotropy are called as hard magnetic materials.[42]

2.8.3 Demagnetization effects

The demagnetization effects are described by the non-uniformity of the induction within a magnetic material due to the magnetic leakage (lines of flux density B), which is dependent on the shape and size. For example, in ferro/ferrimagnetic materials, the domains tend to saturate in different directions and cause the non-uniformity of the magnetic field within the material. The demagnetizing field (H_d) is given by the following equation given below in equation (2.22) below.

$$H_d = -N_d M \tag{2.22}$$

Where N_d is the demagnetization factor, which is dependent on the shape of the magnetic body, and is easy to calculate for an ellipsoid. For ellipsoid, the sum of demagnetization factor along three orthogonal axis is constant.[30]

$$N_x + N_y + N_z = 1 \tag{2.23}$$

But for a sphere or spherical nanoparticle, the value of N_d becomes, (2.24).

$$N_{sphere} = \frac{1}{3} \tag{2.24}$$

The demagnetization stretches out the magnetization loops and cause a reduction in the measured susceptibility in comparison to the true susceptibility value as shown below in equation (2.25).[44]

$$\chi_{measured} = \frac{\chi_{true}}{1 + N \times \chi_{true}} \tag{2.25}$$

2.8.4 Bloch's temperature dependence

The magnetization of an ordered magnetic system follows a Bloch's temperature dependence that decreases with increasing temperature due to thermal fluctuations within magnetically ordered spins. Bloch's law for an ordered ferromagnetic material is shown in equation 2.26.

$$M_s(T) = M_s(0) \times [1 - \beta \times T^n] \tag{2.26}$$

where $M_s(0)$ is the magnetization at zero kelvin, β is the Bloch constant, T is the temperature, and n=3/2.[45] This Bloch expression can be fitted well with the saturation magnetization of the bulk materials. In the case of nanomaterials, the contribution from the spin disordered component is added to Bloch's equation which

is related to the magnetization from the misalignment of the surface spins or spin-disordered component. This can be modeled by using a phenomenological equation (2.27) below.[6, 46]

$$M_s(T) = M_{s,c}(0) \times [1 - \beta \times T^n] + M_{s,d}(0) \times exp(T/T_f) \qquad (2.27)$$

where, the first term, $M_{s,c}$ is the saturation magnetization from the spin-ordered core and described by using the Bloch function and the second term is from a spin-disordered shell $M_{s,d}$. $M_{s,c}$ is the spin-ordered core saturation magnetization at 0K, $M_{s,d}$ is the spin-disordered shell at 0K, and T_f is the characteristic spin-freezing temperature. Due to this a **meta-stable state or spin glass** arises in magnetic nanomaterials as the spins get frozen in random orientation than low energy configuration (ordered phase) due to frustrations in nanomaterials.[46] Figure 2.15 shows the spin-frustrated spherical nanoparticles with the magnetically ordered core.
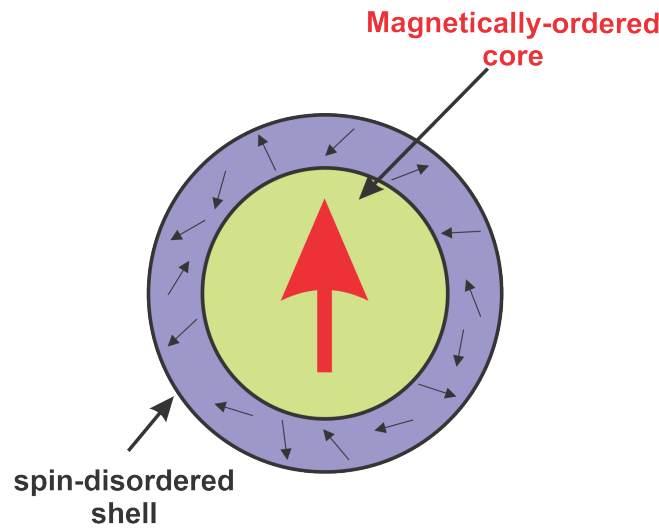
FIGURE 2.15: An illustration of spin-frustrated nanoparticle with magnetically ordered core

2.8.5 Zero field cooled-Field cooled (ZFC-FC) Curves

ZFC-FC curves are important in determining the superparamagnetic behavior of the nanomaterials from their M-H loop. In ZFC measurement the material is cooled down in the absence of the magnetic field, and then the magnetic response is recorded by applying a small magnetic field while heating up the sample. In FC, the sample is cooled down in the magnetic field (same strength as used for ZFC) and magnetization is recorded.[37] A typical example of the ZFC-FC curve is shown in Figure 2.16.
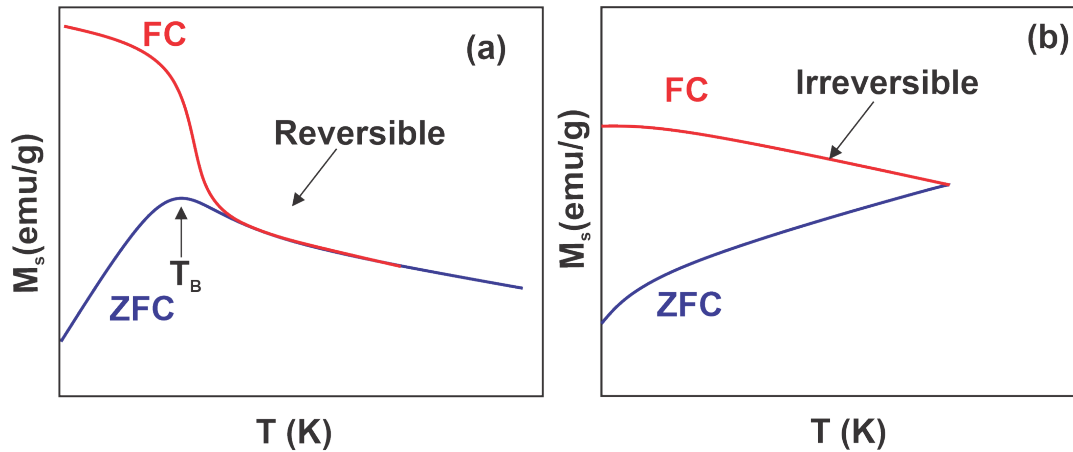
FIGURE 2.16: An illustration of ZFC-FC curves for a typical (a) superparamagnetic, and (b) ferromagnetic material

2.8.6 Hard and soft magnetic materials

The ferro/ferrimagnetic materials are classified as hard or soft magnetic materials depending on their response in an external magnetic field. When an external magnetic is applied to a material, and it retains the magnetization even after the removal of the magnetic field, then it is called a hard magnetic material or permanent magnet. These materials have a very large magnetic crystalline anisotropy and therefore show high values of coercivities, remanent magnetization, and exhibit large hysteresis curves (Figure 2.17 green curve). Due to this, these materials can store magnetic energy without getting drained after repeated use, and therefore can be used in storage devices, electric brakes, telephones, and loudspeakers. Examples of hard magnetic materials include high-carbon steels, rare earth elements, and their alloys.[47]
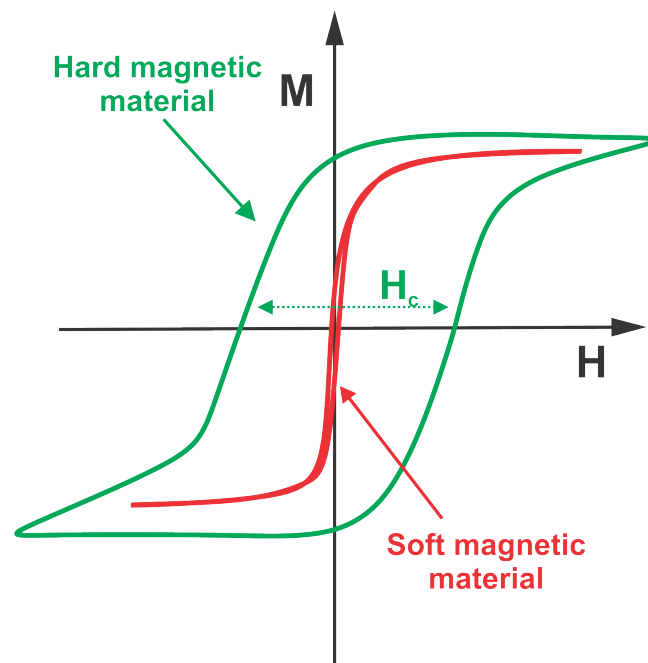
FIGURE 2.17: Hysteresis curves of hard vs soft magnetic material

On the other hand, soft magnetic materials suitable for commercial applications can be easily magnetized and demagnetized and show high permeabilities, high Curie temperatures, low magnetostriction, and negligible hysteresis losses. The hysteresis curves for the soft magnetic materials (in Figure 2.17 (red curve), show negligible coercivity and remnant magnetization (M_r).[48] These properties make them favorable to be used in the cores, loudspeakers, electric motors, and in the cores of inductive high-carbon systems where the power transfer is needed at the expense of minimum energy loss. Examples of soft magnetic materials include iron, silicon steel, ferrites, and bimetallic alloys of iron with cobalt and nickel.[48]

2.9 Soft magnetic materials for inductive applications

The soft magnetic materials in the cores of inductive coils can quickly change the direction of their magnetization with the applied magnetic field that is produced by the current flowing in the coils. The high permeability (μ) of these materials causes an increase in the magnetic induction within the transmitter coil, that is, when coupled with the receiver coil can transfer the energy through an air gap and boosts the performance of the inductive systems.

Another important parameter for effective and robust power transfer is the prevention of power losses at high operating frequencies. There are mainly two types of power losses involved in inductive applications.

1. **Hysteresis losses**

   These losses are caused by the irreversibility of MH curve (coercivity) in the core material operating at high frequencies in an inductive system. Thus, every time a material completes its cycle of magnetization, it will lose energy to be known as hysteresis loss.

2. **Eddy current losses**

   The eddy current losses are directly related to the resistivity of the core material. As the alternating current in the coil causes the generation of the magnetic field in the core material. According to Faraday's law of electromagnetic induction, the time-varying magnetic field causes the current to flow into the magnetic material. These current loops create a magnetic field in opposition to the change in magnetic flux, thus causing a power loss in the inductive system. Eddy-current losses usually increase with the square of operating frequencies.[49]

Soft magnetic materials have been classified on the basis of their magnetic properties which makes them favorable in different applications for optimum performance at a reasonable expense. These properties are given below in Table 2.1.[50]

TABLE 2.1: Magnetic properties of various soft magnetic materials[50]

Material	Permeability (μ) (10^3)	Coercivity (H_c) (A/m)	Electrical resistivity$(\mu$ Ωcm)	Curie temperature(T_c) (°C)	Magnetostriction (λ_s) (ppm)
Soft iron	10-50	4-80	10	771	-2
Silica steel	0.5-5	6	48	745	7
$Ni_{50}Fe_{50}$ permalloy	70	4-20	40-50	480	18
$Ni_{78}Fe_{17}Mo_5$ super-permalloy	80	0.6-2.5	110	570	0-2
Manganese zinc ferrite	0.5-10	10-100	10^8	150-250	±5
Manganese nickel ferrite	0.01-1	14-1600	10^{11}	120-500	-20

2.9.1 Soft iron

Soft iron cores consist of 99% very fine iron powder particles due to the higher permeability of iron materials. Iron has a very high coercivity that results in high core losses, operating even at low frequencies. These iron cores have been improved by compressing them into a pellet or thermally annealing them at room temperature to reduce their coercivities. The processing of iron powders can also reduce the overall permeability as compared to the raw iron material, and is not suitable for high-frequency applications.

2.9.2 Silicon steel

Silicon steel is an alternative to soft iron and is produced by mixing 3% silicon into the iron. This production is favorable for increasing the resistivity as well as the permeability of the material. Another improvement is observed by the invention of grain-oriented silicon steel, where grain growth is promoted along the easy axis of magnetization. Thus a material with a low magnetic crystalline anisotropy axis parallel to the magnetic field is fabricated that can be used at large scales in transformers. Today, silicon steel contributes towards major shares in the soft magnetic materials market due to its low cost and high permeability. However, it has a very low density, which gives high power losses at high frequencies. Therefore, the primary applications of silicon steels are in low-frequency (50-60 Hz) transformer cores. Recently, there have been attempts to improve the density of this material, but still, it is not effective to be used in high-frequency applications.[50]

2.9.3 Permalloy ($Ni_{1-x}Fe_x$)

Bimetallic $Ni_{1-x}Fe_x$ based soft magnetic materials are well known for their remarkable properties including high permeability, high Curie temperature, low coercivity, low magnetostriction[2] and energy losses. Generally, $Ni_{1-x}Fe_x$ alloys are classified on the basis of their metal ion fractions or based on their crystal system. The alloys containing 0.1-0.5 percent iron are called permalloys (from high permeability) and show high permeability at around x= 0.18-0.25. The alloys with 0.6-0.8 percent iron are called Invar alloys (from invariability) and are known to exhibit the zero coefficient of thermal expansion around x= 0.6-0.7. The crystal structure of these alloys also varies from body-centered cubic (bcc) to face-centered cubic (fcc) with increasing iron fraction up to $\sim$ 0.6.[51] (Figure 2.18 (a) and (b))

Similarly, the characteristic magnetic properties of the binary $Ni_{1-x}Fe_x$ alloys also vary considerably with increasing fractions of iron from 0.1-0.5. They exhibit very high permeabilities at about x$\sim$ 0.25 of iron. The reason behind such behavior is the presence of negligible magnetic crystalline anisotropy and magnetostriction that results in the easy axis rotation of domain walls and hence contributes to high

---

[2]Magnetostriction is the change in the dimensions of a ferro/ferrimagnetic material in response to the applied magnetic field.[49]
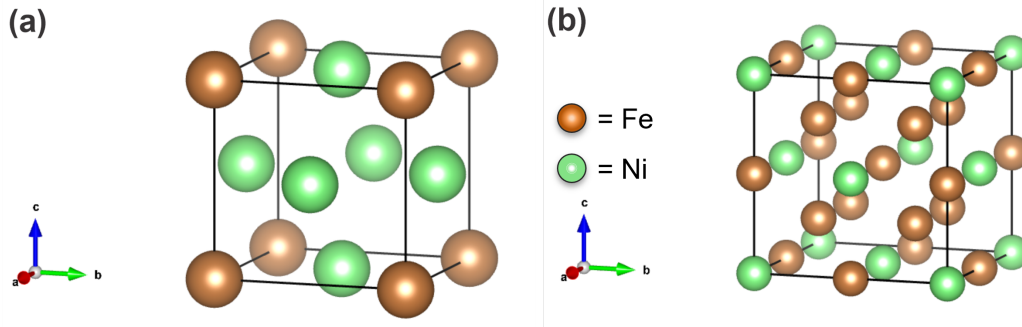
FIGURE 2.18: Crystal structure of (a) FCC ordered phase and (b) BCC ordered phase of NiFe alloy

permeability.[3] However, the metallic nature of $Ni_{1-x}Fe_x$ alloys in the bulk results in very low resistivity and can have hysteresis losses due to pinning effects in the domain wall motion.[52] Both of these factors can result in eddy-current losses and limits their broad range applications.

2.9.4 Soft ferrites

Soft ferrites contribute the second largest market share and are now abundantly used in the cores of inductive systems. They are ferrimagnetic in nature with the chemical formula $MO.Fe_2O_3$. Where M is the divalent metal cation (such as Fe^{2+}, Mn^{2+}, Zn^{2+}, Ni^{2+}, and Mg^{2+}) that is present on both tetrahedral sites (A) and octahedral sites (B) within the crystal lattice and trivalent metal ions (M^{3+}) are present at the tetrahedral site (A). These two ions are separated by the non-magnetic oxygen atoms that cause the superexchange interactions between A and B spin lattices for the overall magnetization in ferrites. They have high permeabilities and low coercivities that make them favorable materials to reduce eddy current losses. The density of ferrite materials is high as compared to silicon steel, which is advantageous to work at high-frequency applications.

Manganese zinc ferrite has been prepared for most applications in power electronics as it has high permeability. The substitution of Fe^{3+} ion with Zn^{2+} ion at the tetrahedral sites increases the antiferromagnetic coupling at B sites, which increases the net magnetization for $MnZnFe_2O_4$. Therefore, it has a high permeability, which reduces the hysteresis losses but still, manganese zinc ferrite has low resistivity, which results in eddy-current losses. An alternative to this is manganese nickel ferrite ($MnNiFe_2O_4$) which has a higher resistivity but it has comparatively less permeability which makes it unsuitable in inductive applications. Moreover, the brittleness of ferrites in bulk is not ideal with the inductive systems embedded within the roads.

The main challenges involved with the use of ferrite materials for robust power transfer applications include,

1. Thick and brittle in nature with low compaction density that can break easily under applied mechanical stress in the dynamic environment of inductive systems.

2. Hysteresis losses at low operational frequencies.

2.10 Nanostructuring of $Ni_{1-x}Fe_x$ alloys and ferrites

Recently, there has been an increased demand for the fabrication of compact cores, that are both effective and efficient for robust power transfer applications. This requires the miniaturization of core materials with low losses, working in a dynamic environment at both a broad range of temperatures and high frequencies. The core material should also be flexible and thin to address the issues with the mechanical strength and energy losses of existing ferrite materials. To address this, nanosized permalloy ($Ni_{1-x}Fe_x$) and soft ferrite (MFe_2O_4) materials are been researched to achieve high permeability and low coercivity. Their synthesis in nanodimensions is particularly interesting, as it can alter the magnetic properties due to size-dependent magnetization, spin glass transition, superparamagnetism, variable magnetocrystalline anisotropy, and high Curie temperature.[53]

There have been various reports on the fabrication of $Ni_{1-x}Fe_x$ nanoparticles by various methods to achieve high saturation magnetization, high resistivity, and low coercivity. For example, Qin. et al have prepared ferromagnetic $Ni_{1-x}Fe_x$ nanoparticles with x~20 with variable sizes and have investigated their magnetic properties as well as magnetic losses at different frequencies. The particle sizes were found to be between 20-440 nm, with the highest saturation magnetization for the sample having large nanoparticles. However, when these nanoparticles were mixed with the micron-sized iron particles, the maximum permeability was achieved by the sample having the smallest size. This sample has also shown reduced losses at increasing frequency due to the negligible hysteresis of small-sized $Ni_{1-x}Fe_x$ nanoparticles at room temperature.[52] Another report on the electrodeposited 200 nm $Ni_{80}Fe_{20}$ powder has shown a decrease in resistivity, and coercivity when the material is pressed into a compact pellet and thermally annealed at high temperatures. The saturation induction was also increased with compaction and sintering of the nanopowder.[54] Another report by Koh. et al for the fabrication of 50-150 nm thick $FeNi_3$ nanoparticles has shown the increased inductance up to 55% for on-chip radio frequency device when they used an insulating SiO_2 shell around NiFe nanoparticles.[55] Similarly, various other reports have shown the variable magnetic properties when they synthesized the $Ni_{1-x}Fe_x$ nanoparticles with varying x depending on the applications.[56–59]

Various reports on the fabrication of ferrites in nanodimensions are present in the literature. Various methods have been used to synthesize magnetic ferrite (MFe_2O_4) nanoparticles to achieve high magnetic saturation moment, low coercivities, and low remnant magnetization for spontaneous magnetization. [53, 60, 61] The magnetic

properties of these ferrites can be tuned depending on their shape and diameter. A hydrothermal-assisted synthesis of $MnFe_2O_4$ nanoparticles has been reported and the resulting nanoparticles were tested for their magnetic properties in pristine form and compared their magnetic properties with a stabilizer coating form. Both of the samples have shown negligible coercivity and high saturation moment. Although there was a slight reduction in the saturation magnetization for the coated sample, the magnetic behavior was unchanged for the desired applications.[62] Other reports have shown the increase in the resistivity of $MnFe_2O_4$ nanoparticles by trivalent rare earth ions doping (Gd^{3+}, Y^{3+}), that can replace the Fe^{3+} ions at the octahedral sites, hence resistivity increases in the absence of charge carriers from Fe^{3+} ion. [63–65]

> **Characteristics of an ideal core material**
> 1- Thin, unbreakable, and flexible.
> 2- Cost effective.
> 3- Low coercivity.
> 4- High permeability.

2.10.1 One dimensional nanofibers

Recently, attention has been drawn to the fabrication of one-dimensional nanostructures including nanotubes, nanowires, and nanofibers as they show distinct properties from their bulk counterparts. Among these materials, one dimensional nanofibers have gained importance due to their longitudinal directions and high shape anisotropy that is favorable for the flux guiding applications, that includes magnetic sensors[4], thin RF antenna[66], and RF shielding.[67, 68] Their advantages include a large surface area and being able to produce very thin sheets for compact magnetic devices. The use of magnetic nanofibers in these applications is also advantageous because the eddy current losses are significantly reduced when compared with the bulk compounds.

The reduction in hysteresis losses can be possible by creating magnetic nanofibers containing superparamagnetic nanoparticles. Superparamagnetic nanoparticles display negligible hysteresis above their blocking temperature. This behavior has been reported in the previous literature, where thin layers of $Ni_{1-x}Fe_x$ nanoparticles show negligible hysteresis above T_B while still with reasonable susceptibility[6] Magnetic nanofibers composed of nanoparticles can further reduce eddy current losses due to higher resistivities from enhanced carrier scattering in non-conducting polymers[69], where the nanoparticles are separated at certain distances from each other. This distance can affect the electrical conductivity, and hence improves resistivity for the materials.

2.11   Aims and objectives

The aim of this thesis was to prepare the metallic ($Ni_{1-x}Fe_x$), and semi-conductor ($MnFe_2O_4$, $MnFe_{2-x}Sm_xO_4$) magnetic nanomaterials in thin dimensions for their potential applications in wireless charging systems. For this reason, the following research has been undertaken,

1. Synthesis of bimetallic $Ni_{1-x}Fe_x$ nanofibers with varying x from 0.1 to 0.5.

2. Synthesis of semiconducting $MnFe_2O_4$ nanofibers.

3. Synthesis of semiconducting Sm^{3+} doped $MnSm_xFe_{2-x}O_4$ nanofibers.

The first objective was to fabricate the polymer nanofibers containing $Ni_{1-x}Fe_x$ nanoparticles by using an electrospinning method at varying fractions of x from x∼0.1 to x∼0.5. To my best knowledge, there have been no good quality reports for the fabrication of bimetallic $Ni_{1-x}Fe_x$ nanofibers by the electrospinning method. There has been only one report in the literature that showed the formation of a brittle $Ni_{1-x}Fe_x$ mat rather thin isolated nanofibers at x=0.53. [5] The advantages of these thin isolated sheets of $Ni_{1-x}Fe_x$ nanofibers include the low eddy current losses and the possibility of flux guidance in long dimensions. Bulk $Ni_{1-x}Fe_x$ is very interesting as it shows the small coercivity at x∼0.2-0.25, and high magnetic moment at x=0.5.[70] This gives a range in x to determine the effect of iron fraction in nanodimensions. For this reason, $Ni_{1-x}Fe_x$ nanofibers at x∼0.1, x∼0.2, and x∼0.5 are prepared to see what happens to the structural properties at increasing x fractions, what fraction gave the highest magnetic moment, and how increasing x changes the magnetic properties.

The second objective was to synthesize the $MnFe_2O_4$ nanofibers as $MnFe_2O_4$ is a known commercially available soft magnetic material. There have been some reports in the previous literature on the synthesis of manganese ferrite nanofibers[71–76], but to my best knowledge, there have been no good quality reports on the magnetic analysis of $MnFe_2O_4$ nanofibers. Therefore, the objective of this study was to synthesize $MnFe_2O_4$ nanofibers by the electrospinning method at two different annealing temperatures. The effect of thermal processing on the nucleation of $MnFe_2O_4$ nanofibers was studied, that what happens to the magnetic properties of these $MnFe_2O_4$ nanofibers when the annealing temperature was varied, and what were the possible reasons for any similarities or differences these nanofibers at two different temperatures.

Third objective was to synthesize Sm^{3+} doped $MnSm_xFe_{2-x}O_4$ nanofibers at varying x. To the best of my knowledge, there have been no reports on the Sm^{3+} doping in the $MnFe_2O_4$ nanofibers in the previous literature. $MnSm_xFe_{1-x}O_4$ nanofibers at varying fractions of x to x= 0.06, 0.1, 0.2, 0.25 are prepared for the first time. It is studied what happens to the structural properties at increasing dopant fractions. How were they different from the undoped sample. What happens to the magnetic

properties and what can be the plausible explanation for any similarities or difference in these samples.

Preface

The next chapter includes the experimental techniques and characterization used for the prepared $Ni_{1-x}Fe_x$, $MnFe_2O_4$, and $MnSm_xFe_{1-x}O_4$ nanofibers. Experimental techniques including electrospinning parameters, chemicals, and thermal treatment are discussed for these nanofibers. Characterizations methods including SEM, TEM, XRD, TGS/DSC, and MPMS measurements are discussed in detail.

Chapter 3

Experimental techniques and characterizations

3.1 Electrospinning method

Electrospinning is derived from the term called "electrostatic spinning", which is used to fabricate very thin smooth surfaced fibers from polymers, ceramics, or different materials. This method has been used for over 100 years but gained primary importance for its applications during the past 20 years. The first patent for electrospinning was filed by John Francis Coley in 1900.[77] This discovery has led many scientists to investigate and explore more about electrospinning. In 1960, Sir Geoffrey Taylor described the formation of the Taylor cone from a single droplet under the effect of electric potential.[78, 79] Electrospinning has gained popularity due to its low operational costs, large-scale synthesis, and easy synthesis.

The electrospinning technique has now been used for various applications from the micro to nano-scaled fibers in drug delivery[80], electronic components[81], fuel cell membranes[82], wastewater treatments[83], and in biomedical applications.[84] The simple principle of the electrospinning technique is based on the preparation of solutions of metal/polymer blends or composites with a reasonable viscosity for electrospinning under the influence of electric charge.[85, 86]

The main components of an electrospinning set-up are a high-power voltage source, a syringe pump, a syringe with a needle, and a collector for fibers or a rotating drum. The schematic illustration of an electrospinning set-up is shown in Figure 3.1. The viscous solution is prepared and loaded in the syringe pump, after which high voltage is used to overcome the surface tension of the solution at the apex of the needle to form a Taylor cone. The solution breaks down into spiral threads and gets collected on the rotating drum. Different mats of random or aligned orientation can be produced by the electrospinning technique.[78, 87] The use of a cylindrical drum collector with a thin wheel and sharp surfaces is advantageous for the production of orientated thin nanofibers under the effect of the applied electrical field. In most cases, aluminum foil is used to wrap around the rotating drum to collect fibers. It is preferred due to its conductive nature which facilitates the collection of a charged mat of nanofibers on the surface of a rotating drum.
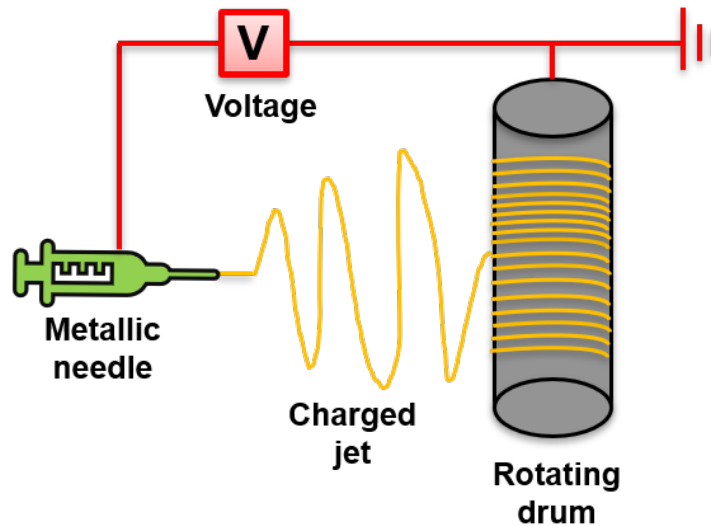
FIGURE 3.1: A typical electrospinning set-up

Electrospinning is the simplest technique to produce continuous fibers from the semi-micron to nanometer dimensions. Other benefits of electrospinning include flexibility, affordability, and versatility in materials selection including polymers, ceramics, composites, and semiconductors. Some other methods include phase separation[88], self assembly[89], template synthesis[90], and drawing have also been used for fiber production. But the slow production in phase separation, selectivity and the complications in self-assembly and drawing, and discontinuity for fiber lengths in template synthesis makes them unfavorable for nanofibers synthesis.[91]

In electrospinning, three important factors are the solution parameters, setup parameters, and ambient parameters which need to be optimized for the fabrication of continuous and smooth nanofibers.[92] (Figure 3.2)
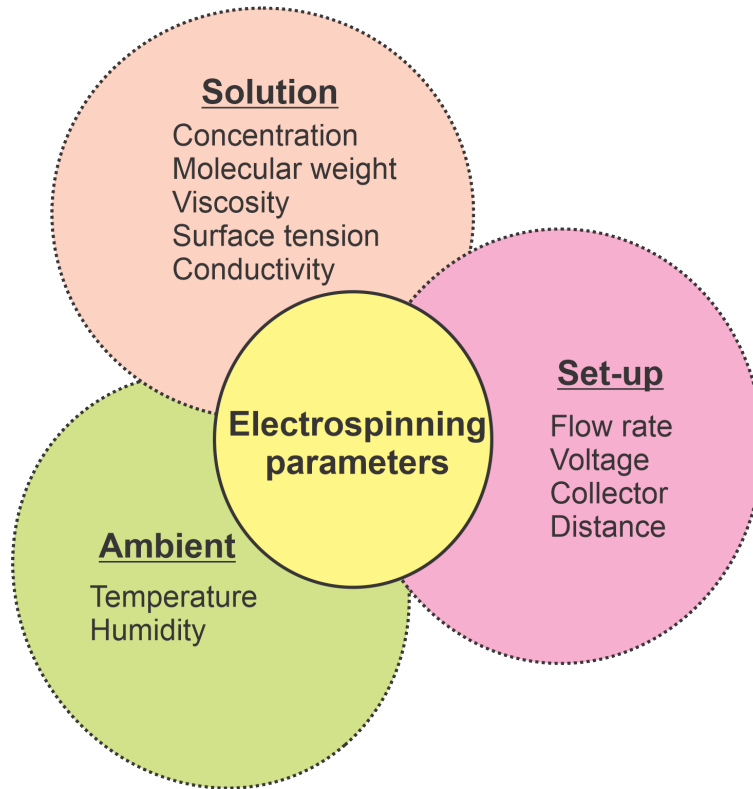
FIGURE 3.2: Electrospinning parameters

3.1.1 Solution parameters for nanofibers

Solution parameters for electrospinning include solvent, solution conductivity, concentration, the molecular weight of the polymer specie, viscosity, and surface tension of the given solvent. These parameters are important for solutions preparation in electrospinning.[92, 93]

Solvent selection is a significant parameter in the electrospinning technique, which requires a suitable solvent that is compatible with the given polymer. According to the solubility principle," like dissolves like", so the solvent should have similar solubility parameters to dissolve a polymer.[92, 93] The thermodynamic solubility of a particular polymer depends on the following expression as given in equation (3.1) below,

$$\Delta G = \Delta H_{mix} - T \Delta S_{mix} \tag{3.1}$$

Where ΔG is the Gibbs free energy of mixing, ΔH_{mix} is the change in enthalpy, T is the absolute temperature, and Δ S is the entropy change for a given solution. A negative value of ΔG is favored for the smooth dissolution of the polymer in the solvent.[94] In most systems, the cohesive energy density (CED) [1] of polymers is important for the solvent selection. To understand this, Hansen divided the total

---

[1]Cohesive energy density (CED)= The energy required to break the inter-molecular interactions to dissolve the polymer

cohesive energy (E_t) into three major components as per shown in the following equation (3.2) below[94, 95],

$$E_t = E_d + E_p + E_h \tag{3.2}$$

Where E_d is the component of dispersion, E_p is the component of polarity, and E_h represents the component of hydrogen bonding. Hansen's solubility parameters (HSPs) were derived by dividing this equation(3.2) by the molar volumes and taking the sum of the square roots of these components as shown in the equation (3.3).[94, 95]

$$\delta_t^2 = \delta_d^2 + \delta_p^2 + \delta_h^2 \tag{3.3}$$

The values of the solubility parameters of a solvent should be similar to the polymer's solubility parameters for greater solubility. The HSPs values for a given polymer (PVP) and solvents, that are used in this dissertation are given below in Table 3.1. [94, 96]

Units for Hansen solubility parameters

The units for the HSPs are similar to the units of solubility parameters as per the given equation (3.4).

$$\delta = (CED)^{0.5} = [\frac{\Delta E_v}{V_m}]^{0.5} \tag{3.4}$$

Where V_m is the molar volume, ΔE_v is the evaporation energy, therefore units are $(J/cm^3)^{0.5}$, or (cal/cm^3), or $MPa^{0.5}$.[95]

Conductivity of the solution should be reasonable for the production of a charged jet in an applied electric field. A solvent with a high dielectric constant is advantageous to obtain a high density of charges at the ejected jet surfaces for better stretching and uniformity in the electrospinning. Therefore, various precursors, ionic salts, or organic acids are used in combination with the polyelectrolytic[2] polymers for the fabrication of smooth fibers.[92, 93]

Concentration of the solution for electrospinning should be optimised for the fabrication of smooth nanofibers. At low concentrations, electrospray containing micro/nanodroplets is obtained on the rotating drum whereas, at high concentrations mixture of beads and fibers is obtained.[92, 93]

Molecular weight of the polymer is an important factor to determine the morphology of the prepared nanofibers. At a low molecular weight of the polymer,

---

[2]Polyelectrolytic= A polymer of electrolytes with several repeating chains that when dissolved is responsible for the conductivity of a solution

beads are obtained in the fibers whereas, at high molecular weight smooth fibers can be obtained. However, the molecular weight should not be too high as it may form micro-ribbons or patterned fibers instead of nanofibers.[92, 93]

Viscosity is closely related to the molecular weight of the polymers for the fabrication of nanofibers. It is a very critical parameter to determine the fabrication of smooth nanofibers, as at low viscosity the formation of beads is observed whereas, at very high viscosity the electrospinning is not feasible due to difficulty in ejection from the needle.[92, 93]

3.1.2 Set-up parameters

These electrospinning parameters include flow rate, voltage, collector, and distance between the tip of the syringe, and the collector.[93]

Flow rate has a significant effect on the formation of thin nanofibers as it gives significant time to the polymer solution for polarization. The high flow rate can lead to the formation of beaded nanofibers.

Voltage role in the formation of smooth nanofibers is not certain, as it is dependent on the other solution parameters: viscosity and molecular weight of the polymer. But the fabrication of smooth nanofibers is facilitated only by the applied voltage, which is greater than the threshold value to form the charged jet.[93]

Collector is the conductive substrate used for the collection of the electrospun nanofibrous mat during electrospinning. In general, an aluminum foil is wrapped around the collector or is used as the collector for the nanofibers. In this research, the electrospinning set-up was wrapped with an aluminum foil around the rotating drum for the collection of electrospun sheets from the electrospinning.[93]

Distance between the tip of the syringe and collector can also affect the morphology of electrospun nanofibers. It is found that at very short or very long distances, beaded nanofibers are obtained. Therefore, it should be optimum enough to facilitate the formation of smooth nanofibers.[93]

3.1.3 Ambient parameters

These parameters include the humidity and temperature of the surrounding environment for electrospinning. Both of these parameters should not be too low or too high for the fabrication of smooth nanofibers. The temperature should not be very high to cause the rapid evaporation of solvent at high viscosity or too low for less viscous solutions. Similarly, humidity should not be very low or too high, if it's too

low then it can lead to the rapid removal of solvent and if it's too high then it can lead to the formation of thick nanofibers.[97]

3.2 Materials and Methods

3.2.1 Chemicals

Nickel (II) acetate tetrahydrate ($Ni(OCOCH_3)_2 \cdot 4 H_2O$) 98% was purchased from Merck. Iron (III) nitrate nonahydrate ($Fe(NO_3)_3 \cdot 9 H_2O$) $\geq$98%, Iron (III) acetylacetonate ($Fe(C_5H_7O_2)_3$) 97%, Polyvinylpyrrolidone (PVP) (C_6H_9NO) average Mw$\sim$1,300,000 by LS method[3] were purchased from the Sigma-Aldrich. Glacial acetic acid was purchased from Carlo Erba. Methanol 99.9% was purchased from the Fischer chemical. Dimethylformamide (DMF) 99.8% was purchased from Acro seal ®. All these chemicals were used in the preparation of $Ni_{1-x}Fe_x$ nanofibers.

Some additional chemicals included manganese (II) nitrate tetrahydrate ($Mn(NO_3)_2 \cdot 4 H_2O$) 99% and samarium (III) nitrate hexahydrate ($Sm(NO_3)_3 \cdot 6 H_2O$) 99.9% were purchased from Acros Organics and used in preparation of the $MnFe_2O_4$ and $MnSm_xFe_{2-x}O_4$ nanofibers.

Tha HSPs values for the PVP, and both solvents methanol, and DMF are given below in Table 3.1

Material	δ_d (MPa$^{1/2}$)	δ_p (MPa$^{1/2}$)	δ_h (MPa$^{1/2}$)
PVP	15.5	11.7	8.6
Methanol	14.7	12.3	22.3
DMF	16.4	11.4	9.2

TABLE 3.1: Hansen's solubility parameters for the PVP and solvents used

3.2.2 Solution preparation

A homogeneous solution of metal ions and polymer with reasonable viscosity is required for the electrospinning method. The fabrication of nanofibers is facilitated with the transfer of this solution in a syringe which is attached in the electrospinning set-up. In this research, various solution mixtures were prepared by first dissolving the metal precursors in a common solvent separately, and then adding them together in required fractions with the addition of polymer. Table 3.2 represents the combination mixtures of homogeneous solutions prepared for fabrication of $Ni_{1-x}Fe_x$ nanofibers with varying x. The detailed synthesis and characterizations for these nanofibers are discussed in Chapter 4 and Chapter 5.

---

[3]LS method=light scattering method to determine the average molecular weight of polymers that depends on the degree of polymerization (DP) of their monomer units)

x	Nickel source	Iron source	Solvent	Sections
0.1-0.2	$Ni(OCOCH_3)_2 \cdot 4\,H_2O$	$Fe(NO_3)_3 \cdot 9\,H_2O$	Methanol	Section 4.2
0.5	$Ni(OCOCH_3)_2 \cdot 4\,H_2O$	$Fe(C_5H_7O_2)_3$	DMF	Section 5.2

TABLE 3.2: Homogeneous mixtures for electrospinning of $Ni_{1-x}Fe_x$ nanofibers with varying x

Similarly, homogeneous mixture for the fabrication of $MnFe_2O_4$ and samarium doped manganese ferrite nanofibers $MnSm_xFe_{2-x}O_4$ were prepared from their respective metal ion salts as per shown in the Table 3.3. The detailed synthesis and characterization are discussed in the Chapter 6.

Manganese source	Iron source	Solvent	Section
$Mn(NO_3)_2 \cdot 4\,H_2O$	$Fe(C_5H_7O_2)_3$	DMF	Section 6.2

TABLE 3.3: Homogenous mixtures for electrospinning of $MnFe_2O_4$ nanofibers

The homogeneous mixtures for samarium doped manganese ferrite nanofibers ($MnSm_xFe_{2-x}O_4$) with varying x were prepared by using the same metal ions sources for iron and manganese, but samarium nitrate ($(NO_3^-)_3Sm$) was used for samarium source (Table 3.4). The experimental and characterization details are discussed in Chapter 7.

x	Manganese source	Iron source	Samarium source	Solvent	Section
0.06-0.25	$Mn(NO_3)_2 \cdot 4\,H_2O$	$Fe(C_5H_7O_2)_3$	$Sm(NO_3)_3$	DMF	Section 7.2

TABLE 3.4: Homogenous mixtures for electrospinning of $MnSm_xFe_{2-x}O_4$ nanofibers

3.2.3 Electrospinning of prepared solutions

These homogeneous mixtures were transferred in a 10 mL syringe with 22-gauge fitted needle attached in the electrospinning set-up. The rotating drum was wrapped with the aluminum foil that was used for the collection of nanofibrous sheets after electrospinning. Various parameters including flow rate, voltage, and distance from the needle to the drum were optimised to get nanofibrous mats. The details of these parameters are explained in the experimental sections of Chapters 4, 5, 6, and 7.

3.2.4 Thermal treatment

The electrospun mats were collected from the electrospinning set-up and first placed in a vacuum oven as shown below in Figure 3.3 (a). These mats were placed for

overnight drying under a vacuum when methanol was used as a solvent. DMF-based samples were dried at 150°C at 0.05 Mpa pressure. These conditions were optimised to evaporate the solvent before thermal processing at high temperatures.
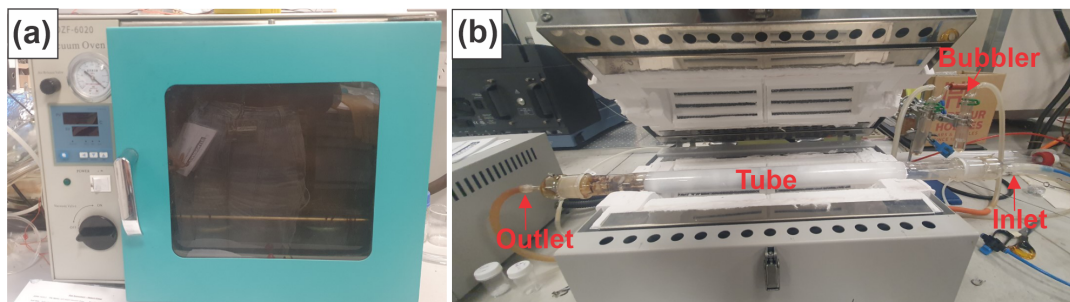
FIGURE 3.3: (a) Vacuum oven (b) Tube furnace for annealing

Figure 3.3(b) shows the tube furnace that was used for the thermal processing of prepared nanofibers. The inlet of this furnace was attached to the inert gas, and the outlet was attached at one side to the two-armed silicon oil bubbler to control the flow rate of the gas. The inert gas flows through the set-up and goes to the outer atmosphere after passing through the bubbler from its other arm. The tube furnace has a proportional integral derivative (PID) controller attached to it that can hold the furnace at the desired temperatures. This controller can run a single program with up to 8 ramp/dwell segments.

The details of the temperature profiles used for the thermal annealing of nanofibers are discussed separately with the experimental in upcoming chapters.

3.3 Characterizations

3.3.1 Scanning electron microscopy (SEM)

In SEM, the surface and structural analysis of all prepared nanofibrous samples was obtained by using secondary electrons, backscattered electrons, and energy-dispersive X-ray spectroscopy from the sample. The incident electron beam in SEM interacts with the surface atoms and produces various types of signals depending on the depth of the electrons within the sample. Figure 3.4 (a) and (b) shows the penetration depth of electrons within the sample that produces various types of signals.[98, 99]

Secondary electrons are the lowest energy electrons, that are knocked out from the surface of the sample when an electron beam from the source (electron gun) strikes the sample's surface. The energy of these electrons is very low $\sim$ 50 eV, which limits their mean free path within the surface. Therefore, it can only penetrate through a few nanometers of the surface and give secondary electron images (SEI) images. Since they are highly localized on the specimen surface, therefore they can provide high-resolution images. The quality of the image gets better if a greater number of secondary electrons hits the detector.[98, 99]
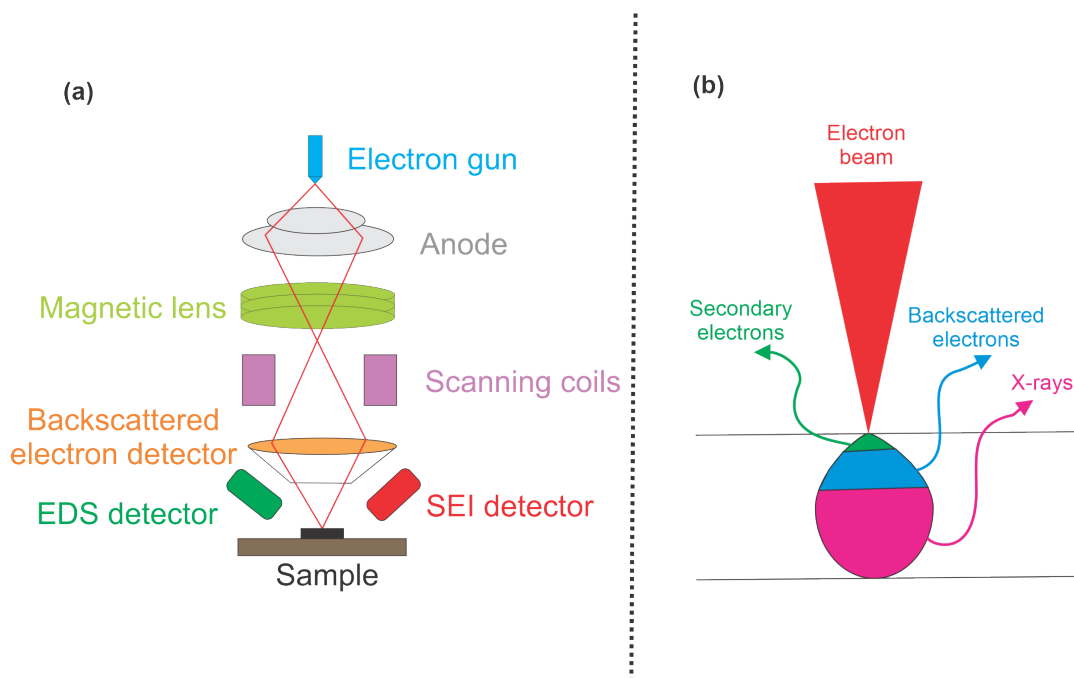
FIGURE 3.4: Scanning electron microscopy (a) Set-up (b) Electron beam penetration within a sample

Back-scattered electrons (BSE) are higher in energy than the secondary electrons and can provide some details of the sample through penetrating in the depth of the sample layers. Backscattered electrons are sensitive to the atomic number of the atoms and a high atomic number is favored to get bright images for the material. As the BSE are the result of the elastic collision of incident electrons to the atoms and larger atoms can scatter more electrons than the lighter atoms. Therefore, the volume of the backscattered electrons is proportional to the atomic number of the elements within a sample. The image provided by BSE provides more details about the composition of the sample and is called a COMPO (from composition) image. The resolution of a COMPO image is comparatively less as compared to the SEI image as it comes from the larger volume of the sample.[98, 99]

Characteristic X-rays are emitted when an inner shell electron is removed by the high-energy incident electrons that cause a high-energy electron to fill the shell and release energy. This energy or characteristic X-rays is measured by the energy dispersive X-ray spectroscopy (EDS) to provide the elemental abundance within a sample and to map their distribution.[98, 99]

3.3.1.1 SEM analysis of samples

A JEOL 6500F SEM was used to analyse the surface, orientation, and elemental composition of the prepared nanofibers. A small cross-sectional area of the prepared sample was placed on a 12 mm stab holder with the help of tweezers. The sample was attached to the surface of the stab with the aid of carbon tape and placed overnight under a vacuum at room temperature. All of the prepared samples were

coated with carbon to achieve good-quality imaging in SEM. The obtained SEI images were further manipulated by ImageJ software to determine the mean diameters of the nanofibers. Different area images have been used to calculate the mean value and the standard deviation for the diameters of prepared nanofibers by using the following formula in equation (3.5) given below.[100]

$$S = \sqrt{\frac{\Sigma_i (X_i - \bar{X})^2}{n-1}} \tag{3.5}$$

where n is the number of data points, X_i is the values of each data point, and $\bar{X}$ is the mean value for these data points.

The mean direction is also calculated by using various SEI images from SEM and taking one reference axis (x-axis) with respect to the other axis (y-axis) which is varied to the direction of the propagation of these nanofibers. EDS analysis and SEM maps were used to determine the elemental composition of all the prepared samples.

3.3.2 Transmission electron microscopy (TEM)

TEM is a high-resolution and very powerful tool for the detailed analysis of materials. In comparison to SEM, a very high-energy electron beam is used in TEM to probe through the very thin layers of the sample. It has different operating modes including high-resolution imaging, scanning TEM imaging (STEM), and diffraction spectroscopy.[101]

In conventional **TEM imaging**, the beam of electrons is focused by using a high condenser aperture that can eliminate the high-angle electrons to focus the beam on a cross-sectional area of the sample. The electron beam interacts with the sample and the transmitted beam from the sample is focused by an objective lense to create an image. (Figure 3.5)
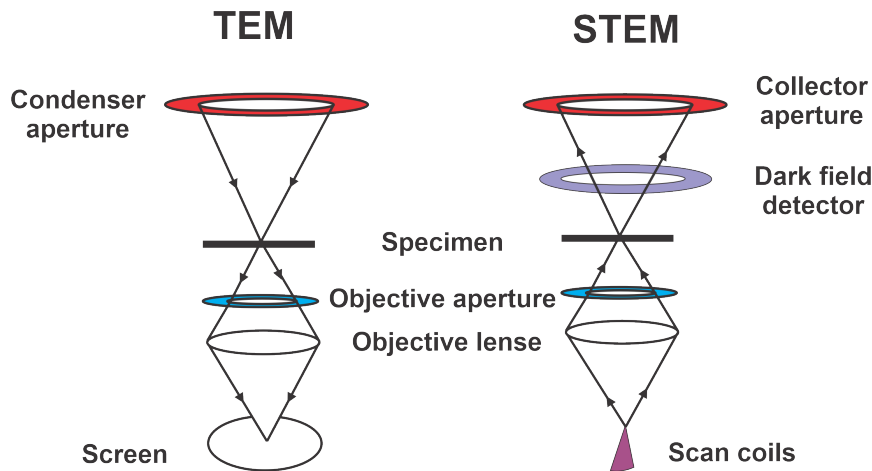
FIGURE 3.5: A schematic illustration of TEM and STEM mode

The **STEM mode** in TEM uses scanning coils to deflect the beam of electrons to focus on a fine spot (typical spot size 0.5-2nm) for scanning over the sample in a raster illumination system. This rastering of the image provides details about energy dispersive X-ray spectroscopy (EDX) and spectroscopic mapping of the sample. In STEM mode, two types of images are produced that depend on the type of detector, where one is called the bright field image and the other is the dark field image. In a bright field image, the illuminated area of the sample appears darker in contrast to the bright background whereas, in a dark field image the area of the sample appeared brighter in contrast to the dark background.[101] (Figure 3.5)

The **diffraction mode** of the TEM uses a selected area aperture to focus the electron beam onto the crystalline sample, and the scattered electrons from the atomic planes within a crystal are projected on the screen for the evaluation of crystalline planes and it's orientation.[101]

3.3.2.1   TEM analysis of samples

A high-resolution JEOL JEM-2100 TEM machine was used to characterize the prepared nanofibers. A small cross-sectional area of the sample was placed using tweezers in a 1.5 mL Eppendorf sample vial and dispersed in ethanol using a sonication bath. A pasture drop pipette was used to pour a small drop of the sample onto a carbon-coated 3mm copper grid. This sample was dried in air and plasma coated before insertion in the TEM machine for analysis.

TEM imaging at high resolution was used to fully resolve the nanostructures in terms of their size dimensions, and morphology. To investigate the size distributions, ImageJ software was used.

STEM mode was used for the elemental mapping within nanofibers as well as the elemental analysis at high magnifications.

Diffraction mode or SAED (Selected Area Electron Diffraction) mode was used to analyse the crystallinity of the samples. All prepared samples were cubic in nature, therefore the lattice parameters of a cubic system were used to determine to the lattice parameters of the crystalline nanomaterials in the samples. The formula used to determine the lattice parameters is given by the equation (3.6).[102]

$$\frac{1}{d^2} = \frac{h^2 + k^2 + l^2}{a^2}$$

(3.6)

d-spacings from the SAED patterns

The d-spacings were calculated from the diameter of the diffraction rings that were given as the reciprocal in real space. Therefore, d-spacings from each ring were calculated by taking the inverse of the diameter, or the distance between 2-spots on the diffraction ring as given in the equation (3.7).

$$\text{d-spacing} = \frac{2}{\text{Diameter of ring or distance between two bright spots}} \quad (3.7)$$

Finally, the values of Miller indexes were found using the d-spacings and the reference pattern from the database, and lattice parameters were calculated.

3.3.3 Powder X-ray Diffraction Spectroscopy (XRD)

XRD is used to study the diffraction of X-rays from the crystalline planes of atoms within a crystalline sample. These atoms are arranged in a periodic array within a material, thus an X-ray interacting with these arrays is scattered at different angles and produces a diffraction pattern specific to the atomic arrangement within the crystal lattice. According to Bragg's law, the interaction of incident X-rays with the crystal planes is given by in equation (3.8).[103, 104] (Figure 3.6)
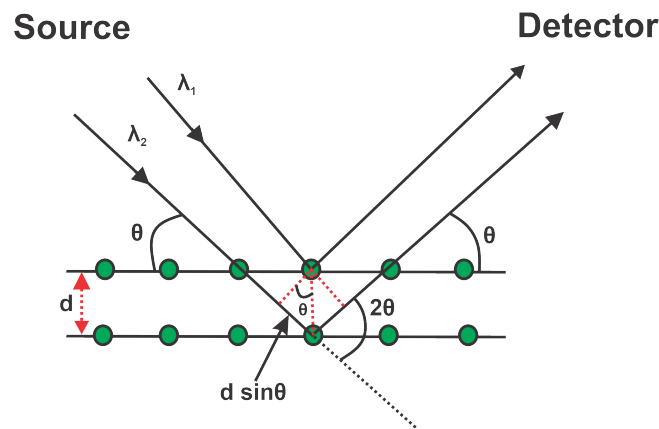
FIGURE 3.6: Working principle of XRD

$$\lambda = 2dsin\theta \quad (3.8)$$

Where λ is the wavelength, d is the distance between two planes, and θ is the angle between the incident ray and the crystal surface.

Each crystalline material has its own unique diffraction pattern which can be identified by using the standard database of diffraction patterns. XRD is a useful technique to identify the crystalline phase, lattice parameters, and crystallite sizes.

It is a non-destructive, reliable, sensitive, low-maintenance, and highly useful technique in various applications. Amorphous materials usually produce very broad peaks due to a lack of periodic arrangement in their atoms.[104]

3.3.3.1 XRD of sample

XRD analysis was used to determine the crystallographic structure of all the samples. The lattice parameters from the peak positions were also calculated by using the above equation (3.6). The crystallite sizes were also calculated from the evaluation of peak broadening by using Debye Scherrer equation (3.9) as given below.[104, 105]

$$\tau = \frac{k\lambda}{\beta cos\theta} \tag{3.9}$$

In equation (3.9), τ is the crystallite size, k is the Scherrer constant and its value is 0.89, λ is the wavelength of X-ray, β is the line broadening of a peak at full width half maximum, and θ is the Bragg angle.

The value of X-ray wavelength is dependent on the type of anode producing X-rays in the XRD diffractometer. For the characterizations of prepared materials, some materials were sent to the XRD facility at Robinson's Research Institute. These samples were characterized by using XRD Bruker D8 diffractometer with Co-k_α anode that produced X-rays of wavelength (λ) 1.79Å. Whereas for others, the Panalytical X-ray diffractometer that has fitted Cu-k_α anode was used and the value of λ of produced X-rays was 1.54Å.

3.3.4 Thermogravimetric coupled with Differential scanning calorimetry (TGA/DSC)

Thermogravimetric analysis (TGA) is a technique that measures the change in the weight of given material at elevated temperatures as a function of temperature or time. The change in material's weight by TGA is usually shown a by TGA curve that consists of turns and curved portions.[106, 107] Differential Scanning Calorimetry (DSC) is important to measure the changes in heat flow passing through the given material. A DSC curve usually appears as upward and downward peaks to represent the exothermic or endothermic behavior from the material. It provides information about the characteristics glass transition temperature of polymeric material. It is useful in determining the oxidation of the samples or the pyrolysis at high temperatures. This is a destructive technique that provides information about both qualitative and quantitative analysis of the given material.

3.3.4.1 TGA/DSC analysis of samples

Thermal analysis (TA) was performed using an instrument named SDT-Q600 with platinum pans. It is equipped with both TGA and DSC functions simultaneously

within the instrument. (Figure 3.7) The samples were heated at high temperatures, purging with an inert gas (argon or nitrogen) at a constant rate. While some samples were heated in the presence of air to observe the thermal degradation of sample contents in the presence of oxygen.
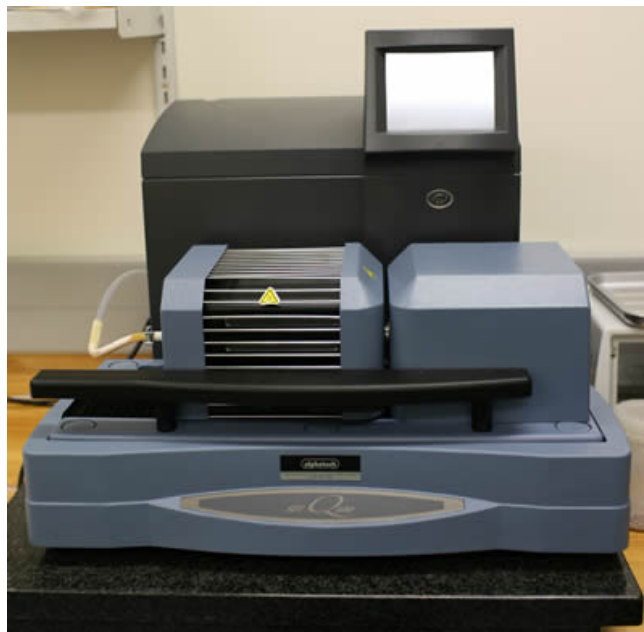
FIGURE 3.7: SDT-Q600 TGA coupled DSC instrument

3.3.5 Magnetic Properties Measurements System (MPMS) magnetometer

An MPMS magnetometer is a superconducting quantum inference device that is used to measure the magnetic response of a material in nanodimensions. Due to its high sensitivity, it can work at low temperatures and at high magnetic fields (7T).[108] The Schematic illustration of the magnetometer is shown below in Figure 3.8

As per seen in Figure 3.8, the sample is placed in such a way that it sits in the middle of four pickup coils. These pickup coils are electrically connected with the superconducting quantum interface device (SQUID). The SQUID is kept away from the applied magnetic field under liquid helium temperature for high sensitivity of signal only from the sample. The sample is physically moved up and down to observe the voltage across the SQUID that depends on sample movement. The pickup coils cancel out the static magnetic flux due to the opposing current flow (two with the clockwise current flow and two with the counterclockwise current flow) and help to provide a signal from the magnetic flux of the sample. The sample is moved vertically over a fixed scan length and stopped at fixed points. At each point, the values of SQUID voltages are recorded and averaged. The obtained voltages versus sample positions are modeled within the magnetometer to give the magnetization of the sample.[108]
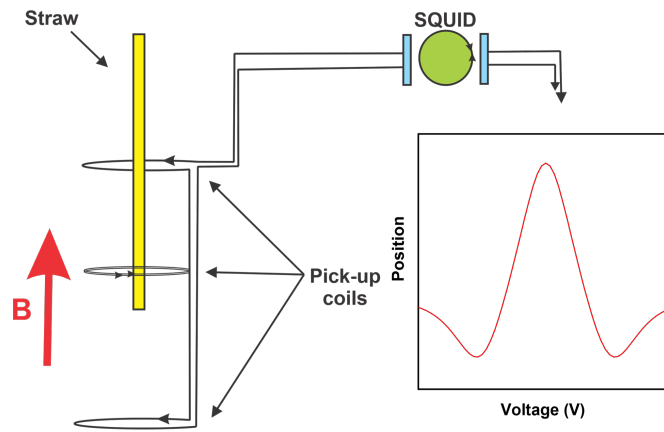
FIGURE 3.8: A schematic illustration of magnetic properties measurement system-superconducting quantum interface

3.3.5.1 MPMS measurements of samples

For magnetic measurements, the samples were loaded into a gelatin capsule by using tweezers to prevent contamination of the sample. This capsule was placed in a drinking straw and inserted in the MPMS magnetometer for magnetic measurements. SQUID measurements for the samples were recorded by applying a high magnetic field, 6T to the samples. The following analysis has been conducted on all the samples,

1. Explanation of M-H curves for a magnetic response.

2. Dependence of magnetization with increasing temperature, and spin glass modeling at an applied magnetic field (6T).

3. Zero field cooled-Field cooled (ZFC-FC) measurements from the sample at a smaller magnetic field range.

The **M-H curves** obtained from the samples were explained, and compared with their bulk counterparts and other literature reports for detailed analysis.

Preface

The next chapter explains the synthesis and characterizations of electrospun $Ni_{1-x}Fe_x$ nanofibers with varying x=0.1-0.2. The structural and magnetic properties at both fractions are discussed in detail.

Chapter 4

Bimetallic $Ni_{1-x}Fe_x$ nanofibers (x ~ 0.1 and ~ 0.2)

4.1 Introduction

Bimetallic $Ni_{1-x}Fe_x$ is a well-known soft magnetic material that has been used for industrial applications since 1920. [109] These applications include drug delivery[110], cancer detection and treatment[111], biomedical applications[112], fuel cells[113], radio frequency (RF) shielding[66], microwave absorption[114], gas sensing[115], and magnetic sensors[4]. The crystal structure for these alloys varies from the FCC at the nickel-rich side to BCC at the iron-rich side. However, the most important property of these alloys is the very small magnetocrystalline anisotropy at $0.18 \leq x \geq 0.25$. Part of the reason for this low magnetocrystalline anisotropy is the compensation of the positive $K_1 = +4.7 \times 10^5$ erg. cm^{-3} of Fe, and negative $K_1 = -5.7 \times 10^4$ erg. cm^{-3} of Ni at this stoichiometry to give overall zero magnetocrystalline anisotropy. At this stoichiometry, $Ni_{1-x}Fe_x$ display very low magnetostriction and high relative permeability.[116] Due to such interesting properties, it is hypothesized that the nanofibrous sheets of $Ni_{1-x}Fe_x$ in polymer nanofibers can be advantageous for potential magnetic flux guiding applications due to their preferred orientation and long lengths that can reduce the demagnetization effects and increase the magnetic permeability.

This chapter reports the synthesis of bimetallic $Ni_{1-x}Fe_x$ nanofibers at the nominal fractions of x$\sim$0.1 and x$\sim$0.2. To the best of my knowledge, there have been no reports on the fabrication of these nanofibers in the previous literature. These prepared nanofibers were characterized by using SEM, TEM, SAED, EDS, XRD, and SQUID analysis. The fabrication and the effect of an increasing fraction of x were studied on the structural and magnetic properties of these prepared nanofibers.

4.2 Experimental

4.2.1 Chemicals used

All chemicals used in this chapter were of high-quality analytical grade with high purities. Nickel acetate tetrahydrate ($Ni(OCOCH_3)_2 \cdot 4 H_2O$) 98% was purchased

from Merck. Iron nitrate nonahydrate ($Fe(NO_3)_3 \cdot 9\,H_2O$) $\geq$98%, and Polyvinylpyrrolidone (PVP) (C_6H_9NO) average Mw$\sim$1,300,000 by LS method were purchased from the Sigma-Aldrich chemical company. Glacial acetic acid was purchased from Carlo Erba. Methanol 99.9% was purchased from the Fischer chemical company.

4.2.2   Solution preparation of $Ni_{1-x}Fe_x$ with x$\sim$0.1-0.2 nanofibers

Nanostructured $Ni_{1-x}Fe_x$ nanofibers with x$\sim$0.1 and x$\sim$0.2 were prepared using a modified method developed in our group[5] that was used for the synthesis of $Ni_{0.55}Fe_{0.45}$ nanostructured mats. The exact method reported in previous literature [5] was unsuitable as the precipitate formation was observed in the solution that can be seen in Figure 4.1. One of the possible reasons for the formation of precipitation may have been a very small fraction of iron as compared to the fraction of nickel in the precursor mixture. The small fraction of iron cations (Fe^{3+}) with a high oxidation state can easily get reduced in the presence of a very strong alkaline medium to form an insoluble precipitate. To mitigate this, a small amount of acetic acid was added to the solutions during the preparation of $Ni_{1-x}Fe_x$ nanofibers with x$\sim$0.1-0.2 nanofibers.
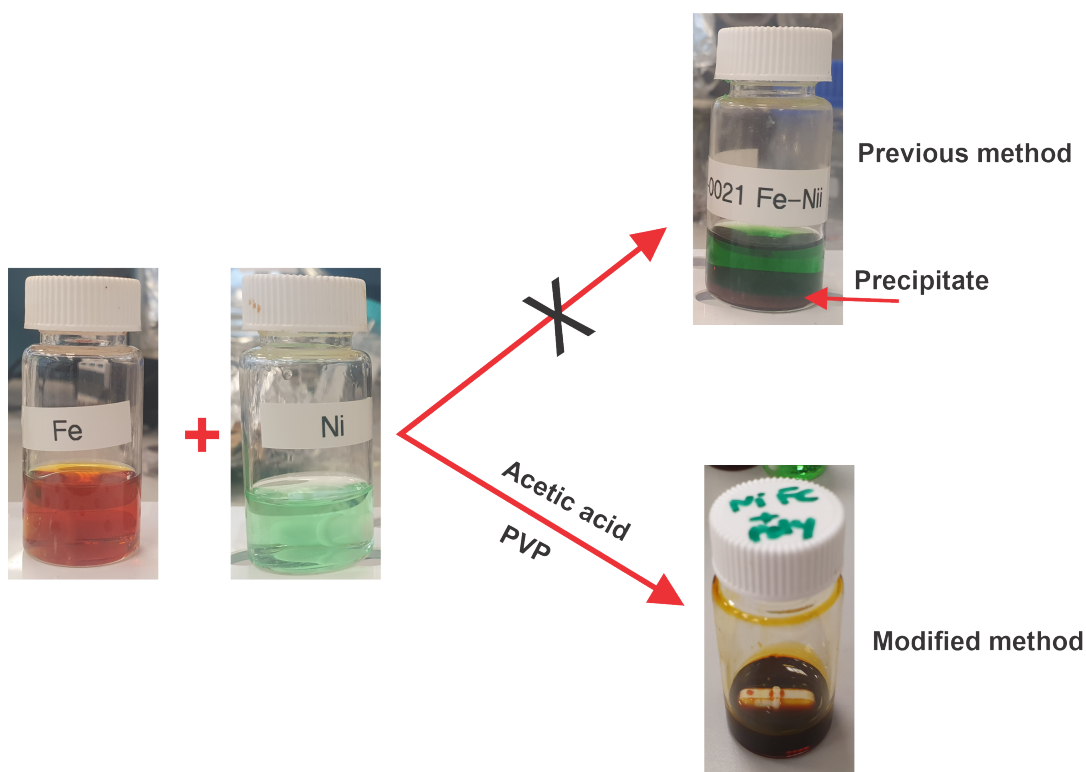
FIGURE 4.1: Sample bottles showing the iron solution (brown), nickel solution (green), and the stirring mixture of both before the addition of polymer (brown) in methanol by previous method[5]. The arrow represents the precipitate formation soon after mixing iron and nickel. Other image has shown the homogeneous mixture after the addition of acetic acid and PVP by modified method

To prepare the homogeneous solution for x$\sim$0.1 nanofibers, 9 mmol of nickel and

6 mmol of iron were first dissolved separately in 10 ml methanol at room temperature. Then 4 mL of nickel acetate was transferred to a separate flask followed by the addition of 1 mL of acetic acid. 1 mL of iron nitrate was added to this solution mixture and stirred to obtain a clear brown solution for 10 minutes. 0.25 g of polymer (PVP) was added upon constant stirring for an hour to obtain a homogeneous solution as per shown in Figure 4.1 for the electrospinning of x∼0.1 nanofibers.

To prepare the homogeneous solution for x∼0.2 nanofibers, 6 mmol of each nickel acetate and iron nitrate were dissolved separately in 10 ml methanol. From their respective solutions, 4 mL of nickel acetate was transferred to a separate flask and 1 mL of acetic acid was added. Then 1 mL of iron nitrate was transferred to this solution and stirred for 10 minutes. 0.25 g of PVP was added later upon constant stirring for one hour to obtain the electrospinning solution for x∼0.2 nanofibers. The fraction of the precursor metals, nickel acetate, and iron nitrate, are also given in the following table.4.1

Metal precursor solution in methanol (10 mL)	x∼0.1	x∼0.2
Nickel acetate (9mmol)	4 mL	
Nickel acetate (6mmol)		4 mL
Iron nitrate (6mmol)	1 mL	1 mL

TABLE 4.1: Fractions of Ni: Fe from their respective solutions

These solutions were loaded into a 5 mL syringe in the electrospinning set-up. The parameters of the electrospinning set-up were slightly modified from the previously reported method to get thinner nanofibers.[5] The following parameters were used for the electrospinning of both x∼0.1 and x∼0.2 samples (Table 4.2).

Infusion rate (mL/hr)	Voltage(kV)	Needle size(G)	drum speed(rpm)
0.4	12.5	22	60

TABLE 4.2: Electrospinning parameters for $Ni_{1-x}Fe_x$ nanofibers with x∼0.1-0.2

After electrospinning, the electrospun sheets of $Ni_{1-x}Fe_x$ nanofibers were collected from the rotating drum that was lined with aluminum foil, and dried overnight under vacuum at room temperature. This step was important to remove the methanol and some trapped water from the electrospun nanofibers. These $Ni_{1-x}Fe_x$ nanofibers were thermally processed without removing them from the aluminum foil to keep the fragile electrospun sheets intact.

4.2.3 Thermal treatment of $Ni_{1-x}Fe_x$ nanofibers with x∼0.1-0.2

The sample was first heated at 300°C for 2 hours in argon to completely remove any residual solvent/moisture content, and partially decompose polymer from the $Ni_{1-x}Fe_x$ nanofibrous sheets. Figure 4.2 (a) showed the the thermally annealed sample at 300°C for $Ni_{1-x}Fe_x$ nanofibers with x∼0.1. The brown appearance of the electrospun mat showed the formation of some metal oxides. The flexibility of the sample has shown the presence of polymer fragments which is anticipated from the TGA analysis of PVP degradation given below in Figure4.2 (a).
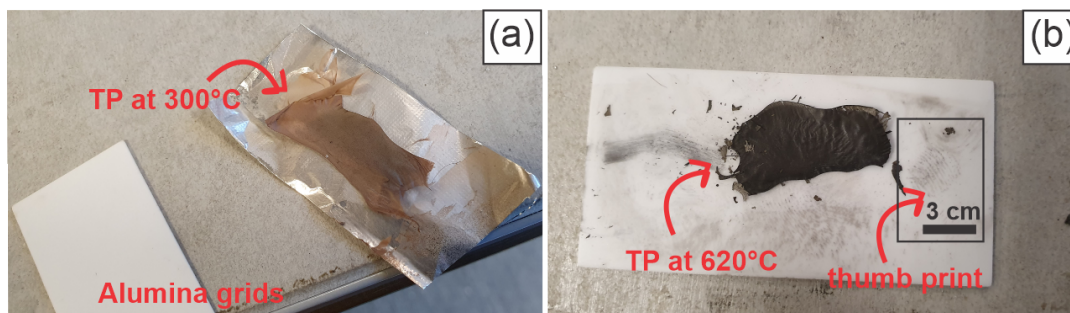
FIGURE 4.2: Thermally treated $Ni_{1-x}Fe_x$ nanofibers with x∼0.1 (a) at 300°C; the alumina plate used for placing the sample into the oven is also mentioned on the image. (b) at 620°C; printed thumbprint is highlighted to show the dimensions of the nanofibers on the grid

The complete thermal treatment profile was comprised of three steps as given below in Figure 4.3. In the first step, the sample was stacked onto the alumina plates and inserted into the tube furnace. The temperature was raised to the 300°C at a ramp rate of 5°C/min under argon gas to partially decompose the counter ions (CH_3COO, NO_3) from the samples.[117, 118] The temperature was increased to 620°C at 5°/min ramp rate, and the gas was switched to 5% H_2/95% Ar for the reduction of nickel and iron ions and to initiate the nucleation and formation of bimetallic $Ni_{1-x}Fe_x$ nanoparticles in these nanofibers. In the final step, the temperature was ramped down to 300°C at 5°C/min then maintained at that temperature for an hour before the furnace was allowed to cool down naturally to room temperature. This step was selected to switch gas safely to argon and remove any residue 5%H_2 95% Ar gas before the sample was allowed to furnace cooled. Thin black sheets of $Ni_{1-x}Fe_x$ nanofibers were obtained after this thermal processing as shown in Figure 4.2 (b)
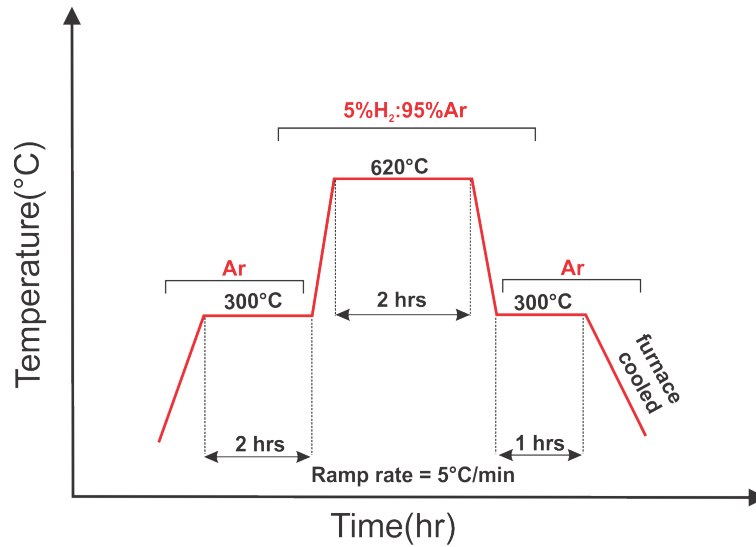
FIGURE 4.3: Thermal treatment profile for $Ni_{1-x}Fe_x$ nanofibers with x∼0.1 and x∼0.2

4.3 Results and discussion

The nominal composition of $Ni_{1-x}Fe_x$ has been stated with x∼0.1 and x∼0.2. These two fractions are used for the characterization and comparison of $Ni_{1-x}Fe_x$ nanofibers at each fraction.

4.3.1 x∼0.1 nanofibers

4.3.1.1 SEM of electrospun nanofibers

The surface morphologies and orientations of the electrospun x∼0.1 nanofibers are shown in the SEM images in Figure 4.4. It can be seen that there was no evidence of branching, beading, and/or interlinking of these nanofibers. Figure 4.4 (b) shows a high-resolution image of the fibers, which look more like nanoribbons than tubes. The width distribution of the nanofibers is shown in the inset of Figure 4.4 (b) determined from different areas. This showed that the x∼0.1 nanofibers are indeed in nanodimensions with a mean diameter of 440 nm and a standard deviation of 61 nm. There were also some thinner nanofibers in the range of ∼120 nm widths. The arrow in red in Figure4.4 (a) showed the preferential orientation of the nanofibers. This was determined by using an imagej software with various SEM images, where the x-axis is used as the reference axis and the propagation of these x∼0.1 nanofibers varied along the y-axis.
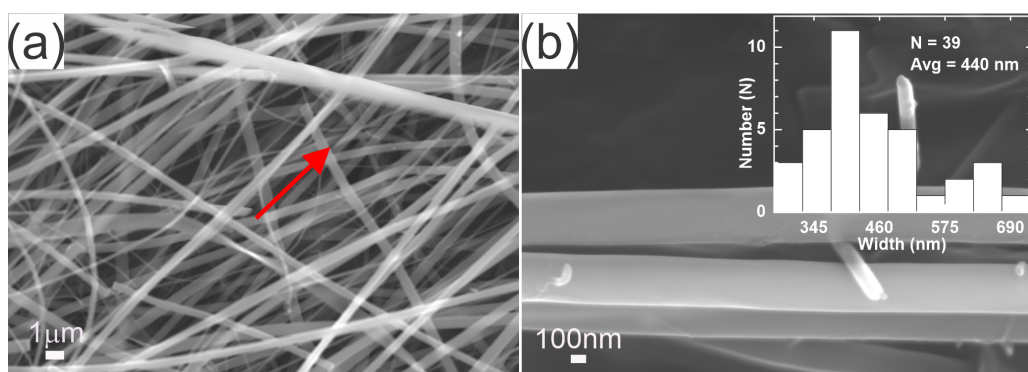
FIGURE 4.4: SEM images of the x∼0.1 nanofibers sample after electrospinning at (a) low resolution and (b) high resolution. The arrow in (a) is a guide to the eye and indicates the average nanofiber direction. The inset to (b) is the nanofiber width distribution for the wider nanofibers

4.3.1.2 TGA and DSC analysis of electrospun ∼0.1 nanofibers

To study the effect of thermal annealing on the electrospun x∼0.1 nanofibers, thermal degradation analysis coupled with differential scanning calorimetry (TGA/DTA) was used to analyse the change in the composition, and morphology in presence of metal ions and their counter salts. The results from the thermal treatment of an x∼0.1 nanofibers sample were compared with that of pure PVP sample as shown in Figure 4.5.

The TGA and DSC measurements under argon gas flow from PVP are plotted in Figure 4.5(a). The initial mass was 22.8 mg for PVP. The TGA data shows an initial weight loss due to the evaporation of methanol and water from the nanofibrous sheet. This was followed by the onset of weight loss at ∼400 C, followed by a large loss in weight that finishes at ∼480°C with a maximum slope at ∼440°C. This weight loss can be attributed to the thermal degradation of the PVP.[119] The remaining weight percentage was 5%, similar to that obtained when PVP is heated in nitrogen according to ref. [119] where the residual product was black carbonaceous powder. The DSC data showed a broad endotherm at ∼110° C that can be attributed to a glass transition of PVP.[120] There was a rapid endothermic decrease at the same temperature where the high-temperature weight loss starts (∼400° C) due to the pyrolysis of PVP. The heat flow above ∼500°C in Figure 4.5 (a) is shown by a circle. The heat flow at this value was not accurate due to the very small residual mass, which can cause fluctuations and drifts in the signals.
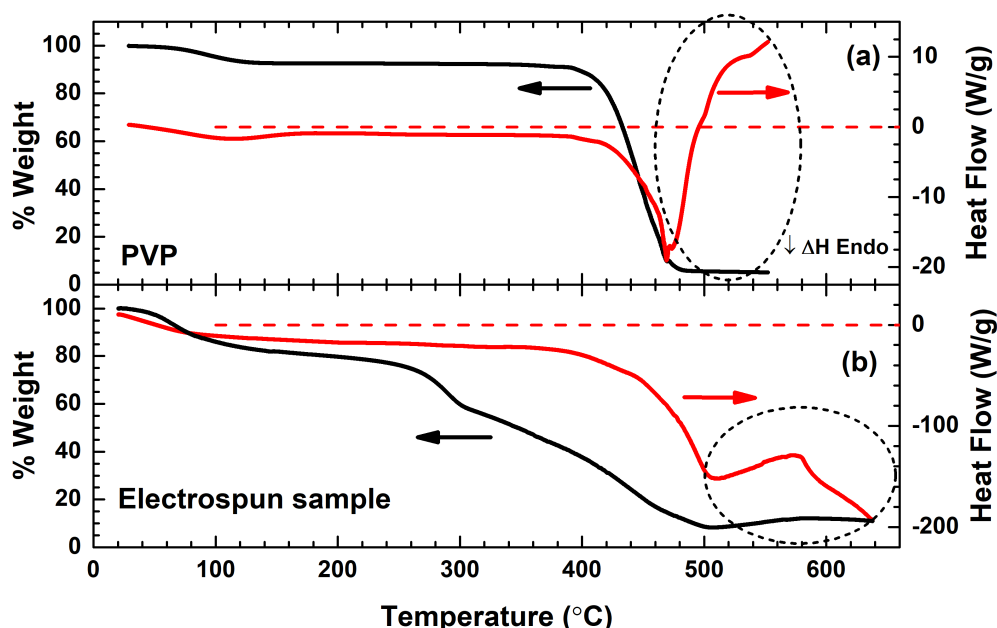
FIGURE 4.5: TGA and DSC of (a) PVP and (b) the electrospun x∼0.1 nanofiber sample under argon (Ar) with a heating rate of 20°C/min. The horizontal red dashed lines show zero heat flow. The black circles show the heat flow signals when the residual mass was very low

In comparison, the TGA and DSC plot for electrospun x∼0.1 nanofibers is shown in Figure 4.5(b). The initial weight for the electrospun x∼0.1 sample was 0.784 mg. Similar to the thermal weight loss profile of PVP, there was an initial weight loss at low temperatures from methanol and water evaporation. However, unlike pure PVP, after methanol and water have evaporated weight loss continued to ∼260° C followed by a rapid drop to 300° C with a maximum slope at 285° C. This may be due to partial degradation of the acetate in the presence of the oxidising nitrate. A more gradual and continual weight loss was seen at the ∼500° C with a maximum slope at 440° C due to the degradation of PVP that is enhanced by the oxidants like nitrate and oxygen-containing precursors from the thermal decomposition of counter ions (CH_3COO^-, NO_3^-). The remaining weight percentage above 500° C was 10%. The change in weight loss above 500° C was very small, where the weight percentage was 12.2% at 586° C. This increase in the weight percentage could be due to the fluctuations from the very small residual weight. This weight loss at higher temperatures indicates the removal of polymer and precursor's counter ions (acetates, nitrates). From this, the motivation was to use a slightly higher temperature 620°C for the thermal processing of the electrospun $Ni_{1-x}Fe_x$ nanofibers at x∼0.1. The DSC data showed a significant endothermic decrease that starts above ∼360° C. This behavior is attributed to the complete degradation of PVP.[120] However, the heat flow component above 550°C in the TGA and DSC plot is highlighted as the dotted black lines on the graph which is not accurate at very small residual weight of the sample.

4.3.1.3 SEM analysis of thermally processed nanofibers

The SEM images in Figure 4.6 showed that after the thermal treatment, the orientation of x∼0.1 nanofibers remained intact, while a significant difference in surface morphology is observed. It can be seen in the SEM image of Figure 4.6 (a) that the x∼0.1 nanofibers contained small nanoparticles on the surface. Figure 4.6 (b) showed the reduction in the mean widths of $Ni_{1-x}Fe_x$ nanofibers to ∼160 nm with the standard deviation of 40 nm after thermal processing (see the upper right inset of 4.6 (b)). These nanofibers have retained quasi-one dimensional orientation as was seen for electrospun x∼0.1 nanofibers with the mean orientation that is shown by an arrow in Figure 4.6 (a). Some broken nanofibers were also present in this image.
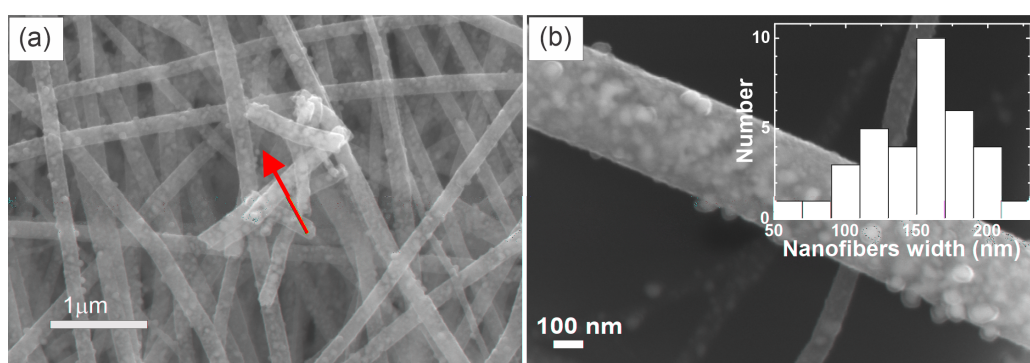
FIGURE 4.6: (a) SEM image after thermal processing for x∼0.1 nanofibers. The arrow in (a) is a guide to the eye and indicates the average nanofibre direction. (b) Large-scale image of a single nanofiber. The inset is the nanofibre width distribution

4.3.1.4 TEM analysis

The TEM images are in Figure 4.7 (a) and 4.7 (b) provided detailed information about the size of $Ni_{1-x}Fe_x$ nanoparticles within x∼0.1 nanofibers. The low-resolution image in Figure 4.7 (a) showed a cluster of nanofibers containing bimodal sized $Ni_{1-x}Fe_x$ nanoparticles distribution within x∼0.1 nanofibers. The other image in Figure 4.7 (b) showed a single nanofiber of 200 nm width with detailed information about the bimodal particle size distribution with small nanoparticles embedded within nanofibers (as shown in the lower right inset of 4.7 (b)), and large surface nanoparticles (Figure 4.8). There were many more small nanoparticles as compared to the large nanoparticles. Therefore, the size for small nanoparticles was calculated from an area shown in Figure 4.7 (b), whereas, the size for large nanoparticles was calculated by using multiple images from different areas of the same sample. The mean size for large nanoparticles was 35 nm.
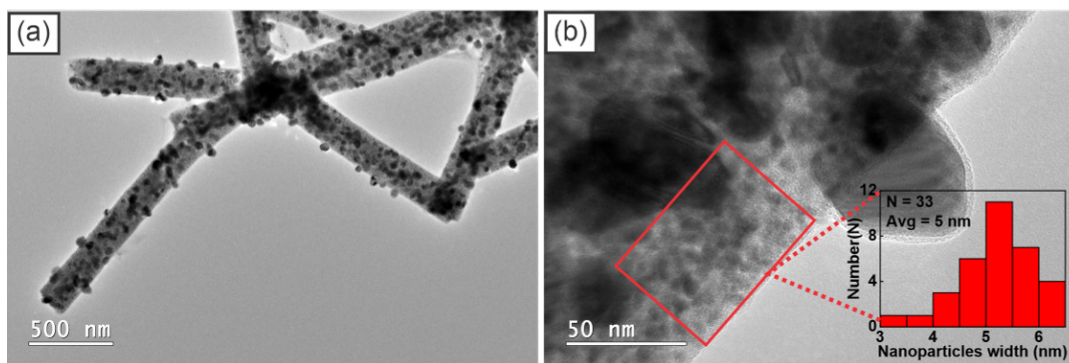
FIGURE 4.7: (a) Low resolution TEM image from the $Ni_{1-x}Fe_x$ nanofibers. (b) High-resolution TEM image of a single nanofibre
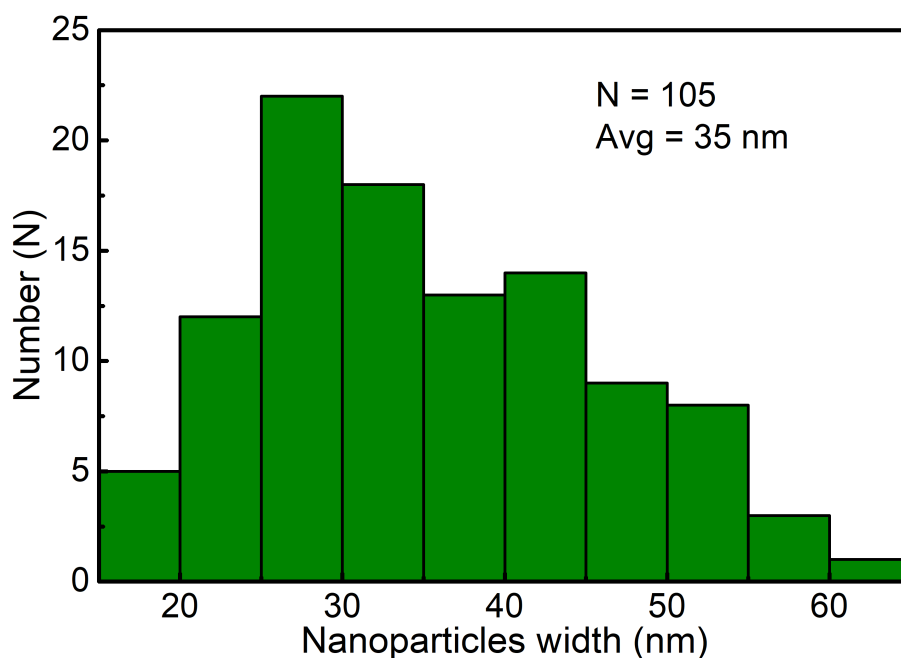
FIGURE 4.8: Large nanoparticle size distributions for x~0.1 nanofibers

4.3.1.5 STEM maps and elemental composition

The STEM maps for x~0.1 nanofibers are shown in Figure 4.9(b) to (f). The first image in Figure 4.9 (a) has shown the reference image used for the STEM maps. The second image in Figure 4.9 (b) showed the nickel map for x~0.1 nanofibers. It can be seen that nickel is equally distributed within $Ni_{1-x}Fe_x$ nanoparticles within x~0.1 nanofibers. The third image in Figure 4.9(c) showed the iron map which correlated with the nickel map in equal distribution of iron within $Ni_{1-x}Fe_x$ nanoparticles. Figure 4.9 (d) showed a carbon STEM map, and the presence of carbon in x~0.1 nanofibers confirmed the presence of carbon-containing component. This carbon-containing component provided a backbone to hold $Ni_{1-x}Fe_x$ nanoparticles in a nanofibrous morphology and prevented them from aggregation with each other.

The other two images in Figure 4.9 (d) and (e) showed oxygen and nitrogen maps that were attributed to the functional groups of remaining PVP fragments in these nanofibers. Some oxygen can be also seen at the edges of the nanoparticle surfaces which could indicate a $NiFe_yO_z$ shell formation.
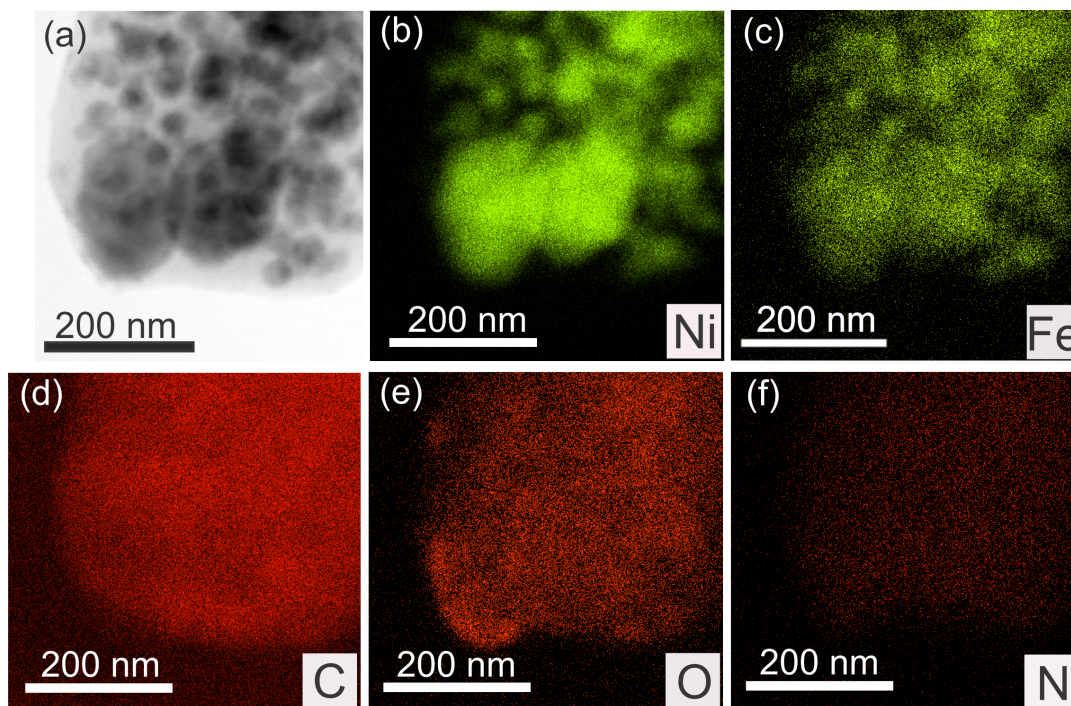
FIGURE 4.9: (a) TEM image of part of a thermally processed $x \sim 0.1$ nanofiber and (b to f) STEM maps of different elements from the same area. The diamond symbols shows the copper (Cu) K peaks that is from the Cu grid used for sample preparation

The EDS analysis for $x\sim0.1$ nanofibers is given in Figure 4.10 where the first image showed the reference image used for EDS analysis. The values of nickel and iron were 0.11 and 0.89 from the EDS spectrum in Figure 4.10. These values are close to the nominal fractions of $x\sim0.1$. This was also confirmed from various area EDS analyses of the same sample. However, the presence of carbon, nitrogen, and oxygen was attributed to the polymer fragment in the sample. The other two peaks represented by the black diamond symbol were from the copper (Cu) K_α, used as a grid in sample preparation.
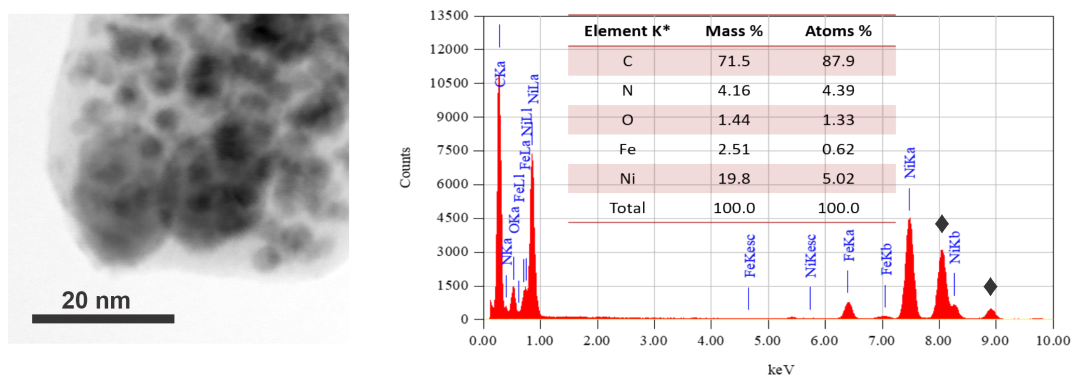
FIGURE 4.10: TEM image and EDS spectra for the x~0.1 nanofibers

4.3.1.6 SAED analysis

The SAED pattern for x~0.1 nanofibers is shown in Figure 4.11. In this pattern, four diffraction rings can clearly be seen, and they can be indexed to face-centered cubic $Ni_{1-x}Fe_x$ where the Miller indices are (111), (200), (220), and (311) with increasing radius from the center spot. The lattice parameter (*a*) was calculated from the d-spacings of these rings which is found to be 3.53Å with a standard deviation of 0.02 Å. This was in range with the expected lattice parameter value for $Ni_{1-x}Fe_x$ at low x fraction.[59, 70, 121] The bimodal nanoparticle size distribution was also evident in the electron diffraction image, where the bright spots were attributed to the larger nanoparticles, and the more diffuse spots and rings were attributed to the diffraction from the smaller nanoparticles.
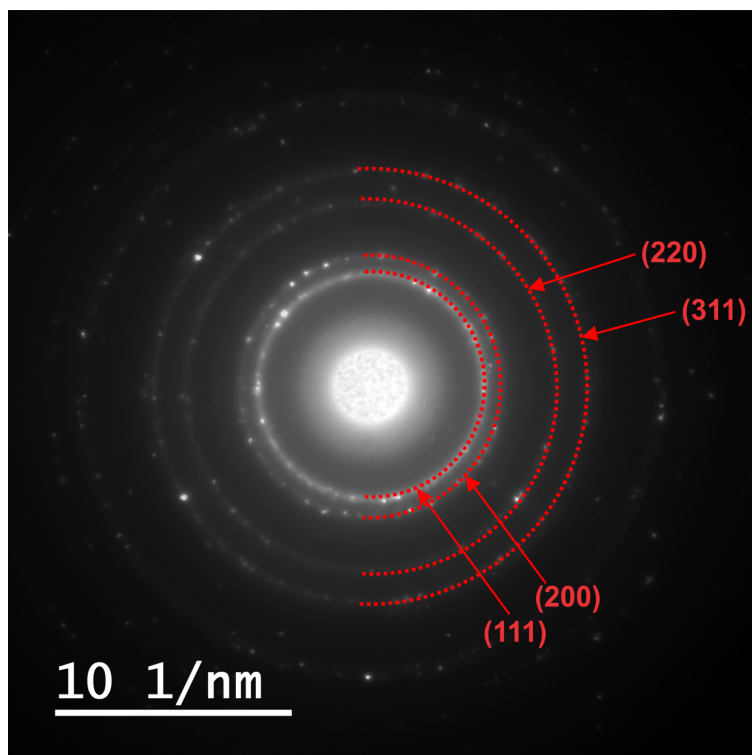
FIGURE 4.11: Electron diffraction image of a single nanofiber x∼0.1 from the thermally processed sample. Electron diffraction was done on the sample area shown in Fig. 3(b). The dashed half circles are the Miller indices (111), (200), (220), and (311) for a face centred cubic $Ni_{1-x}Fe_x$

4.3.1.7 XRD analysis

The XRD data is plotted in Figure 4.12. The first two broad reflections were indexed to the polymer, PVP reflections from the literature.[122] The other two sharper reflections at higher angles were indexed to the face-centered cubic crystal structure of $Ni_{1-x}Fe_x$ that is expected for x<0.6.[70] The fitted lattice parameter was 3.534± 0.002 Å, which was calculated from the d-spacing from the XRD reflections by using the standard formula for cubic crystal system as shown in equation (3.6).

The value of the lattice parameter was the same as that found from the electron diffraction within the experimental uncertainty. The average particle size estimated from the Scherrer equation (equation (3.9)) and using the (111) peak width was 39 nm. This was comparable to that estimated from the TEM data for the larger nanoparticles which have dominated the XRD peak line width. This showed that the $Ni_{1-x}Fe_x$ nanoparticles were not polycrystalline in nature.
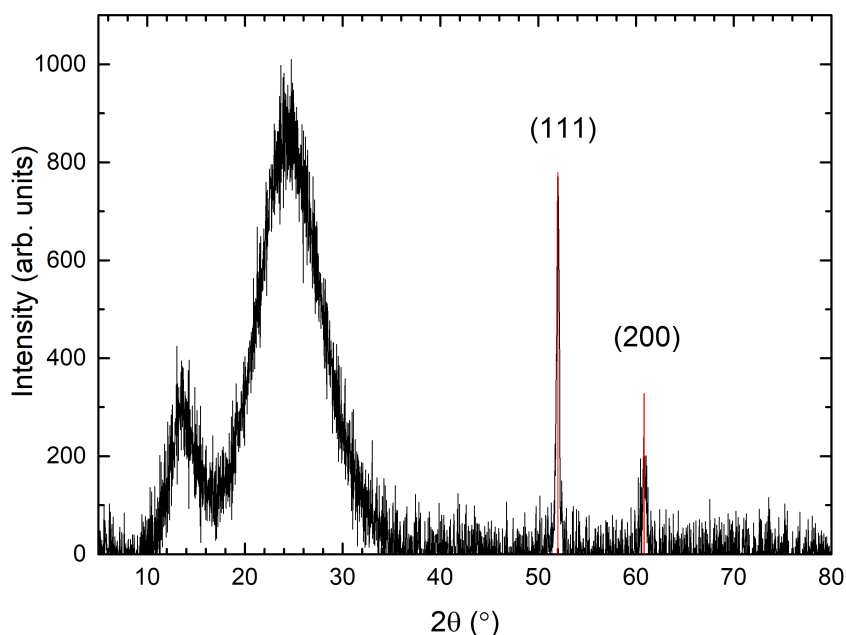
FIGURE 4.12: XRD pattern after thermal processing. The higher angle reflections can be indexed to the (111) and (200) reflections of an fcc Ni reference pattern (ICDD 00-004-0850), which is the closest reference pattern to $Ni_{0.89}Fe_{0.11}$

The formation of $Ni_{1-x}Fe_x$ nanoparticles is likely to be via Ostwald ripening.[123] This is a nanoparticle growth process that is driven by a reduction in the total surface free energy where nanoparticles larger than a critical radius, Rc, grow and those less than Rc dissolve in the surrounding matrix. The rate of nanoparticle growth depends on the Ni and Fe diffusivities.[123] Thus, the appearance of smaller nanoparticles within the nanofibres indicates that the Ni and Fe diffusivities in the presence of the remaining PVP fragments are lower than that in the surface region. One mechanism by which that can occur is the effect of functional groups (e.g. -C=O) from the residual polymeric fragments that strongly bind to the Fe^{3+} and Ni^{2+} ions. It is also possible that the PVP fragments are less dense or shorter near the surface when compared with the interior, which could lead to larger near-surface Ni and Fe diffusivities. The formation of surface nanoparticles and their aggregation to form large clusters of nanoparticles is unlikely. This is because it would lead to polycrystalline nanoparticles with an average particle size estimated from the Scherrer equation that is significantly less than the average size from TEM, which is not what is found here.

4.3.1.8 Magnetic studies

The results from the magnetic measurements are shown in Figure 4.13. The main graph shows the magnetization plotted against the applied magnetic field at 5K and 300K. It can be seen that the magnetization starts to saturate above 0.7 T, which is consistent with the ferromagnetic order expected for $Ni_{1-x}Fe_x$ where the Curie

temperature is above room temperature. The high field saturation magnetization was 42 emu/g at 5K. This value was slightly less than what is expected for bulk Ni (60 emu/g) or the bulk $Ni_{0.89}Fe_{0.11}$ where the saturation magnetization is around 90 emu/g.[70] The decrease in the saturation magnetization could be due to the mass of the non-magnetic polymer component in the nanofibers. This was expected to be larger than the measured ~46% of the bulk value if the polymer component was absent. The reduction in the saturation moment is comparable to the literature-supported values for other nickel-rich $Ni_{1-x}Fe_x$ nanoparticles with x~0.1-0.25.[70, 123, 124] Another report on the preparation of electrospun nickel nanofibers also showed a similar reduction in magnetic saturation to only 42 % of the bulk Ni.[125]
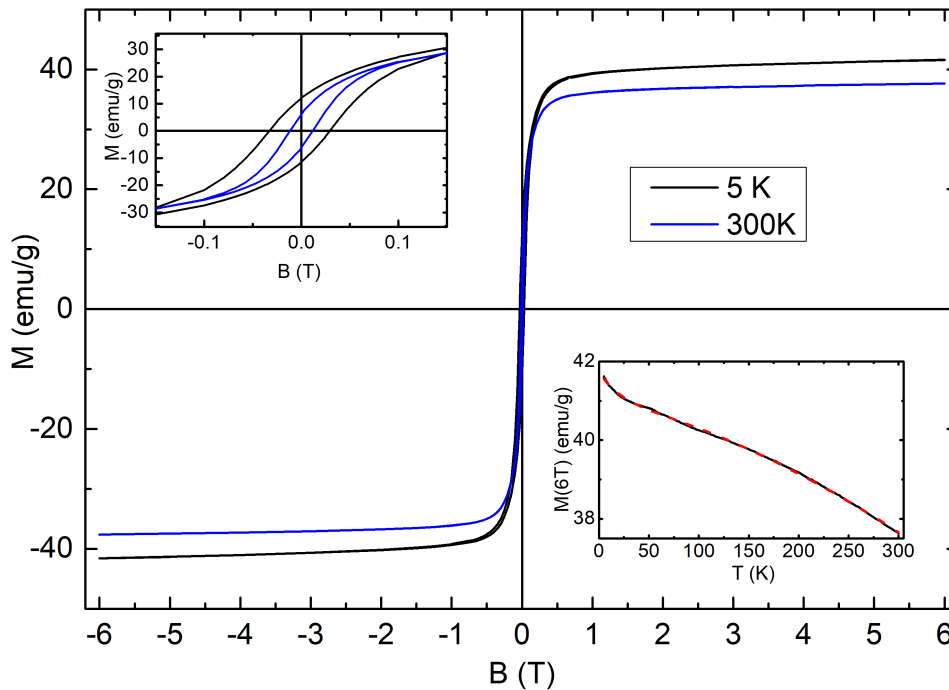
FIGURE 4.13: Plot of the magnetization against the applied magnetic field, B, at 5 K (black curve) and 300 K (blue curve) for the nanofibers sample after thermal processing for x~ nanofibers. Upper left inset: a plot of magnetization over a smaller magnetic field range. Lower right inset: a plot of the magnetization at 6 T against temperature (black curve). Also shown is a fit to the data using equation.(2.27) (red dashed curve)

The upper left inset in Figure 4.13 shows a magnetization plot over a smaller magnetic field range. The coercivity was found to be 31 mT at 5K and 12 mT at 300 K. The appearance of hysteresis at room temperature showed the absence of superparamagnetism. In this sample, while the ~5 nm nanoparticles were small enough to exhibit superparamagnetism [6], the ~35 nm nanoparticles were too large, leading to the hysteresis at 300 K. In comparison to the bulk, the coercive field at 300 K was higher than the reported unannealed Ni (3 mT) [126] and was also found to higher than when compared with electrospun Ni nanofibers.[125] However, it

was similar to that reported for $Ni_{1-x}Fe_x$ nanoparticles with x=0.2 with diameters of 22 nm (10.5 mT)[127], and was twice of that reported for 18 nm diameter at x=0.1 nanoparticles (6 mT).[128]

The lower right inset of Figure 4.13 shows the magnetization at 6T, M(6T), plotted against temperature. The saturation magnetization, M_s, in bulk $Ni_{1-x}Fe_x$ has a Bloch temperature dependence, which is given as equation (2.26). It can be seen from the lower right inset in Figure 4.13 that there was a departure from the Bloch temperature dependence at low temperature, where M_s showed an upturn below 30K. Similar behavior was also observed in the previous literature on other ferromagnetic nanoparticles.[6, 46, 129] It was attributed to the presence of spin-disordered shells. The effect on the spin disorder on M_s can be modeled by including a phenomenological spin-disorder term[6, 46], that leads to equation (2.27). The lower right inset in Figure 4.13 has shown a good fit to the phenomenological equation (2.27). The saturation magnetization, M, at 6T has shown a fitting at n=3/2 that is expected for bulk ferromagnetic $Ni_{1-x}Fe_x$. The values of the fitted parameters are given below,

$M_{s,c}$(6T,0K) (emu/g)	$M_{s,d}$(6T,0K) (emu/g)	n	β K^n	T_f(K)
40.92	0.82	1.53	1.53×10^{-5}	21

TABLE 4.3: Fitted Magnetization (6T) with n=3/2

The value of β was larger than the bulk β, but it was comparable to the other nanoparticles from previous studies on $Ni_{1-x}Fe_x$ nanoparticles.[30, 45, 130] For example, it was 3.1×10^{-5}K$^{3/2}$ for 2.7 nm $Ni_{0.8}Fe_{0.2}$ nanoparticles and 3.8×10^{-5}K$^{3/2}$ for 4.6 nm $Ni_{0.8}Fe_{0.2}$ nanoparticles made by dual implantation.[6] The fitted T_f was 21K. The value of spin-disordered component $M_{s,d}$ from Table.4.3 was very small, only 2% of the total magnetization value which showed the presence of a very thin spin-disordered shell.

The value of differential susceptibility (dM/dH) is plotted in Figure 4.14. The value for the differential susceptibility was 6. This value was higher in comparison to the spherical nanoparticle's relative permeability ($\mu_r \equiv 1$) where the demagnetization effects (N_d=0.33) are very high due to its shape anisotropy.[30]
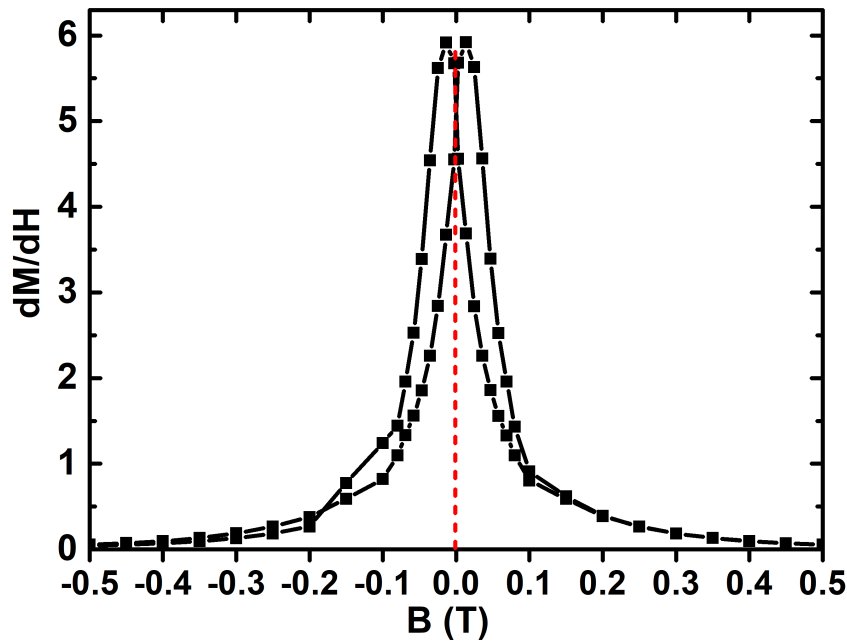
FIGURE 4.14: Differential susceptibility (dM/dH) of of $Ni_{1-x}Fe_x$ nanofibers at x∼0.1

4.3.2 x∼0.2 nanofibers

In this section, the fraction of x is x∼0.2 to observe the difference in the nucleation and magnetic properties of $Ni_{1-x}Fe_x$ nanofibers. The nominal values of x are used to compare x∼0.2 with x∼0.1 nanofibers.

4.3.2.1 SEM of electrospun x∼0.2 nanofibers

In comparison to x∼0.1, it can be seen in the Figure 4.15 that the x∼0.2 nanofibers show a negligible difference in the surface morphology of the as-prepared electrospun nanofibers. The SEM images in Figure 4.15 showed the preferred orientation of the nanofibers after electrospinning in the direction of an arrow as per shown in Figure 4.15(a) Similar to x∼0.1, the electrospun x∼0.2 nanofibers displayed smooth surfaces with no evidence of branching or beading. As noted for the x∼0.1 sample, the x∼0.2 nanofibers were more like elongated nanoribbons than tubular morphology. They appeared thinner with a mean diameter of 169 nm with the standard deviation of 38 nm as compared to x∼0.1 (525 nm with a standard deviation of 61 nm). Some even thinner nanofibers with diameters down to ∼70 nm can also be seen in the high-resolution image of Figure 4.15(b). A very small fraction of very thin branching nanofibers can also be seen in Figure 4.15 (a) and (b) which were not included in the mean diameter values.
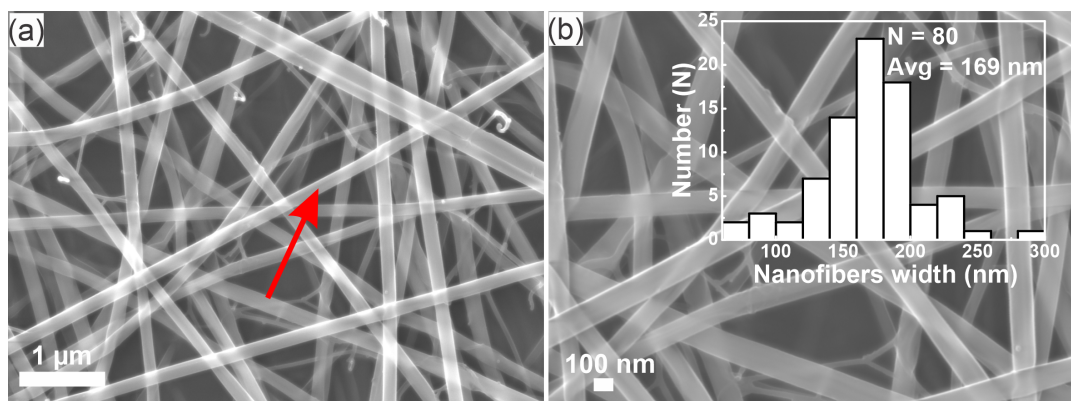
FIGURE 4.15: SEM images of electrospun x∼0.2 nanofiber sample at (a) low resolution and (b) high resolution. The arrow in (a) shows the nanofiber's direction. The inset to (b) is the nanofiber width distribution for the electrospun sample

4.3.2.2 TGA and DSC of electrospun x∼0.2 nanofibers

TGA and DSC analysis of x∼0.2 nanofibers was performed at high temperature in nitrogen to investigate the effect of high temperature on the nucleation of $Ni_{1-x}Fe_x$ nanofibers as well as the pyrolysis of PVP. Part of the reasons for increasing temperature was also to observe the difference at high temperature with the temperature profile that was used in the thermal processing of x∼0.1. The TGA/DSC was run at 20°C/min in the presence of an inert atmosphere with nitrogen gas flow. The initial weight of the sample at room temperature was 4.409 mg. The TGA spectra in Figure 4.16 (a) displayed three distinct degradation stages. The first degradation is accompanied by a 14% weight loss at 103°C that is attributed to the loss of water from the nanofibers. The second degradation was observed at 245°C with a 23% weight loss and is attributed to the decomposition of the various precursors (NO_3^-, CH_3COO^-, etc.) The third major degradation has a significant weight loss of 64% and is comparable to the PVP disintegration at 476°C (see Figure 4.5). The complete degradation is apparent at 680°C with 80% weight loss. This behavior is similar to the degradation of PVP found in previous reports.[119, 120] The residue mass was 20% of the initial mass of the samples and no further change was observed. This residual mass is attributed to the mass of both metallic oxides that clustered into a black lump in the pans. This detailed TGA investigation also confirms the optimum temperature range is around 600-650°C, similar to the x∼0.1 sample.

The DSC result in Figure 4.16 (a) revealed a dominant exothermic degradation with respect to the decreasing weight of x∼0.2 nanofibers. The thermal degradation started with an endothermic signal at 93°C, which is attributable to the solvent (methanol) and absorbed water H_2O loss. The other two signals were observed at ∼257°C and at ∼311°C. These two exothermic signals are assigned to the degradation of precursors counter ions, (NO_3^-, CH_3COO^-). Part of the reason for this exothermic behavior is attributed to the larger amount of more oxygen-contained species present in the x∼0.2 nanofibers as compared to the x∼0.1. Although the
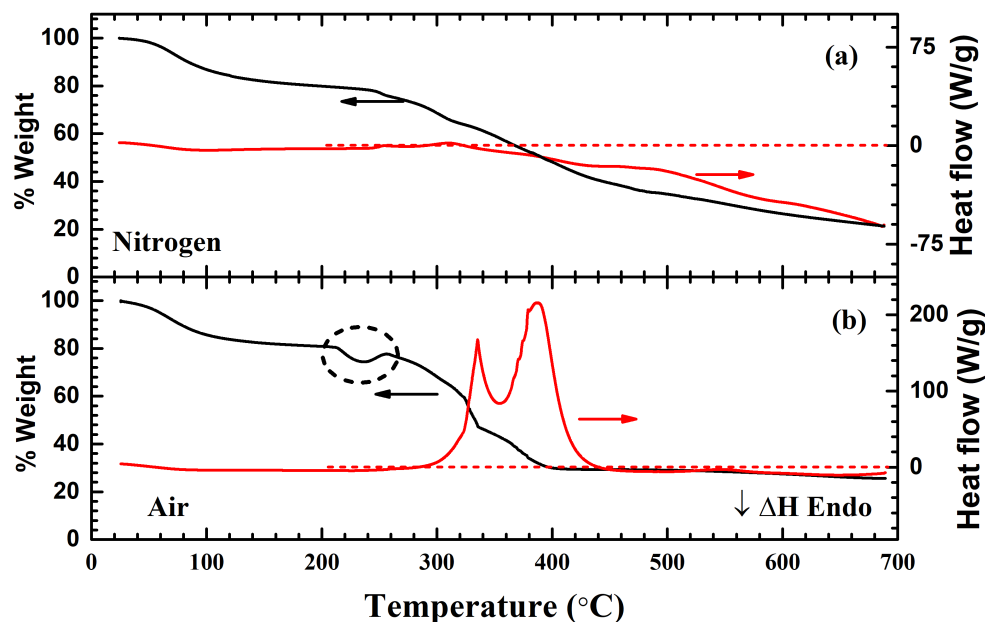
FIGURE 4.16: (a) TGA analysis of $Ni_{1-x}Fe_x$ nanofibers at x~0.2 in the presence of (a) nitrogen and (b) air

degradation followed the same path as was observed for x~0.1, another difference was observed above 550°C. The degradation curve did not show any unusual behavior similar to that observed for x~0.1. This was due to the relatively high residual mass at the end of thermal degradation, which is within the instrumental sensitivity range used for TGA and DSC measurements.

To investigate the effect of the oxygen atmosphere on the degradation of x~0.2 nanofibers, the TGA/DSC analysis has also been performed in the presence of dry airflow. The initial mass of the nanofibers was 2.2 mg. As expected, TGA analysis in Figure 4.16 (b) showed a prominent initial degradation at 100°C, which is attributed to the removal of water (H_2O) and methanol in the x~0.2 nanofibers. In contrast to Figure 4.16 (a) it can be seen that a prominent signal is observed at 239°C. This signal is assigned to the degradation of polymer fragment (PVP), which is accelerated early in the presence of oxygen and is more rapid than nitrogen or argon (used for x~0.1). This behavior was supported by another report on PVP degradation in the presence of air from literature.[131] However, the weight gain at 250°C was not real and is more likely to be from the instrumental artifact (shown with the dotted circle on Figure 4.16 (b)) that can be caused by a very small movement of the sample in the instrument. The residual mass was ~25% at 690°C and no other degradation was observed after this temperature.

The heat flow from DSC in Figure 4.16 (b) showed two strong exothermic signals at 335°C and at 389°C. The first signal at 335° is attributed to the rapid degradation of polymer fragments in these nanofibers and the other at 389°C is attributable to

the formation of nickel and iron oxides within samples.

In these experiments, the thermal treatment profile for x~0.2 was kept similar (maximum temperature 620°C) to the x~0.1 nanofibers in the experimental conditions. As all three environments including argon, nitrogen, and air did not show any further change in mass between 620°C-650°C, therefore the temperature profile was not changed to further high temperatures. This temperature (620°C) was also advantageous for the experimental conditions as the aluminum foil was used for the collection of nanofibrous sheets from the rotating drum which has a melting point of 650°C.

4.3.2.3 SEM analysis of thermally processed nanofibers

Figure 4.17 (a) and (b) show the SEM images for thermally treated x~0.2 nanofibers. It can be seen from the SEM image (Figure 4.17 (a)) that a distinct difference with x~0.1 in morphology is observed after the thermal treatment of x~0.2 nanofibers. These nanofibers have shown more smooth nanofibrous surfaces as compared to the x~0.1 nanofibers which showed the rough-surfaced nanofibers. The small upper left inset in Figure 4.17 (b) shows the nanofibers widths distribution of the x~0.2 nanofibers with a mean value of 112 nm with a standard deviation of 20 nm. The diameter for x~0.2 nanofibers was comparable to x~0.1 nanofibers (160 nm with a standard deviation of 40 nm). Similar to x~0.1, the reduction in nanofibrous widths is attributed to the removal of precursor counter ions, and the partial removal of polymer from these nanofibers. The small arrow in Figure 4.17 (a) showed the preferred orientation for the x~0.2 nanofibers.
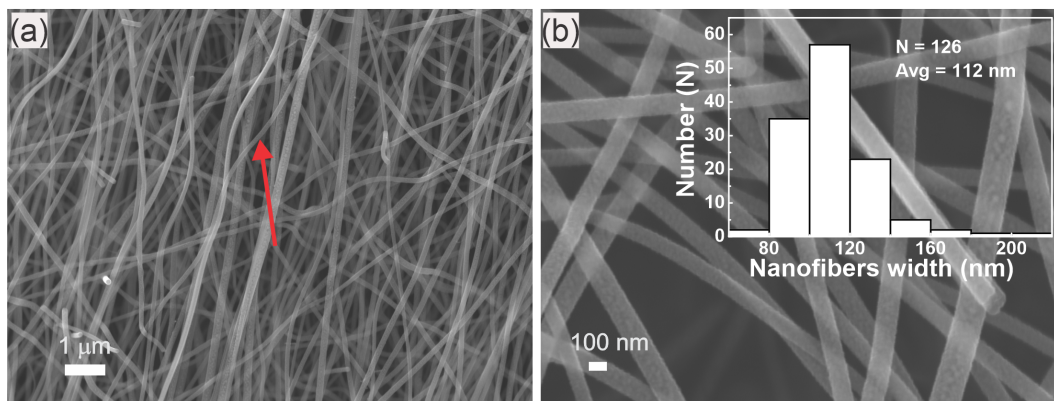
FIGURE 4.17: (a) Low-resolution SEM image after thermal processing. The arrow in (a) shows the mean nanofiber's direction. (b) High-resolution SEM image of x~0.2 nanofibers. The inset is the nanofiber width distribution

4.3.2.4 TEM analysis

The TEM images in Figure 4.18 have shown the formation of thinner nanofibers when compared to the x~0.1 nanofibers. From the high-resolution image in Figure 4.18 (b), the width of a single nanofiber was ~133 nm which is less than what has

been found for x~0.1 nanofibers with 200 nm. The reduction in the x~0.2 nanofibers widths is attributed to the effect of the increasing amount of oxidants from increasing NO_3^- when the Fe^{3+} ion fraction is increased to x~0.2. It is possible that the additional oxygen content can help to speed up the pyrolysis of polymer fragments (PVP) to give thinner x~0.2 nanofibers.
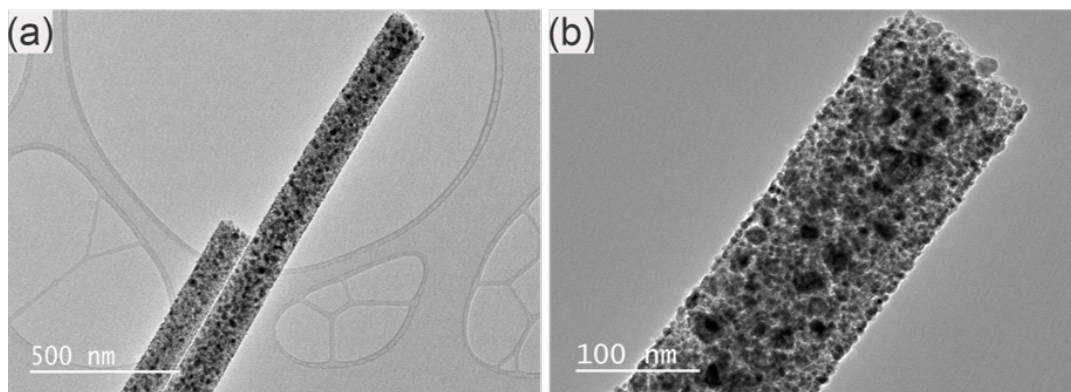
FIGURE 4.18: (a) large area TEM image showing x~0.2 nanofibers containing larger and smaller nanoparticles (sample prepared on a holy copper TEM grid). (b) Small area image of a single nanofiber

From Figure 4.18 (a) and (b), it can be seen that these nanofibers contain small homogeneously distributed nanoparticles as well as some few large nanoparticles on the surface. The presence of these more homogeneous $Ni_{1-x}Fe_x$ nanoparticles can be explained by the more favorable fraction of x~0.20-0.25, which can lead to the formation of increased nucleation centers due to minimal enthalpy change in the system to give smaller nanoparticles.[132] Another plausible explanation is the robust pyrolysis of PVP in the presence of higher oxygen content from the oxidative sources (NO_3^-, CH_3COO^-) that leads to the enhanced diffusivities of both ions to give rise to smaller nanoparticles. The role of polymer is also important to hold the nanoparticles at certain distances from each other to prevent agglomeration. Furthermore, the reactive surfaces of smaller nanoparticles cause them to attach with the carbon backbone and retain the morphology of the nanofibers.

The nanoparticle size was calculated from Figure 4.18 (b), and the mean nanoparticle size was 8 nm as shown in the particle size distribution in Figure 4.19. Some large nanoparticles in the range of 12-18 nm were also present in this size distribution. The particle size distribution for x~0.2 has shown more size fraction for the smaller nanoparticles and it was skewed towards the larger sized nanoparticles. This was different from the x~0.1 nanofibers, where more prominent bimodal particle size distribution was observed. This showed that by increasing x, the fraction in small nanoparticles increases with slightly skewed particle size distribution.
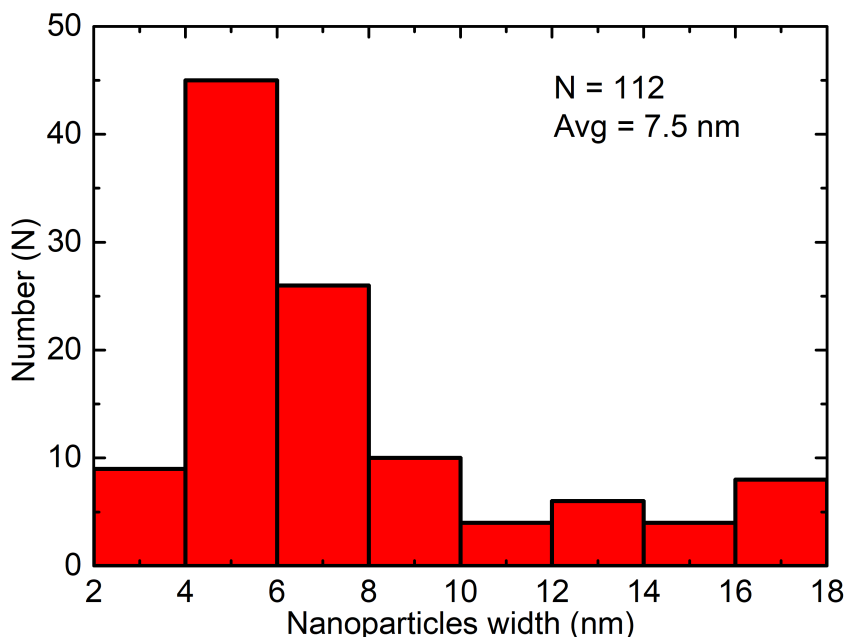
FIGURE 4.19: $Ni_{1-x}Fe_x$ nanoparticles distribution for x~0.2 nanofibers by using 4.17 (b)

4.3.2.5 STEM maps and elemental composition

Elemental maps from STEM mapping are shown in Figure 4.20 (a) to (e), whereas Figure 4.20 (a) showed the TEM image used for elemental mapping. The second image in Figure 4.20 shows an iron map, and it can be seen from the elemental maps that Fe is homogeneously distributed within $Ni_{1-x}Fe_x$ nanoparticles. The third image in Figure 4.20 (c) showed a nickel map, which correlates with the homogeneous distribution of Ni within $Ni_{1-x}Fe_x$ nanofibers. The carbon backbone was also clearly evident in Figure 4.20 (d) which confirmed the presence of polymer fragments within the x~0.2 nanofibers. The presence of the carbon backbone could prevent the aggregation of $Ni_{1-x}Fe_x$ nanoparticles and retain the nanofibrous morphology. The oxygen content was also clearly visible in Figure 4.14 (e), and is attributed to the functional group of the polymer repeating unit pyrrolidone (C=O). This has also been observed in a previous report of willemite chains containing PVP. [133] Furthermore, no evidence of oxygen in the $Ni_{1-x}Fe_x$ nanoparticles in these SAED patterns. In Figure 4.19, the three arrows (red) represent the unresolved areas by the TEM due to the dense surfaces of these nanofibers where more than one nanofiber coincided with each other.
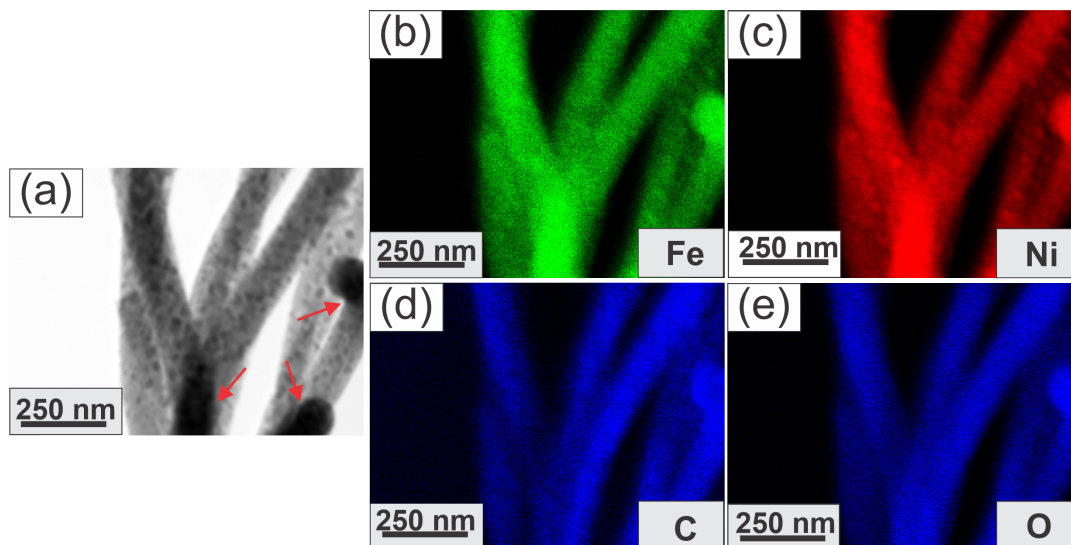
FIGURE 4.20: (a) TEM image of the thermally processed x∼0.2 nanofibers and (b to f) STEM maps of different elements of (a)

The EDS analysis of x∼0.2 nanofibers is given in Figure 4.21. The TEM image in this Figure 4.21 was used for the EDS analysis. Since the STEM maps are consistent with the uniform distribution of iron and nickel in the nanoparticles, it can now be seen that there was 0.22 of x (Fe) to the 0.78 of nickel. These fractions are close to the original stoichiometry. Moreover, the presence of other elements including carbon and oxygen was attributed to the carbon backbone from the polymer fragment in the sample. EDS analysis from the other areas of the samples has shown similar values for these elements for confirmation.

Element K*	Mass %	Atoms %
C	54.2	81.2
O	5.36	6.05
Fe	9.05	2.93
Ni	31.4	9.66
Total	100.0	100.0
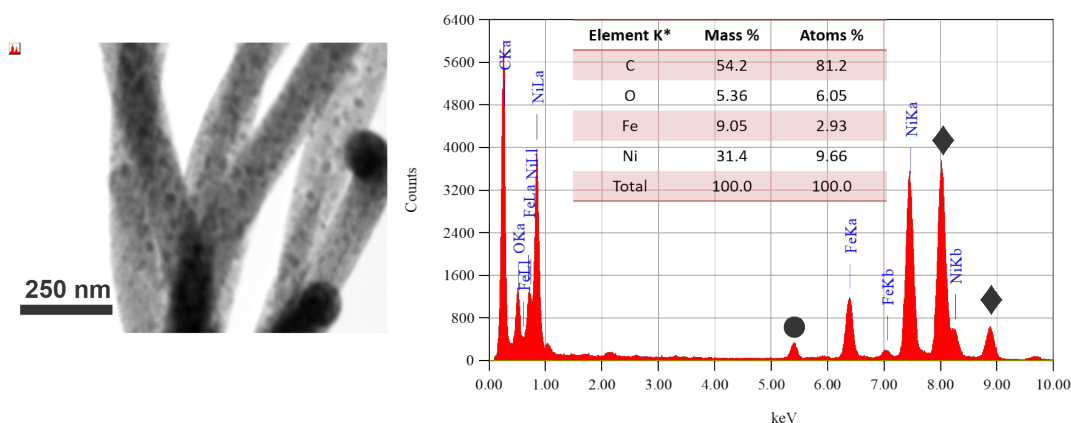
FIGURE 4.21: TEM image and EDS spectra for the x∼0.2 nanofibers

4.3.2.6 SAED analysis

The SAED pattern in Figure 4.22 has shown the diffraction pattern for x∼0.2 nanofibers. It can be seen that similar to x∼0.1, the most prominent four diffraction rings have been indexed for $Ni_{1-x}Fe_x$ nanoparticles. These were indexed to the FCC crystalline phase of $Ni_{1-x}Fe_x$ with Miller indices (111), (200), (220), and (311). The lattice parameter calculated from the d-spacings was 3.55 with a standard deviation of 0.01 Å. This was increased from the lattice parameter value found for x∼0.1 (3.53 with the standard deviation of 0.02 Å), and found in range with literature-supported values for $Ni_{1-x}Fe_x$ at increasing x.[5, 70, 134] Similar to the x∼0.1, the diffraction pattern has shown the presence of bright spots over diffused rings due to the presence of both smaller and large nanoparticles in these x∼0.2 nanofibers. The bright spots were attributed to the presence of larger nanoparticles, while the diffused rings were attributed to the smaller nanoparticles.
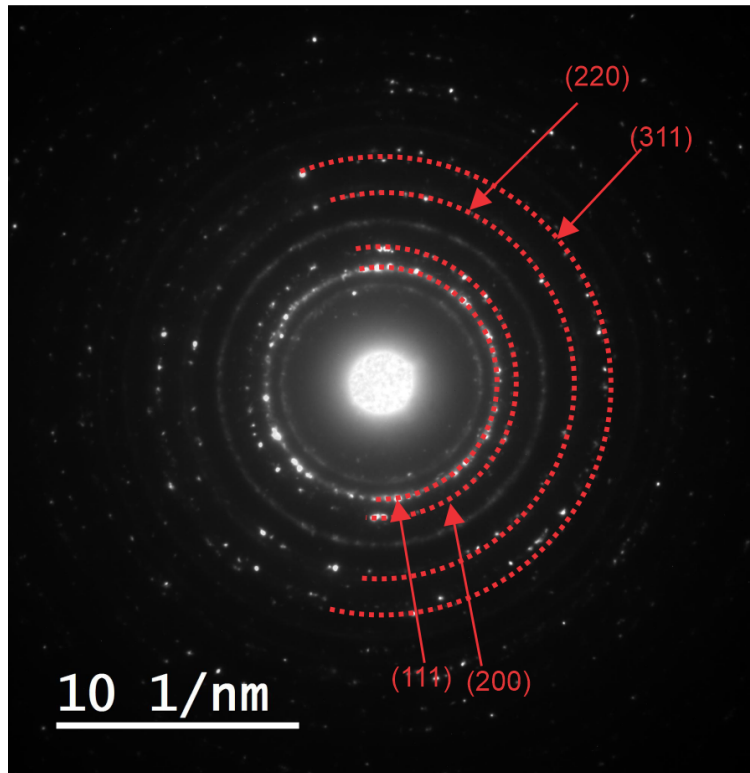
FIGURE 4.22: SAED image from an area containing multiple x∼0.2 nanofibers after thermal processing. The dashed half circles are the Miller indices (111), (200), (220), and (311) for face centred cubic $Ni_{1-x}Fe_x$

4.3.2.7 XRD analysis

The XRD pattern is shown in the Figure 4.23 where the first two XRD peaks were indexed to the literature-reported reflections for the polymer (PVP) component within x∼0.2 nanofibers.[133, 135] The other two peaks at higher angles were indexed to the miller indexes (111) and (200) values from the FCC crystal phase of the $Ni_{1-x}Fe_x$ nanoparticles.
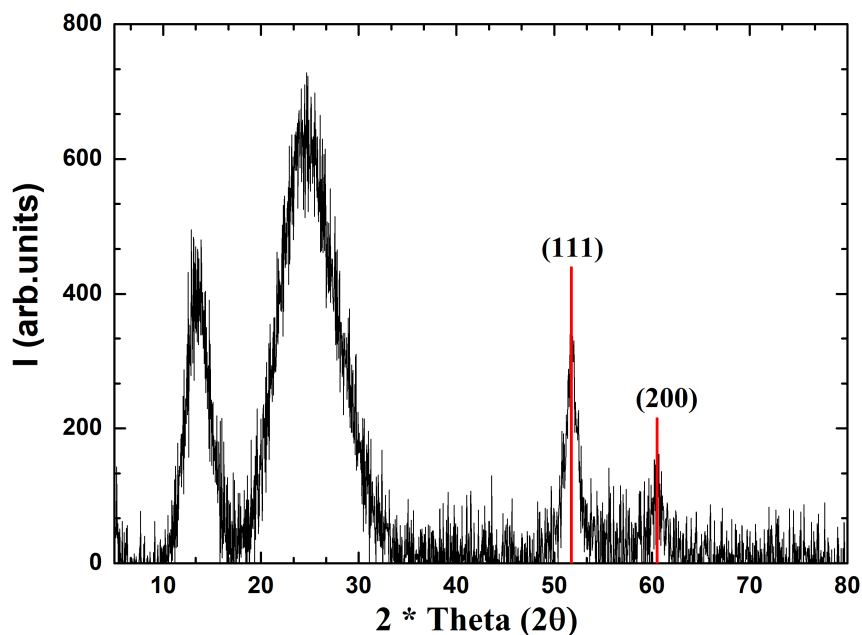
FIGURE 4.23: XRD pattern of $Ni_{1-x}Fe_x$ nanofibers at x∼0.2 after thermal processing. The fitted lines correspond to the 2-theta angles of the (111) and (200) reflections. These two reflections are indexed to the ICDD reference pattern 00-004-0850 for Ni

In comparison to x∼0.1, broader peaks at higher angles are observed due to the presence of smaller $Ni_{1-x}Fe_x$ nanoparticles. The particle size was 8 nm. It was calculated from the full-width half maximum of the high-intensity peak at (111) by using a Scherrer equation (3.9). This value was consistent with the average particle size from TEM analysis in Figure 4.18 (b). In x∼0.2 nanofibers the peak broadening was dominated by the presence of smaller nanoparticles (∼8 nm) while x∼0.1 showed high-intensity peaks where the peak broadening was dominated by the larger 35 nm nanoparticles calculated by the Scherrer equation (3.9).

In comparison to x∼0.1, the two peaks corresponding $Ni_{1-x}Fe_x$ nanoparticles were shifted towards the high angle values at 51.75° (111) and 60.52° (200) of 2θ. That showed an increase in the lattice parameters to 3.550±0.001 Å for x∼0.2 as compared to 3.530±0.002 Å for x∼0.1 nanofibers. This increased value is comparable to the literature-reported values of x∼0.2.[52] This value was also in agreement with the value calculated from the SAED. Moreover, the nanoparticles in the prepared

sample were single crystalline in nature and no impurity peak is observed in the XRD pattern for x∼0.2 nanofibers.

4.3.2.8 Magnetic studies

The magnetic measurements are shown in Figure 4.24. Here, the main graph show the magnetization plotted against varying magnetic field at 5K and 300K. It can be seen that the magnetization begins to saturate at ∼0.7T and the saturation magnetization, M_s, was 86 emu/g at 5K. This value was increased when compared to the x∼0.1, 42 emu/g at 5K. The value of saturation magnetization was 72 percent of the total bulk value. Similar to x∼0.1, the reason for this reduction in comparison to the bulk could be due to the mass of non-magnetic polymer component present in the x∼0.2 nanofibers. However, the saturation magnetization was comparable to the reported from the previous literature that showed the synthesis of $Fe_{20}Ni_{80}$ nanoparticles of 440 nm by wet chemical method with saturation magnetization value ∼81 emu/g.[52] But it was higher than the saturation magnetization value of 28.7 emu/g for ∼20 nm $Fe_{20}Ni_{80}$ nanocrystals.[52] Another report on large nanocrystalline particles of $Fe_{20}Ni_{80}$ (∼79 emu/g), chains (∼81 emu/g), and wires(∼75 emu/g) shown comparable values to our findings for x∼0.2 nanofibers.[136] The upper left inset in Figure 4.24 indicates a relative decrease in coercivity for x∼0.2 nanofibers at increasing temperature with the smallest value 8 mT appearing at 300K (slightly above the room temperature ∼298K) In comparison to the x∼0.1 coercivity, 12 mT at 300K, the coercivity for x∼0.2 nanofibers was slightly reduced to 8 mT at 300K(∼room temperature). This value was in the same range as bulk iron (9 mT), but was higher than that of bulk nickel (3 mT).[126] as shown in the Figure 4.24.
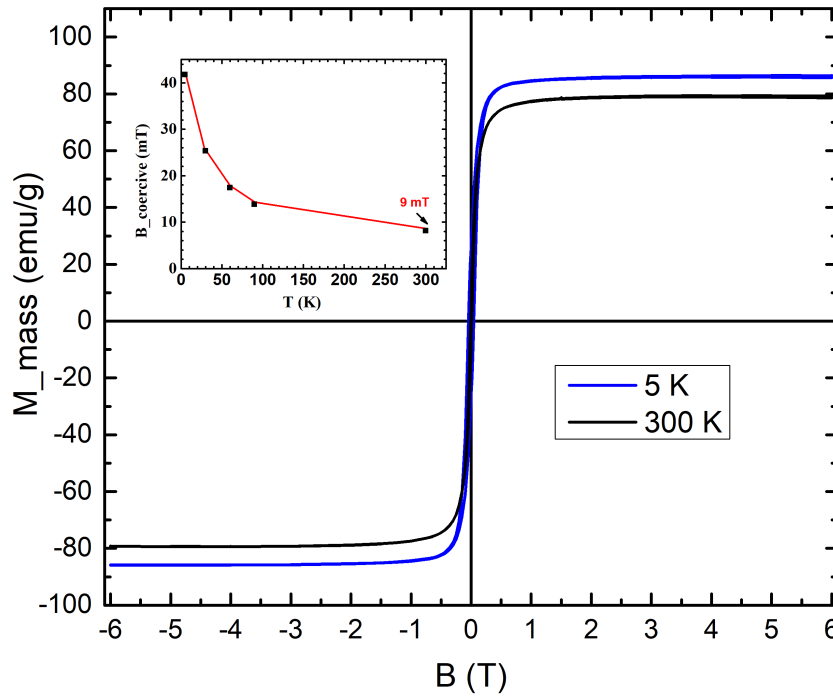
FIGURE 4.24: Plot of magnetization against the magnetic field, B, at 5 K (blue curve) and 300 K (black curve) after thermal processing for x∼0.2 nanofibers. Upper left inset: a plot of coercivity with varying temperature

The main graph in Figure 4.25 shows the dependence of M_s at 6T with increasing temperature. Similar to x∼0.1, the magnetization is modeled against the phenomenological equation (2.27). The departure in the magnetization was evident at lower temperatures (∼30K) due to the presence of a spin-disordered shell. The parameters of the fittings are given below in Table. 4.4

$M_{s,c}$(6T,0K) (emu/g)	$M_{s,d}$(6T,0K) (emu/g)	n	β (K^n)	T_f(K)
84.4	2.0	1.93	1.3×10^{-6}	17

TABLE 4.4: Fitted Magnetization(6T) at phenomenological equation (2.27)

It can be seen that the value of n=1.93 deviates from the bulk value, and was also different than what was observed for x∼0.1 (n=1.53). Part of the reason for this deviation could be the nanodimensions of $Ni_{1-x}Fe_x$ down to a certain size of nanoparticles and the spin disordered component from these nanofibers. The reports from the previous literature have also shown similar behavior due to the nanosized dimensions and the presence of spin-disordered component from the nanoparticles.[137] This behavior was comparable to other nanoparticles from the previous literature with large values of n.[138–140] The value of β was comparable to bulk iron (3×10^{-6} $K^{3/2}$).[141] Similar to x∼0.1, T_f was 17 K, and the value for $M_{s,d}$ (6T, 0 K) was only
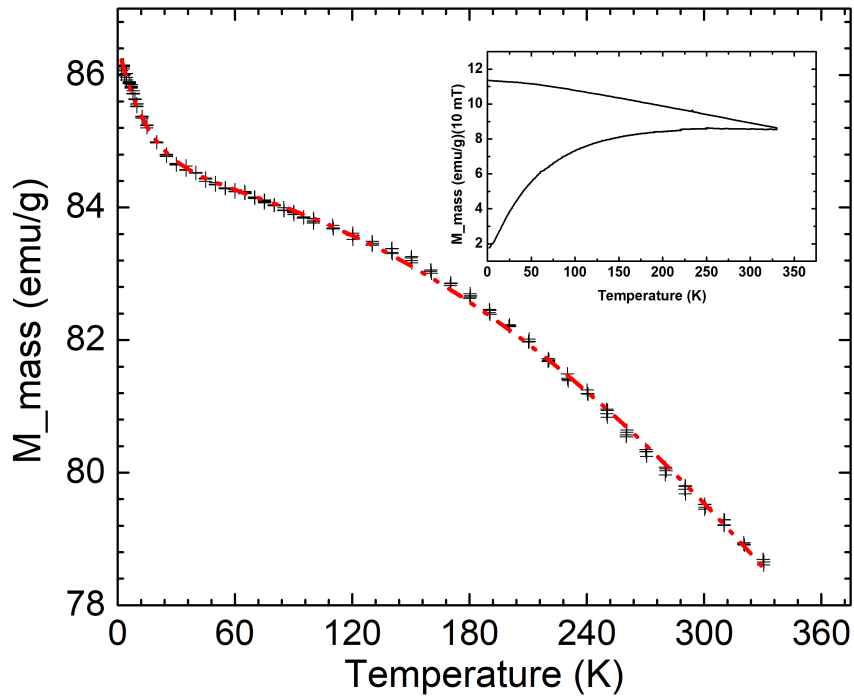
FIGURE 4.25: Main plot showing the dependence of spin glass magnetization with varying temperature for x∼0.2 nanofibers. Upper right inset: ZFC-FC magnetization plot for x∼0.2 nanofibers

∼2% of the total magnetization value that suggested a very thin spin disordered shell (Figure 2.15 around the magnetically ordered core with an $M_{s,c}$ (6T, 0K) 84.4 emu/g.

The upper right inset of Figure 4.25 showed the zero field cooled-field cooled (ZFC-FC) curves for x∼0.2 nanofibers at 10mT. These curves have suggested the ferromagnetic behavior for x∼0.2 nanofibers. It is interesting to note that the particle size for $Ni_{1-x}Fe_x$ in x∼ nanofibers is small enough (∼8 nm) and expected to show superparamagnetic behavior, but the ZFC-FC curve showed a range in nanoparticle sizes. Due to this, the hysteresis from the large nanoparticles in the ZFC-FC curve dominated the superparamagnetic response.
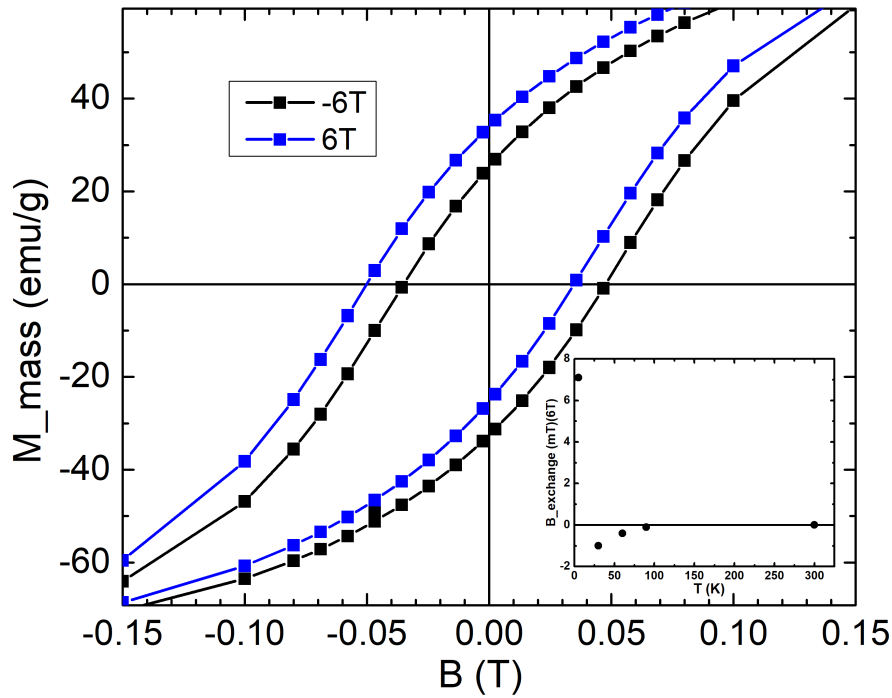
FIGURE 4.26: Plot of magnetization over a smaller magnetic field range. Lower right inset: exchange bias in mT with varying temperature (0K-300K)

These x∼0.2 nanofibers have also shown exchange bias as seen in Figure 4.26. It can be seen from the main graph of Figure 4.26 that a hysteresis shift was observed over a small value of magnetic field 7.5 mT when the magnetization is plotted under (field cooled at -6T). Exchange bias (B_E) can be explained by the simplest model that shows the exchange interactions at an interface between the ferromagnetic layer and antiferromagnetic layer in thin films from equation (2.20). The lower right inset in Figure 4.26 has shown the dependence of exchange interactions on varying temperatures. It can be seen that the exchange interaction appeared at very low temperatures and disappeared soon after increasing the temperature (in the range of T_F). This could be due to the magnetic disorder or spin glass moment from the magnetically ordered core and spin disorder shell. This has already been explained in the other nanoparticles where magnetically disordered surface and spin glass moment causes an additional term in magnetic energy density for exchange bias.[142, 143]

The differential susceptibility (dM/dH) curve for x~0.2 is shown in comparison to x~0.1 in Figure 4.27 The value of dM/dH was increased to 11 when compared with x~0.1 nanofibers dM/dH=6. This value was high in comparison to the susceptibility of spherical isolated nanoparticles with demagnetization value of (N_d=0.33) from the equation (2.25).[30]
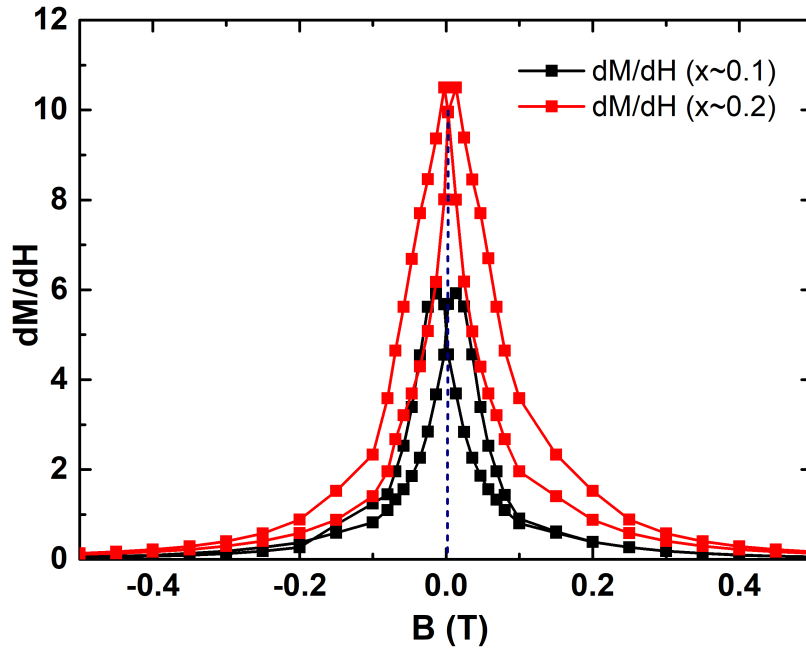
FIGURE 4.27: Differential susceptibility of x~0.2 vs x~0.1 nanofibers

4.4   Summary

In this chapter, nanofibers containing bimetallic $Ni_{1-x}Fe_x$ nanoparticles with a varying fraction of x from x~0.1 to x~0.2 were successfully synthesized using the electrospinning method. These nanofibers showed thin widths and there was an average orientation for both $Ni_{1-x}Fe_x$ nanofibers at both fractions of x~0.1 and x~0.2. $Ni_{1-x}Fe_x$ nanofibers at x~0.1 showed thicker widths of nanofibers to the mean value of 200 nm, which was reduced to ~133 nm for x~0.2 nanofibers.

Interestingly, both x~0.1 and x~0.2 nanofibers have shown the formation of $Ni_{1-x}Fe_x$ nanoparticles within the polymer backbone. A bimodal particle size distribution was found for x~0.1 nanofibers whereas, it was slightly skewed for x~0.2 towards the large nanoparticles end. This has been explained due to the different diffusivities of both Fe and Ni ions at the surface as well as within nanofibers for x~0.1. At high temperatures, the accelerated removal of counter ions and polymer increases the diffusivities of both Fe^{3+} and Ni^{2+} ions on the surface and increased the surfaced nanoparticle sizes. In x~0.2, the reason behind the smaller-sized nanoparticles is explained in terms of minimal enthalpy change during the nucleation process at the most favorable fraction of x~0.20-0.25, which can lead to the formation of more nucleation centers within nanofibers and more small-sized nanoparticles formed.

The saturation magnetization for $Ni_{1-x}Fe_x$ nanofibers was significantly improved when x was varied from 0.1 to 0.2. The value of magnetization reaches up to ~72 percent (86 emu/g) of the bulk value (120 emu/g) x~0.2 when compared with x~0.1 that showed only 46 percent (42 emu/g) of the bulk value (90 emu/g). The value of coercivity was slightly decreased from 12 mT for x~0.1 to 9 mT for x~0.2 nanofibers. However, both of these $Ni_{1-x}Fe_x$ nanofibers have shown a high differential susceptibility (dM/dH) when compared with the spherical nanoparticles ≤ 0 due to the demagnetization effects. In this study, the value of differential susceptibility was increased from 6 for x~0.1 to 11 for x~0.2 nanofibers.

The results in this chapter have shown very interesting structural and magnetic properties for the electrospun $Ni_{1-x}Fe_x$ nanofibers at varying x from x~0.1 to x~0.2. These nanofibers have shown thin widths at both fractions but more thinner nanofibers were obtained at x~0.2. The differential susceptibility was also increased higher at x~0.2 nanofiber. However, an ideal material requires negligible coercivity and very high permeability. Since the increasing fraction of x has provided encouraging results, it will be interesting to investigate that,

1. what happens if x is increased further?

2. Can we further reduce the coercivity and increase the differential susceptibility with increasing x?

To address these questions $Ni_{1-x}Fe_x$ nanofibers have been prepared at x~0.5 and the effect of further increasing fraction of x is investigated in the next chapter.

Preface

The next chapter explains the synthesis and characterizations of the electrospun $Ni_{1-x}Fe_x$ nanofibers at x~0.5. An alternative method is used for the preparation of x~0.5 nanofibers. The structural and magnetic properties differences are highlighted in detail at an increasing fraction of x to x~0.5.

Chapter 5

Bimetallic $Ni_{1-x}Fe_x$ nanofibers with x ~0.5

5.1   Introduction

The promising results from $Ni_{1-x}Fe_x$ with x~0.1 and 0.2 was the main motivation to further increase the fraction of x to 0.5. A trend in decreased fraction of large nanoparticles was observed with increasing x from x~0.1 to x~0.2. The saturation moment also increased concurrent with an increasing iron fraction (x), from x~0.1 to x~0.2. Therefore, the idea was to investigate the effect of increasing x on the structural and magnetic properties of $Ni_{1-x}Fe_x$ nanofibers at x~0.5. Literature investigation on the $Ni_{1-x}Fe_x$ alloy has shown a significant increment in the magnetic moment when the fraction of x increases in the bulk with the maximum value at x~0.5-0.55, as per shown in Figure 5.1. [70] Another interesting characteristic is the phase transition from face-centered cubic to body-centered cubic when the value of x increases to ~0.6. [70]
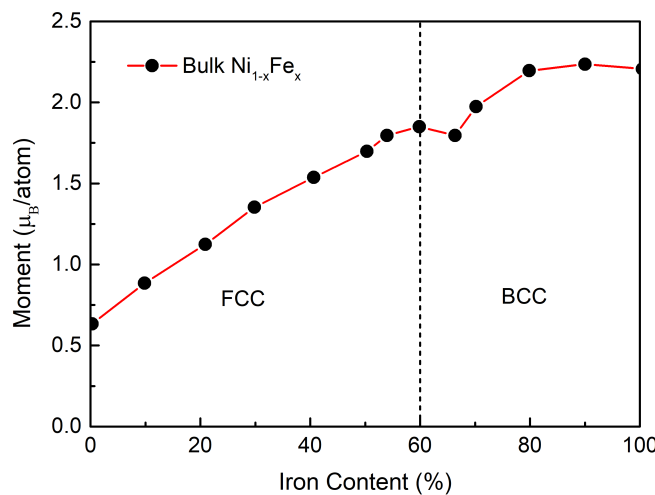
FIGURE 5.1: The plot of magnetic moment against increasing iron content [70]

There is only one report in the literature for the preparation of x~0.5 nanofibers,

but the results showed the formation of a fused mat than isolated nanofibers.[5] The preparation of x~0.5 nanofibers by pre-existing method (used for x~0.1 and x~0.2) was not suitable for x~0.5, which produced melted sheets of x~0.5 nanofibers after electrospinning. Therefore, there was a need to develop an alternative method for the fabrication of isolated sheets of x~0.5 nanofibers.

This chapter describes the different methods and approaches to make x~0.5 nanofibers. It represents an investigation of different solvents and compared their results to select the best method for x~0.5 nanofibers. Another key point was to find out the differences in the magnetic and physical properties at this fraction x~0.5.

5.2 Experimental

5.2.1 Chemicals used

Analytical grade reagents were used in this chapter for the preparation of x~0.5 nanofibers. These chemicals include Nickel acetate tetrahydrate ($(CH_3COO^-)_2Ni \cdot 4\,H_2O$) 98% purchased from Merck.Iron nitrate nonahydrate ($(NO_3^-)_3Fe \cdot 9\,H_2O$) $\geq$98%, Iron acetylacetonate ($(C_5H_7O_2)_3Fe$) 97% and Polyvinylpyrrolidone (PVP) (C_6H_9NO) average Mw~1,300,000 by LS method, Toluene 99.8% and Ethyl acetate 99% were purchased from the Sigma-Aldrich. Methanol 99.9% and acetone 99% were purchased from the Fischer chemical. Dimethylformamide (DMF) 99.8% was purchased from Acro seal Ⓡ.

5.2.2 Replication using the hydrated iron precursor (iron nitrate) from the literature

In the first attempt, x~0.5 electrospun nanofibers were prepared using the exact method as described in the literature. [5] For this typical synthesis, 1.5 g of nickel acetate and 2 g of iron nitrate were dissolved in 10 mL of methanol followed by the addition of 1 g PVP. The solution was stirred overnight to obtain a colourless mixture. This sample was electrospun using similar parameters as stated in the reference [5].

Infusion rate (mL/hr)	Voltage (kV)	Drum speed (rpm)	Distance (cm)	needle size (Guage)
0.6	17.5	60	10	18

TABLE 5.1: Electrospinning parameters from reference
[5]

The electrospun x~0.5 nanofibers in Figure 5.2 (a) showed highly branched nanofibers that melted and crumbled with the other nanofibers. This could happen due to the higher moisture content in the electrospinning solution from the hydrated iron salt

(iron nitrate nonahydrate) as a result of x being increased to x∼0.5, and also from the solvent. The high moisture content could lead to the melting of x∼0.5 nanofibers as can be seen from Figure 5.2 (a). In another attempt, it was found that electrospinning for only a short time period ranging from 1 to 2 hours can give the isolated nanofibers, but only if nanofibers were placed directly in a vacuum after electrospinning. However, these x∼0.5 nanofibers were not stable to thermal processing and diffused again into a mat as shown in Figure 5.2 (b) The reason behind this could be due to the high oxygen content of nitrates, which leads to the different degradation pathway for the polymer at high temperature, and eventually can lead to the melting of x∼0.5 nanofibers into a mat. Another possible reason could be that due to the low boiling point of methanol in combination with hydration, the nanofibers melt when processed at high temperatures. These results are similar to what was observed from the report[5] and persisted after many attempts, therefore, an alternate method was necessary to fabricate the x∼0.5 nanofibers.
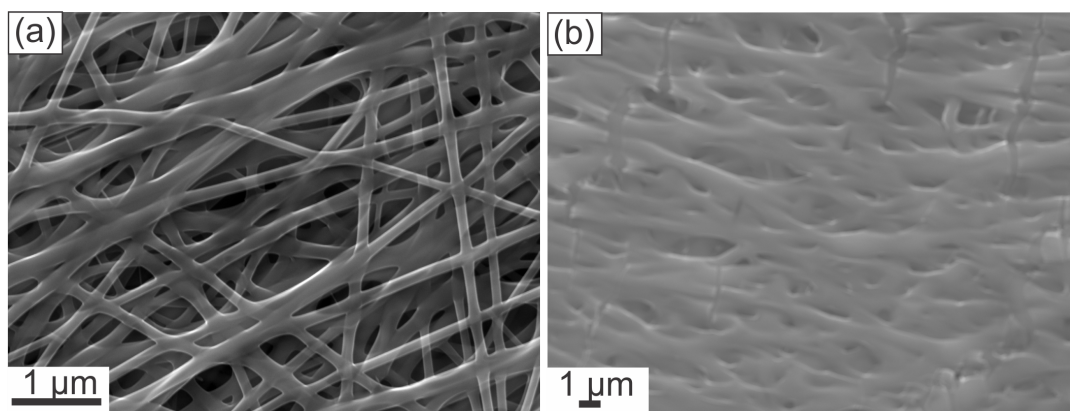
FIGURE 5.2: SEM images of x∼0.5 nanofibers. (a) electrospun (b) thermally processed

5.2.3 Solution preparation by using an alternative salt for iron (x) source

The idea behind the change in x source was to avoid the use of hydrated salt of iron and a solvent with high moisture content. The change in iron precursor was done by replacing iron nitrate with iron acetylacetonate in solution preparation. Iron acetylacetonate has already been found promising for the fabrication of various iron oxide nanofibers, and nickel-iron oxides (Ni_xFe_yO) nanofibers in the previous literature.[144, 145] The change in the iron source also required a change in the solvent for solution preparation. This is because iron acetylacetonate is only soluble in polar aprotic solvents. Therefore, a solvent with low moisture content was needed to dissolve both iron and nickel precursor ions for electrospinning. The solubility studies by using different solvents are given in Table 5.2.

On the basis of solubility, the last three solvents/solvent mixtures were further investigated to prepare the x∼0.5 nanofibers. Since both metal precursors are soluble in DMF (dimethylformamide), this solvent was first selected to optimize the other parameters.

Solvents	Nickel acetate	Iron acetylacetonate
Methanol	✓	×
Toluene	×	✓
Ethyl acetate	×	sparingly soluble
Acetone	×	sparingly soluble
DMF	✓	✓
20%Methanol : 80%DMF	✓	✓
50%Methanol : 50%DMF	✓	✓

TABLE 5.2: Solubility of iron acetylacetonate and nickel acetate in different solvents (where ×= not dissolved and ✓= dissolved)

5.2.4 Polymer concentration and voltage optimization in DMF

The electrospinning process depends on the uniaxial stretching of the charged jet under an applied electric field. The stretching of this jet is highly dependent on the viscosity of the solution. If the viscosity is too low, the jet will break under applied voltage and form droplets to be collected on the rotating drum. These droplets are called "beads", and more beading was observed at low polymer solution concentrations. Therefore, polymer concentration was adjusted first at the minimum fractions of metal ions (1 mmol).

In the first procedure, the polymer mass was kept the same (0.25g) as was used for the x∼0.1 and x∼0.2 nanofibers. But the concentration was adjusted to 1 mmol for both metal precursors. For this, 0.25 g of nickel acetate (1 mmol) and 0.35 g of iron acetylacetonate (1 mmol) were dissolved separately in 5 mL of DMF (0.2 mmol/mL). From these stock solutions, 2 mL each (1:1) was transferred into a flask and stirred to get the clear solution. 0.25 g of polymer was added to the mixture and the solution was stirred to get a homogeneous mixture. There was no need to add acetic acid in the solution as was used for x∼0.1 and x∼0.2 as a different iron source and solvent were used for these nanofibers. This solution was electrospun using the same parameters as x∼0.1 and x∼0.2 and the resulting nanofibers are shown in the Figure 5.3.
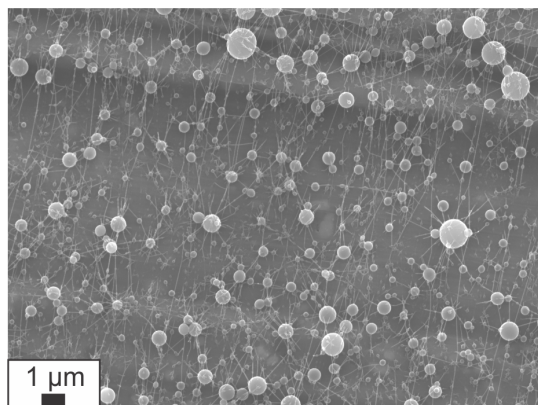
FIGURE 5.3: As prepared x∼0.5 nanofibers using the same parameters as x∼0.1 and 0.2 at 0.25 g of PVP

It can be seen that the electrospun x∼0.5 nanofibers show the formation of beads on a web-like morphology. The formation of beads suggests the difficulty in stretching the Taylor cone droplet under applied voltage to break down into nanofibers. It could be due to either a low viscosity of the solution or the ineffective electric field on the electrospinning solution at an applied voltage of 12.5 kV. To investigate the effect of voltage, the same solution was electrospun at higher voltages spanning from 15 kV to 20 kV (with an increment value of 2.5 kV). The resulting nanofibers are shown in Figure 5.4.
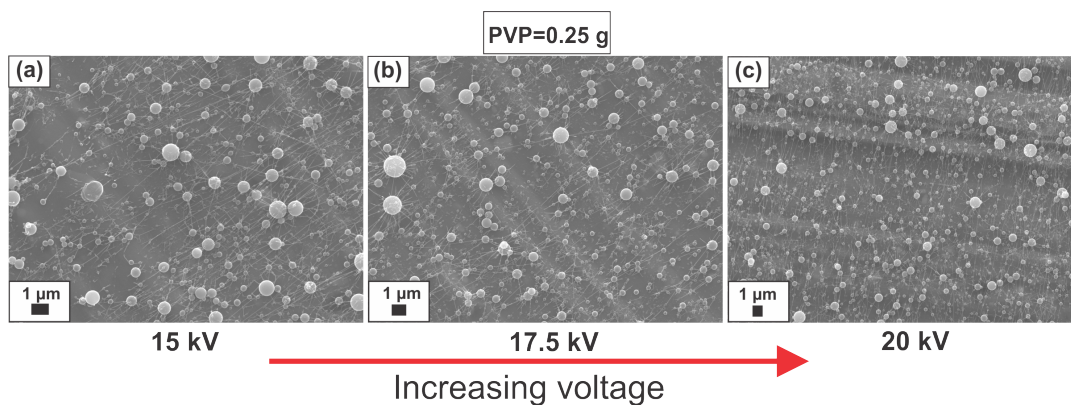
FIGURE 5.4: Electrospun nanofibers with x∼0.5 with increasing voltage at 0.25 g of PVP

Figure 5.4 shows that the voltage increase has a negligible effect on the resulting morphology, as all images show beaded nanofibers. Therefore, the concentration of polymer was increased systematically at 15% increment to give three solutions using 0.40g, 0.55g, and 0.70g PVP. Each prepared solution was again electrospun at three different applied voltages (15, 17.5, and 20 kV) to investigate optimised electric field strength during electrospinning (the rest of the parameters on the electrospinning set-up were kept constant). The results are shown in the Figures.5.5 5.6, 5.7.
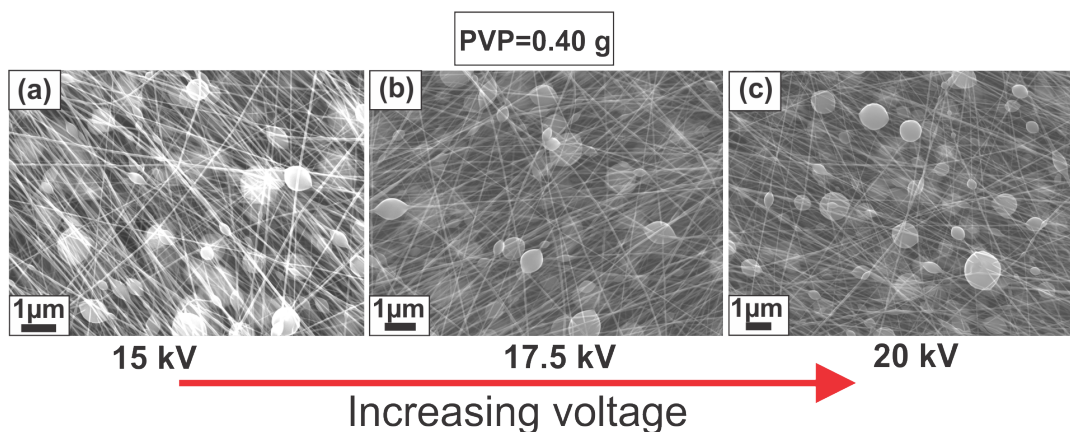
FIGURE 5.5: Electrospun nanofibers with x∼0.5 with increasing voltage at 0.40g of PVP

The first incremented polymer concentration (0.40 g) shows a clear difference from the initial sample using 0.25 g of PVP. From Figure 5.5 (a,b,c), it can be seen that beading is reduced significantly and some smooth fibers are formed.
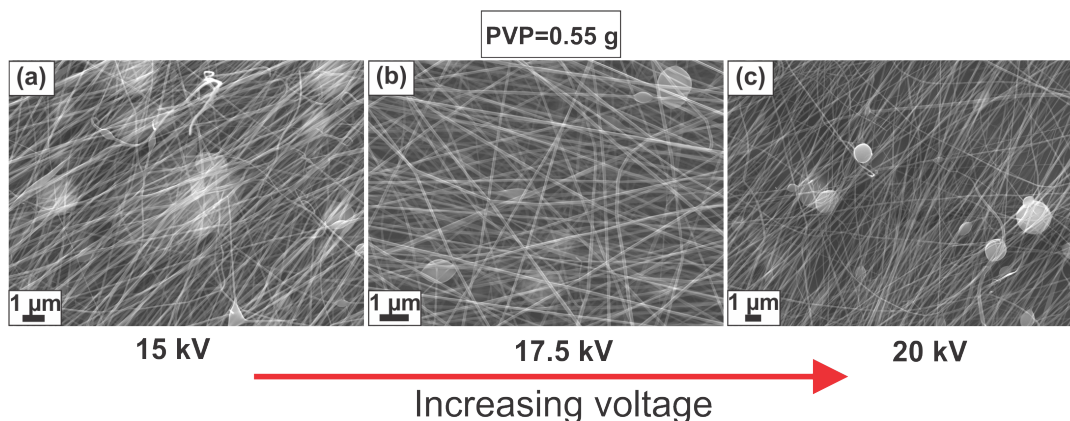
FIGURE 5.6: Electrospun nanofibers with x∼0.5 with increasing voltage at 0.55g of PVP

To further improve the morphology of the nanofibers, the PVP concentration is further increased to 0.55 g. It can be seen that the beading is significantly reduced as a function of increased applied voltage as seen in the Figure 5.6 (c). However, there is still some beading present. Therefore, the amount of PVP was further increased to 0.70 g.
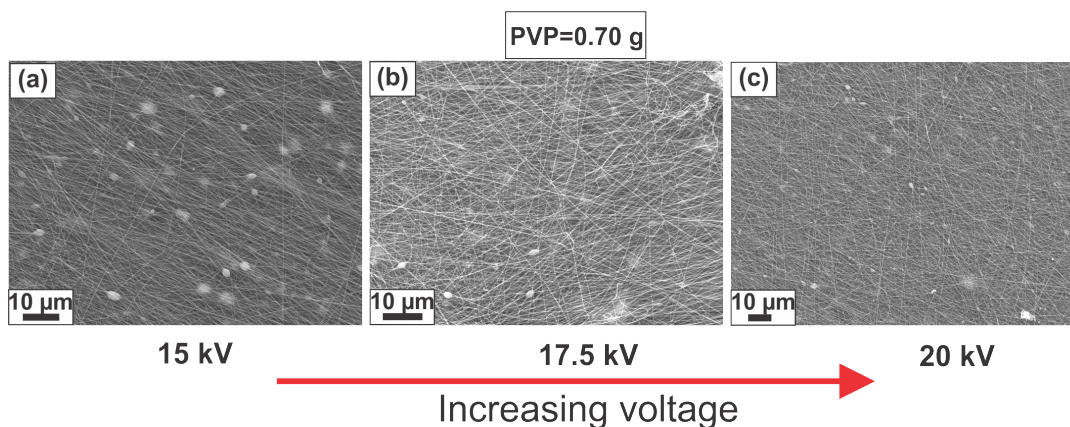
FIGURE 5.7: Electrospun nanofibers with x∼0.5 with increasing voltage at 0.70g of PVP

From Figure 5.7 it can be seen that the beading is negligible when the PVP concentration was increased to 0.70 g. It can be seen that all three electrospun samples at different voltages have smoother surfaces and a small amount of beading. The most effective result was obtained by electrospinning the solution at a maximum voltage (20 kV), which shows negligible beading on the electrospun nanofibers Figure 5.7 (c).

5.2.5 Optimization of metal ions concentration in DMF

The metal ion concentration was then optimised by up-scaling the amount dissolved in the separate solutions. For this, the metal ion concentration was increased two-fold in separate solutions. 2 mmol of each nickel acetate (0.50 g) and iron acetylacetonate (0.70 g) were first dissolved separately in 5 mL of DMF. After which, 2 mL of each of the solutions was transferred into another flask and mixed together. Into this stirred solution, 0.70 g of PVP was added and stirred continuously to obtain a homogeneous mixture. This prepared solution was electrospun with a slight variation of voltages ranging from 17.5 kV to 20 kV (as these two voltages have given good results, as shown above). All other parameters were similar to the above. The SEM images of the electrospun sample are shown in Figure 5.8.

It can be seen from the Figure 5.8 (a and b) that increase in metal ion concentration has no effect on the morphology of electrospun nanofibers. But when the voltage was increased to 20 kV, the beading was significantly reduced. Therefore, 20 kV was selected for all future electrospinning experiments for the x∼0.5 nanofibers.
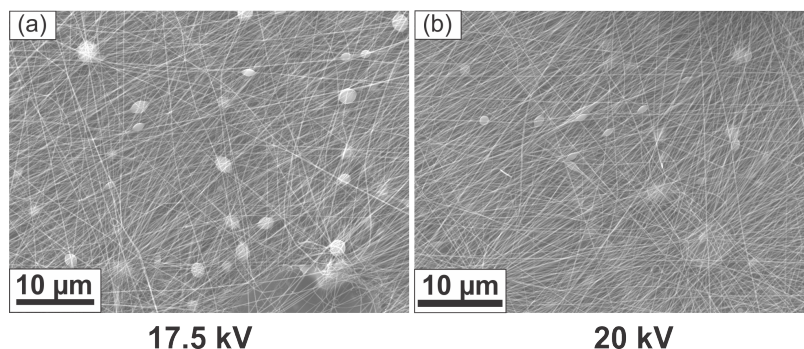
FIGURE 5.8: Electrospinning of x~0.5 nanofibers with 2 mmoles of metal ions concentration at (a) 17.5 kV and (b) 20 kV

A further increase in the concentration of metal ions to 4 mmoles (with 1 g of nickel acetate and 1.4 g of iron acetylacetonate dissolved in 6.5 mL of DMF, separately) showed the complete removal of beading as shown in Figure 5.9. Due to negligible beading at this concentration of metal ions and polymer, this concentration was used to synthesize the x~0.5 nanofibers for a more detailed investigation of physical, thermal, and magnetic properties.
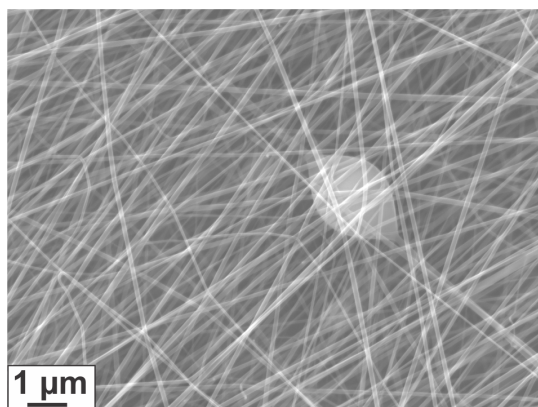
FIGURE 5.9: Electrospinning of x~0.5 nanofibers with 4 mmols metal ions concentration at 20 kV. Other electrospinning parameters were the the same as x~0.1 and x~0.2 (ir = 0.4 mL/hr, distance = 10 cm, needle size = 22 G, and drum speed = 60 rpm)

5.2.6 Thermal treatment of x~0.5 nanofibers

5.2.6.0.1 Replication using the thermal treatment profile of x~0.1 and x~0.2 nanofibers

First, the x~0.5 nanofibers prepared using a 4 mmol concentration solution were thermally treated using the same thermal treatment profile as used for $x \sim 0.1$ and 0.2. For this, the sample was dried overnight at room temperature under vacuum and then placed in a tube furnace for the thermal annealing step. As spun nanofibers were too sticky on the aluminum foil to be separated, they were instead placed with aluminum foil in the tube furnace. The SEM results are shown in Figure 5.10.
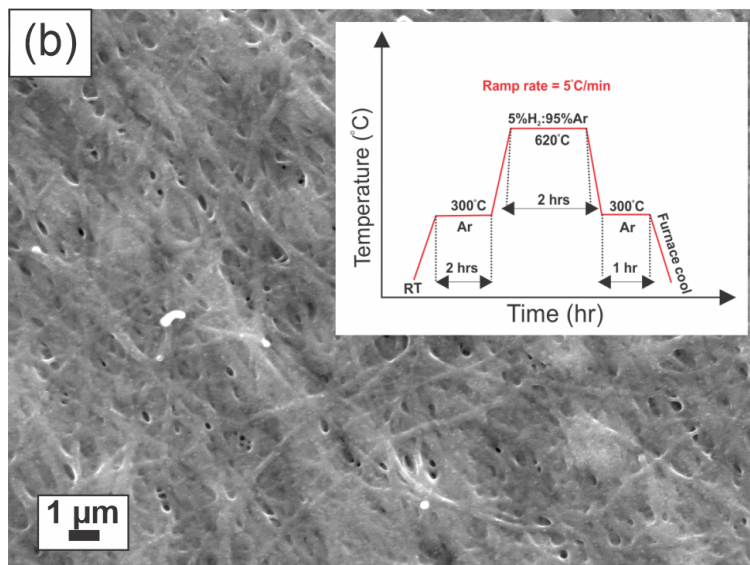
FIGURE 5.10: Thermal annealing of the electrospun x∼0.5 nanofibers using already developed x∼0.1-0.2 thermal treatment profile. upper left inset: thermal treatment profile

It can be seen in Figure 5.10 that the nanofibers have lost their morphology due to melting, and dissolved into a mat (Figure 5.10). Therefore, thermal conditions needed to be optimized for more desirable nanofibers.

5.2.6.0.2 Effect of initial ramp rate on the processed nanofibers

The ramp rate was investigated to determine the effects of a sudden rise in the initial temperature at the first step of removing DMF. The boiling point of DMF is ∼150°C, which is higher than the glass transition temperature of PVP, 110 °C, and the slow removal could cause the melting of the polymer strand at high temperature leading to the disintegration of x∼0.5 nanofibers. To investigate this hypothesis, the ramp rate was increased from 5°/min to 10°C/min in the first step when heating to 300°C, which showed the melted nanofibers. Therefore, the ramp rate was increased to 20°C/min to 300°C and left for two hours, while the heating rate for the rest of the steps wes maintained at 5°C/min when heating to 620°C in 5% H_2/Ar flow and then again back to 300°C before it cooled down to room temperature. The results are shown in Figure 5.11 below.
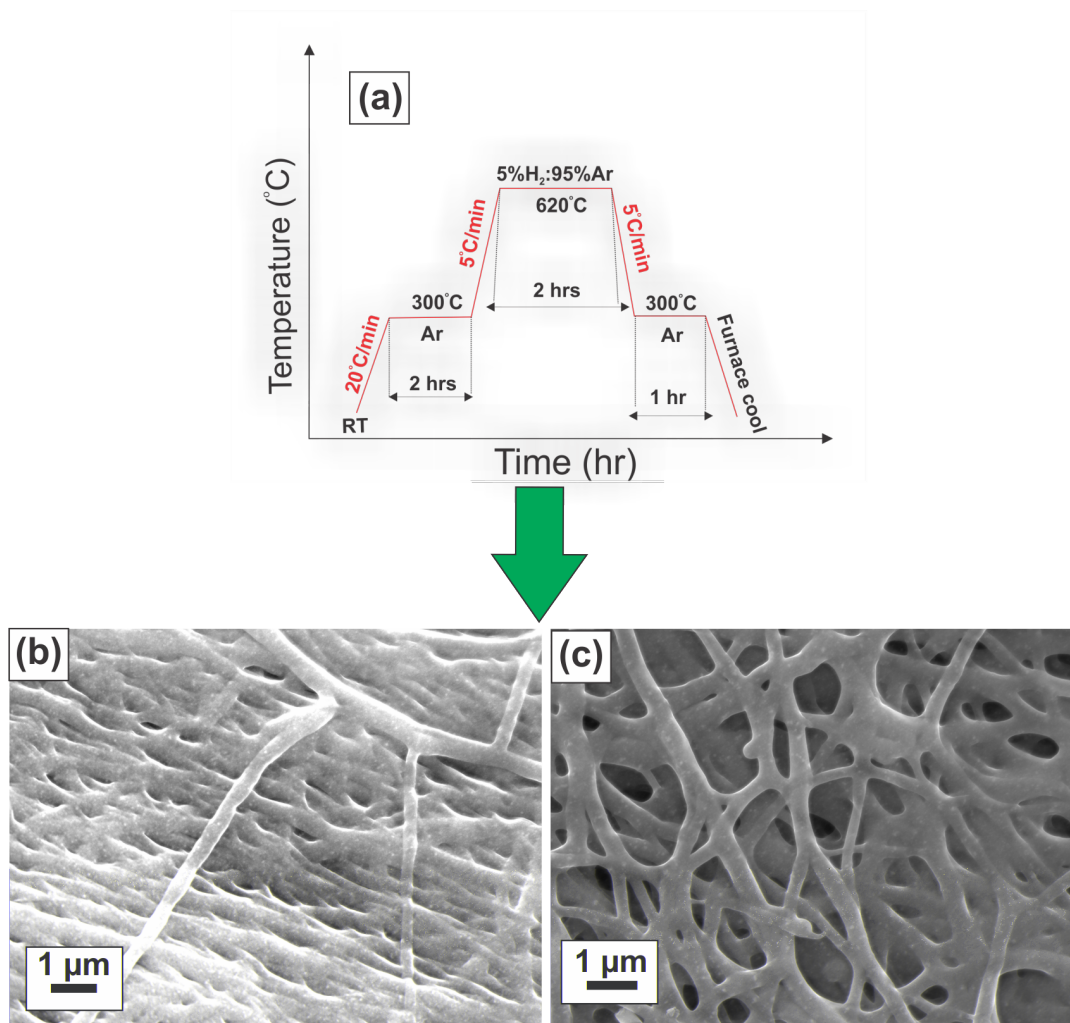
FIGURE 5.11: Change of ramp rate at first step to 300°C for x~0.5 nanofibers at 20°C/min. Both (a) and (b) are different part of the same sample

It can be seen in Figure 5.11 (b and c) that melted nanofibers were formed with increasing ramp rate to 20°C/ min to 300°C, but some fiber-like morphology was observed. In both images, more nanofiber-like structures are visible as compared to the other x~0.5 nanofibers samples presented above. Therefore, instead of continuing with changing the ramp rate, the samples were dried in a vacuum oven at various temperatures, at constant pressure (0.05 MPa) prior to the thermal treatment steps. The idea behind this was to have the optimum amount of solvent from the nanofibers before the thermal processing to see if the nanofiber morphology can be improved.

5.2.6.0.3 Vacuum oven heating

The temperature in the vacuum oven was increased from room temperature at multiple steps to see the effect of the change in temperature up to the boiling point of DMF at constant pressure, 0.05 MPa (0.5 bar). Table 5.4 summarises the conditions used to pretreat the prepared x∼0.5 nanofibers, and the morphologies of the resulting nanofibers are shown in Figures 5.12 (a) to (e). Note that the same stock solutions were used for the electrospinning of all separately prepared samples. The stock solutions were almost four to five days old when the samples of 100°C and 150°C were electrospun.

Temperature (°C)	Duration	Observations	Reference Figure 6.15
25	overnight under vacuum	Fused nanofibers	(a)
35	overnight under vacuum	Fused nanofibers	(b)
45	overnight under vacuum	Fused nanofibers	(c)
100	2 hours at 100°C and left overnight under vacuum	Less fused nanofibers	(d)
150	2 hours at 150°C and left overnight under vacuum	Improved nanofibers	(e)

TABLE 5.3: Temperature variation in vacuum oven before furnace annealing

Figure 5.12 (a to e) shows the effect of increasing the temperature in vacuum annealing. The first three thermally treated samples at low temperatures still show the branching and melting of nanofibers, but more fiber-like morphology was observed when the as-spun x∼0.5 nanofibers were treated at 100°C in vacuum leaded thermal annealing. The temperature was raised to 100°C for two hours, and then the furnace cooled to room temperature under vacuum. This step was selected to completely remove the moisture content from the nanofibers before thermal treatment.
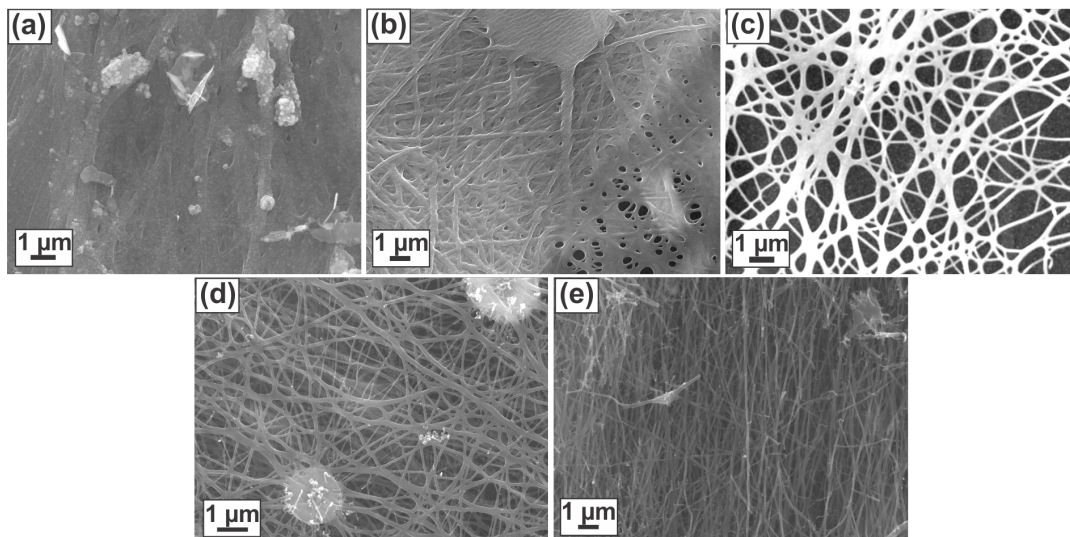
FIGURE 5.12: Thermally treated x∼0.5 nanofibers by using different pretreatment conditions used to dry the x∼0.5 nanofibers in vacuum oven at (a) at 25°C (b) at 35°C (c) at 45°C (d) at 100°C and (d) at 150°C. The first three samples were left overnight (∼18 hrs) at these temperatures under vacuum. Whereas, the last two samples at 100°C and 150°C were treated at this temperature for two hours of heating at 0.05 Mpa, and then furnace cooled, and left overnight(∼15 hrs) under vacuum

The dramatic change in the sample morphology was observed when the temperature was further increased to 150°C in a vacuum oven for 2 hours, and after which the sample was left overnight at 0.05 Mpa. This sample has shown the presence of isolated x∼0.5 nanofibers after thermal annealing, as can be seen in Figure 5.12 (e). The most likely reason for this improved morphology is attributed to the partial removal of DMF from the nanofibers prior to the thermal treatment steps. For this sample, nanofibers could easily be peeled off the Al foil and placed directly on the alumina grids for thermal processing in the tube furnace.

5.2.6.0.4 Effect of vacuum annealing time on nanofibers morphology from freshly made stock solution

As the reproducibility of the x∼0.5 nanofibers was one of the crucial challenges, we next investigated the effect of vacuum annealing time optimization on the freshly prepared stock solutions. As stated above, the time optimization was done on the electrospinning solutions from the four to five days old stock solutions. Therefore, ∼0.5 nanofibers from fresh stock solutions were prepared without aging and heated at 150°C for 2 hours under vacuum at 0.05 Mpa. However, after thermally treating the electrospun nanofibers, the results were not reproducible. The reason behind this could be the invariability in the moisture content that has caused the instability in these nanofibers. Therefore, the duration of drying is varied from 4-6 hours at 150°C in the vacuum oven and left it overnight under vacuum kept at 0.05 MPa. After which the samples were thermally processed in the furnace, and the results have been shown in Figure 5.13.
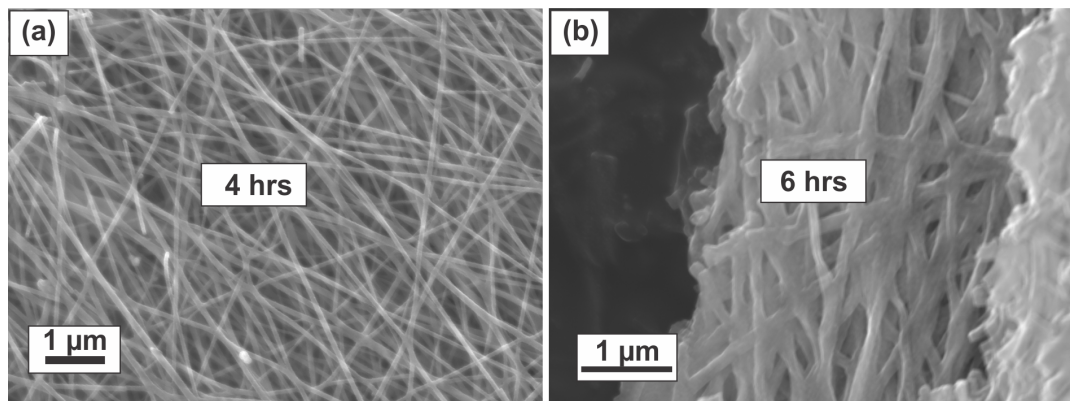
FIGURE 5.13: Effect of changing the length of time for the thermally processed x∼0.5 nanofibers from the freshly prepared stock solutions and dried under vacuum at (a) 4hrs and (b) 6 hrs

Figure 5.13 (a) and (b) show a comparison between the thermally processed sample left for 4 hours and 6 hours at 150°C at 0.05 MPa. It can be seen that the nanofibers dried for 4 hours have improved morphology compared to the samples left longer in the vacuum oven at the same pressure. This means that the optimum amount of DMF was still required for the x∼0.5 nanofibers to retain their morphology. From this, the optimum time was decided to be 4 hours for the fabrication of x∼0.5 nanofibers as the longer exposure under vacuum may cause instability in the nanofibers that can disintegrate the nanofibers in the furnace at high temperatures. The samples were scaled up using this temperature and we observed great reproducible x∼0.5 nanofibers after three to four attempts.

5.2.7 Fabrication using a 20:80 mixture of methanol: DMF

The effect of solvent on the structural and magnetic properties of the x∼0.5 nanofibers was also studied by using a 20: 80 mixture of methanol: DMF as a solvent. The objective of this study was to see what happens to the structural and magnetic properties of x∼0.5 nanofibers; if they could be improved any further by using a solvent mixture. For this, a mixture of methanol: DMF was prepared by mixing 3 mL of methanol with 12 mL of DMF. Specifically, 0.434 g of iron acetylacetonate (0.6 mmol/m) and 0.306 g of nickel nitrate (0.6 mmol/mL) were dissolved separately in 2 mL of the 20:80 solvent mixture. These two precursor solutions were mixed together and stirred for 15 mins to get a homogeneous mixture. To this mixture, 0.70 g of PVP was added and the solution was stirred to get a clear solution. This solution was loaded into a 5 mL syringe in the electrospinning setup and the solution was electrospun by using the already developed parameters for x∼0.5 nanofiber: injection rate=0.4 mL/hr, needle= 22 G, drum speed= 60 rpm, distance = 10 cm and applied voltage= 20 kV. The electrospun mat was collected from the rotating drum and placed in a vacuum oven at 150°C for 4 hours dried overnight at vacuum at constant pressure (0.05 MPa) at room temperature. These prepared x∼0.5 nanofibers were thermally processed in the tube furnace with the optimised thermal treatment

profile where the first step was ramped for 2 hours to 300°C at 20°C in an argon flow. The second step was ramped up to 620°C at 5°C/min under 5% H_2 : 95% Ar atmosphere for 2 hours. The gas was switched back to Ar and was ramped down to 300°C in an hour for uniform heating before the sample was furnace-cooled to room temperature (This extra last step is to prevent the sudden drop in the temperature and to control the uniform heating in the tube furnace). The results are given in the results and discussion section.

5.2.8 Fabrication using a 50:50 mixture of methanol: DMF

The x∼0.5 nanofibers were also synthesized by using a 50:50 mixture of methanol: DMF by dissolving the 0.435 g of iron acetylacetonate in 2 mL of DMF (0.6 mmol/mL) and 0.306 g of nickel acetate in 2 mL of methanol (0.6 mmol/mL). These two separate solvent solutions were combined and stirred together to prepare a homogeneous solution. After which, 0.70 g of PVP was added to the stirring mixture for electrospinning. The prepared solution was electrospun at the optimised parameters mentioned above and thermally processed by using the same protocol given above. The x∼0.5 nanofibers produced by this procedure had a mixture of both fused mats and isolated nanofibers. This showed that a high amount of methanol in combination with DMF is not suitable which could be due to the moisture content from the methanol. Therefore, this method was not used for the fabrication of x∼0.5 nanofibers.

5.3 Results and discussions

5.3.1 x∼0.5 nanofibers prepared using DMF as solvent

5.3.1.1 SEM of electrospun nanofibers

The surface morphology of quasi-unidirectional x∼0.5 nanofibers can be seen in the Figure 5.14 (a) and (b). Similar to x∼0.1 and x∼0.2, these nanofibers show smooth surface morphology with no evidence of branching, beading, and/or interlinked nanofibers. Figure 5.14 (b) shows the high-resolution SEM image of x∼0.5 nanofibers where the nanofibers were relatively thinner as compared to x∼0.1 and x∼0.2 with a mean diameter of ∼144 nm and the standard deviation of 21 nm (Figure 5.14 (a).

The thin diameters for x∼0.5 are attributed to the solvent effect when DMF was used as a solvent rather than methanol (which was used for x∼0.1 and x∼0.2). DMF has a high dielectric constant (36.71) compared with methanol (32.70) at room temperature, which can contribute to the formation of smooth nanofibers at an applied voltage. This could happen due to the charge stabilization on the solution jet above a threshold voltage in the electrospinning setup.[96] The role of the dielectric constant is important for determining the role of cohesion between the polymer and the solvent for the overall charge density. DMF also has relatively close values of Hansen's solubility parameters (HSPs) with PVP HSPs values compared to methanol (Table
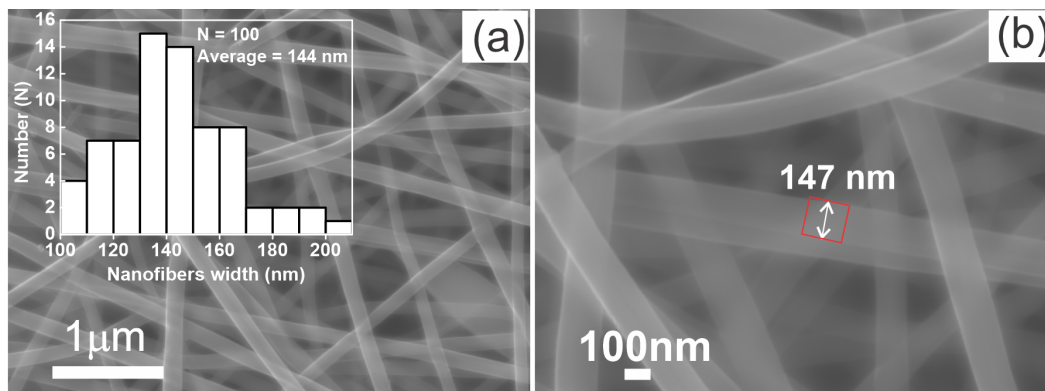
FIGURE 5.14: SEM images of x∼0.5 nanofibers (a) Low resolution image at 1μm. Upper right inset: Average width of nanofibers. (b) High-resolution image (at 100 nm) of (a) showing the diameter of a single nanofiber

3.1), this could also have contributed towards the morphology of the nanofibers as a result of increased interactions between solvent and polymer.[96, 146] The voltage was also increased to 20 kV for x∼0.5, whereas the applied voltage to make x∼0.1 and x∼0.2 nanofibers was 12.5 kV. The applied voltage could affect the width of thin nanofibers due to the more "stretching" of the solution to get collected on the rotating drum.

5.3.1.2 SEM analysis of thermally processed nanofibers

The surface morphology of thermally treated x=0.5 nanofibers using the optimised heating profile is shown in the SEM images in Figure 5.15 (a) and (b). It can be seen that thermal treatment further reduced the diameter of nanofibers to a mean diameter of 71 nm with a standard deviation of 17 nm for the x∼0.5 nanofibers as per shown in the histogram in the Figure 5.15 (a). Some even thinner nanofibers of ∼35 nm were also present in these nanofibers. In comparison to x∼0.1 (∼160 nm) and x∼0.2 (∼112nm), these nanofibers are thinner in diameter. Moreover, the thermally treated x∼0.5 nanofibers have also shown smoother surfaces than those at lower iron fractions (x∼0.1-0.2). The high-resolution image in Figure 5.15 (b) indicated the presence of some small nanostructures on the surfaces of these x∼0.5. This is not clarified by these SEM images, therefore TEM for the detailed analysis was required for the detailed structural analysis of x∼0.5 nanofibers.
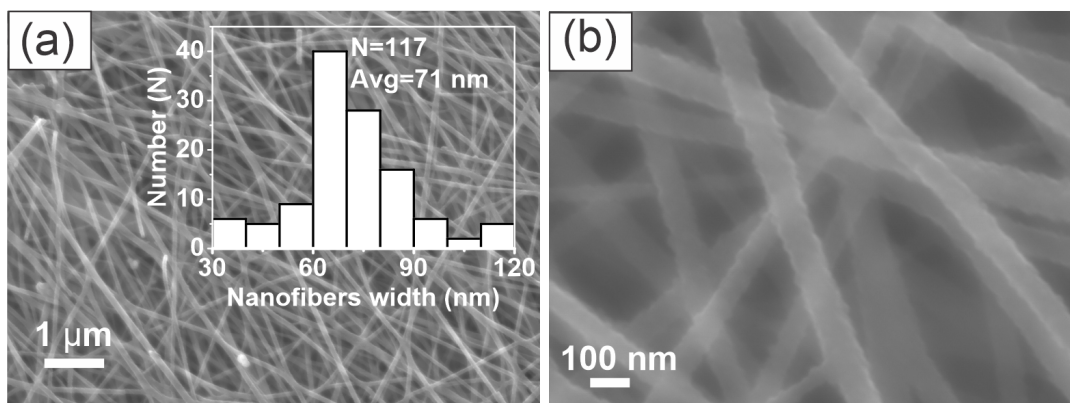
FIGURE 5.15: SEM images of thermally processed x∼0.5 nanofibers (a) Low- resolution image and. Upper right inset: Average width of nanofibers. (b) High- resolution image at 100 nm showing the diameters of nanofibers

5.3.1.3 TEM analysis

The TEM analysis for the thermally processed x∼0.5 nanofibers is shown below in Figure 5.16. It can be seen from the Figure 5.16 (a) that the prepared nanofibers have very thin diameters as the single nanofiber of ∼75 nm can be seen in Figure 5.16 (b). Both images in Figure 5.16 (a) and (b) have shown the presence of nanoparticles with the more prominent skewed particle size distribution, where the number of large nanoparticles was greatly reduced as compared to x∼0.1 and x∼0.2.
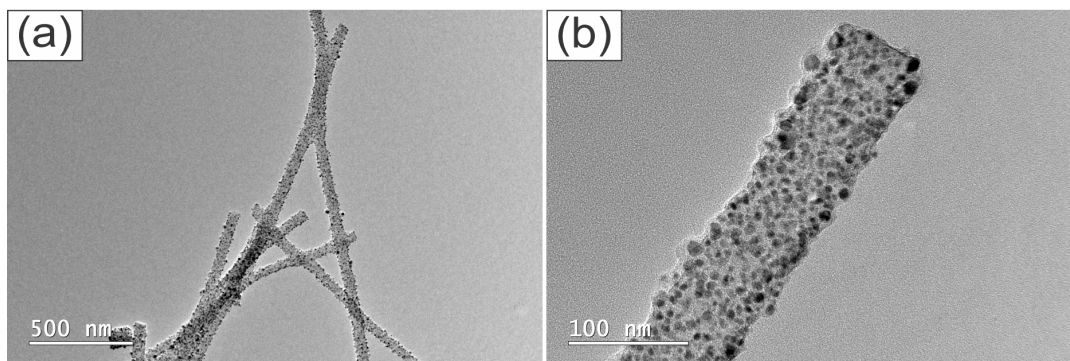
FIGURE 5.16: TEM images of thermally processed x∼0.5 nanofibers at (a) Low resolution (b) High resolution

The overall average nanoparticle size was ∼5 nm with a standard deviation of 2.5 nm. But as can be seen from the image the average particle size from the small nanoparticles was found to be 4.5 nm whereas, ∼9 nm was found for the large nanoparticles as per shown in Figure 5.17.

In comparison to the strong bimodal particle size distribution for x∼0.1 and skewed distribution for x∼0.2, narrow-sized skewed distribution with the increased fraction of smaller nanoparticles was observed for x∼0.5 nanofibers. This showed that by increasing x, more small-sized nanoparticles formed for x∼0.5 nanofibers.
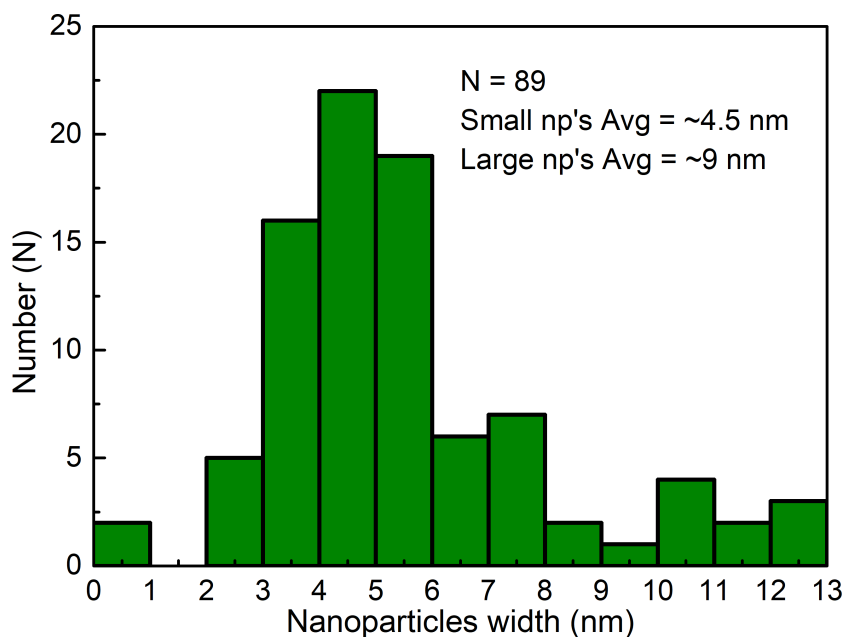
FIGURE 5.17: Size distributions of nanoparticles from Figure 5.16 (b)

5.3.1.4 STEM maps and elemental composition

STEM maps of x∼0.5 are given in Figure 5.18 (a) to (e), where (a) shows the TEM image of a single ∼0.5 nanofiber. The distribution of iron and nickel in the $Ni_{1-x}Fe_x$ nanoparticles can clearly be seen from figures 5.18(d) and 5.18(e). However, the presence of carbon and oxygen was also visible in 5.18(b) and 5.18(c) in these nanofibers due to the remaining polymer fragment, PVP, similar to the previous fractions of x∼0.1 and x∼0.2 nanofibers.

Figure 5.19 shows the STEM maps for the overlay of iron and nickel, it can be seen from the map that both iron and nickel coincide with each other in these $Ni_{1-x}Fe_x$ nanoparticles. This also showed no evidence of the separate nickel and iron in these nanoparticles.
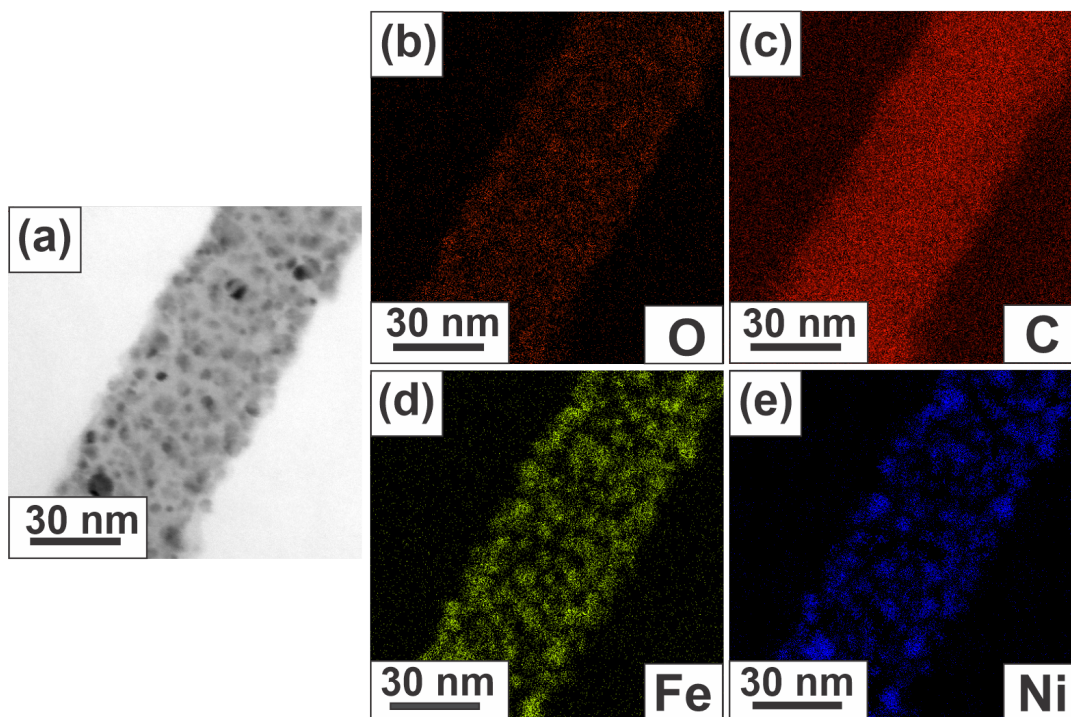
FIGURE 5.18: STEM maps of x∼0.5 nanfibers. (a) A single x∼0.5 nanofiber. (b) oxygen map, (c) carbon map, (d) iron map, and (e) nickel map of (a)
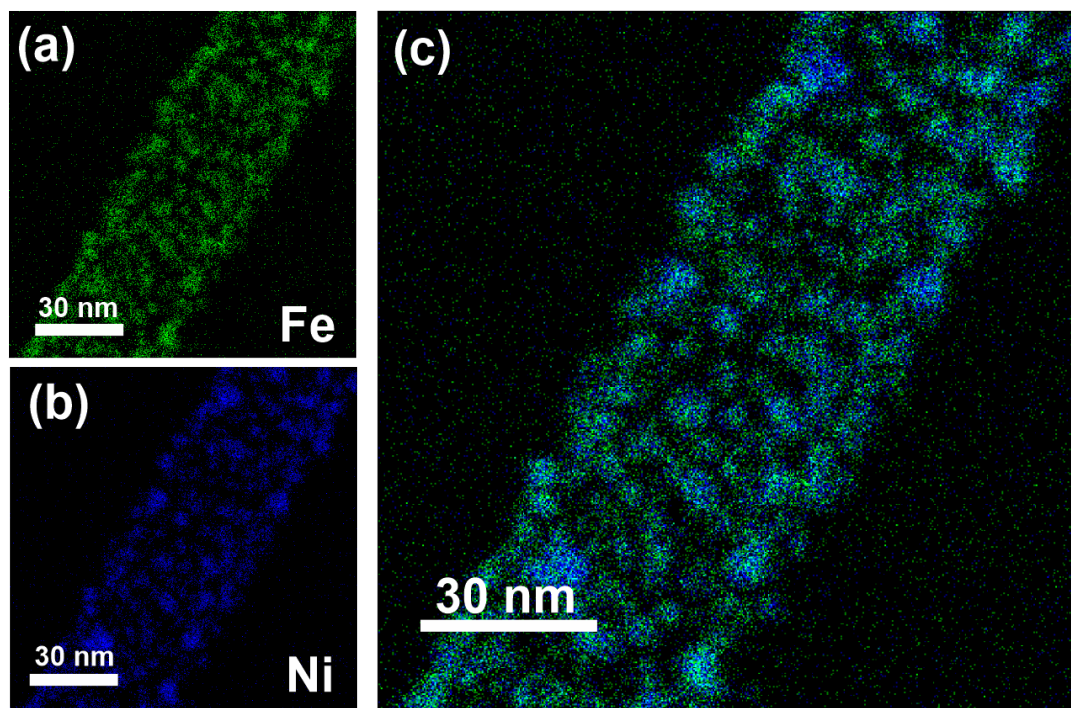
FIGURE 5.19: STEM maps of (a) iron, (b) nickel, and (c) overlay of iron and nickel

In another Figure 5.20 the overlay of oxygen with iron (Figure 5.20 (a)), and oxygen with nickel (Figure 5.20 (b)) is shown. This overlay was important as to observe the presence of any oxide formation in these x∼0.5 nanofibers. It can be seen that there was no apparent formation of oxides from all these images. This showed that

even if there were some oxides present, the fraction of oxides was very small compared to the overall fraction of the sample to be observed from these STEM maps.
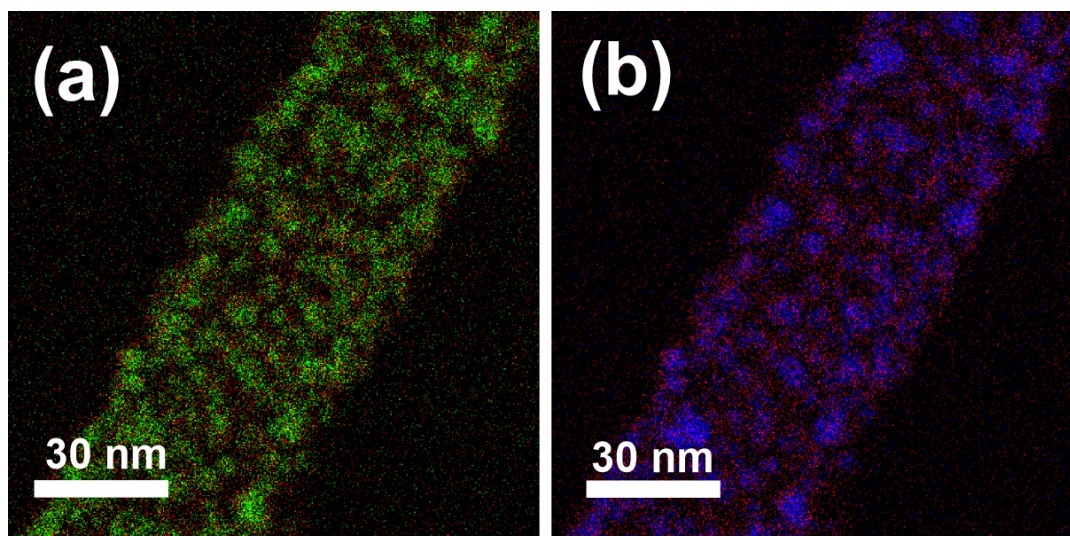
FIGURE 5.20: STEM maps of (a) overlay of oxygen (red) and iron (green), and (b) overlay of oxygen (red) and nickel (blue)

The EDS spectrum and elemental composition of x~0.5 nanofibers are shown in the Figure 5.21. The image in Figure 5.21 showed the nanofiber used for elemental analysis. The EDS spectrum confirmed the presence of both nickel and iron in these nanofibers with the overall elemental composition given in the table. The elemental fraction of iron was ~51% which confirms the presence of similar amounts of both metal ions. EDS analysis from the other areas of the sample has also shown consistent results with the given EDS spectrum.

Element K*	Mass %	Atoms %
C	87.33	95.29
O	2.96	2.42
Fe	0.17	1.10
Ni	0.19	1.06
Total	100.0	100.0
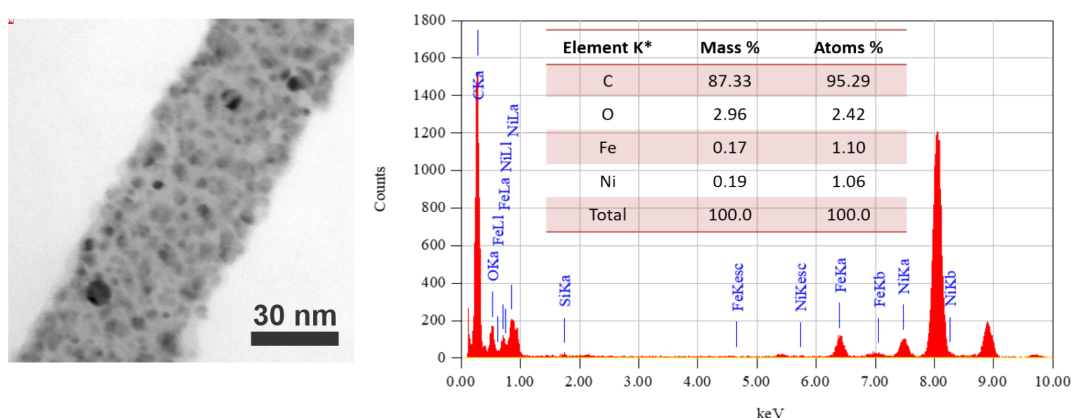
FIGURE 5.21: TEM image and EDS Spectrum of a x~0.5 nanofiber

5.3.1.5 SAED analysis

The SAED analysis of the x~0.5 nanofibers shows various diffraction rings in Figure 5.22. Similar to those observed for x~0.1 and x~0.2 nanofibers, the four diffracted rings (red circles) of x~0.5 are indexed to the FCC crystalline phase of $Ni_{1-x}Fe_x$ with

the Miller indexes (111), (200), (220) and (311). The value of the lattice parameter was also calculated to be 3.57Å with a standard deviation of 0.02Å. The increased value of the lattice parameter was in agreement with the expected range for the iron fraction x~0.5. Two additional diffraction rings (yellow circles) were also observed from this SAED pattern shown in Figure 5.22. The d-spacings of these rings were 2.49 Å and 1.78 Å and are attributable to the diffraction peaks from (311) and (440) reflections of either magnetite or nickel ferrite, respectively. The calculated lattice parameter from these two diffraction rings was 8.28 Å, which is close to nickel ferrite (NiFe$_2$O$_4$) 8.32 Å than magnetite (Fe$_3$O$_4$) 8.39 Å. The presence of these two rings shows the formation of some NiFe$_2$O$_4$ in these x~0.5 nanofibers during thermal processing. This was not observed in the other fractions with lower iron content. This could be due to the increased oxygen content (iron acetylacetonate), in x~0.5, that leads to the formation of nickel ferrite. All the diffraction rings have shown bright spots over the diffused rings that were also similar to the other fractions. This behavior was attributed to the presence of larger Ni$_{1-x}$Fe$_x$ (~9 nm) nanoparticles responsible for the bright spots and diffused rings from the smaller nanoparticles in these x~0.5 nanofibers.
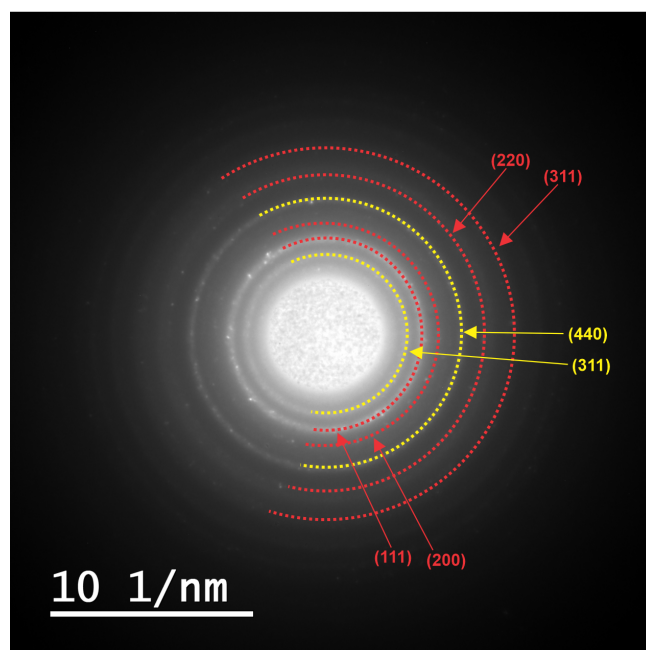
FIGURE 5.22: SAED pattern for x~0.5 nanofibers. Red rings for the Ni$_1 - x$Fe$_x$ and yellow rings for NiFe$_2$O$_4$

5.3.1.6 XRD analysis

The XRD pattern of x∼0.5 nanofibers is given in the Figure 5.23. In the XRD plot, the first reflection was indexed to the carbon component of the polymer backbone with a d-spacing of 1.04 nm, and the other two reflections were indexed to the FCC crystal structure of $Ni_{1-x}Fe_x$ (reference pattern no 00-047-140). Two other impurity peaks from $NiFe_2O_4$ were also shown in the expanded pattern of Figure 5.23. These peaks were indexed to the cubic crystalline phase of $NiFe_2O_4$ (reference pattern no 00-054-0964), however, the intensity for these peaks was very low, and can only be seen in the background noise. It suggested that the impurity was very small to the overall fraction of the sample. In comparison to the low angle reflections of PVP for x∼0.1 and x∼0.2, only one peak for carbon fragment was observed at a low angle for x∼0.5 nanofibers. This could happen due to the alternative synthesis technique to prepare x∼0.5, where a different method using DMF and iron precursor was used. That can lead to the different degradation pathway of PVP and give only one peak at a low angle. The fittings for the $Ni_{1-x}Fe_x$ by using the upper right inset of the reflections (111) and (200) gave a lattice parameter of 3.570 Å with the standard deviation of 0.001 which is less than the bulk $Ni_{1-x}Fe_x$ with 3.59 Å but in agreement with the lattice parameters found for the other $Ni_{1-x}Fe_x$ nanoparticles from the previous literature[70, 147, 148]. The mean crystallite size calculated using the Scherrer equation was 3.7 nm. Which showed that the number of small-sized $Ni_{1-x}Fe_x$ was increased with increasing x∼0.5.
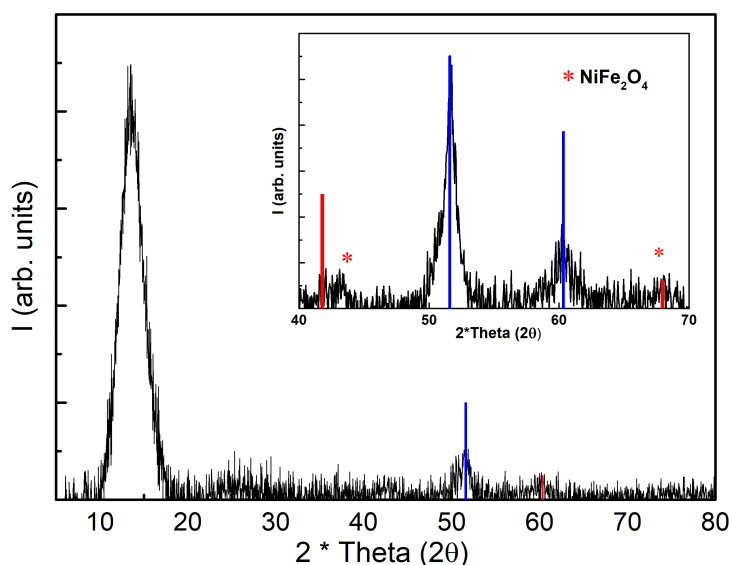
FIGURE 5.23: XRD pattern of x∼0.5 nanofibers. Upper right inset: Enlargement of the $Ni_{1-x}Fe_x$ reflections. Blue bars are lattice patterns from reference pattern no 00-047-140 of $Ni_{1-x}Fe_x$. The red asterisk (∗) symbol shows the impurity $NiFe_2O_4$ from reference pattern no 00-054-0964

5.3.1.7 Magnetic studies

The results from the magnetic measurements are shown in Figure 5.24. The main graph shows the magnetization plotted against the applied magnetic filed at 5K (black), 300K (blue), and 350K(red). It can be seen that the magnetization begins to saturate above 0.5T, and the high field magnetization was ~139 emu/g at 5K. This value was less than that found in the bulk for $Ni_{0.5}Fe_{0.5}$ at 170 emu/g[70], but still reasonably high considering there is still some carbon component from the polymer remaining in these nanofibers. The magnetization was also plotted at 300k and 350K and the values for the saturation moment were 115 emu/g and 110 emu/g, respectively. The value for the high field magnetization was increased to 82% of the bulk value in comparison to the x~0.1 (46%) and x~0.2 (72%). This showed that the saturation magnetization gets closer to the bulk saturation magnetization when x was increased. The saturation magnetization value for the bulk $NiFe_2O_4$ is 56 emu/g[149] which is very low in comparison to the obtained value for x~0.5. This suggested that the fraction of impurity $NiFe_2O_4$ was very small as compared to the overall fraction of the sample.
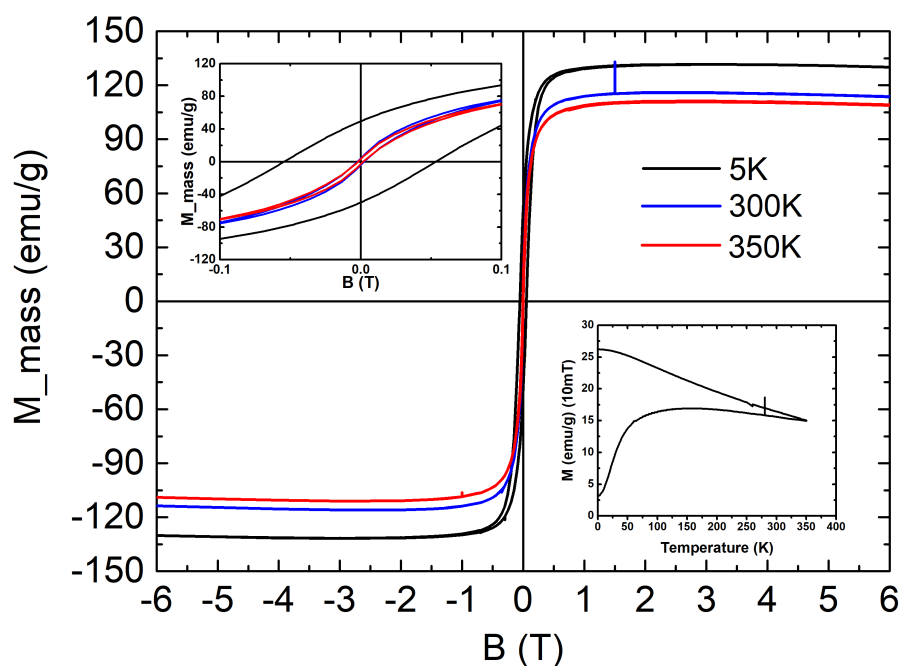
FIGURE 5.24: Plot of magnetization versus applied magnetic field, B, at 5K(black curve), 300K (blue curve, and 350K (red curve) for the x~0.5 nanofibers after thermal processing. Upper left inset: Plot of magnetization over a smaller magnetic field range. Lower right inset: ZFc-FC curve for x~0.5 nanofibers

The upper left inset in Figure 5.24 showed that x~0.5 nanofibers have negligible coercivity: 2.1 mT at 300 K and 1.8 mT at 350 K. The small value of coercivity 2.1 mT when compared to the x~0.1 (12 mT) and x~0.2 nanofibers (8 mT) at room temperature (300°C) suggested that the majority of nanoparticles within x~0.5 nanofibers

are superparamagnetic in nature, while a few large nanoparticles have caused the residual coercivity within x∼0.5 nanofiber. This was also confirmed from the lower right inset of Figure 5.24 where the ZFC-FC curve is plotted against increasing temperature at 10mT. ZFC-FC curve in Figure 5.24 has shown a range in blocking temperature for x∼0.5 nanofibers, where the small nanoparticles (∼5 nm) were small enough to show superparamagnetic response with the blocking temperature (T_B) ∼125K. Both curves overlapped above room temperature which suggested that the residual coercivity from the large nanoparticles (10 nm) has caused a variation in the blocking temperature.

Figure 5.25 shows a plot of magnetization against increasing temperature at 6T for x∼0.5. Similar to x∼0.1 and x∼0.2 nanofibers, there was a departure from the Bloch temperature dependence at lower temperature magnetization, where M_s showed an upturn below 15 K. This was attributable to the spin-disordered shell that disappeared at high temperature. The effect on the spin-disordered shell has shown a good fit to the phenomenological equation (2.27) as explained for x∼0.1 and x∼0.2 nanofibers. The values are shown below in Table 5.4 given below.
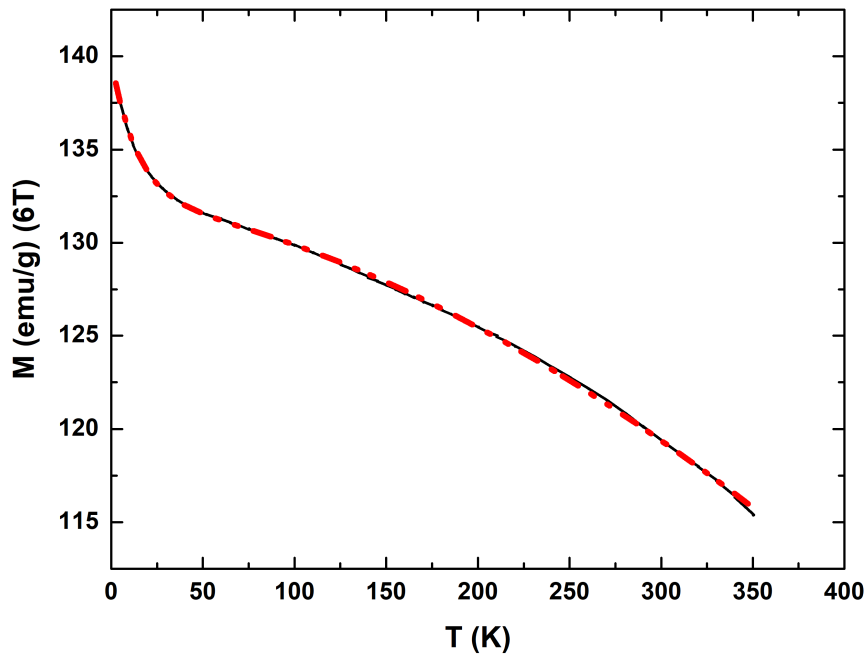
FIGURE 5.25: Magnetization against temperature (black curve) plot at 6 T . The curve was fitted (red dashed curve) with the Bloch's equation (2.27)

$M_{s,c}$(6T,0K) (emu/g)	$M_{s,d}$(6T,0K) (emu/g)	n	β(K$^{3/2}$)	T_f(K)
132.3	7.2	1.51	1.76×10^{-5}	14.5

TABLE 5.4: Fitted Magnetization (6T) to the phenomenological equation

The value of n was found similar to x~0.1 (1.53) and was also close to the bulk value (1.5) [45] for x~0.5 nanofibers. The value of β was larger than bulk iron (3×10^{-6}) or bulk nickel (7.5×10^{-6}[141, 150, 151] for x~0.5 nanofibers. This was similar to x~0.1[152] and other $Ni_{50}Fe_{50}$ nanoparticles[150] from the literature. The fraction of spin disordered component, $M_{s,c}$ was found to be very small (1.3%) with 1.76 emu/g. This was comparable to the $M_{s,c}$ for both x~0.1 (0.82 emu/g) and x~0.2 (2 emu/g) nanofibers. The value of $M_{s,c}$ was larger than the x~0.1 (40.9 emu/g) and x~0.2 (84.4 emu/g) nanofibers and also from the literature reported value for the electrospun $Ni_{1-x}Fe_x$ mats from the previous literature. [5]

Figure 5.26 shows the differential susceptibility (dM/dH) curve plotted against the applied magnetic field, B. The value of dM/dH was increased to 18 when compared with the x~0.1 (dM/dH=6) and x~0.2 (dM/dH=11) nanofibers as well as with other nanostructures.[153] This showed that an increase in x causes a progression in the formation of small- sized nanoparticles, which is encouraging as small super-paramagnetic nanoparticles can potentially have high differential susceptibility.
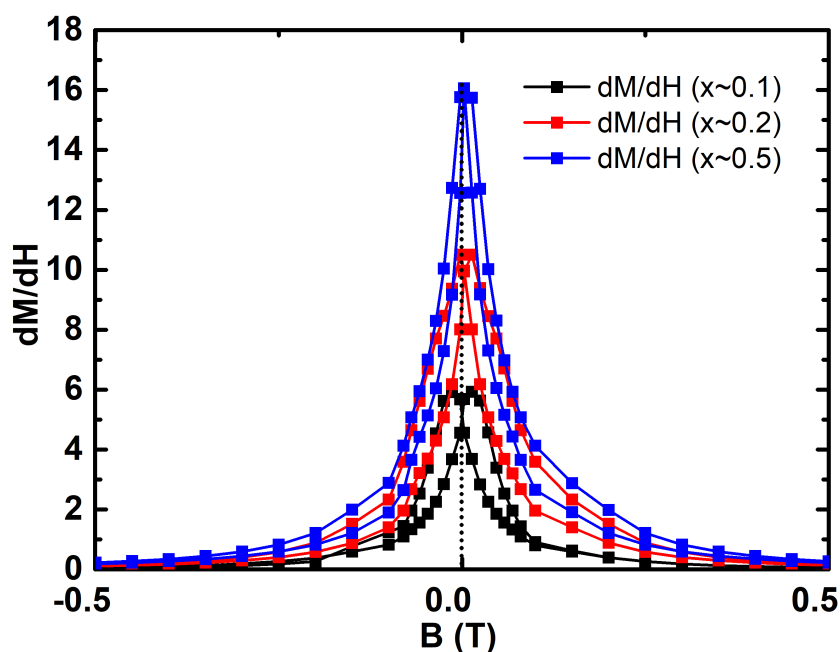
FIGURE 5.26: The plot of differential susceptibility for x~0.5 nanofibers in comparison to the x~0.1 and x~0.2 nanofibers

5.3.2 x∼0.5 nanofibers prepared using 20:80 mixture of Methanol/DMF

The synthesis of these x∼0.5 nanofibers was important to study the effect of using a solvent mixture of 20% methanol: 80% DMF on the structural and magnetic properties of x∼0.5 nanofibers.

5.3.2.1 SEM of electrospun nanofibers

The SEM images for the electrospun sample are shown in Figure 5.27 (a) and (b). It can be seen from the low-resolution image in Figure 5.27(a) that these nanofibers have shown a quasi-unidirectional orientation similar to the DMF-based x∼0.5 nanofibers and other fractions of x. The upper right inset in Figure 5.27 (a) showed the nanofiber's diameters distribution and the mean diameter was 271 nm with a standard deviation of 70 nm. The other image in Figure 5.27 (b) provide a clear estimation of the nanofiber's width at high resolution. In comparison to the DMF-based x∼0.5 nanofibers (147 nm), the diameter of these nanofibers was slightly increased. No difference was observed in the morphology of these electrospun nanofibers.
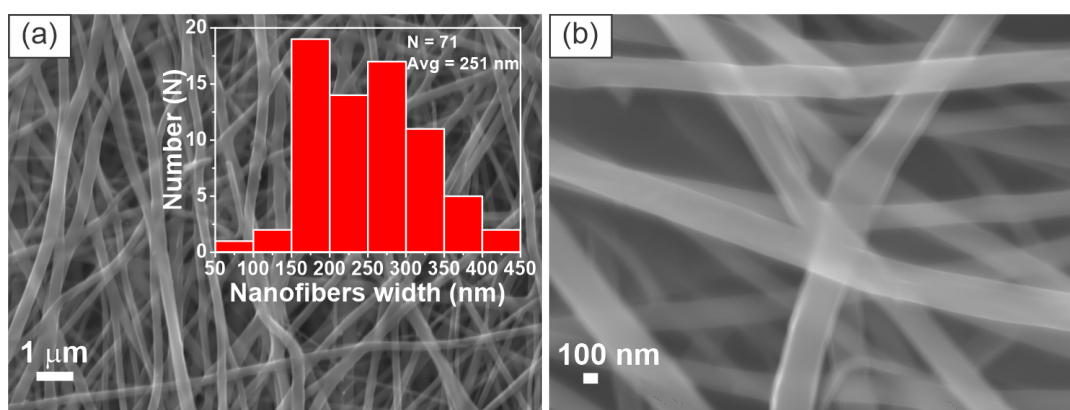
FIGURE 5.27: SEM images of electrospun nanofibers using a 20:80 methanol to DMF mixture as the solvent. (a) Low resolution SEM image of the nanofibers at 1μm. Upper left inset: A bar grapgh showing the average width of nanofibers. (b) A higher resolution SEM image of (a) at 100 nm

5.3.2.2 SEM analysis of thermally processed nanofibers

The SEM images of the thermally processed x∼0.5 nanofibers are shown in Figure 5.28(a) and (b). The first image in Figure 5.28 (a) showed the formation of thin nanofibers with retained morphology. The upper right inset of this image in Figure 5.28(a) showed the diameter size distribution with an average diameter of 158 nm at a standard deviation of 50 mn. These nanofibers have shown larger diameters in comparison to the DMF-based x∼0.5 nanofibers (71 nm with a standard deviation of 20 nm). However, the diameter was in the range of the diameters of x∼0.1 (160 nm with a standard deviation of 40 nm) and x∼0.2 (112 nm with a standard deviation of 20 nm) nanofibers. This indicates that the addition of 20% methanol has changed the diameter of these nanofibers. The high-resolution second image in Figure 5.28

(b) shows rough surfaced nanofibers. Similar to x∼0.1 and x∼0.2, these nanofibers showed more rough surfaces, whereas relatively smooth surfaced nanofibers were observed for DMF based x∼0.5 nanofibers. From this image, it can be seen that these nanofibers have surface-decorated $Ni_{1-x}Fe_x$ nanoparticles that were large enough to be seen at the SEM resolution. The estimated size for these nanoparticles could be in-between ∼30-40 nm, which is comparatively larger than DMF based x∼0.5 nanofibers. These large-sized $Ni_{1-x}Fe_x$ nanoparticles could be polycrystalline in nature. The results show that even a small addition of methanol (20%) in 80% DMF caused a difference in the nucleation of x∼0.5 nanofibers. Furthermore, the sample exhibits a similar structural characteristic to x∼0.1 and 0.2 nanofibers prepared using 100% methanol as the solvent.
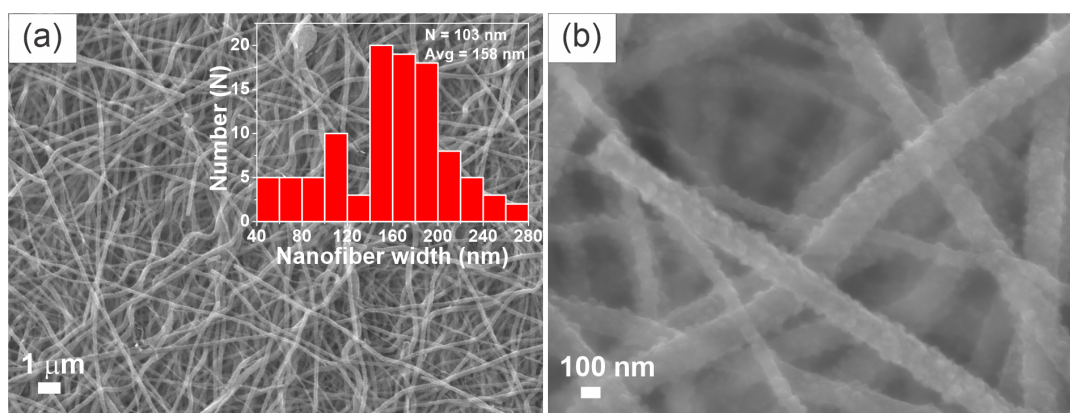
FIGURE 5.28: Thermally processed x∼0.5 nanofibers prepared using a 20:80 methanol to DMF mixed solvent. (a) Low-resolution SEM image at 1 μm. Upper right inset: Average widths of nanofibers. (b) High-resolution SEM image at 100 nm

5.3.2.3 XRD analysis

The XRD pattern is shown in the Figure 5.29. The first two peaks at lower angles were indexed to the PVP peaks from the literature[122, 135] and the other two peaks were indexed to the FCC crystalline phase of $Ni_{1-x}Fe_x$.[70] Likewise, DMF based x∼0.5 XRD pattern, the impurity peaks from the $NiFe_2O_4$ (shown by asterisk = *) were very small and could only be seen in the background noise. This XRD pattern has shown the presence of a different carbon component as compared to the DMF based x∼0.5 nanofibers, but it was found similar to the XRD patterns for x∼0.1, and x∼0.2 nanofibers. It showed that the degradation pathway in 20% methanol was similar to the degradation pathway of 100% methanol-based nanofibers (x∼0.1, and x∼0.2). Such behavior highlighted the role of methanol addition, wherein that even a small percentage can change the degradation pathway. The Scherrer crystallite size was 13 nm for these nanofibers, which showed that the large nanoparticles from the SEM images could be polycrystalline in nature. The calculated lattice parameter was 3.560 Å with a standard deviation of 0.003 Å. This value was found close to the lattice parameter by DMF-based nanofibers (3.570 Å with the standard deviation of

0.001 Å) and was in agreement with the value for lattice parameter at this fraction x from the previous literature. [70]
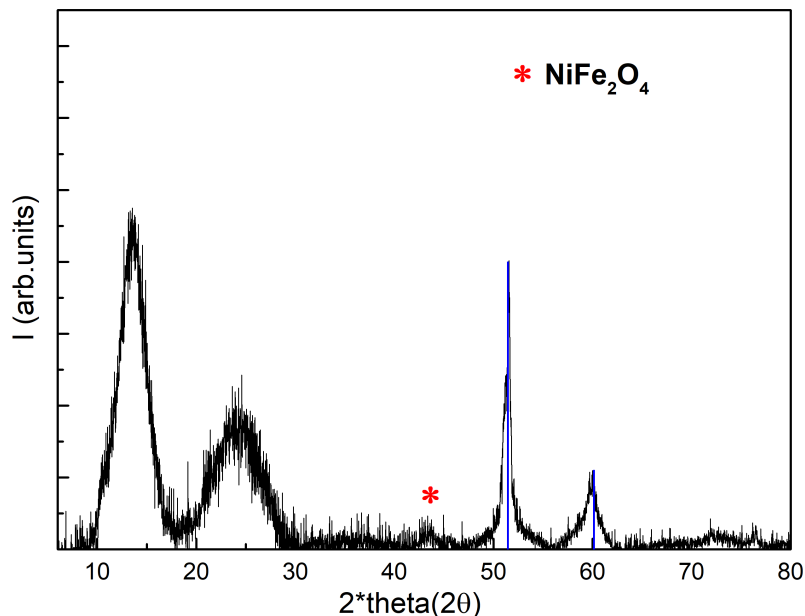
FIGURE 5.29: XRD pattern of x∼0.5 nanofibers prepared from a 20:80 mixture of methanol to DMF

5.3.2.4 Magnetic studies

The results from the magnetic studies are shown in Figure 5.30. The main graph in Figure 5.30 shows the magnetization plot against the applied magnetic field at 5K (black) and at 300 K (blue). It can be seen that the magnetization begins to saturate above 0.5 T to reach an overall value of 25 emu/g. The value of high field magnetization (M_s) at 5 K was reduced to only 14% of the bulk value (170 emu/g). This value was significantly reduced when compared to the M_s value for the DMF-based x∼0.5 nanofibers (82%) and the M_s values for x∼0.1 (46%), and x∼0.2 (72%). The reduction in the magnetic moment suggests the formation of highly disordered $Ni_{1-x}Fe_x$ phase within x∼0.5 nanofibers. The other reasons include increased surface disorder, dangling bonds at the surface, strain, and oxidation of the surface.[154–156]
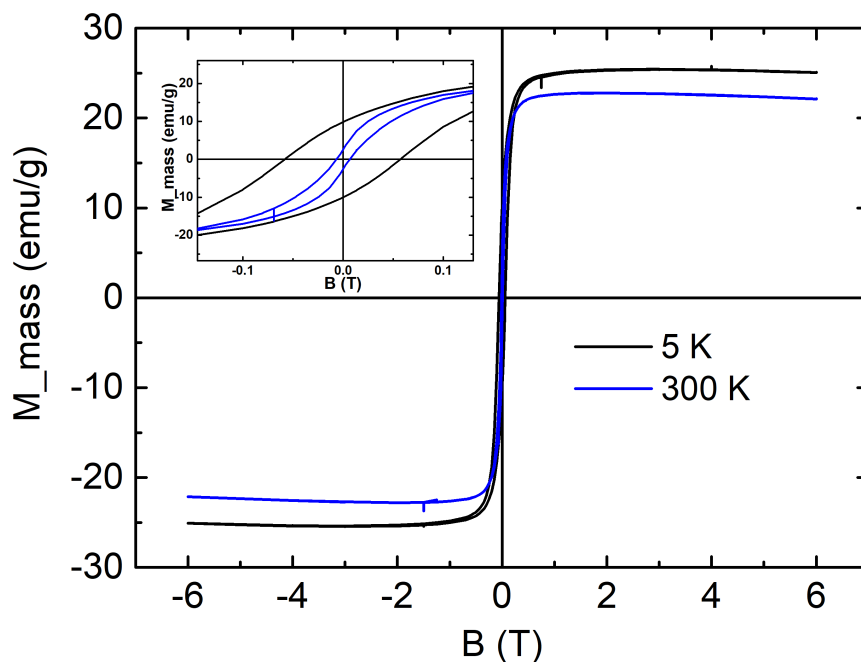
FIGURE 5.30: Plot of magnetization versus the applied magnetic field, B, at 5k (black) and 300K (blue), for x∼0.5 nanofibers made from 20:80 mixture of methanol: DMF. Upper left inset: Plot of magnetization at a smaller field region

The coercivity was 55 mT at 5 K, which reduces to 6.8 mT at 300 K. In comparison to the coercivity 2.1 mT of DMF based x∼0.5 nanofibers, the value of coercivity was greater at room temperature. Whereas, it was less than that of the found values of coercivity for x∼0.1 (12 mT)and x∼0.2 (8 mT) nanofibers. The appearance of coercivity at room temperature indicates that the $Ni_{1-x}Fe_x$ nanoparticles were not superparamagnetic. The absence of superparamagnetism suggests the presence of large nanoparticles within these nanofibers. This was consistent with the SEM images where the presence of large $Ni_{1-x}Fe_x$ nanoparticles was observed on the surface of the nanofibers.

The main plot in Figure 5.31 shows the dependence of M_s at 6T with increasing temperature. Likewise, DMF-based x~0.5 nanofibers, the departure from the Bloch temperature dependence was observed for the M_s below 20K. This was also seen for x~0.1 and x~0.2 nanofibers and was attributed to the presence of spin-disordered shell. The effect of the spin disordered shell was fitted with the previously used phenomenological equation (2.27), similar to the DMF based x~0.5 nanofibers, and other fractions of x. The fitted parameters are shown below in Table 5.5.
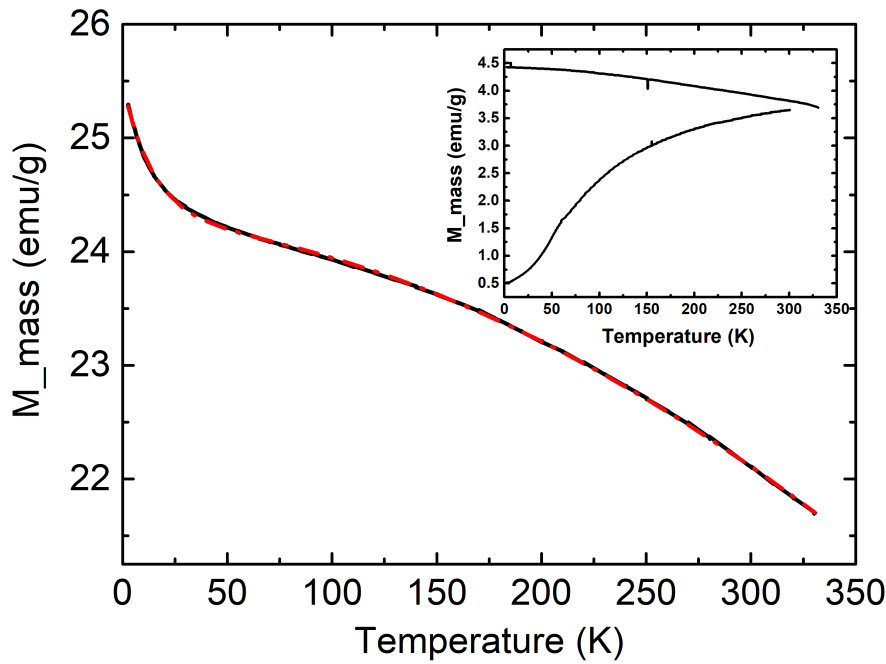
FIGURE 5.31: Magnetization plot at 6T (black curve); the red curve is a fit using Bloch's equation (2.27). Lower right inset: ZFC-FC curves above 300K at a smaller applied field 10 mT

$M_{s,c}$(6T,0K) (emu/g)	$M_{s,d}$(6T,0K) (emu/g)	n	β (K$^{1.8}$)	T_f(K)
24.1	1.2	1.8	3.2×10^{-6}	15

TABLE 5.5: Fitted Magnetization(6T) parameters from phenomenological equation (2.27)

The value of n=1.8 has shown a deviation from the bulk value n=1.5 for $Ni_{1-5}Fe_x$. The n was also large when compared to the DMF-based x~0.5 nanofibers (1.51), and x~0.1 nanofibers (1.53). However, this was found similar to the n=1.8 for x~0.2 nanofibers. The increase in the value of n could be due to various complicated reasons including oxidation of the polycrystalline core regions, surface disorder, or the oxidation of the surface. However, it requires further analysis for confirmation. The fitted value of the Bloch's constant (β) was 3.2×10^{-6} that was found in range with the bulk iron ($\beta=3 \times 10^{-6}$), similar to the β value ($1.3 \sim 10^{-6}$) for x~0.2 nanofibers. However, it was found to be larger when compared to the DMF based

x~0.5 nanofibers with β=1.76×10^{-5}, and x~0.1 nanofibers with β=1.53×10^{-5}. The value for spin freezing temperature (T_F=15K) was found in the range of the observed value of T_F=15 for DMF based x~0.5 nanofibers. This was also in range with the values of T_F= 21K for x~0.1 and T_F= 17K for x~0.2 nanofibers. This showed that the magnetic behavior from the magnetically ordered core does not change by increasing the fraction of x.

The upper right inset in Figure 5.31 shows the ZFC-FC curves measured at 10 mT. There was no evidence of superparamagnetism from this ZFC-FC curve, which is consistent with the formation of larger nanoparticles ($\geq$ ~30-40 nm) than the superparamagnetic regime (>8-10 nm). [157]

5.4 Summary

In this chapter, a novel method for the preparation of high-quality $Ni_{1-x}Fe_x$ nanofibers with x~0.5 was successfully developed. This method has resolved the issues from the existing method in the literature which includes the instability of isolated x~0.5 nanofibers formation and melting to form sheets when methanol was used as a solvent in a combination of hydrated salts of metal ions. In this method, DMF was used a solvent, and iron acetylacetonate was used as an iron source with nickel acetate. The other parameters including the applied voltage (20 kV) in the electrospinning setup, vacuum annealing (150°C at 4 hrs and 0.05 MPa), and the ramp rate in the furnace (20°C/min to reach 300°C at the first step) were also optimized in this method.

These nanofibers have shown thinner diameters and contained narrow skewed size nanoparticle distribution with the formation of the increased number of smaller-sized nanoparticles (~ 5 nm). This was different from the bimodal particle size distribution of x~0.1 and the skewed distribution of x~0.2 nanofibers. Unlike x~0.1 and x~0.2, a different residual carbon component was observed in the XRD pattern Which showed the degradation pathway for polymer fragments was different in the presence of DMF. The saturation magnetization was significantly increased to 82% of the bulk value for x~0.5 nanofibers when compared with x~0.1 (46%) and x~0.2 (72%) nanofibers. The coercivity was also decreased to 2.1 mT at room temperature as compared to the 12 mT for x~0.1, and 8 mT for x~0.2 nanofibers. Due to the formation of smaller nanoparticles, the ZFC-FC curve showed a superparamagnetic curve-like behavior (T_B ~125) with some residual coercivity from larger nanoparticles (9 nm). The differential susceptibility for x~0.5 nanofibers was also increased to 18 when compared to the values of 6 for x~0.1 and 11 for x~0.2 nanofibers. Increased differential susceptibility and negligible coercivity are favorable for the potential applications in wireless charging applications.

The formation of $Ni_{1-x}Fe_x$ nanofibers with x~0.5 was also investigated by using a 20:80 mixture of methanol/DMF to study the effect of methanol addition in the formation of x~0.5. Similar to x~0.1, these nanofibers have shown the formation of large surfaced nanoparticles. The residual carbon fragments in the XRD pattern were found to be similar with x~0.1 and x~0.2 nanofibers, which suggested that the degradation pathway differs in the presence of methanol than pure DMF based x~0.5 nanofibers. The Scherrer size was 13 nm which suggested the formation of polycrystalline nanoparticles as the particle sizes were estimated between ~30-40 nm from the SEM images. These nanofibers have shown a significant reduction in the saturation magnetization 25 emu/g which is only 14 % to the bulk with the coercivity of 6.8 mT. The reduction in the magnetization suggested the formation of highly disordered polycrystalline $Ni_{1-x}Fe_x$ nanoparticles within these nanofibers. This has shown that the addition of methanol has caused detrimental effects on the properties of these x~0.5 nanofibers.

5.5   Future outlook

The results from this study is encouraging and can be of further interest to investigate these following points in the future:

- What will happen in the nucleation of magnetic nanofibers, if the x is further increased?

- Will it further decrease the $Ni_{1-x}Fe_x$ nanoparticles size/ more homogeneity in nanoparticles?

- Will it shift the saturation moment to higher values with increasing fraction of x?

- Will it shift the magnetic hysteresis to zero at room temperature when x is further increased?

Preface

The next chapter explains the synthesis and characterizations of the electrospun $MnFe_2O_4$ nanofibers. These nanofibers were processed at two different thermal processing temperatures. The structural and magnetic properties differences are highlighted in detail at these thermal processing temperatures.

Chapter 6

Manganese ferrite ($MnFe_2O_4$) nanofibers

6.1 Introduction

Manganese ferrite is a well-known soft magnetic material owing to its low magnetocrystalline anisotropy, low coercivity, low remnant magnetization, and high permeability. It has been advantageous in the reduction of eddy-current losses due to its high resistivity. [158, 159] The applications of $MnFe_2O_4$ have been widely exploited in electronic devices[160], magnetic inductors[161], high density recording media[162], and in high frequency transformers[158]. The crystal structure of manganese ferrite is an isomorphic form of the mineral spinel $Mg^{2+}Al_2^{3+}O_4^{2-}$ where trivalent Fe^{3+} replaces the Al^{3+} and divalent cation Mn^{2+} replaces the divalent Mg^{2+} in the formula unit. $MnFe_2O_4$ crystallizes as a spinel structure with a space group of Fd-3m where the O^{2-} atoms occupy the tetrahedral (A) and octahedral sites (B). In normal spinel structures, the divalent metal ions Mn^{2+} occupy the tetrahedral (A) site whereas, the trivalent Fe^{3+} will only occupy the octahedral site (B).(Figure 6.1) Whereas, in inverse spinel structures, divalent cations (Mn^{2+}) occupy half of the B sites and other halves of B sites and all A sites are occupied by the trivalent cations (Fe^{3+}).[163, 164] The high temperature synthesis of $MnFe_2O_4$ can cause the migration of some Mn^{2+} ions from site A to site B. Therefore, it is characterized as a mixture of both spinel and inverse spinel structures.[164]

The net magnetic moment of manganese ferrite varies between (3-5 μ_B) depending upon the degree of inversion indicated as ($Mn_{1-x}^{2+} Fe_x^{3+}$) [$Mn_x^{2+}Fe_{2-x}^{3+}$], where the parentheses show the tetrahedral site occupancy and square brackets show the octahedral site occupancy and x is the degree of inversion (5 μ_B when x=0, and $3\mu_B$ when x=1).[165, 166] The magnetic properties of manganese ferrite are dependent on the occupancy and exchange of cations in the two sites. The A-B interaction is the strongest super-exchange interaction, followed by the B-B, and then A-A super-exchange interaction in spinel ferrites, and the total magnetic moment can be calculated by the magnetic moment of ions and the exchange interactions between them.[166–169] The preparation of manganese ferrite in nanodimensions is interesting as it can alter the magnetic properties, as in superparamagnetic state, it shows
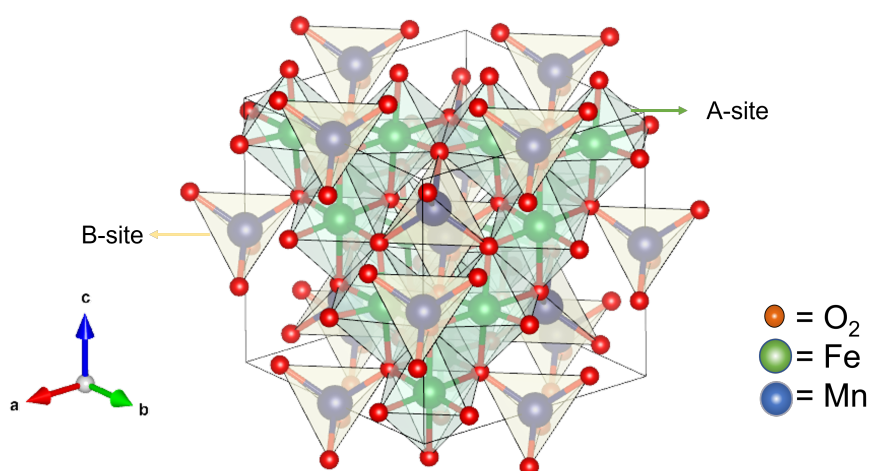
FIGURE 6.1: Spinal crystal structure of manganese ferrite

the size-dependent magnetization and can reduce the eddy current losses due to high resistivities. Other magnetic properties includes spin glass transition and variable magnetic crystalline anisotropy in nanodimensions which is dependent on the synthesis method. [53] There have been various reports for the synthesis of magnetic $MnFe_2O_4$ nanoparticles to achieve high magnetic saturation moment, low coercivity, and low remanent magnetization. For example, a report on superparamagnetic nanoparticles (5 nm in size) prepared by a chemical precipitation method showed an M_s value 69 emu/g [53] Similarly, polymer coated (PVP) superparamagnetic $MnFe_2O_4$ nanoparticles showed values between 32-54 emu/g (depends on the coating thickness) that are used for drug delivery applications.[60] Another report on electro-chemically prepared $MnFe_2O_4$ nanoparticles has shown a reasonable saturation magnetization 73 emu/g with small coercivity 12 mT at 5 K. [61] The magnetic properties of $MnFe_2O_4$ can be tuned depending on their size, shape, diameter, and the mode of preparation.[163] There is a potential in the fabrication of uni-directional nanofibers/nanorods that can lead to low demagnetization with high susceptibility due to their shape anisotropy.

There are some reports that investigate the preparation of $MnFe_2O_4$ nanofibers for their magnetic properties by electrospinning, where various combination mixtures with metal precursor salts and polymers were used. [71, 76, 170] The motivation for this study was to explore the characterization of $MnFe_2O_4$ nanofibers, as the magnetic properties were not studied in detail in the previous literature.[72, 74, 76] For this, manganese ferrite nanofibers were prepared by electrospinning and characterized in detail to evaluate their structural and magnetic properties.

This chapter reports the exploration of synthetic methods for $MnFe_2O_4$ nanofibers by electrospinning, and the effect of thermal processing on $MnFe_2O_4$ nanofibers that were processed at two different temperatures. The prepared nanofibers were fully characterized to study the effect of annealing temperature on the nucleation and

structural properties. The magnetic properties were also analyzed in comparison to the bulk and at two different temperatures.

6.2 Experimental

6.2.1 Chemicals used

Manganese chloride tetrahydrate ($MnCl_2 \cdot 4\,H_2O$) 99%, Iron nitrate nonahydrate ($Fe(NO_3)_3 \cdot 9\,H_2O$) 98%, Tris acetylacetonate iron ($Fe(C_5H_7O_3)_3$) 97%, Polyvinylpyrrolidone(PVP) (($C_6H_9NO)_n$), and Polyvinyl butyral ($C_8H_{24}O_{2n}$) (M_W=70,000-100,000) were purchased from Sigma-Aldrich. Manganese nitrate tetrahydrate ($Mn(NO_3)_2 \cdot 4\,H_2O$) 99% was purchased from Acros Organics. Dimethylformamide (DMF) 99.8% was purchased from Acro seal Ⓡ.

6.2.2 $MnFe_2O_4$ solution preparation for electrospinning

6.2.2.1 Selection of the ideal solutions using different polymers, solvents, and precursors

For the preparation of $MnFe_2O_4$ nanofibers, different combinations of both metal ions salt and solvents were used. As for the electrospinning, a homogeneous mixture of both precursor salts in (1:2, Mn^{2+} to Fe^{3+}) was used and the compatibility of both metal precursors with the solvent and polymer was explored. A summary of the various combinations tried is studied in Table 6.1. 6.1

The first row in Table 6.1 showed that manganese chloride tetrahydrate and iron nitrate nonahydrate were dissolved in ethanol in a stoichiometric ratio of 1:2. The addition of PVP to this solution was not stable and resulted in a gel formation that precipitated out in the solution. Similar results were obtained when manganese nitrate was used with iron nitrate and PVP in the second attempt.

The third row in Table 6.1 showed the effect of changing the polymer and solvent by using polyvinylbutyral (PVB) with water. The metal precursors were kept unchanged (manganese nitrate and iron nitrate). Similar results were obtained with the precipitation of gel when polymers were added to the dissolved metal ions solutions.

The fourth row in Table 6.1 showed that a homogeneous mixture was obtained when a combination mixture of ethanol: water was used as a solvent for manganese nitrate, iron nitrate as metal precursors, and PVP as polymer. But due to the high ionic strength of the solution including the high content of nitrate ions (NO_3^{2-}), the solution was not able to electrospun.

In the final two attempts, DMF was used as a solvent, and iron acetylacetonate was used as an iron source separately with manganese chloride tetrahydrate and manganese nitrate tetrahydrate with the addition of PVP. While both solutions were electrospun separately, only successfully isolated nanofibers were obtained with

manganese nitrate tetrahydrate, iron acetylacetonate, PVP, and DMF (as solvent), as given in the last row in the Table. 6.1.

Manganese salt	Iron salt	Polymer	Solvent	Comments
Manganese chloride tetrahydrate	Iron nitrate nonahydrate	PVP	Ethanol	Gel precipitation
Manganese nitrate tetrahydrate	Iron nitrate nonahydrate	PVP	Ethanol	Gel precipitation
Manganese nitrate tetrahydrate	Iron nitrate nonahydrate	PVB	Water	Gel precipitation
Manganese nitrate tetrahydrate	Iron nitrate nonahydrate	PVP	Water:Ethanol	Ionic strength using both nitrates hindered electrospinning
Manganese chloride tetrahydrate	Iron acetylacetonate	PVP	DMF	Fused nanofibers
Manganese nitrate tetrahydrate	Iron acetylacetonate	PVP	DMF	Isolated nanofibers

TABLE 6.1: The different combinations of solution mixtures tried for electrospinning

6.2.2.2 Electrospinning of $MnFe_2O_4$ nanofibers

The combination mixture was first optimized to obtain a suitable viscosity by changing the PVP concentration in the solution as given in Table. 6.2.

In a typical synthesis, 4 mmol of each, 1 g of manganese nitrate tetrahydrate, and 1.4 g of iron acetylacetylacetonate were dissolved separately in 6.5 mL of DMF. From their separate solutions, 1 mL of dissolved manganese nitrate and 2 mL of iron acetylacetonate were transferred into a separate flask and stirred at a constant speed. Into this homogenised mixture, an optimised quantity of polymer from Table 6.2 was added. For this, three separate solutions were prepared starting from the high concentration of PVP, 1g, 0.5g, and the lowest 0.4g of PVP was added and stirred for an hour to get homogeneous solutions. While the first two solutions were too thick to electrospun, only 0.4g of PVP was found with optimum viscosity for electrospinning. Finally, the prepared solution was transferred into a 5 mL metallic syringe attached to the electrospinning set-up fitted with a 22 gauge needle. The electrospinning parameters were the same as were used for x∼0.5 nanofibers in the previous chapter as per given Table 6.3.

Manganese nitrate tetrahydrate (mmol)	Iron acetylacetonate (mmol)	PVP (g)	DMF (mL)	Comments
0.6	1.2	1	3	Too thick for electrospinning
0.6	1.2	0.5	3	Too thick for electrospinning
0.6	1.2	0.4	3	Good for electrospinning

TABLE 6.2: The concentration of solutes and polymer in DMF tried to obtain an optimised viscosity for electrospinning

Infusion rate (mL/hr)	Voltage (kV)	Distance (cm)	Needle (G)	Drum speed (rpm)
0.4	20	10	22	60

TABLE 6.3: The electrospinning parameters used to prepare $MnFe_2O_4$ nanofibers

6.2.3 Thermal treatment of electrospun $MnFe_2O_4$ nanofibers

The prepared electrospun $MnFe_2O_4$ nanofibers were placed under a vacuum and heated at $150°C$ for 4 hours at 0.05 MPa to remove the solvent (DMF). After this, the sample was left overnight in a vacuum, at the same pressure, to further dry the sample before thermally annealing it in the tube furnace. For the final heat treatment process, the sample was peeled off from the aluminum foil and placed on alumina grids, and placed into the tube furnace. The oxidation of the sample was optimised by changing various conditions as explained below.

6.2.3.1 Thermal processing in the presence of argon

For the fabrication of $MnFe_2O_4$ nanofiber, the electrospun sheet was first thermally annealed using the same heating profile previously used for $x\sim0.5$ ($Ni_{1-x}Fe_x$) nanofibers. In this three-step temperature profile, the electrospun $MnFe_2O_4$ sheet was first heated to $300°C$ at a $20°C/min$ ramping rate for two hours. Then the temperature was raised to $620°C$ at $5°C/hr$ for two hours to promote the nucleation of $MnFe_2O_4$ nanoparticles within nanofibers. At the final step, the temperature is again reduced back to $300°C$ at a ramp rate of $5°C/min$ for 2 hours before it was furnace cooled to room temperature. All three steps were performed in the presence of a continuous flow of 99.9% argon gas.
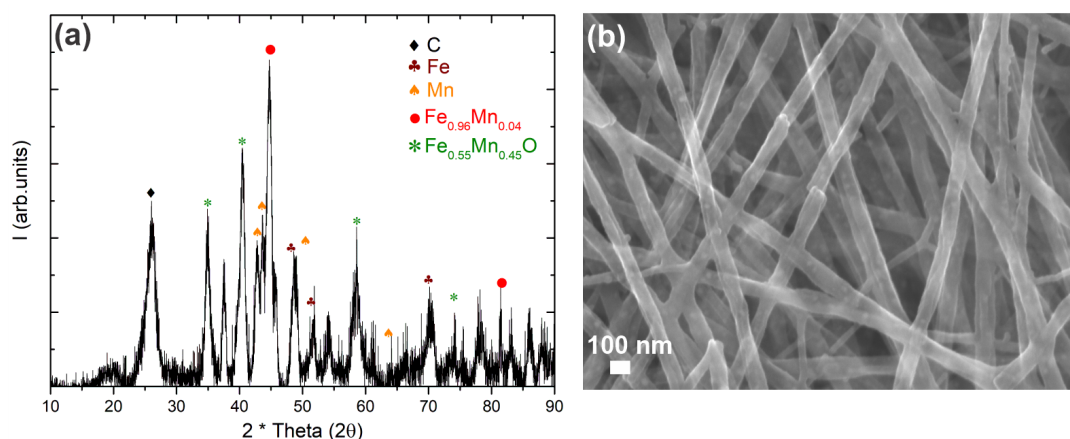
FIGURE 6.2: (a) XRD patterns and (b) SEM image for the $MnFe_2O_4$ nanofibers processed in argon

The XRD pattern in Figure 6.2(a) shows the presence of a mixture of bimetallic manganese-iron alloy ($Fe_{0.96}Mn_{0.04}$, powder diffraction pattern no 04-003-7049), manganese iron oxide ($Fe_{0.55}Mn_{0.45}O$, powder diffraction pattern no 04-024-7262), carbon component (powder diffraction pattern no 01-073-5918), and some elemental manganese (powder diffraction pattern no 04-006-6398) and iron (powder diffraction pattern no 04-018-8483) in the nanofibers. The SEM image in the Figure 6.2 (b) showed the formation of predominately isolated nanofibers. The formation of this mixture shows that the environment used (argon) for thermal processing was not oxidising enough to obtain the manganese ferrite nanofibers. Therefore, in the next

step, the nanofibers were thermally processed in the air since pure argon has very minute amounts of oxygen content to oxidise the Mn and Fe to form $MnFe_2O_4$.

6.2.3.2 Thermal processing in the presence of air

To see the effect of air, the prepared electrospun $MnFe_2O_4$ nanofibers were processed by using two different temperature profiles. At first, the same three-step temperature profile was used as discussed above for thermal annealing in argon, where the highest temperature used was 620°C.

The other temperature profile was a four-step temperature profile where the highest annealing temperature was increased to 800°C. In the first step, the temperature was ramped up to (300°C) at 20°C/min for two hours. This was then ramped up to (620°C) at 5°C/min for two hours, and then further ramped up to 800°C at 5°C/min for two hours in the third step. The final step was ramped down to 300°C at 5°C/min for an hour before it was furnace cooled to room temperature. All steps were performed in the presence of air.
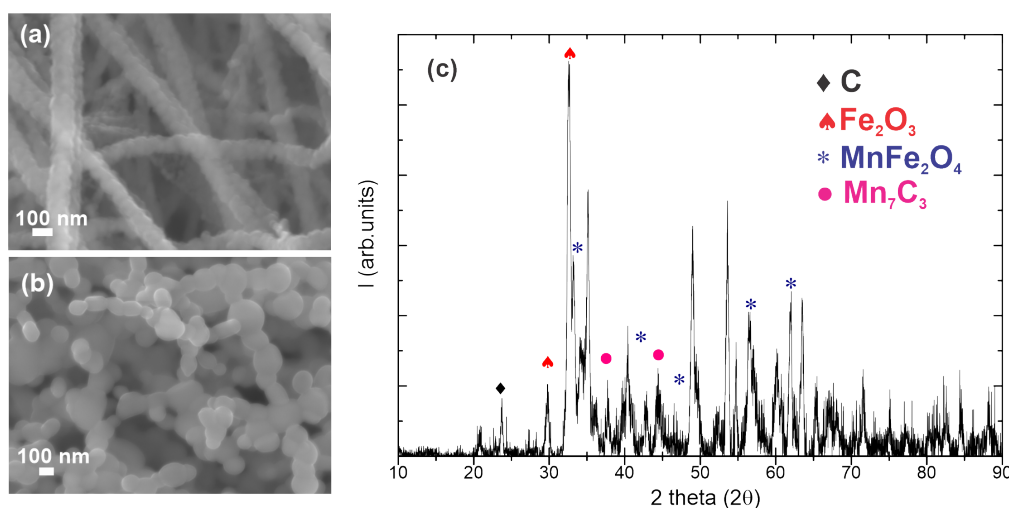
FIGURE 6.3: SEM images for the $MnFe_2O_4$ nanofibers processed in air (a) at 620 °C, (b) at 800 °C, and (c) XRD patterns at 800°C

The result in Figure 6.3 (a) showed that at low temperature 620°C the nucleation of nanofibers was more like beaded-chains. These beaded chains were broken down into smaller fragments when the temperature was increased to 800°C, which showed that the high temperature was not suitable for the growth of $MnFe_2O_4$ nanofibers. Figure 6.3 (c) shows the XRD pattern of the sample annealed at high temperature (800°C). It can be seen that in excess of oxygen, the sample was composed of a mixture of hematite (Fe_2O_3, powder diffraction pattern no 04-006-6579), manganese ferrite ($MnFe_2O_4$, powder diffraction pattern no 04-016-1572), and some manganese carbide (Mn_7C_3, powder diffraction pattern no 04-007-1048). This showed that the annealing atmosphere contained more oxygen than required to obtain $MnFe_2O_4$ nanofibers.

6.2.3.3 Thermal processing in the presence of argon and air

The thermal annealing profile was further modified based on the observations above, where both argon and air give impurity phases for the $MnFe_2O_4$. There was not enough oxygen to oxidise the electrospun sample in the former case with argon, and there was too much oxygen in the later case where the electrospun sample formed the iron oxide as a major component of the sample in the air. Therefore, the environment for thermal annealing was optimised where the sample was treated in argon at a low temperature, and then the argon was turned off to allow the air to leak into the furnace tube for the oxidation of the sample at high temperatures.

The two different temperature profiles were used where the sample was treated first by using the four-step temperature profile. In this, the temperature was ramped up to 300°C/min for two hours, and then ramped up to 620°C at 5°C/min for two hours in presence of argon. This was further ramped up to 700°C at 5°C/min and when the high temperature was reached, argon was turned off. The sample was heated at this step for an hour in the presence of some residual argon in the tube and leaked in air from the inlet. The temperature was ramped down to 300°C at 5°/min for an hour and then furnaced cooled at room temperature. This step has allowed some air to leak into the tube furnace for the oxidation of $MnFe_2O_4$ nanofibers to create an argon-air gas mixture to aid the oxidation of Mn and Fe to form $MnFe_2O_4$. This sample was named MN-700°C.

Another batch of $MnFe_2O_4$ nanofibers at 620°C in the same argon-air mixture presented above was prepared. To recap, the temperature was first ramped up to 300°C at 20°C/min for two hours under argon flow. After that, the ramp rate was changed to 5°C/min to increase the temperature to 620°C in the second step, and argon was turned off, when the high temperature (620°C) was reached. The sample was annealed at 620°C for 2 hours and then ramped down to 300°C at 5°C before it was allowed to furnace cool down to room temperature. This sample was assigned as MN-620°C.

6.3 Results and analysis

6.3.1 SEM of electrospun $MnFe_2O_4$ nanofibers

Figure 6.4 shows the electrospun $MnFe_2O_4$ nanofibers before (6.4 (a)) and after (6.4 (b)) vacuum treatment. Both images show that the nanofibers' surfaces are smooth with no branching. A reduction in the diameter of the nanofibers after vacuum treatment at 150°C for 4 hours, showed that there was some removal of solvent (DMF) from the electrospun sheets. The slow removal of DMF has not caused a disintegration of the nanofibers and they retained the fibrous morphology. The histogram plotted in Figure 6.5 shows the average diameter of the as-prepared nanofibers (green) that was found to be ∼248 nm with a standard deviation of 45 nm. Whereas, the average diameter of the vacuum-treated nanofibers' (red bars) has reduced to ∼178 nm
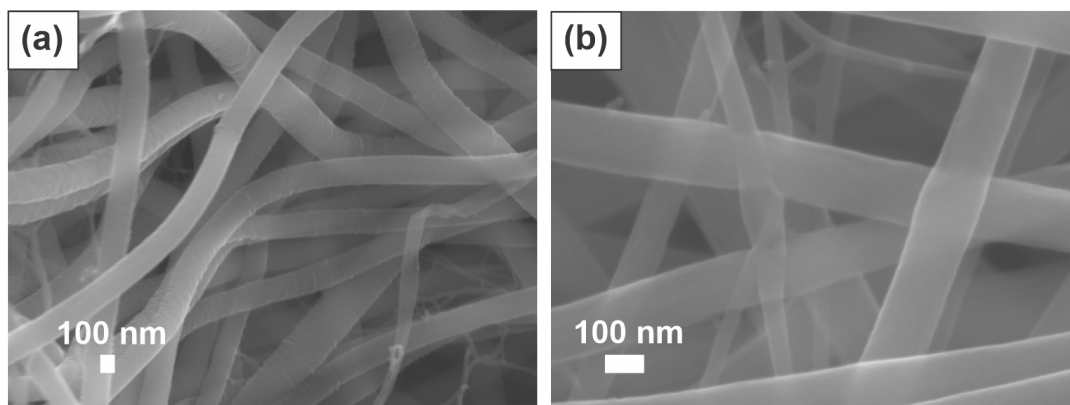
FIGURE 6.4: SEM images of electrospun MnFe$_2$O$_4$ nanofibers. (a) After electrospinning. (b) After vacuum treatment

with a standard deviation of 25 nm. The role of vacuum annealing was important which is already discussed in the previous chapter for DMF based x$\sim$ 0.5 nanofibers.
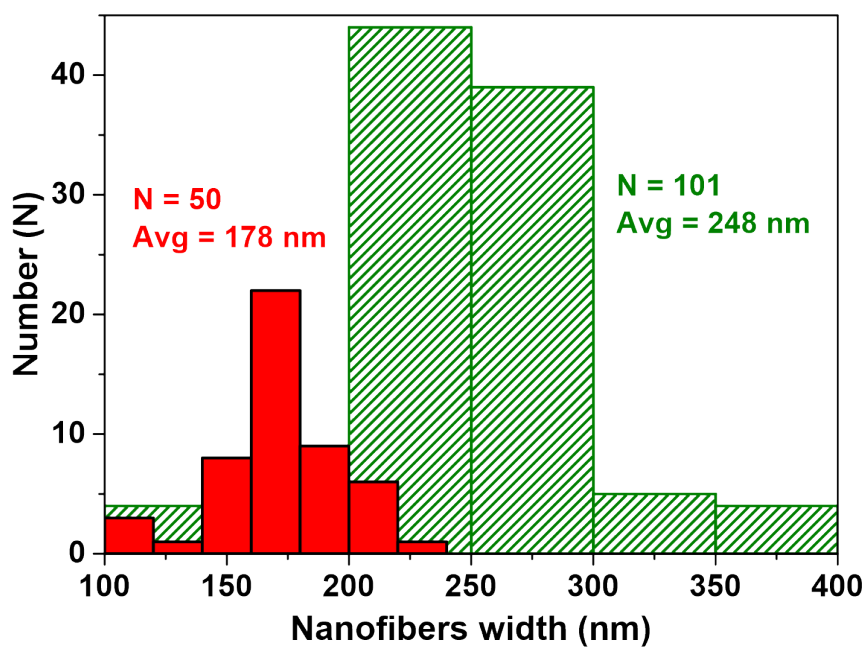
FIGURE 6.5: A bar graph of the distribution of the diameters of the MnFe$_2$O$_4$ nanofibers before vacuum treatment (green) and after vacuum treatment (red). The average diameters are also indicated on the plot

6.3.2 SEM analysis of thermally processed MN-700°C and MN-620°C nanofibers

SEM result from the MN-700°C nanofibers is shown in Figure 6.6. It can be seen from Figures 6.6 (a) that the MN-700°C nanofibers surfaces were decorated with nanostructural particles. The thermally annealed MN-700°C nanofibers show rough surfaces when compared to the electrospun sample. The high-resolution SEM image in Figure 6.6 (b) shows the formation of ribbon-like nanofibers of thin widths. The mean width for MN-700°C nanofibers was reduced to ∼134 nm with a standard deviation of 35 nm, which indicates the removal of polymer and other precursors ions at high temperatures. Some thinner nanofibers of ∼40 nm were also seen in this sample.
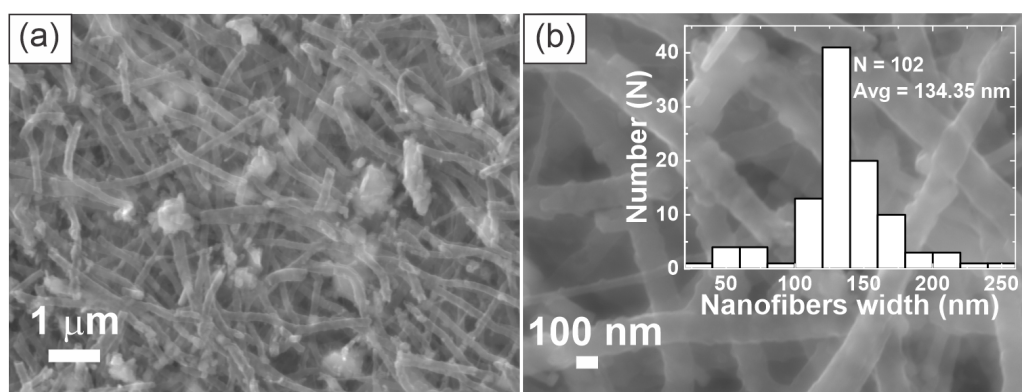
FIGURE 6.6: SEM images of MN-700°C nanofibers. The higher magnification image is shown in (b). Upper right inset: mean diameter and distribution of the diameters of these nanofibers

The SEM results for MN-620°C nanofibers are shown in Figure 6.7. It can be seen from the low-resolution image in Figure 6.7 (a) that the nanofibers show rough surfaces with the presence of smaller nanobeads. Figure 6.7 (b) shows the high-resolution image for MN-620°C nanofibers that showed the beaded nanofibers have thin widths. The mean diameter for MN-620°C nanofibers was 153 nm with a standard deviation of 33 nm which is in range with the MN-700°C nanofibers. However, more prominent beaded nanofibers were observed for MN-620°C nanofibers.
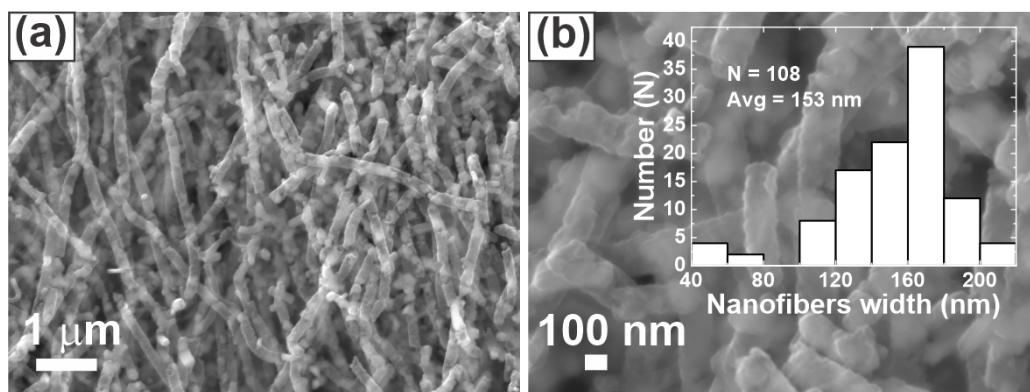
FIGURE 6.7: SEM images of MN-620°C nanofibers. The higher magnification image is shown in (b). Upper right inset: mean diameter and distribution of the diameters of these nanofibers

6.3.3 TEM analysis

TEM analysis for the MN-700°C nanofibers is shown in Figure 6.8. It can be seen in Figure 6.8 (a) that the nanofibers surfaces were decorated with small nanoparticles that range from 30-50 nm. The image was taken at high magnification in Figure 6.8 (b) showed the scales on the surface of MN-700°C nanofibers. These scaly surfaced nanofibers show the presence of lattice fringes with d-spacing 3.48Å which is attributable to the nanostructured graphitic carbon from the literature.[171–173] Under normal conditions a higher temperature, 850°C, is required to induce the crystallinity of graphitic carbon but the results have shown the formation of the graphitic component at 700°C under Ar/air environment for these nanofibers. This was also reported in a study on the thermal conductivity of graphitic carbon nanoparticles where 700°C temperature has shown to be sufficient temperature to induce slight crystallinity in the sample. [174] Figure 6.8 (c) shows the presence of some single crystalline $MnFe_2O_4$ nanorods on the nanofibers (indicated with a red arrow), while some broken single crystals can also be seen on the decorated nanofibers. The presence of dark nanoparticles on the light background in Figure 6.8 (d) showed the difference in atomic mass of these nanoparticles which is due to the formation of $MnFe_2O_4$ nanoparticles discussed below in the XRD of these nanofibers. This sample ($MnFe_2O_4$ nanofibers) contained both $MnFe_2O_4$ nanoparticles decorated on a carbon backbone nanofibers and $MnFe_2O_4$ single nanorods.
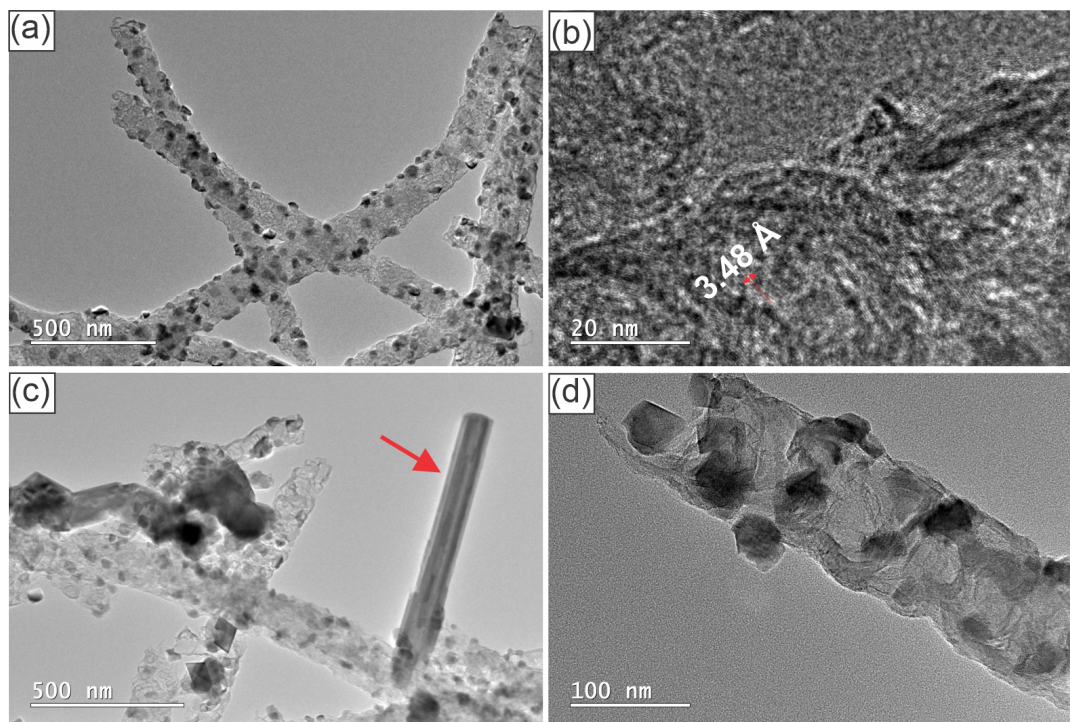
FIGURE 6.8: TEM images of MN-700°C. (a) Low magnification image showing the MnFe$_2$O$_4$ nanoparticles decorated nanofibers. (b) Lattice fringes from the carbon component. (d-spacing is shown on the image). (c) Image at low magnification showing a single crystal MnFe$_2$O$_4$ nanorods. (d) Small scale image showing scaly carbon backbone with surfaced MnFe$_2$O$_4$ nanoparticles.

TEM images from MN-620°C in Figure 6.9 (a) and (b) showed the nanofibers are composed of MnFe$_2$O$_4$ nanoparticles. There was a range in these nanoparticle sizes, where the size of smaller nanoparticles of 11-13 nm and some large nanoparticles of 26 nm were present. There are also some very large nanocrystals of ∼62 nm that protrude out from the surface. The presence of large nanocrystals indicated a difference in nucleation, where a thermal degradation at 620°C has led to the formation of nucleation sites for the slow growth of large nanocyrstals. This is different than MN-700°C nanofibers where the nucleation of large surfaced MnFe$_2$O$_4$ nanoparticles was observed. That could be due to the annealing at higher temperature (700°C) that can facilitate the Ostwald ripening for the nucleation of larger surfaced MnFe$_2$O$_4$ nanoparticles. No lattice fringes from the graphitic carbon component were observed for these nanofibers.

Figure 6.9 (b) show that these nanofibers also contain some single crystalline nanorods of MnFe$_2$O$_4$ as was seen from MN-700°C nanofibers. There was some amorphous component attached around the surface of nanofibers, which indicated the presence of carbon components in these nanofibers. The d-spacing from the lattice fringes on Figure 6.9 (b) was calculated to be 2.54 Å, which is indexed to the crystal plane [311] of the MnFe$_2$O$_4$ from the reference pattern 04-016-1572. This provided an indication for the preferred direction that was along the short axis in direction of [311] lattice plane.
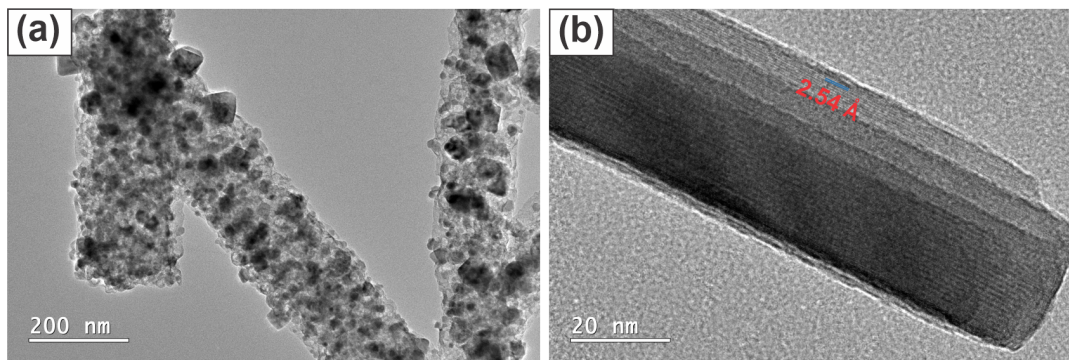
FIGURE 6.9: TEM images of MN-620°C nanofibers. (a) MN-620°C nanofibers containing $MnFe_2O_4$ nanoparticles. (b) Single crystalline $MnFe_2O_4$ nanorod found among the nanofibers showing lattice fringes with the calculated d-spacing on this figure

6.3.4 STEM maps and elemental composition

STEM maps of MN-700°C are given in Figure 6.10 (a) to (e), where image 6.10 (a) was the reference image used for the analysis. The reference image was selected to show the nanoparticles decorated $MnFe_2O_4$-700°C nanofibers as well as to show the $MnFe_2O_4$ single crystal nanorod. Only one nanorod is shown in the upper right corner of the TEM image in Figure 6.10 (a) The second image (6.10 (b)) showed the uniform distribution of carbon throughout the length of these nanofibers which provided a backbone to adhere the surfaced $MnFe_2O_4$ nanoparticles. There was no evidence of carbon around the nanorod in the upper right corner of the carbon map. The third image Figure 6.10 (c) showed the oxygen was evenly distributed on the nanoparticles as well as on the nanorod presented in the upper right corner of the Figure 6.10 (a). Oxygen can also be seen in the backbone of MN-700°C nanofibers but it was less dense as compared to the nanoparticles and nanorod. Figure 6.10 (d) and (e) show both manganese and iron maps, which showed a uniform distribution of both within the nanoparticles as well as in the nanorod. There was no indication of their presence in the carbon backbone. Therefore, this STEM analysis confirms the presence of Mn, Fe and O on the nanoparticles and nanorod which was later confirmed by XRD that they are $MnFe_2O_4$.
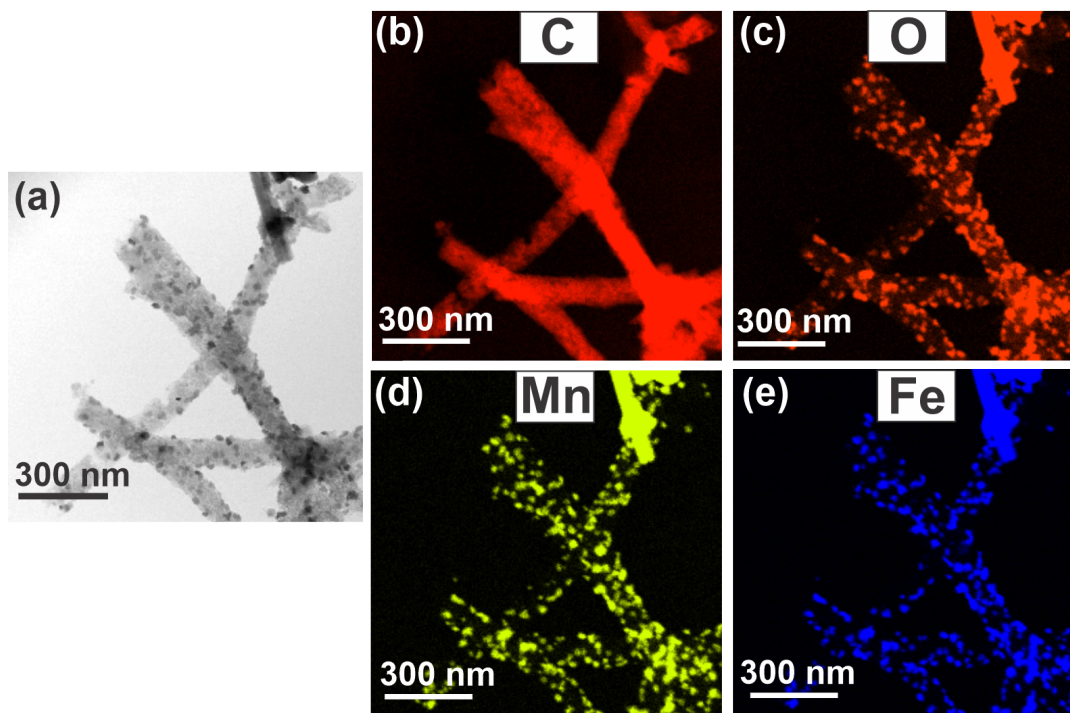
FIGURE 6.10: STEM maps of MN-700°C nanofibers. (a) TEM image of the nanofibers used for the maps. (b) Carbon map. (c) Oxygen map. (d) Manganese map. (e) Iron map

The STEM maps of MN-620°C are shown in Figure 6.11 (a) to (e). Figure 6.11 (a) represents the reference image used for the STEM mapping of MN-620°C nanofibers. This image has shown $MnFe_2O_4$ nanoparticles loaded nanofibers. The presence of a carbon backbone was further elucidated in Figure 6.11 (b) which showed the carbon was homogeneously distributed along the length of the MN-620°C nanofibers. Figure 6.16 (c) show that oxygen was not homogeneously distributed together in the carbon backbone but as discrete spots on the nanofibers where nanoparticles were present. The areas/spots with oxygen coincide with that of Mn and Fe as shown in Figures 6.11 (d) and 6.11 (e). Similar to MN-700°C, these maps conclude that the nanoparticles were $MnFe_2O_4$ attached to the carbon backbone.
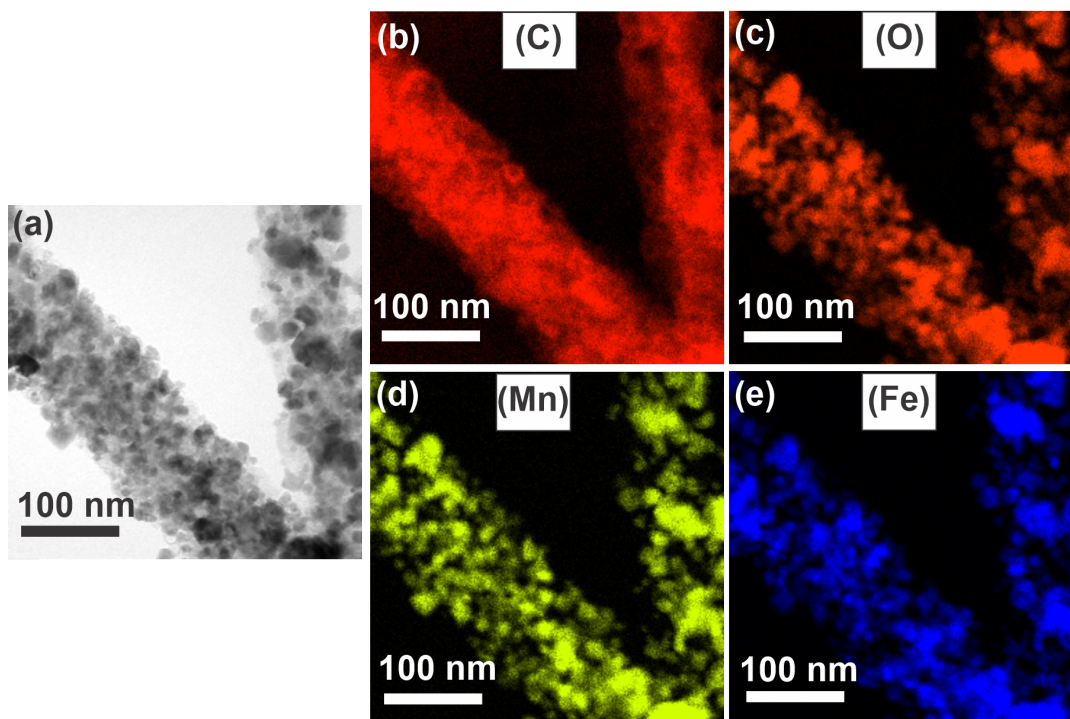
FIGURE 6.11: STEM maps of MN-620°C nanofibers. (a) The reference TEM image for the maps. (b) Carbon map. (c) Oxygen map. (d) Manganese map. (e) Iron map

The EDS analysis of MN-700°C is given in Figure 6.12. It can be seen from the EDS spectra that manganese and iron were present in a close value to what is expected in these nanofibers. The presence of oxygen is attributable to the formation of oxide nanoparticles in these nanofibers and some fragments of PVP from the graphitic carbon component. However, the carbon component is maintained to the overall length of nanofibers as a backbone substrate to adhere the $MnFe_2O_4$ nanofibers. The detailed elemental analysis for these nanofibers is given in the table attached to the Figure 6.12

Element K*	Mass %	Atoms %
C	88.57	95.01
O	4.07	3.28
Fe	4.62	1.07
Mn	2.74	0.64
Total	100.0	100.0
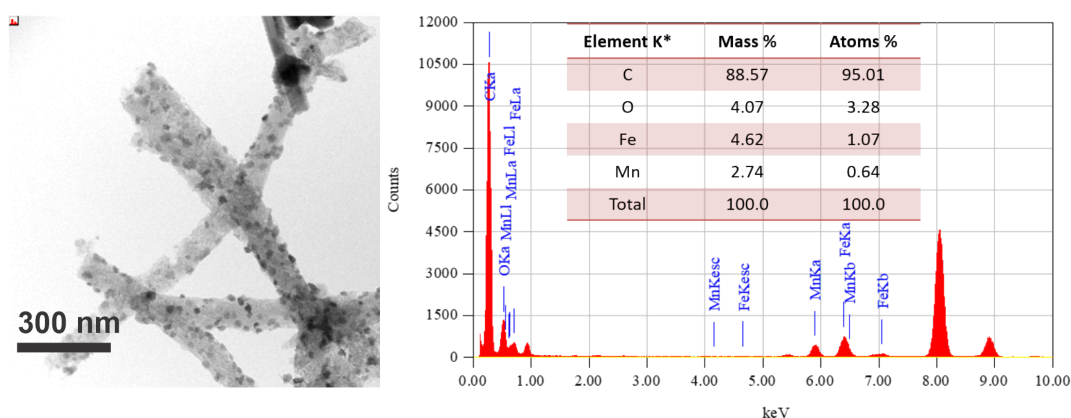
FIGURE 6.12: TEM image and EDS spectrum of MN-700°C nanofibers

The EDS spectrum of MN-620°C (Figure 6.13) indicates a close value to the expected fraction for manganese, iron and oxygen. Since the same electrospun nanofibers

were used for both samples there should not be any significant difference in the fractions of both iron or manganese.
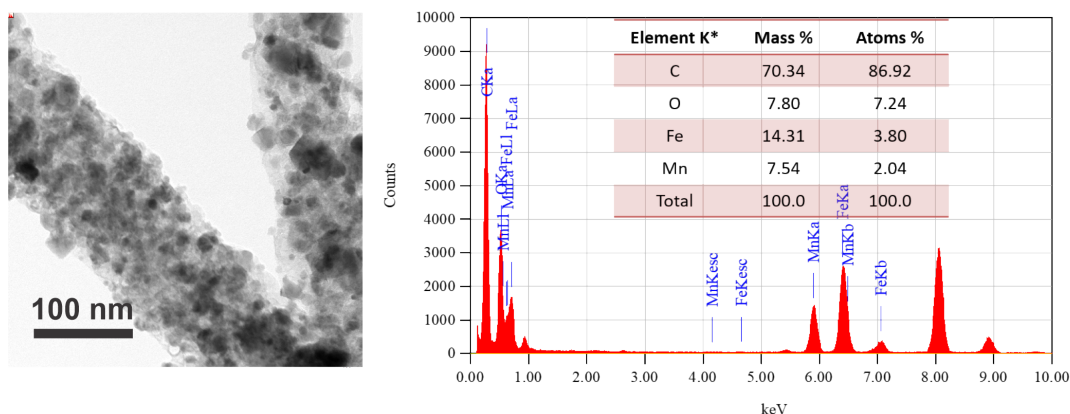
FIGURE 6.13: TEM image and EDS spectrum of MN-620°C nanofibers

6.3.5 SAED analysis

SAED of MN-700°C nanofibers is shown in the Figure 6.14. The six major rings were indexed to the cubic spinel phase of $MnFe_2O_4$ with an Fd-3m space group (reference pattern no 04-016-152). The mean value of the lattice parameter calculated was 8.478 Å with a standard deviation of 0.036 Å. This value is in range with that of bulk $MnFe_2O_4 \sim 8.4938$ Å given by reference no. 04-016-1572. Similar to the previous diffraction results from $Ni_{1-x}Fe_x$ nanofibers, bright spots over the diffused rings were observed on these diffraction patterns, which can be attributed to the presence of different sized $MnFeO_4$ nanoparticles. This sample has shown the appearance of more bright spots due to the presence of bigger size nanoparticles, which is in agreement with the TEM results above. The more brighter spots were attributable to the rods or the large crystals of MN-700°C nanofibers as per shown on the upper right inset of Figure 6.14.
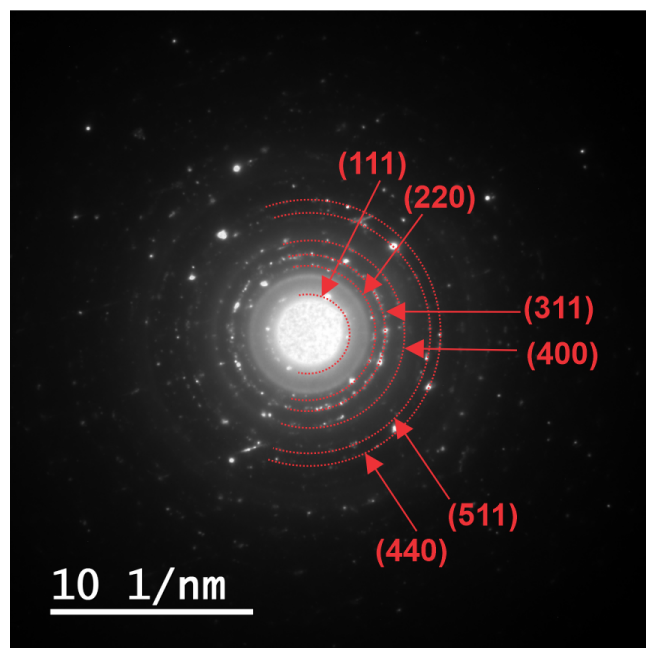
FIGURE 6.14: SAED pattern of MN-700°C nanofibers

The SAED pattern of MN-620°C nanofibers is shown in Figure 6.15. Similar to MN-700°C, the five rings shown in the figure were indexed to the cubic spinel phase of $MnFe_2O_4$. Here, the very first ring, (111), was not observed but was present for MN-700°C nanofiber due to the large exposure of the sample to the electron beam in TEM that can lead to the more brighter middle spot. This diffraction has shown the bright spots over diffused rings, which is attributed to the small and large $MnFe_2O_4$ nanoparticles in MN-620°C nanofibers. The mean value of the lattice parameter was found to be 8.47 Å with a standard deviation of 0.05 Å, which is in range with the bulk value (8.4938 Å). The diffraction rings have shown less intense bright spots as compared to the MN-700°C due to the range of different-sized nanoparticles and the area chosen within the sample for diffraction.
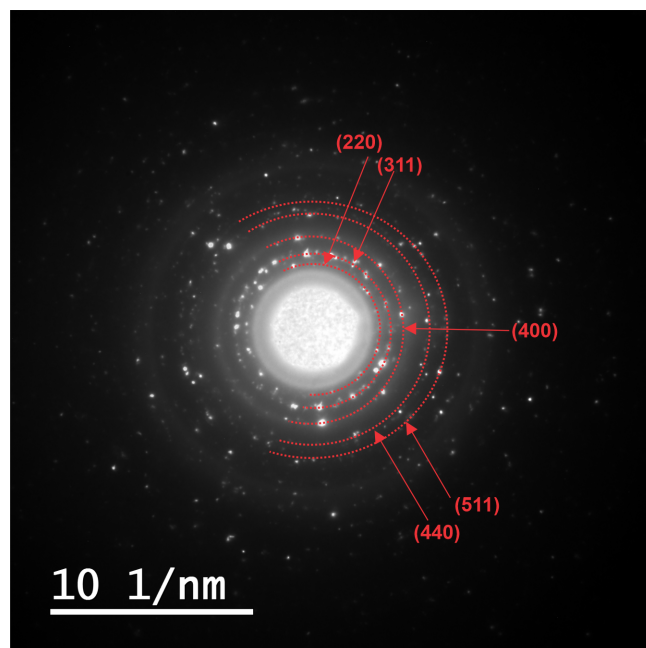
FIGURE 6.15: SAED patterns of MN-620°C nanofibers

6.3.6 XRD analysis

The XRD patterns of MN-700°C and MN-620°C in comparison with the bulk (04-016-1575) are shown in Figure 6.16. The reflections in both XRD patterns can be indexed to the face-centered cubic phase (FCC) of $MnFe_2O_4$ with Fd-3m space group. An extra broad reflection from graphitic carbon (reference pattern no 01-073-5918) was also apparent at 26 degrees 2θ (shown as an asterix) which is more pronounced when the sample is annealed at a lower temperature (620°C). This could be due to the less degradation of the carbon component in the nanofibers when the temperature was low. Overall, the intensity of this reflection was small in comparison to the other $MnFe_2O_4$ reflections. No other impurity peaks were observed in both XRD pattern.

The mean crystallite size was calculated by using the Scherrer equation from the highest intensity peak, the (311) reflection, and it was increased from 14 nm for MN-620° to the value of $\sim$23 nm for MN-700°C. The particle size for the MN-700°C nanoparticles suggested that large surfaced $MnFe_2O_4$ nanoparticles were polycrystalline in nature as larger-sized nanoparticles were seen in TEM images. Whereas, the small value of particle size ($\sim$14 nm) from the Scherrer equation suggested a range of nanoparticles sizes, where the mean value was dominated by the small-sized nanoparticles (11-13 nm) within MN-620°C nanofibers from the TEM results above.

The calculated lattice parameter for MN-700°C was 8.475Å with the standard deviation of 0.002 Å and 8.475Å with the standard deviation of 0.001 Å. These value were in agreement with that obtained from the SAED patterns and also in range with the bulk (8.489Å). However, the slight decrease in the value could be due to the cationic distribution in the spinel lattice.[175]
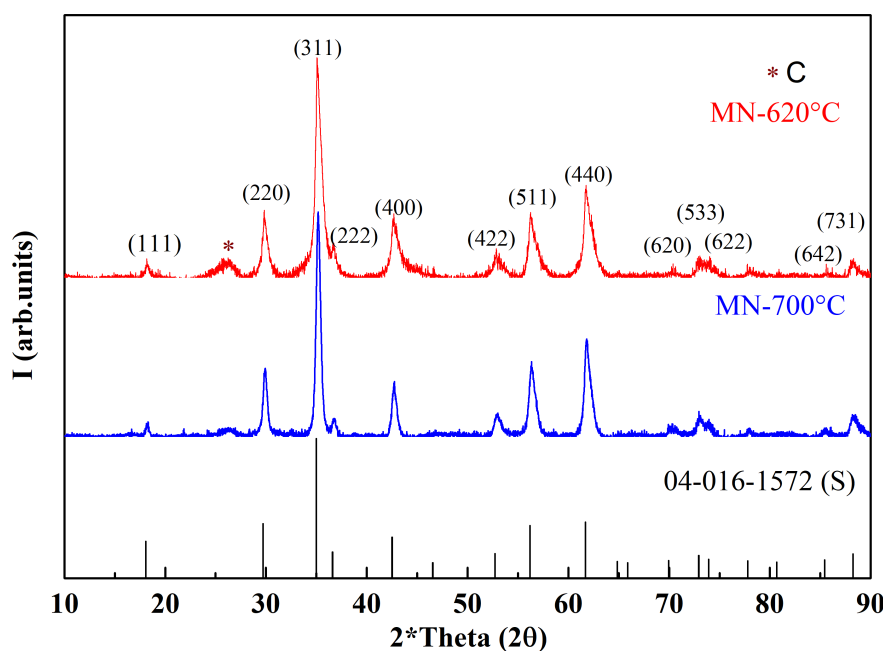
FIGURE 6.16: XRD patterns of bulk MnFe$_2$O$_4$ (black bars), MnFe$_2$O$_4$-700°C (blue), and MnFe$_2$O$_4$-620°C nanofibers

6.3.7 Magnetic studies

The comparison of the magnetic behavior between MN-700°C and MN-620° is given in Figure 6.17. Figure 6.17(a) shows the magnetization plots of MN-700°C at 5K (black), 300K (blue), and 330K (red) up to ±6T. All of the field-dependent magnetization curves showed the ferrimagnetic behavior expected for MnFe$_2$O$_4$. The high field magnetization at 5K was ~46 emu/g that reduced to ~33 emu/g at 300K and ~31 emu/g at 330K. In comparison, the magnetization plots from MN-620°C 6.18 (b) showed a further decrease in saturation moment. It was 36.5 emu/g at 5K, 22 emu/g at 300K, and 20 emu/g at 330K, both samples show a comparatively less value than the bulk value reported (80 emu/g).[176] The decrease in the saturation magnetization is also reported in other MnFe$_2$O$_4$ nanofibers from the literature.[71, 75, 76] The reason for this decrease in value was possibly due to the anti-site disorder or spin-disordered shell. This could also be due to the presence of non-magnetic carbon component which is even higher in MN-620°C nanofibers according to the XRD pattern.

The lower right inset of 6.17 (a) shows the plot of magnetization plotted over a small field range. The value of coercivity was reduced from 35 mT at 5K to 8.8 mT at 330K for MN-700°C nanofibers. Whereas, it was reduced from 40 mT at 5K to 5 mT for MN-620°C (inset in (b)). The coercivity value was comparable for both MN-620°C and MN-700°C nanofibers, but it was less than the previously reported MnFe$_2$O$_4$ nanofibers prepared at similar annealing temperature (80 mT and 100 mT
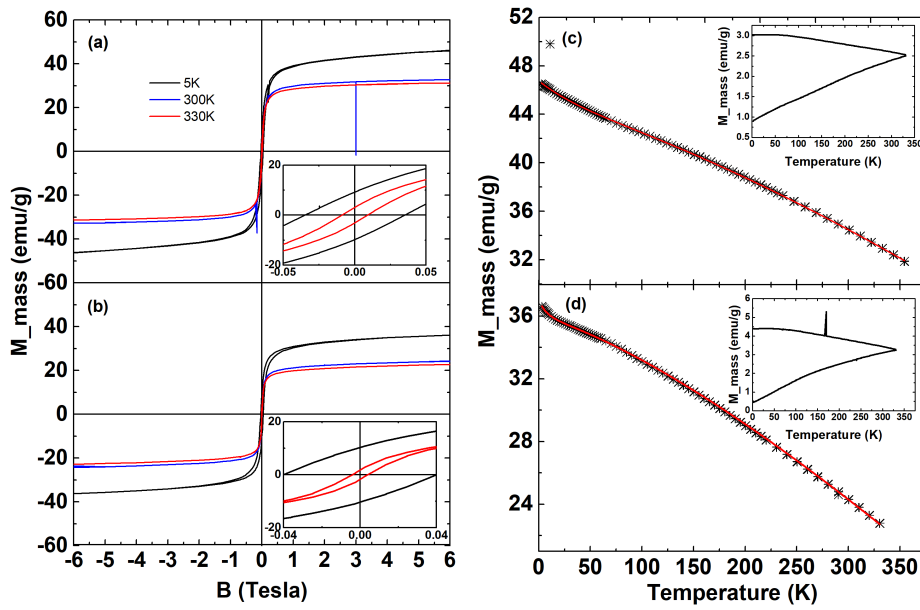
FIGURE 6.17: Magnetization plots for (a) MN-700°C nanofibers and (b) MN-620°C nanofibers. Lower right insets: magnetization plots over a small field range at 5K and 330K. Temperature-dependent magnetization for (c) MN-700°C and (d) 620°C nanofibers measured at 6T (main plot), a red curve showing the fitting by phenomenological equation (2.27). Upper right insets: ZFC-FC curves at 10mT

at 600°C).[71, 76]

The main plots in Figure 6.17(c) and (d) show the magnetic moment plotted against increasing temperature at 6T. It can be seen that for both samples, there was a deviation in the Bloch temperature dependence at low temperature, where M_s has shown a slight upturn at $\sim$40K for MN-700°C and at $\sim$43K for MN-620°C. This can be attributed to the spin-disordered shell over a magnetically ordered core.[177] Both of these curves can be modelled to the phenomenological spin-disorder term (equation (2.27)) and calculated values are given in Table. 6.4

Sample	$M_{s,c}$(6T, 0K) (emu/g)	$M_{s,d}$(6T, 0K) (emu/g)	n	β (K^n)	T_f(K)
MN-700°C	43.5	2.5	1.44±0.06	1.26×10^{-4}	40
MN-620°C	35	1.5	1.50 ±0.02	5.92×10^{-5}	43

TABLE 6.4: Fitted magnetization (6T) of Figure 6.18 (c) and (d) with the phenomenological equation (2.27) (red curve)

The saturation magnetization for magnetically ordered core ($M_{s,c}$) was found to be 43.5 emu/g for MN-700°C and 35 emu/g for MN-620°C, whereas the value for the spin-disordered component was 5% of the total magnetization for MN-700°C and 4% for MN-620°C, respectively. The values for n were 1.44 with a standard deviation

of 0.06 for MN-700°C and 1.50 with a standard deviation of 0.02. These values were consistent with the bulk (n=1.5) within experimental uncertainty. The β for MN-700°C (1.26×10^{-4}K$^{1.44}$) was larger than the β (5.92×10^{-5} K$^{3/2}$) for MN-620°C which is comparable to the bulk value (6.33×10^{-5} K$^{-3/2}$). The values of spin-freezing temperature T$_F$ were 40 K for MN-700°C, and 43K for MN-620°C nanofibers.

The upper right insets in the Figure 6.17 (c) and (d) have shown the FC-ZFC curves at 10 mT. There was no evidence of superparamagnetic bahavior from the ZFC-FC curves for both samples due to the presence of large nanoparticles in MN-700°C (Scherrer size 23 nm) and (14 nm Scherrer size) for MN-620°C nanofibers.

6.3.8 A nanofiber sample with nanorods

One of the nanofiber samples out of total of four nanofiber samples has shown the single crystalline nanorods morphology at the same temperature as was used for MN-620°C. This could be due to the amount of oxygen that varied slightly with the manual control of the airflow rate. This sample showed the presence of MnFe$_2$O$_4$ long nanorods as well as nanoparticles decorated nanofibers. This sample is assigned as SC-620°C. The results obtained from this sample are encouraging and showed the formation of nanorods can be possible with control of the oxygen flow. This can be the subject of another study with a series of experiments to control the percentage of oxygen in argon gas by using various mixtures of oxygen-argon gas tubes. Some of the results for SC-620°C are discussed below as a complete characterization was not feasible with a small amount of sample available.

6.3.8.1 SEM analysis

The large-scale SEM image in 6.18 (a) shows the nanofibers were broken into smaller rod-like structures, which could be due to the very small amount of carbon fragment presence within these nanofibers. The high-resolution image in 6.18 (b) shows that there were also some nanofibers that could have nanoparticles over a carbon backbone. The mean diameter of the nanorods was 100 nm with a standard deviation of 25 nm, which is less than the other samples processed at the same temperature MN-620°C (153 nm) as well as compared to the MN-700°C nanofibers (134 nm).
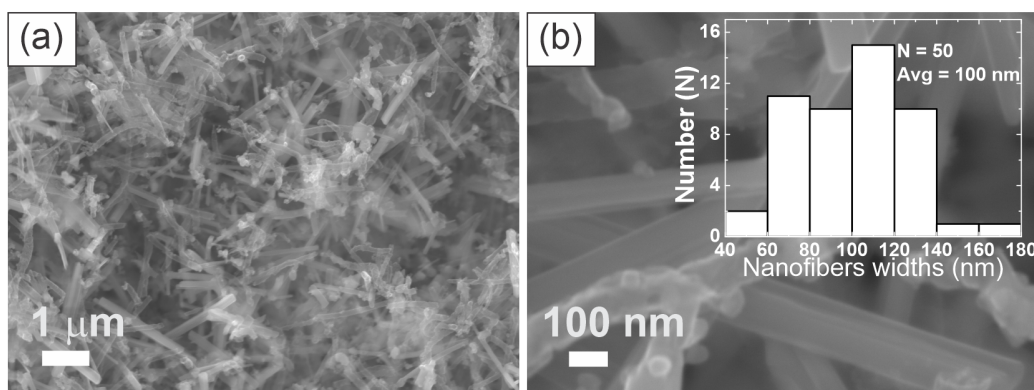
FIGURE 6.18: SEM images of SC-620°C nanofibers. (a) Low-resolution image and (b) High-resolution image. Upper right inset: mean diameter of the SC-620°C nanofibers

6.3.8.2 TEM analysis

The TEM images of SC-620°C are shown in Figure 6.19. The high-resolution image in Figure 6.19 (a) shows various single crystal-like $MnFe_2O_4$ nanorods. Some amorphous component from the carbon can also be seen in this image which could be from the leftover carbon component in these nanofibers. The dimensions of these nanofibers were somewhat between 100-200 nm. The second image 6.19 (b) showed only the SC-620°C nanofiber with a diameter even smaller than 100 nm. Figure 6.19 (c) showed the presence of lattice fringes on these nanofibers, the d-spacing from these lattice fringes was 2.95 Å which is from the hkl [200] lattice plane of $MnFe_2O_4$. This was different from the MN-620°C where the preferred lattice plane for the crystal growth was [311] with 2.54 Å d-spacings and it showed the preferential growth of nanofibers along the long axis in the direction of [200] lattice plane.
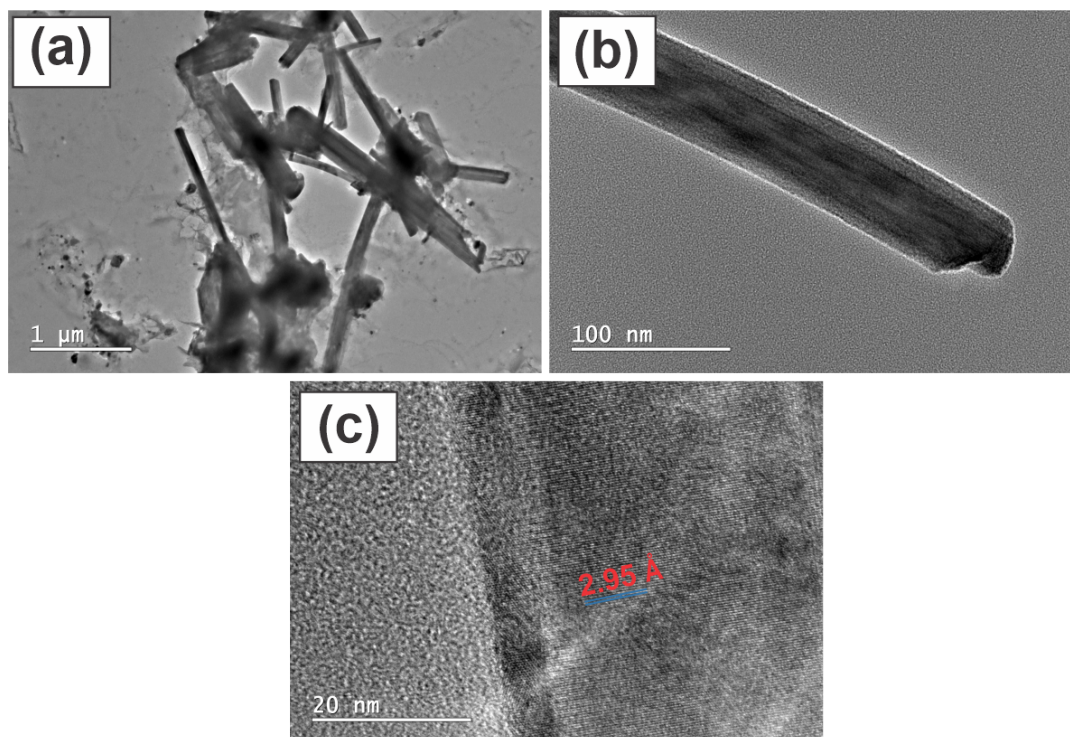
FIGURE 6.19: TEM images of SC-620°C. (a) Low-resolution image of a mixture of nanofibers with the amorphous component. (b) High-resolution image of a single nanofiber(c) Lattice fringes on the single nanofiber in (b)

6.3.8.3 STEM maps and elemental composition

The STEM maps for SC-620°C are given in the Figure 6.20 (a) to (e), where 6.20 (a) represents the reference image used for the elemental maps. Figure 6.20 (b) shows the carbon map and it can be seen there was no indication of carbon present in the nanofiber. The only carbon component was found to be surrounding the nanofibrous outer surface to form what looks like a "carbon shell". The oxygen map in Figure 6.20 (c) shows that oxygen was homogeneously dispersed within this nanofiber. The presence of oxygen confirms the formation of metal oxide(s). The last two images 6.20 (d) and (e) show the presence of manganese and iron, respectively, which coincides with where oxygen was. These maps are found consistent with the formation of $MnFe_2O_4$ nanofibers.
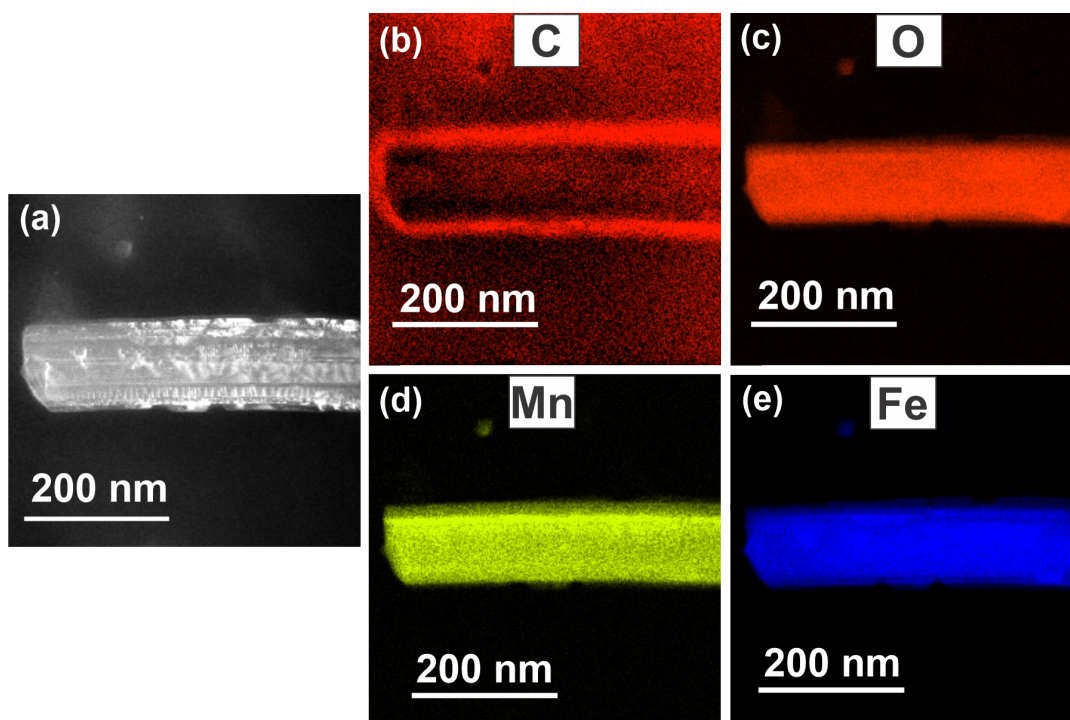
FIGURE 6.20: STEM maps of SC-620°C nanofibers. (a) Reference image for the maps. (b) Carbon map. (c) Oxygen map. (d) Manganese map. (e) Iron map

To study the elemental composition, EDS analysis was performed and is shown in Figure 6.21. The image attached is where the EDS was taken and graph on the right shows the elemental analysis of this single nanofiber. It can be seen that the elemental fraction of manganese, iron and oxygen were roughly in the expected range for EDS. The table on the graph shows the presence of carbon, which is still very high but the carbon component from the grid holding the sample can not be ignored due to the penetrating TEM beam.

Element K*	Mass %	Atoms %
C	70.29	85.70
O	9.92	9.08
Fe	14.18	3.72
Mn	5.61	1.50
Total	100.0	100.0
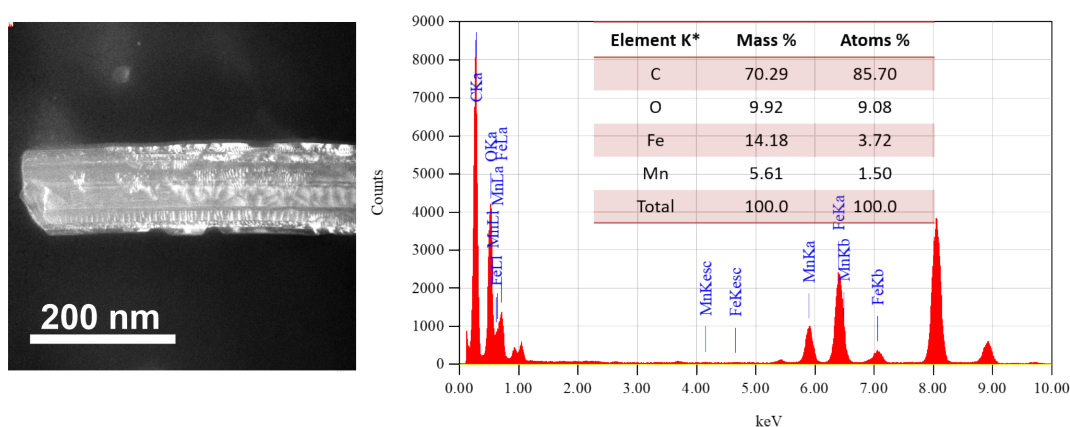
FIGURE 6.21: TEM image and EDS spectra of SC-620°C nanofibers

6.3.8.4 XRD analysis

The XRD pattern for SC-620°C is shown in the Figure 6.22. These XRD peaks were indexed to the Miller indices of phase centered cubic (FCC) phase of bulk $MnFe_2O_4$ with Fd-3m space group. The XRD pattern did not show any other impurity peaks, which confirms the sample is of good quality. Also, there was no clear carbon peak as was shown by the XRD patterns from the other two samples above. This was consistent with the STEM maps, that the carbon component is apparently absent or too little to be detected by XRD. The fitted lattice parameter was 8.496 Å, which is very close to the bulk value (8.498 Å). The mean crystallite size was 42 nm calculated using the Scherrer formula. The mean crystallite size from the high-intensity peak (311) was increased in comparison to the above two samples, suggesting that there were thinner nanofibers that dominated the Scherrer size.
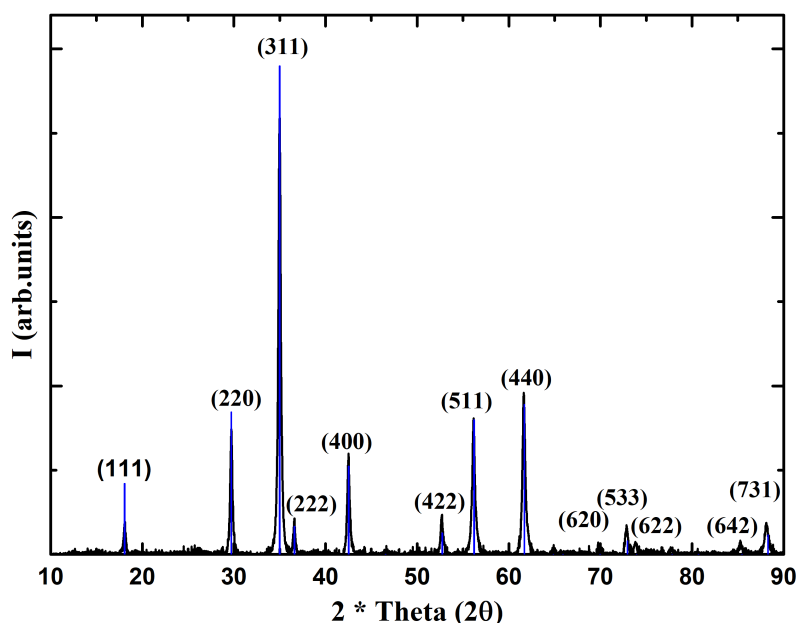
FIGURE 6.22: XRD pattern of SC-620°C. Peaks fitted well with the bulk $MnFe_2O_4$ (lines are from reference pattern no 04-016-1575)

6.3.8.5 Magnetic studies

The magnetization plots for the SC-620°C nanorods are given in the Figure 6.23. The main plot shows the magnetization is taken at 5K (black), 300K (blue), and 330K (red) up to $\pm$ 6T. All these magnetization curves showed a ferrimagnetic behavior. The high field magnetization at 5K for these nanofibers was ∼61 emu/g which is increased up to the 76% of the bulk $MnFe_2O_4$ (80 emu/g). This was also high as compared to the high field magnetization values for both MN-700°C (46 emu/g) and MN-620°C (36.5 emu/g). The saturation magnetization was decreased to ∼42

emu/g at room temperature (300K) and further reduced to 29 emu/g at 330K. The larger reductions in the magnetic moment at 300 K, by increasing the temperature, highlight the effect of thermal vibrations of magnetic moment in an applied magnetic field that can fluctuate the magnetic moment. The reduction in the saturation magnetization at a low temperature, 5K, could happen due to the anti-site disorder, redistribution of magnetic ions, and surface disorder.[178] Another study on the fabrication of $MnFe_2O_4$ nanorods (20 nm in diameter) by hydrothermal synthesis showed a slightly higher value of magnetic moment (68 emu/g) than our sample.[178]
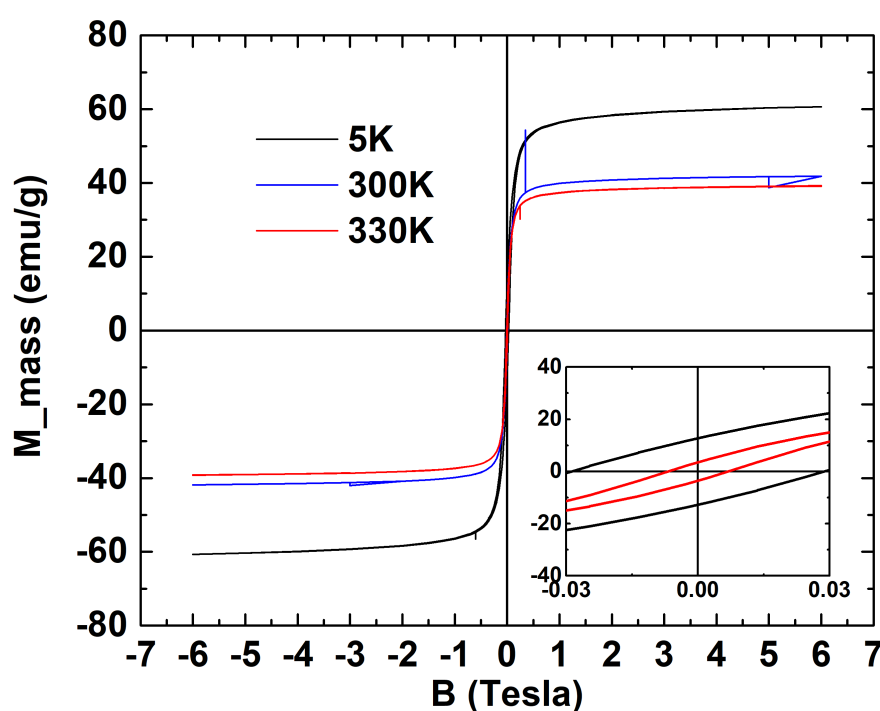
FIGURE 6.23: Magnetization plots for SC-620°C nanorods at 5K (black curve), 300K (blue curve) and at 330K (red curve). Lower right inset: Magnetization plots over a smaller field range at 5K and at 330K

The lower right inset is in the Figure 6.23 showed the value of coercivity, 6.8 mT at 330K for these SC-620°C nanorods, which is in range with the MN-700°C nanofibers (8 mT), and MN-620°C nanofibers (5 mT). This value was smaller than the previously reported $MnFe_2O_4$ nanorod. [178].

The main plot in the Figure 6.24 represents the magnetic moment plotted against the increasing temperature at 6T for SC-620°C nanofibers. There was a deviation at low temperature, where M_s has shown a slight upturn at ~22k but it becomes more uniform and resembles to Bloch magnetization at high temperature. This was fitted with the phenomenological equation (2.27) (shown in red) and the values for $M_{s,c}$, $M_{c,d}$, n, and β are given in the table. 6.5 below.
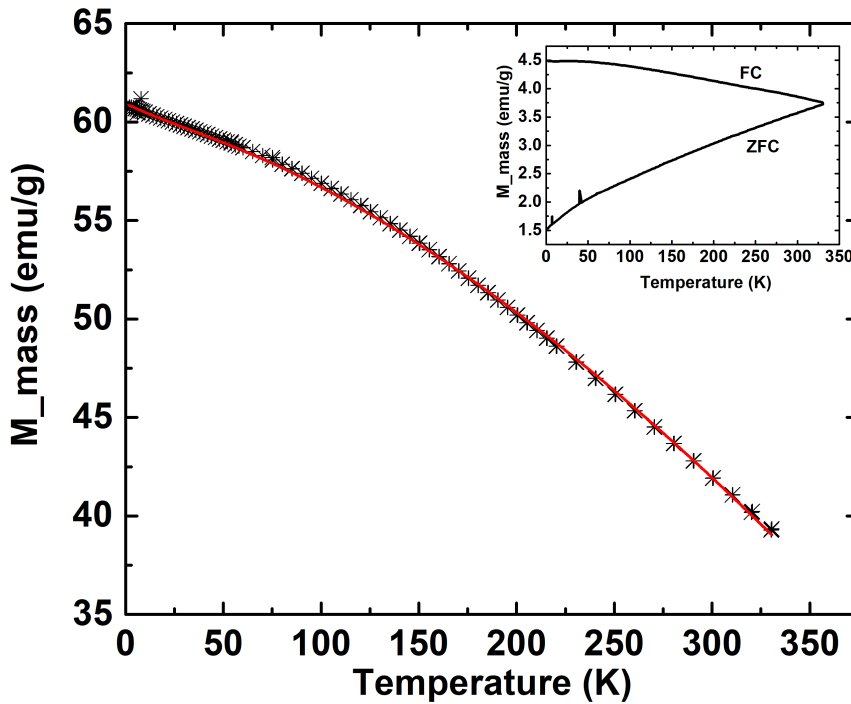
FIGURE 6.24: Magnetization against the temperature (black curve) for SC-620°C nanofibers.The curve was fitted (red curve) with the phenomenological equation (2.27). Upper right inset: ZFC-FC curves taken at 10 mT

M_s, c(6T,0K)	$M_{s,d}$(6T,0K)	n	β (K^n)	T_f(K)
60	0.9	1.54	4.6×10^{-5}	22k

TABLE 6.5: Fitted magnetization value (6T) by phenomenological equation (2.27) for SC-620° nanofibers

The saturation magnetization for magnetically ordered core ($M_{s,c}$) was 60 emu/g and for spin disordered shell ($M_{s,d}$) was 0.9 emu/g. This showed that the spin-disordered component was only 1.5 % of the total magnetization which is less than the spin-disordered component seen in MN-700°C (5%) and MN-620°C (4%) nanofibers. The value of n was 1.54 with a standard deviation of 0.09 which is in range with the bulk value (1.5). The value of n was consistent with the MN-700°C (1.44) and MN-620°C (1.50). β was 4.5×10^{-5} which is also in range with the bulk value (6.33×10^{-5}).

The upper right inset in the Figure 6.24 showed the ZFC-FC curves for SC-620°C nanorods. Likewise, in other samples, there was no evidence of superparamagnetic behavior and the overlap between the ZFC-FC curve appeared above 300K due to the residual coercivity from the larger nanoparticles of 42 nm.

This fabrication of these nanorods has shown encouraging results, but the reproducibility would require a series of experiments to systematically control the experimental parameters such as the flow rate of oxygen, and the volume fraction of oxygen to argon to induce the growth of these nanorods. This study has given some direction to aid the synthesis of singly crystalline nanorods that will be useful for future investigations.

6.4 Summary

In this chapter, manganese ferrite ($MnFe_2O_4$) nanofibers have been synthesized by using manganese nitrate, iron acetylacetonate, DMF, and PVP. After electrospinning at optimized parameters, various temperature profiles were used to find the best route for the fabrication of $MnFe_2O_4$ nanofibers, and the two best temperature profiles were selected to produce high-quality samples for characterizations. One temperature profile followed 4-steps with the highest temperature of $\sim 700^\circ$C and the second temperature profile was the typical 3-step temperature profile as was used for x$\sim$0.5 nanofibers with a maximum heating temperature of 620°C. The TEM results showed the presence of a scaly carbon backbone (with lattice fringes) containing large surfaced $MnFe_2O_4$ nanoparticles whereas, an amorphous carbon backbone (with no observed lattice fringes) containing variable-sized $MnFe_2O_4$ nanoparticles was observed for Mn-620°C nanofibers. Both samples have shown the formation of thin-width nanofibers but thinner nanofibers were obtained for MN-700°C at high temperatures. Both samples were indexed to the crystallographic phase of the pure bulk standard $MnFe_2O_4$ and the lattice parameters were found to be in agreement with bulk.

Magnetic analysis of both samples was consistent with the ferrimagnetic behavior, where the high field magnetization was 56% for MN-700°C and 45% for MN-620°C nanofibers to the bulk value. The reduction in the saturation magnetization can be attributed to the cationic distribution within the crystal lattice and the anti-site disorder within $MnFe_2O_4$. Part of the reason for this reduction was also the presence of a non-magnetic carbon component within these nanofibers. The coercivity was comparable for both samples with 8.8 mT for MN-700°C and 5 mT for MN-620°C nanofibers. The spin disordered components were 5% for MN-700°C and 4% for MN-620°C nanofibers with comparable values of T_F. No evidence of superparamagnetism was found for both samples.

Interestingly, One of the samples processed at 620°C showed the formation of single crystalline nanorods. It is attributed to the presence of an exact fraction of oxygen inside the furnace which is required to accelerate the formation of nanorods. These nanofibers have shown thinner widths up to $\sim$100 nm as compared to the other two samples. The STEM maps for these SC-620°C nanofibers have revealed that there was a uniform distribution of manganese, iron, and oxygen in the nanofibers, whereas, carbon was only present as a layer around these nanofibers. The high field magnetization was increased to 76% of the bulk for these nanofibers, which was higher than other samples. The value of coercivity (6.8 mT) was comparable to the MN-700°C (8 mT) and MN-620°C (5 mT) nanofibers. A smaller spin-disordered component with 1.5% was observed for this sample and there was no evidence of superparamagnetism from the ZFC-Fc curve. The results from this study were encouraging for future investigations with controllable oxygen content that can lead to the formation of nanorods.

6.5 Future outlook

The results obtained from this study are encouraging and can be of further interest to investigate the following points in the future:

1. Preparation of single-rod $MnFe_2O_4$ nanofibers with a series of experiments that controlled the content of oxygen by using various combination mixtures of oxygen: argon tubes to optimize conditions for nucleation.

2. Preparation of $MnFe_2O_4$ nanofibers with smaller nanoparticle size to observe the difference in structural and magnetic properties.

Preface

The next chapter explains the synthesis and characterizations of the electrospun Sm^{3+} doped $MnFe_2O_4$ nanofibers. These nanofibers were prepared by varying x at x=0.06-0.25. The structural and magnetic properties differences are highlighted in detail at each fraction of x.

Chapter 7

Sm^{3+} doped Manganese ferrite ($MnFe_{2-x}Sm_xO_4$) nanofibers

7.1 Introduction

Rare earth elements have unique electromagnetic properties due to their 4f electrons. They show magnetization at a very low temperature and are paramagnetic at room temperature. The spin-orbit coupling in rare earth elements is very strong which makes them favorable for permanent magnetization.[179] The magnetic moment of trivalent lanthanide ions varies from diamagnetic La^{3+} to 10.5 (μ_b) for Dy^{3+} ions. Such properties make them interesting for doping into spinel ferrites to modulate their magnetic behaviour.[180, 181]

In general, the rare earth ions are too large to occupy either tetrahedral or octahedral sites during sintering processes and may contribute towards the formation of some secondary phases in spinel ferrites.[179, 182, 183] The substitution of trivalent rare earth elements in ferrites can cause disorder in the crystal structure that hinders crystal growth. This is due to their large ionic radii as compared to Fe^{3+} ions. Recently, there has been an increased interest in soft metal ferrites doping with rare earth ions, to determine their crystal structure dependence on composition as well their magnetic behavior. A report on rare earth ion (Nd, Gd, Lu, Yb) doped nickel zinc ferrite materials has shown an increase in their saturation magnetization and a decrease in coercivity at increasing dopants percentage.[184] Similarly, Ce^{3+} doped $Zn_{0.5}Mn_{0.43}Cd_{0.07}Ce_yFe_{2-y}O_4$ has shown an increase in the saturation moment with increasing fraction of Ce^{3+} cation up to y= 0.1 and decreased with further increasing Ce^{3+}. The strain in the crystal structure causes a decrease in the lattice parameters with increasing Ce^{3+} fraction.[185] Another report on La^{3+} doped $MnFe_2O_4$ nanoparticles showed that there is a decrease in the lattice parameters with an increase in La^{3+} ion doping.[186]

In this chapter, Sm^{3+} doped $MnSm_xFe_{2-x}O_4$ nanofibers are prepared at an increasing fraction of x=0.06-0.25 (Sm^{3+}). Only a few reports from the previous literature have shown the $MnFe_2O_4$ doping with various trivalent rare R^{3+} earth ions (R= Pr, Nd, Eu, Gd, Tb, Pr, Ce, Y) and intriguing results were obtained for both structural and magnetic properties.[187, 188] To the best of my knowledge, there has been

no report on the doping of $MnFe_2O_4$ nanomaterials with Sm^{3+}. The objective of this study was to investigate the effect on structural and magnetic properties of MN-620° sample from the previous chapter that has both low magnetic moment and coercivity. This sample was selected to see how magnetic moment and coercivity change with Sm^{3+} ions doping. Sm^{3+} (coordination no VI) has a large ionic radii (0.964 Å)[189] than Fe^{3+} ions with ionic radii of 0.67 Å (coordination no VI)[189], that can cause the structural strain/defects in the crystal lattice. It can also affect the particle size as well as the lattice parameters of the cell unit. This study investigates the changes to the crystal lattice, particle size, and magnetic properties when Sm^{3+} ions have been doped at various fractions (x=0.06-0.25) in $MnFe_{2-x}Sm_xO_4$ nanofibers prepared by electrospinning method.

7.2 Experimental

7.2.1 Chemicals used

Manganese nitrate tetrahydrate ($Mn(NO_3)_2 \cdot 4\,H_2O$) 99% and samarium nitrate hexahydrate ($Sm(NO_3)_3 \cdot 6\,H_2O$) 99.9% were purchased from Acros Organics. Tris acetylacetonate iron ($Fe(C_5H_7O_3)_3$) 97% and Polyvinylpyrrolidone(PVP) (($C_6H_9NO)_n$) were purchased from Sigma-Aldrich. Dimethylformamide (DMF) 99.8% was purchased from Acro seal ®.

7.2.2 $MnSm_xFe_{2-x}O_4$ solution preparation for electrospinning

In this typical synthesis, $MnSm_xFe_{2-x}O_4$ nanofibers are prepared with varying x from 0.06 to 0.2. For this, 6 mmol of each manganese nitrate (1.004 g) and iron acetylacetonate (1.41 g) were prepared in 6.5 mL of DMF. 6 mmol of samarium nitrate (0.889 g) were separately prepared in 3.25 mL of DMF. From these three stock solutions, various combinations of iron and samarium salts are given below in the table. 7.1 were used to prepare electrospun $MnSm_xFe_{2-x}O_4$ nanofibers with x=0.06, 0.1, 0.2, 0.25. The volume of manganese precursor was kept constant (1 mL) in all these solutions.

Sample	Fe^{3+}-salt (mL)	Sm^{3+}-salt (mL)
$MnSm_{0.06}Fe_{1.94}O_4$	1.94	0.06
$MnSm_{0.1}Fe_{1.9}O_4$	1.9	0.1
$MnSm_{0.2}Fe_{1.8}O_4$	1.8	0.2
$MnSm_{0.25}Fe_{1.75}O_4$	1.75	0.25

TABLE 7.1: Solution mixtures for electrospinning

0.4 grams of PVP was added to all solutions and these are stirred at a constant speed to get homogeneous mixtures for electrospinning. The same parameters on

electrospinning set-up from the previous chapter (Chapter 6 for $MnFe_2O_4$ nanofibers synthesis) were used for these solutions to electrospun the nanofibers (Table 6.3). All these prepared electrospun samples were compared with the MN-620°C nanofibers from the previous chapter to see the effect of x on $MnSm_xFe_{2-x}O_4$ nanofibers.

7.2.3 Thermal treatment of electrospun $MnSm_xFe_{2-x}O_4$ nanofibers with x=0.06, 0.1, 0.2, 0.25

All the electrospun samples of $MnSm_xFe_{2-x}O_4$ with x= 0.06, 0.1, 0.2, 0.25 were placed in the vacuum oven at 150°C for 4 hours at 0.05 Mpa. (same conditions as were used for MN-620°C nanofibers) These samples were left overnight under vacuum at constant pressure and processed the next day in the tube furnace.

For the thermal annealing in the tube furnace, the same steps were replicated, as previously developed in chapter 6 (subsubsection 6.2.3.3) under partial oxidation in the presence of argon in the first step and later annealing in the air for MN-620°C nanofibers.

7.3 Results and discussions

7.3.1 SEM analysis of electrospun $MnSm_xFe_{2-x}O_4$ nanofibers
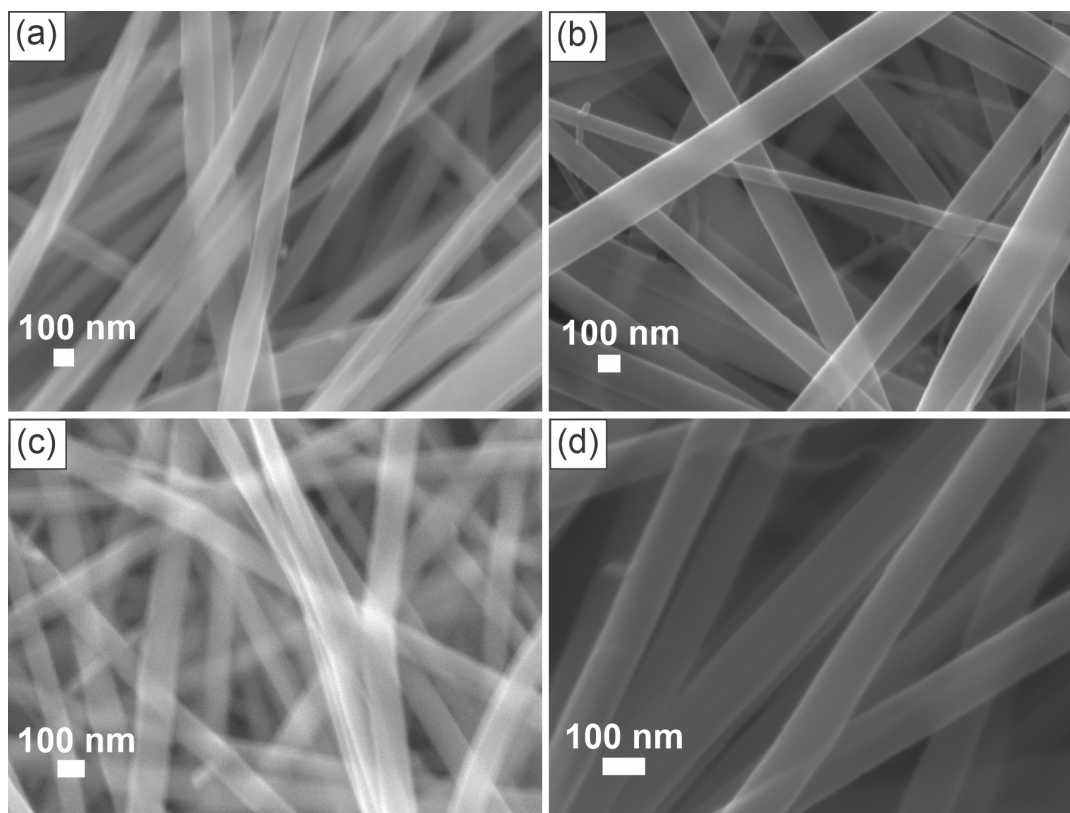
FIGURE 7.1: SEM images of electrospun $MnSm_xFe_{2-x}O_4$ nanofibers with (a) x= 0.06, (b) x= 0.1, (c) x= 0.2 and (d) x= 0.25

The electrospun doped $MnSm_xFe_{2-x}O_4$ nanofibers with x=0.06-0.25 after annealing in vacuum are shown in the Figure 7.1. It can be seen that all of these electrospun $MnSm_xFe_{2-x}O_4$ nanofibers have shown smooth surfaces. The mean diameter for these nanofibers was also calculated and is given in the Table. 7.2 below.

x	Nanofiber widths (nm)
0	178 ± 25nm
0.06	139 ± 36
0.1	144 ± 48
0.2	110 ± 20
0.25	120 ± 17

TABLE 7.2: Mean Widths (nm) for the electrospun $MnSm_xFe_{2-x}O_4$ nanofibers with x=0-0.25

The first value in the above table has represented the mean widths from the undoped (x=0) $MnFe_2O_4$ nanofibers from the previous chapter 6. From the table, the nanofiber widths at the low fractions (x=0.06-0.1) of Sm^{3+} (x) doped samples were in range with the undoped x=0 within experimental uncertainty. However, the calculated mean widths for x=0.2 and x=0.25 were reduced when compared with the x=0.06 and x=0.1, which showed that the increased fraction of x has given more thin nanofibers as compared to the other samples.

7.3.2 SEM analysis of thermally annealed $MnFe_{2-x}Sm_xO_4$ nanofibers

The high-resolution SEM images for all four samples are shown in Figure 7.2 (a) to (d). It can be seen from the SEM images 7.2 (a) and 7.2 (b) that both x= 0.06 and x= 0.1 nanofibers have shown similar morphology to the undoped MN-620°C sample with the formation of small nanostructures within these nanofibers. They have elongated rod-like morphology and it can be seen that x= 0.06 has shown more agglomeration of small nanostructures on the surfaces of nanofibers. Whereas, in the case of x= 0.1, the nanofibers showed more contained nanostructures within these nanofibers. When x was further increased to 0.2 and 0.25, more ribbon likes nanofibers were obtained. Both of the samples shown in 7.2 (c) and 7.2 (d) have shown no surface agglomerated nanoparticles but the rough surfaces in both cases have indicated the presence of some nanostructures, that can only be resolved with high-resolution TEM analysis of the sample.
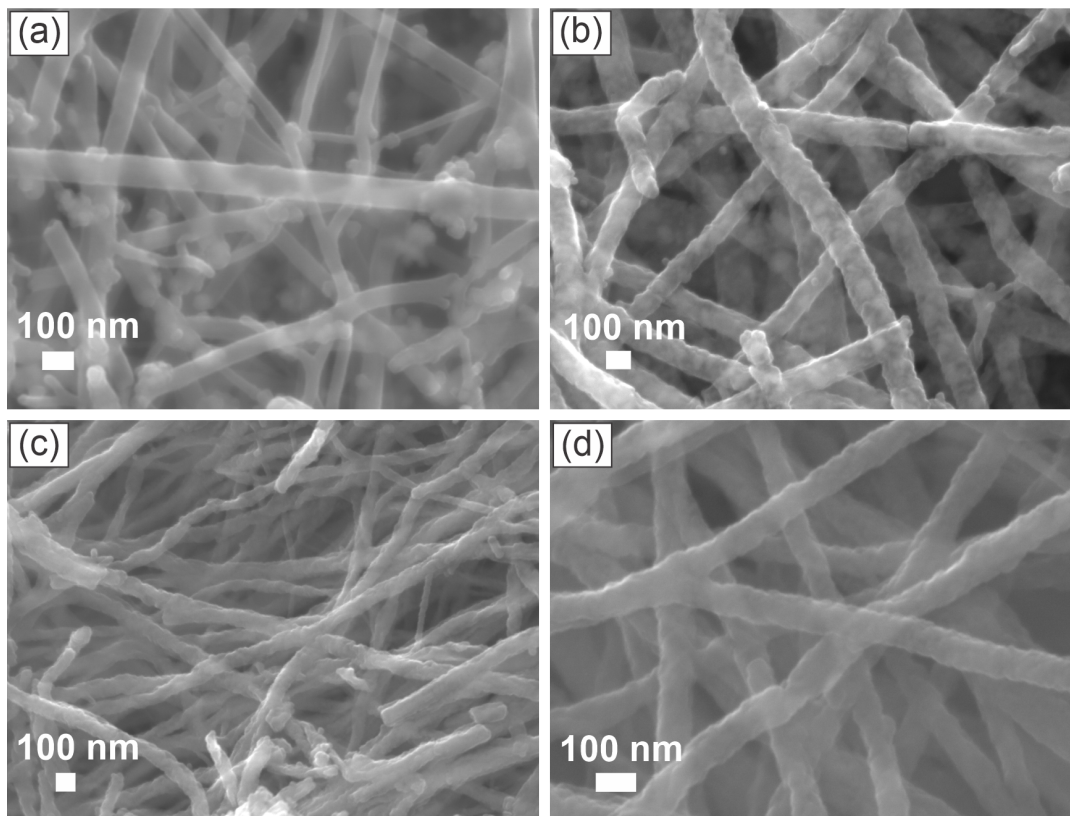
FIGURE 7.2: SEM images for thermally processed MnSm$_x$Fe$_{2-x}$O$_4$ nanofibers with (a) x=0.06 (b) x= 0.1 (c) x= 0.2 and (d) x= 0.25

The mean widths for all the samples were also calculated and histograms were plotted to compare the widths of all four samples in Figure 7.3. There was no systematic change in the nanofiber's widths with increasing x from 0.06 to 0.2. In comparison to the electrospun samples, the nanofiber's widths at low fractions for x= 0.06-0.1, were decreased to ∼76 nm with a standard deviation of 20 nm and ∼102 nm with a standard deviation of 16 nm. Further increase in the x to x= 0.2 and x= 0.25 showed the decrease in nanofibers widths to ∼81 nm with a standard deviation of 19 nm and ∼90 nm with a standard deviation of 18 nm. All these samples showed the formation of thin widths nanofibers after thermal processing due to the oxidative degradation of polymeric components and other ions in the electrospun sheets at high temperatures.
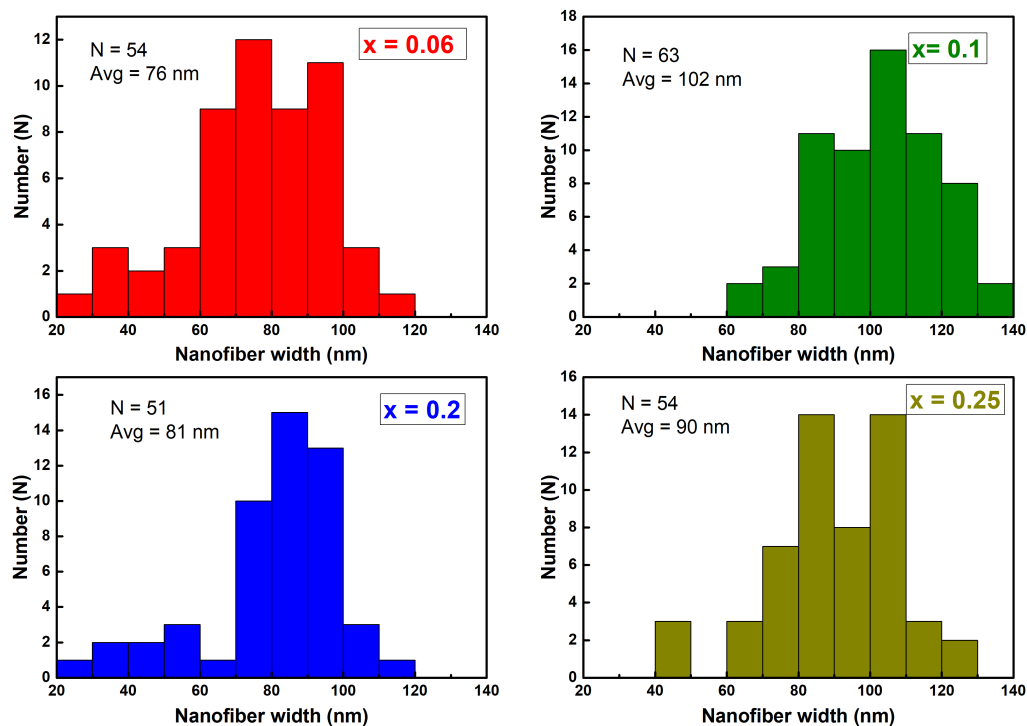
FIGURE 7.3: Average widths of thermally processed $MnSm_xFe_{2-x}O_4$ nanofibers with (a) x= 0.06 (b) x= 0.1 (c) x= 0.2 and (d) x= 0.25

7.3.3 Energy dispersive x-ray spectroscopy (SEM-EDS)

SEM-EDS analysis was done on the three selected samples of x=0.1, 0.2, and 0.25. SEM-EDS was selected to cover the large area from the sample for the precise values of Sm^{3+} at low fractions as compared to the total mass of the sample. The results from the x=0.1 doped $MnFe_{2-x}Sm_xO_4$ are shown in Figure 7.4, where the first image showed the large area SEM image for the EDS analysis. The scale bar showed the bulk area from the sample at low resolution. The other two images showed the EDS spectrum from the sample that contains the elemental composition of the whole sample, and a comparison between the doped samples. These results were consistent with the presence of manganese-rich $MnFe_{2-x}Sm_xO_4$ nanofibers with 38 atomic percentages. The atomic percentage of samarium per total transition metal ions atomic percentage was 5 %, which was slightly larger than the expected value (3.4 %) of x used.

Element K*	Mass %	Atoms %
Mn	35	38
Fe	52	57
Sm	13	5
Total	100.0	100.0
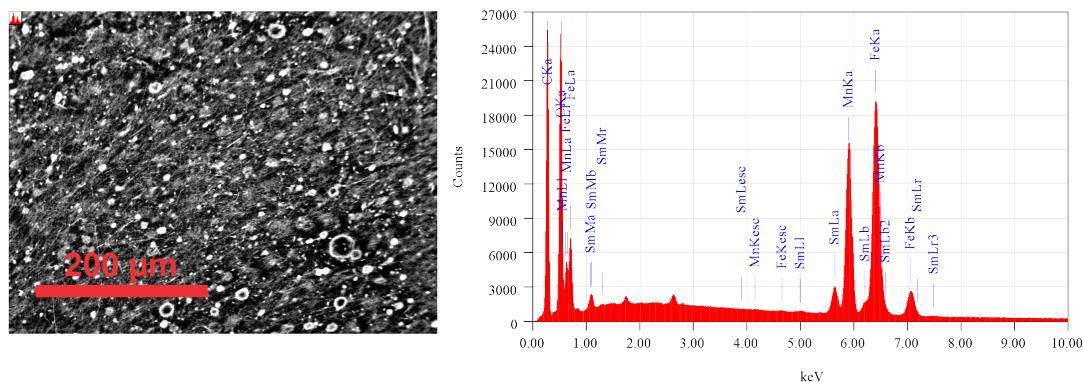
FIGURE 7.4: Low resolution SEM image of $MnFe_{2-x}Sm_xO_4$ nanofibers with x=0.1 for EDS analysis with EDS spectrum, and EDS table for manganese, iron, and samarium (x)

Figure 7.5 shows the low resolution image and EDS analysis of $MnFe_{2-x}Sm_xO_4$ nanofibers with x=0.2. The results were consistent with the presence of manganese-rich nanofibers with an overall 40 atomic percentage of the sample. The atomic percentage of samarium was increased to 7 atomic percentage with increasing x. This value was found in the range (7 atomic percentage) of the experimental value used for x=0.2.

Element K*	Mass %	Atoms %
Mn	35	40
Fe	48	53
Sm	17	7
Total	100	100
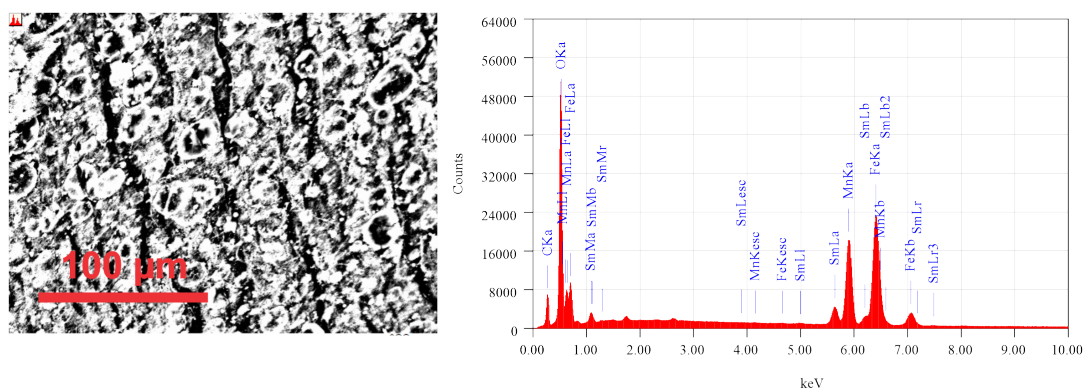
FIGURE 7.5: Low-resolution SEM image of $MnFe_{2-x}Sm_xO_4$ nanofibers with x=0.2 for EDS analysis with EDS spectrum, and EDS table for manganese, iron, and samarium (x)

Figure 7.6 shows the low resolution image and EDS analysis of $MnFe_{2-x}Sm_xO_4$ nanofibers at x=0.25. Similar to the previous two samples, this sample has also shown similar results with the presence of manganese-rich material with 38 atomic percent. The value of x was increased to 9 atomic percentage for this sample. This value was also in the expected range (9 atomic weight percentage) at x=0.25. All these three samples have shown the formation of manganese-rich $MnFe_{2-x}Sm_xO_4$ nanofibers.
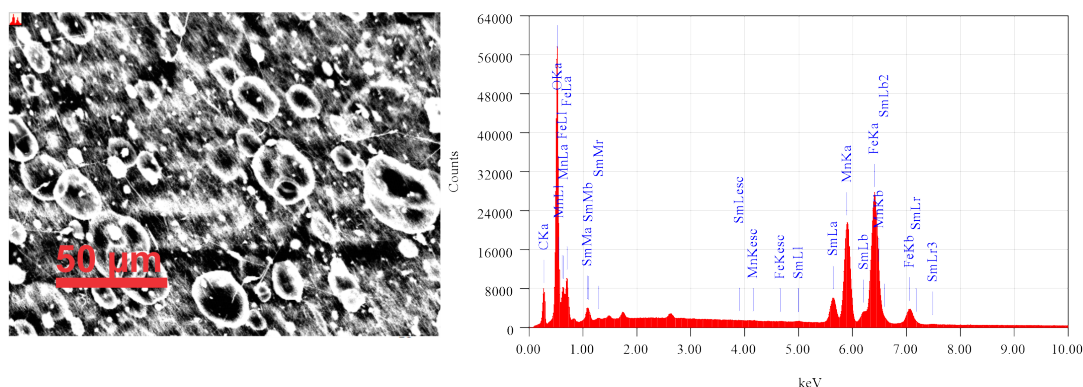
Element K*	Mass %	Atoms %
Mn	33	38
Fe	47	53
Sm	20	9
O	100	100

FIGURE 7.6: Low-resolution SEM image of $MnFe_{2-x}Sm_xO_4$ nanofibers with x=0.25 for EDS analysis with EDS spectrum, and EDS table for manganese, iron, and samarium (x)

7.3.4 TEM analysis

The TEM analysis for the low fractions of x= 0.06 and 0.1 is given in the Figure 7.7 (a) to (d), where 7.7 (a) and 7.7 (b) are from x= 0.06 and 7.7 (c) and 7.7 (d) are for x= 0.1 nanofibers. From the Figure 7.7 (a), it can be seen that these nanofibers have shown nucleation of nanocrystals with non-uniform shapes and sizes. In Figure 7.7 (a), it can be seen that some nanofibers have contained both large and small nanocrystals, whereas others appeared as nanofibers without large nanocrystals, with their contrasting dull color in comparison to the dark color shown by big crystals. To understand the features of these apparent hollow nanofibers, a single nanofiber was selected at a high resolution that can be seen in the main image of Figure 7.7 (a). This image showed that the nanofiber also contained very small nanoparticles, and this was further clarified with a further high-resolution image on the upper right inset of Figure 7.7 (b). These x= 0.06 nanofibers were compared with x= 0.1, which are shown in the Figures. 7.7 (c) and (d). Similar features were obtained for increasing x. Both images are in Figure 7.7 (c) and (d) have shown the presence of small and large nanocrystals with a difference in color contrast for these nanofibers (more

darker color for large nanocrystals). No difference was observed in the nucleation and morphology for these two samples.
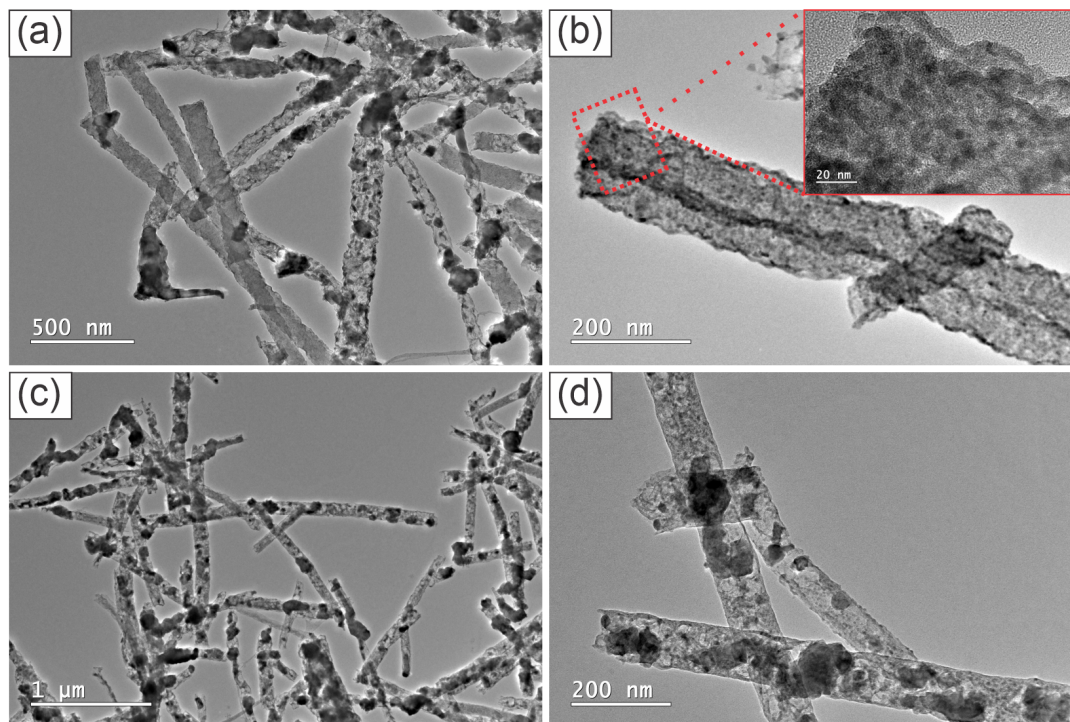
FIGURE 7.7: TEM images for thermally processed $MnSm_xFe_{2-x}O_4$ nanofibers (a) Low resolution image for x=0.06 (b) High resolution image for x= 0.06. Upper right inset: Higher resolution TEM image showing nanocrystals for x= 0.06 nanofiber. (c) Low-resolution image for x= 0.1 (d) High-resolution image for x= 0.1

Another Figure 7.8 from (a) to (d) has shown the morphology of $MnSm_xFe_{2-x}O_4$ nanofibers when x was further increased to x=0.2 (7.8 (a) and 7.8 (b)) and x=0.25 (7.8 (c) and 7.8 (b)). It can be seen that a further increase in x= 0.2 and x=0.25 caused a decrease in the crystal size for $MnSm_xFe_{2-x}O_4$ nanofibers. Both of these samples (x= 0.2 and 0.25) have shown a more uniform shape and particle size for the nanoparticles. It showed that the increase in the x can cause the formation of small-sized nanoparticles in these nanofibers with uniform shapes and sizes. The first two images in Figure 7.8 (a) and 7.8 (b) showed the $MnSm_xFe_{2-x}O_4$ nanofibers with x= 0.2. It can be seen that there were some nanofibers with both large and small nanoparticles (lower right inset is an expansion of 7.8 (a)). The second image in Figure 7.8 (b) showed more uniform-sized nanoparticles between 10-25 nm (upper right inset of 7.8 (b)). Similarly, the other two images in Figure 7.8 (c) and 7.8 (d) have shown that the nanofibers contained smaller nanoparticles as well as large nanoparticles on the surface of some nanofibers. Overall, there were still some large nanocrystals in these nanofibers for both cases. The expanded large-scale image is Figure 7.8 (d) which showed that the particle sizes were in between 8-30 nm in x=0.25 nanofibers. Both fractions of x with 0.2 and 0.25 have shown that increasing fractions of x can cause more homogeneity in nanoparticle sizes within $MnSm_xFe_{2-x}O_4$ nanofibers.
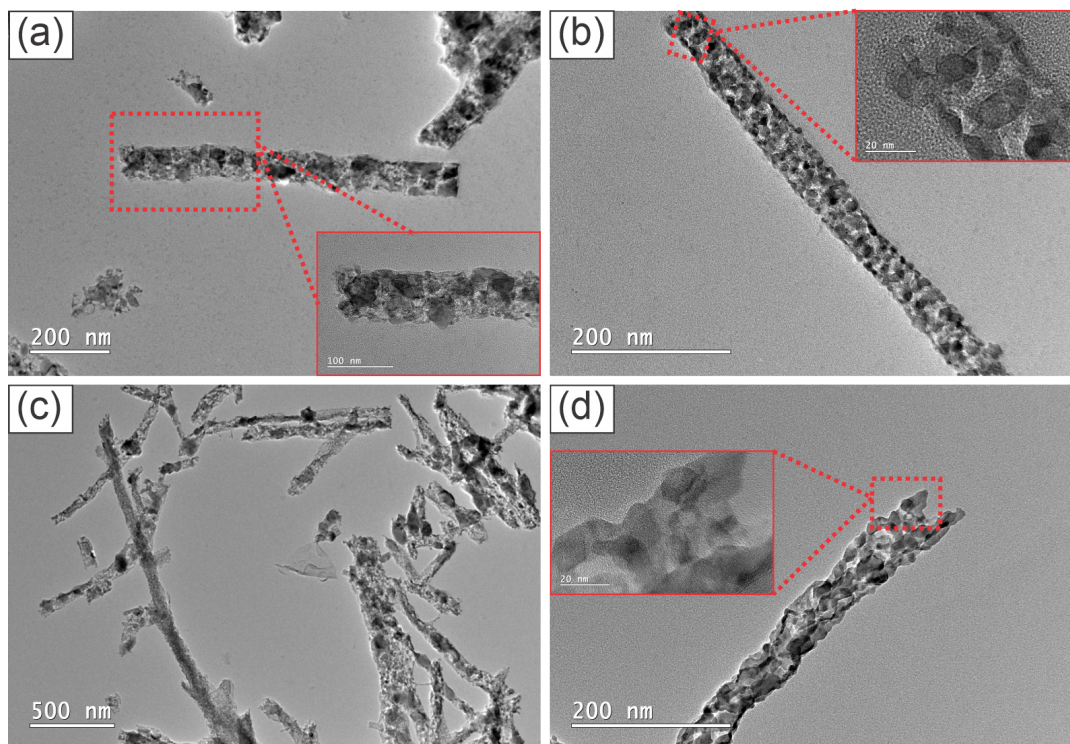
FIGURE 7.8: TEM images for thermally processed $MnSm_xFe_{2-x}O_4$ nanofibers (a) Low resolution image for x= 0.2. Lower right inset: High resolutions image of a single nanofiber. (b) Low-resolution image for x= 0.2. Upper right inset: High-resolution image at 20 nm scale bar. (c) Low resolution image for x= 0.25 (b) High-resolution image for x= 0.25. Middle left inset: Higher resolution image at 20 nm scale bar

7.3.5 STEM maps

STEM maps for x=0.06 doped $MnFe_{2-x}Sm_xO_4$ nanofibers are shown in the Figure 7.9. It can be seen from Figure 7.9 (a) that the TEM reference image has shown the presence of some large nanocrystals (intense color due to high electron density) and in contrast, some areas display less sharp colors. The second image in Figure 7.9 (b) showed that carbon is present in the overall length of the nanofiber but it was more intense in the area where no large nanocrystals were present from the reference image. The oxygen map in Figure 7.9 (c) showed the presence of oxygen in the overall length of the nanofiber, but it was sharper in the nanocrystals than in the fiber backbone. Figure 7.9 (d) shows the distribution of manganese in the nanofibers, it can be seen that the manganese was present in the large nanocrystals but some small manganese-rich nanoparticles were also seen in this sample. These nanoparticles have more manganese than iron as was seen in the iron map in Figure 7.9 (e). The iron map showed more iron in the large nanocrystals. Figure 7.9 (f) shows the samarium map and it is very interesting to note that samarium is equally distributed in the overall length of the nanofibers. It showed that the sample contained Sm^{3+} doped $MnFe_{2-x}Sm_xO_4$ nanoparticles within these nanoparticles.
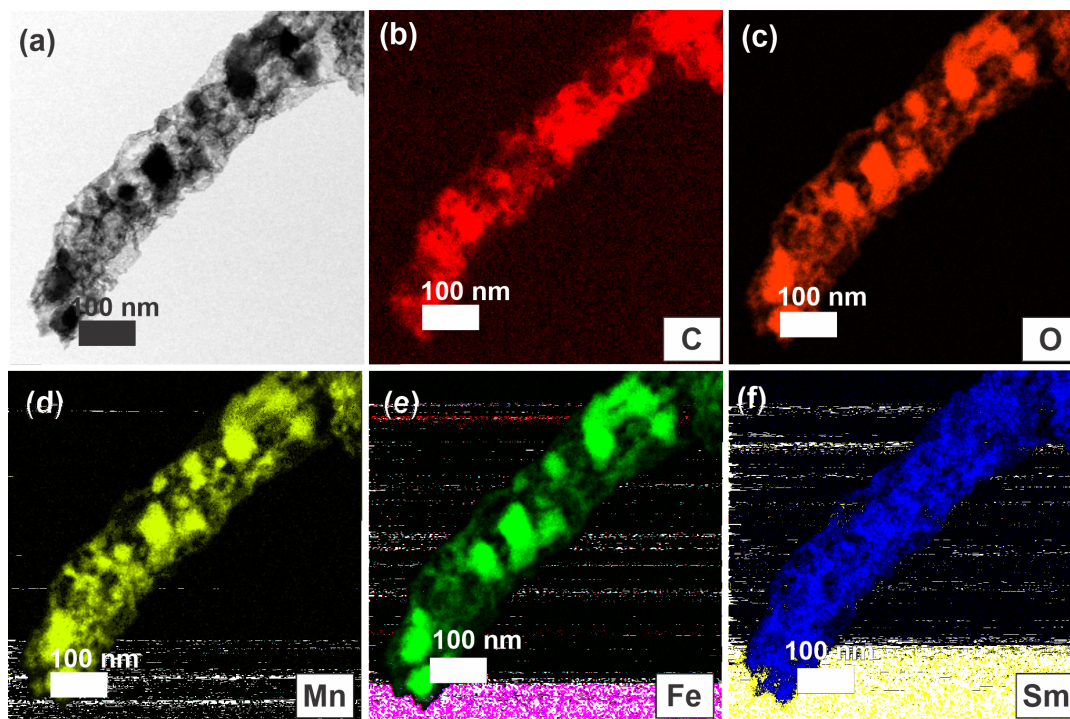
FIGURE 7.9: MnFe$_{1-x}$Sm$_x$O$_4$ nanofibers with x=0.06 (a) Image used for the maps, (b) Carbon map (red) (c) Oxygen map (orange), (d) Manganese map (yellow), (e) Iron map (green), and (f) Samarium map (blue)

STEM maps for x=0.1 doped MnFe$_{2-x}$Sm$_x$O$_4$ nanofibers are shown in the Figure 7.10. Figure 7.10 (a) was used as a reference TEM image for the STEM mapping that showed a single nanofiber containing both large and small nanocrystals adhered to the carbon backbone. Similar to x=0.06, the carbon map in Figure 7.10 (b) showed that the carbon is non-homogeneously distributed in this nanofiber, and it was more intense in some areas where large nanocrystals were not present. The oxygen map in Figure 7.10 (c) showed the presence of more intense oxygen in the large nanocrystals whereas, it was also present in the carbon backbone. The other two maps in Figures 7.10 (d) and (e) showed the presence of manganese and iron in the large nanocrystals, that similar to the x=0.06, showed the presence of some manganese-rich nanoparticles. In this sample, some areas have also shown iron-rich small nanoparticles. Figure 7.10 (f) showed the samarium map, and it can be seen that samarium was equally distributed in small nanoparticles within these nanofibers but some samarium-rich large nanocrystals were also found.
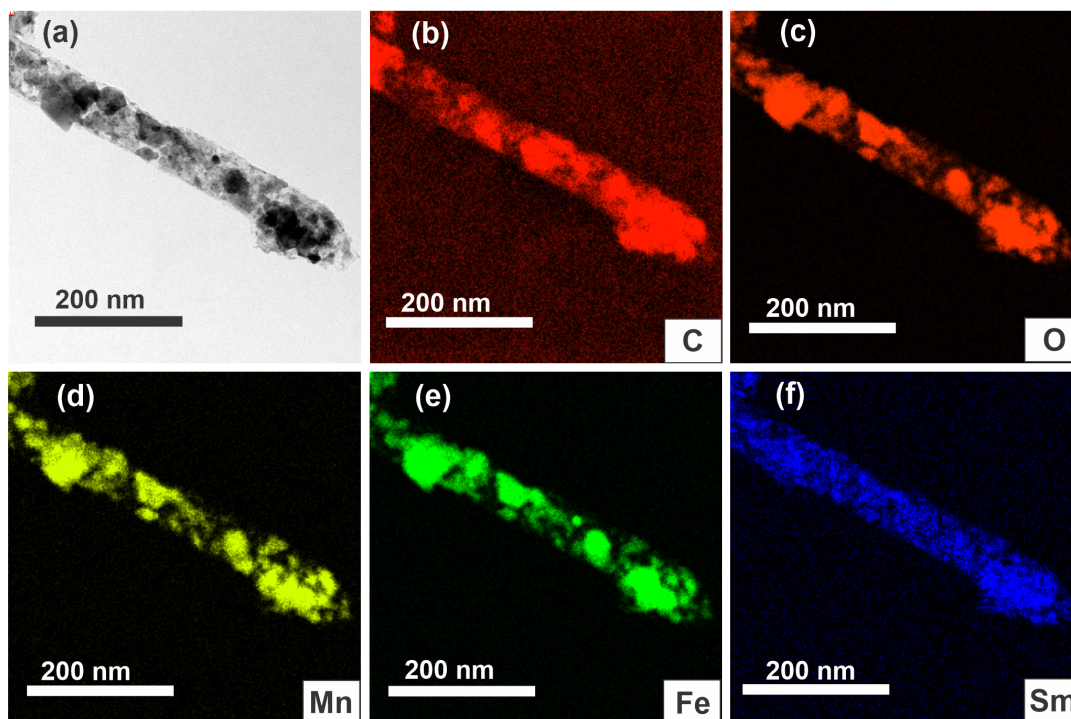
FIGURE 7.10: MnFe$_{2-x}$Sm$_x$O$_4$ nanofibers with x=0.1 (a) Image used for the maps, (b) Carbon map (red) (c) Oxygen map (orange), (d) Manganese map (yellow), (e) Iron map (green), and (f) Samarium map (blue)

STEM maps for the x=0.2 doped MnFe$_{2-x}$Sm$_x$O$_4$ are shown in the Figure 7.11. The first image in Figure 7.11 (a) was a reference TEM image showing a single nanofiber that contained small nanoparticles. This image has also shown the damage to the grid containing the sample due to high-intensity TEM beam exposure at high resolution (50 nm scale bar). Due to the damage in the carbon-coated copper grid containing the sample, the carbon map did not appear clear in Figure 7.11 (b) but it can be seen that carbon is present in the nanofiber. Figure 7.11 (c) showed the oxygen map and more concentrated oxygen was found in areas where nanoparticles were present. Figures 7.11 (d) and 7.11 (e) show the manganese and iron maps. Unlike the above two samples, there was a uniform distribution of both elements within the nanoparticles and no manganese or iron-rich nanoparticle was observed. The samarium map in Figure 7.11 (f) was also consistent with the uniform distribution of samarium in the nanoparticles, with iron and manganese, and no excess samarium was observed. These results were different than what was observed at low fractions of x≤0.1.
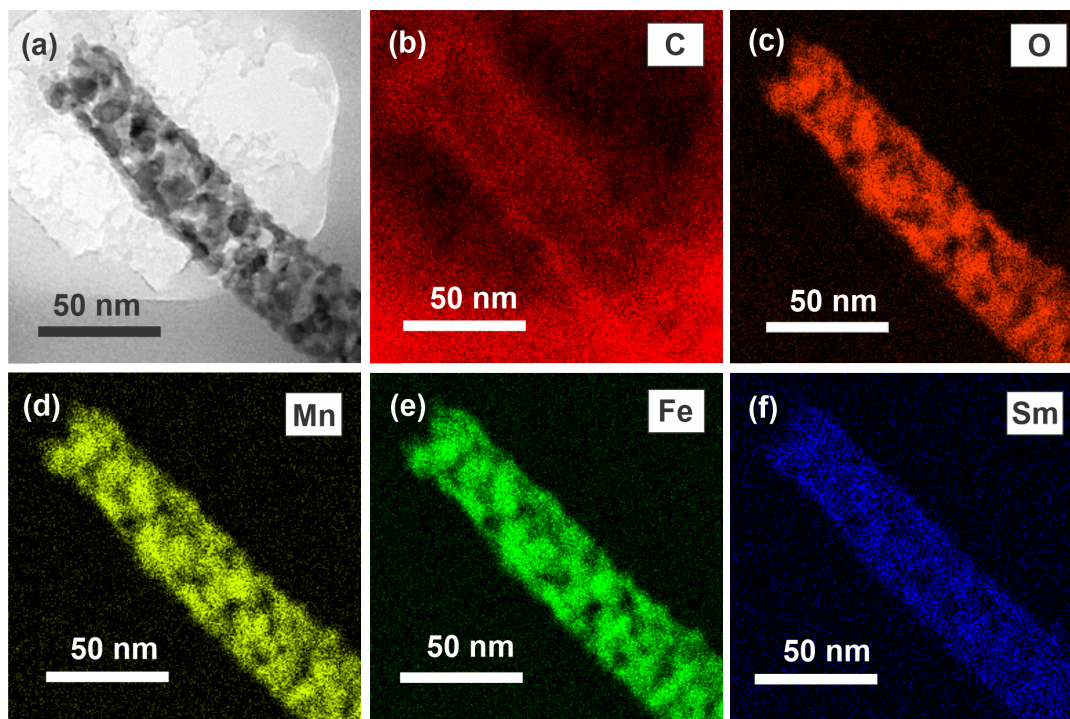
FIGURE 7.11: $MnFe_{2-x}Sm_xO_4$ nanofibers with x=0.2 (a) Image used for the maps, (b) Carbon map (red) (c) Oxygen map (orange), (d) Manganese map (yellow), (e) Iron map (green), and (f) Samarium map (blue)

STEM maps for the x=0.25 doped $MnFe_{2-x}Sm_xO_4$ nanofibers are shown in the Figure 7.12. Figure 7.12 (a) showed the reference image used for the STEM mapping. This image was taken from the dark field detector, where the crystalline nanofibers appeared bright on the dark background. The large nanocrystals appeared to be denser due to the high electron density of these nanocrystals. The carbon map in Figure 7.12 (b) showed the in-homogeneity in carbon distribution and it was more intense in some areas than others. Figure 7.12 (c) showed the oxygen map and it can be seen that oxygen was present within all parts of these nanofibers, but it was more intense in areas containing large nanocrytsals. The next two images in Figure 7.12 (d) and 7.12 (e) showed the manganese and iron maps for x=0.25 nanofibers, both these maps correlated with each other showing the presence of iron and manganese in the nanofibers with more intensity in the large nanocrystals. Figure 7.12 (f) showed the STEM map for samarium and it can be seen that samarium was present in all parts of these nanofibers.
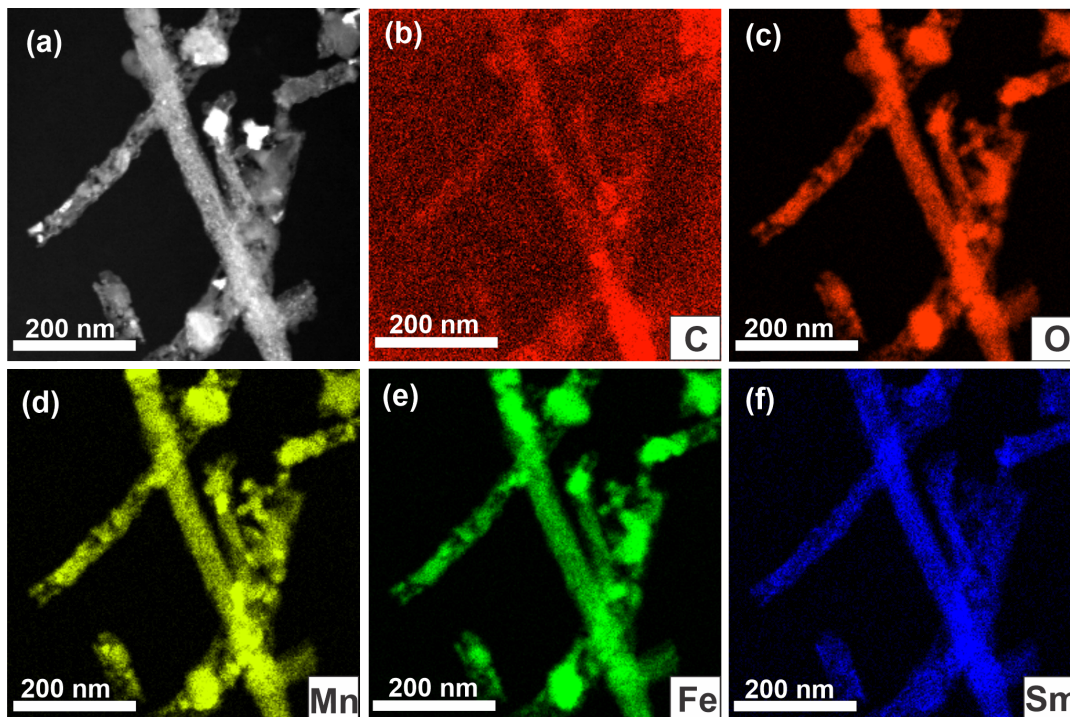
FIGURE 7.12: MnFe$_{2-x}$Sm$_x$O$_4$ nanofibers with x=0.2 (a) Image used for the maps, (b) Carbon map (red) (c) Oxygen map (orange), (d) Manganese map (yellow), (e) Iron map (green), and (f) Samarium map (blue)

7.3.6 SAED analysis

The SAED analysis for all four samples of MnSm$_x$Fe$_{2-x}$O$_4$ with x= 0.06, 0.1, 0.2, and 0.25 are shown in the Figure 7.13 (a) to (d). All the six major diffraction rings were indexed to the cubic phase of MnFe$_2$O$_4$ from reference no 04-016-1572 with miller indexes (220), (311), (400), (511), (440), and (533). The presence of sharp bright spots over diffused rings is attributed to the presence of both large nanocrystals and small nanoparticles that are more clear for x= 0.06 in Figure 7.13 (a) and for x= 0.1 in Figure denser(b). Whereas, bright spots are less sharp for x= 0.2 in Figure 7.13 (c) for x= 0.25 in Figure 7.13 (b) due to the presence of more smaller nanoparticles within MnSm$_x$Fe$_{2-x}$O$_4$ nanofibers.
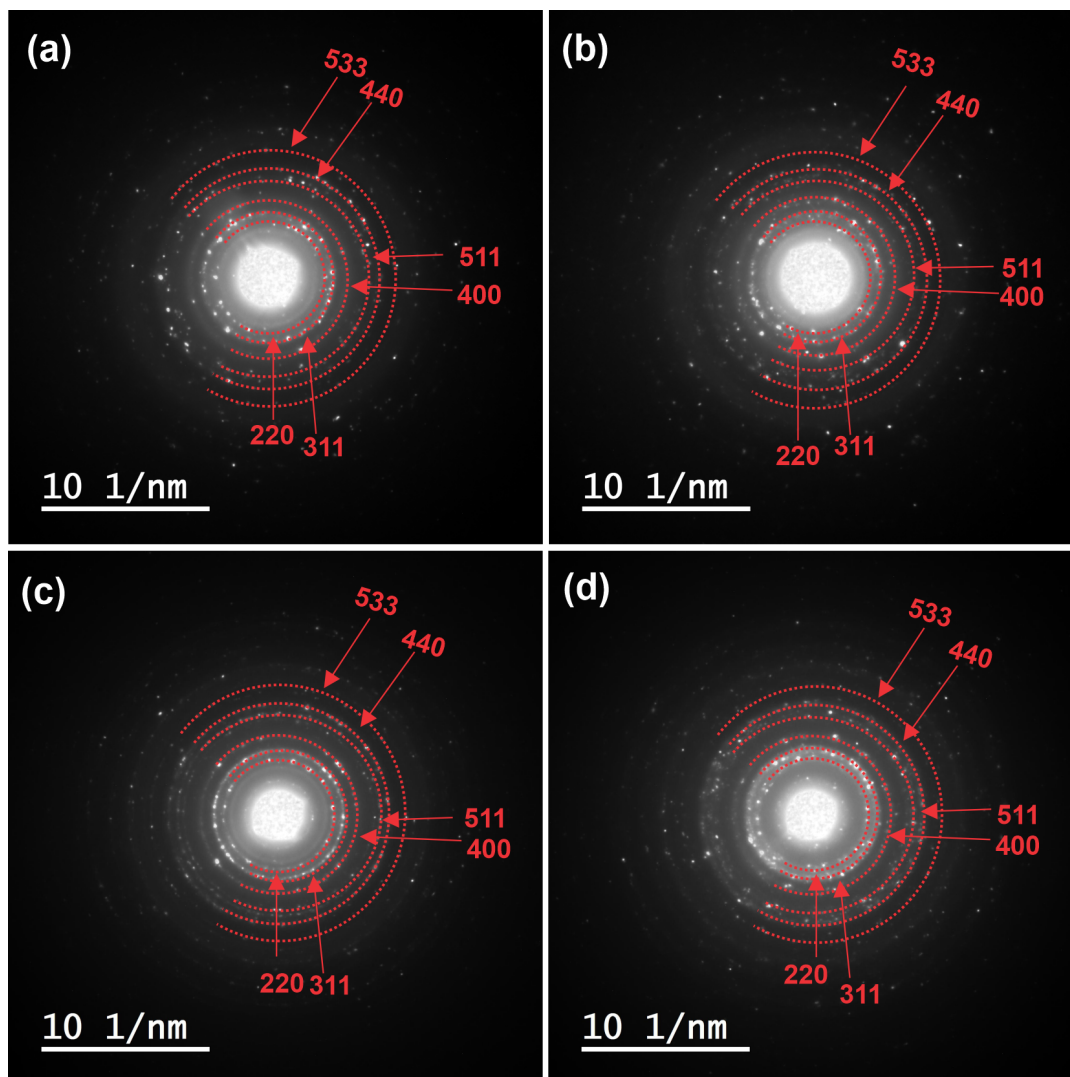
FIGURE 7.13: SAED patterns for MnFeSm$_x$Fe$_{2-x}$O$_4$ nanofibers with (a) x= 0.06, (b) x= 0.1, (c) x= 0.2, and (d) x= 0.25. Dashed circles are from the d-spacings from reference pattern no. 04-016-1572.

The values for the lattice parameters are calculated from these images as well as from other areas of the samples and the mean values with standard deviation are given below in the Table 7.5 given below.

x	Lattice parameters (Å)
0 (MN-620°C)	8.47 ± 0.05
0.06	8.43 ± 0.04
0.1	8.42 ± 0.06
0.2	8.39 ±0.01
0.25	8.39 ± 0.02

TABLE 7.3: Lattice parameters for MnSm$_x$Fe$_{2-x}$O$_4$ with varying x

The values for the lattice parameters for $MnFe_{2-x}Sm_xO_4$ samples were in a similar range with increasing x (within experimental uncertainty). However, with an increase in x to x=0.2 and x=0.25, the lattice parameter values were decreased when compared to the undoped sample x=0. It suggested the contraction of the crystal lattice at high fractions of x. This is interesting because Sm^{3+} has large ionic radii than Fe^{3+} and the decrease in the lattice parameter suggested some sort of strain and disorder in the crystal structure.

7.3.7 XRD analysis

The XRD patterns for $MnSm_xFe_{2-x}O_4$ nanofibers with varying x from 0.06 to 0.25 are shown in the Figure 7.14 below. All of these obtained samples with varying x were compared to the un-doped MN-620°C nanofibers (shown by the black patterns). The XRD patterns for these samples were successfully indexed to the FCC cubic phase of $MnFe_2O_4$ with Fd-3m space group (reference pattern no 04-016-1575 shown in the pattern as purple bars). Contrary to the STEM maps, all the samples with x<0.25 have shown no impurity peaks within the sample which suggested that the fraction of excess Sm^{3+} was very small. Hence, no secondary phases were observed in the XRD spectra for the samples having x<0.25. When x is increased to 0.25, the presence of some impurity peaks was observed within the sample (diamond symbol). These are indexed to the Sm/SmO based secondary phases within the sample. An extra peak from the carbon is also shown in the XRD pattern (shown as an asterix) which is indexed to the graphitic carbon with the reference pattern no 01-073-5918.
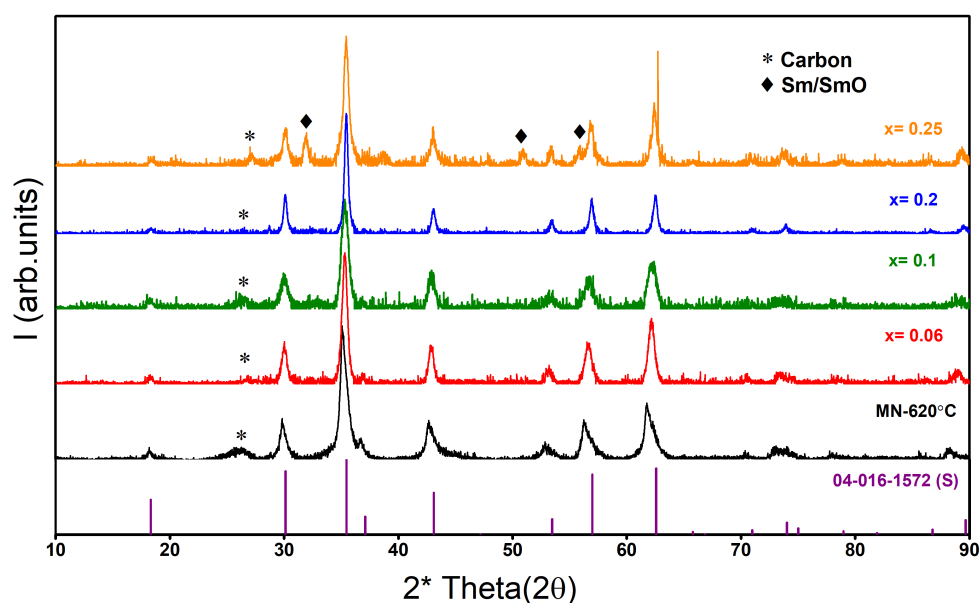
FIGURE 7.14: XRD of $MnSm_xFe_{2-x}O_4$ nanofibers with $MnFe_2O_4$ reference pattern no. 04-016-1572 (star-quality used to indexed samples), MN-620°C (black pattern) as a reference from previous chapter, x= 0.06 (red pattern), x= 0.1 (green pattern), x= 0.2 (blue pattern), x= 0.25 (orange pattern)

The high-intensity peak (311) was used to calculate the Scherrer sizes for all the samples as per shown in Figure 7.15 (a). The Scherrer size did not change at the lower fractions of x (x= 0.06, 0.1), but increased for x=0.2 and x=0.25, when compared with the TEM images shown there were smaller nanoparticles of <10 nm and larger around 20-25 nanometers (Figure 7.8). Therefore, the mean size is dominated by the

large nanoparticles from these XRD patterns. The values for the Scherrer size are given in Table 7.4.
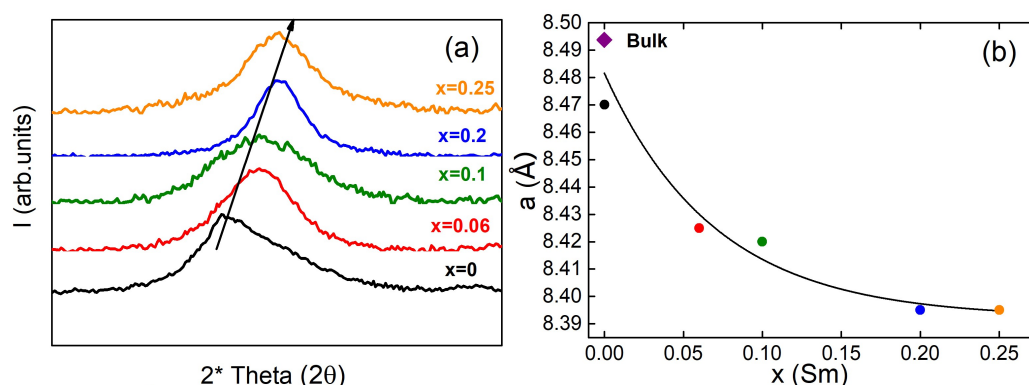
FIGURE 7.15: (a) Effect of Sm doping at 2θ ($35°$) peak shift (b) Lattice parameters shift with increasing Sm^{3+} fraction with purple diamond symbol showing the bulk value of $MnFe_2O_4$ and black for x=0, red for x= 0.06, green for x= 0.1, blue for x= 0.2, and orange for x= 0.25 of Sm^{3+} doped $MnFe_{2-x}Sm_xO_4$ nanofibers

The expanded intense peak at $35°$ (2θ) in Figure 7.15 (a) show that by increasing x, the peaks were shifted to the higher angle which results in a decrease in the lattice parameters (a) with increasing x (Figure 7.15 (b)). The systematic decrease in the lattice parameter showed the successful incorporation of Sm^{3+} in the crystal lattice with increasing x from x=0.06 to x=0.2 and with no impurity peaks. A further increase in the x=0.25 led to the formation of secondary phases (shown as a diamond symbol) where the redundant Sm3+ ions segregate on the grain boundaries and form some secondary phases. The values of lattice parameters are shown in the Table 7.4. This behavior is unusual when a large ionic radii 0.964Å of Sm^{3+} (x) replaces the small ionic radii 0.645Å of Fe^{3+} ions in the crystal lattice. This behavior is also reported in the previous literature, where the large ionic radii of doping cations with R(Sm, Gd, Eu, and La) causes the strain/defects in the ferrite crystal structure and lattice parameter decrease due to the strain compensation, and the redistribution of the cations between the tetrahedral and octahedral sites. ([190–192] Another report on the rare earth ions (Dy, Gd, and Sm) doped $MnCr_{0.5}R_{0.02}Fe_{1.48}O_4$ showed the decrease in the lattice parameters with increasing size for dopant ion. This happened due to an induced microstrain in the crystal structure. [193] The decrease in the lattice parameters in this study can be explained by the crystal structure for $MnFe_2O_4$. At high temperatures, $MnFe_2O_4$ crystallizes in partial inverse spinel crystal structure, where up to 20% of Mn ions can migrate to the octahedral sites as shown by the formula $(Mn_{1-x}Fe_x)[Mn_xFe_{2-x}]O_4$ (parentheses show the tetrahedral sites and square brackets show the octahedral sites). Since EDS spectrum showed the formation of manganese-rich material, which increases the migration of Mn^{2+} from the tetrahedral sites to the octahedral sites (Mn^{3+}). This means the compression in the crystal lattice can be explained by the following possibilities,

1. Redistribution of metal ions between tetrahedral and octahedral sites due to strain in the crystal lattice.

2. Point defects in crystal structure due to ionic vacancies, i.e. O^{2-}/Fe^{2+}.

3. Shift from the low spin configurations to the high spin configuration of metal ions for strain compensation.

The large ionic radii Sm^{3+} have more tendency to occupy the octahedral sites that can substitute either Mn^{3+} or Fe^{3+} ions on the octahedral sites (B) due to the same ionic radii 0.645 Å. The substitution of Sm^{3+} at the octahedral sites induces strain in the crystal lattice on the octahedral sites. This can cause the migration of some Mn^{2+} ion with large ionic radii 0.66 Å from the tetrahedral sites to the small ionic radii 0.645 Å Mn^{3+} ions at the octahedral sites. This migration is also accompanied by the migration of some Fe^{3+} from the octahedral sites to the tetrahedral sites (Fe^{2+}). However, the redistribution of both charges is a complicated phenomenon that requires further analysis, for example, XPS or Mössbauer spectroscopy for clearer understanding.

The substitution of large ionic radii Sm^{3+} can also create point defects due to oxygen deficiencies that can lead to Fe^{2+} vacancies due to charge balance. This can also cause compression in the crystal lattice and decrease lattice parameters. However, further studies, for example, X-ray synchrotron are required for justification.

Another important idea is the potential of Sm^{3+} ions to shift the ions (Fe^{3+} ions or Mn^{2+} ions) at the octahedral sites from high spin configurations to the low spin configurations. As the ionic radii are larger for both ions in high spin configuration than in low spin configuration to compensate for the expansion caused by the Sm^{3+} ions at the octahedral sites. This can cause the compression of the crystal lattice and decreases the lattice parameters. However, this can only be proved by some more analysis from the Mössbeur spectroscopy to support this hypothesis.

x (Sm^{3+})	Lattice parameter (a) Å	Scherrer size (nm)
0	8.475 ± 0.001	14
0.06	8.430 ± 0.002	16
0.1	8.425 ± 0.002	15
0.2	8.395 ± 0.002	29
0.25	8.395 ± 0.001	23

TABLE 7.4: The values for lattice parameters and average Scherrer size from (311)

7.3.8 Magnetic studies

The magnetic studies for all the Sm^{3+} doped samples are given in the Figure 7.16 below. The first two plots in Figure (7.16 (a) and 7.16 (b) show the magnetization plots and the respective hysteresis against the applied magnetic field (6T) at 5K. Whereas, the other two plots in Figure 7.16 (c) and 7.16 (d) show the magnetization plots and respective hysteresis at 300K. It can be seen that there is a slight increase in the magnetization (36.5 emu/g to 46 emu/g) with first doping of $MnFe_{2-x}Sm_xO_4$ at x=0.06. The increase in magnetization can be explained by the rearrangement of ions at the tetrahedral and octahedral sites due to strain compensation, which increases the exchange interactions at the octahedral sites to increase magnetization. Further increase in x$\leq$0.2 decreases the M_s this can happen due to various reasons:

1. Increasing Sm^{3+} ion substitution that can break/change exchange pathways.

2. Shift from the high spin Fe^{3+} ions with large ionic radius 0.645 Å to the low spin Fe^{3+} with small ionic radius 0.55 Å to compensate the crystal distortions on octahedral sites.

The substitution of Fe^{3+} ions with Sm^{3+} ion in the crystal lattice decreases the magnetization, as Sm^{3+} has a low magnetic moment (1.5 μ_B) as compared to Fe^{3+} (5 μ_B) or Mn^{3+} (4 μ_B). This is because the super-exchange interaction at the tetrahedral sites between Fe^{3+}-Fe^{3+} decreases to affect the overall magnetization. The effect of Sm^{3+} substitution can also change/break the exchange pathways due to the migration of ions between tetrahedral and octahedral sites, an increased disorder in the crystal lattice, or due to the point defects in the crystal lattice (O^{2-} or Fe^{3+} vacancies). The magnetic dipoles originating from the 4f orbitals from the Sm^{3+} ions do not have strong interactions with the neighboring 3d orbital dipoles of Fe^{3+} ions at octahedral sites and with the Mn^{2+} ions at A-sites. They behave as paramagnetic-like defects atoms at octahedral sites reducing the M_s value. This behavior is commonly seen in the previous reports on the Sm^{3+} doped ferrites. [192–194] Another important reason could be the shift of Fe^{3+} ions from high spin (ionic radius 0.645 Å) to the low spin (0.55 Å) to compensate the strain in crystal lattice at high Sm^{3+} fractions. The magnetic moment of the high spin Fe^{3+} ion is 5 μ_B due to unpaired electrons in the 3d orbitals whereas the magnetic moment of low spin Fe^{3+} is only 1 μ_B, which causes the reduction in the overall magnetization. A further increase in x=0.25 causes an increase in the saturation magnetization, which can be attributed to the formation of some secondary phases as can be seen from the XRD (7.14) which has contributed to the overall M_s value. However, this is all very complicated and needs further investigation by Mössbauer spectroscopy for this behavior. The values for the magnetization and coercivity are given in the Table. 7.5 below.
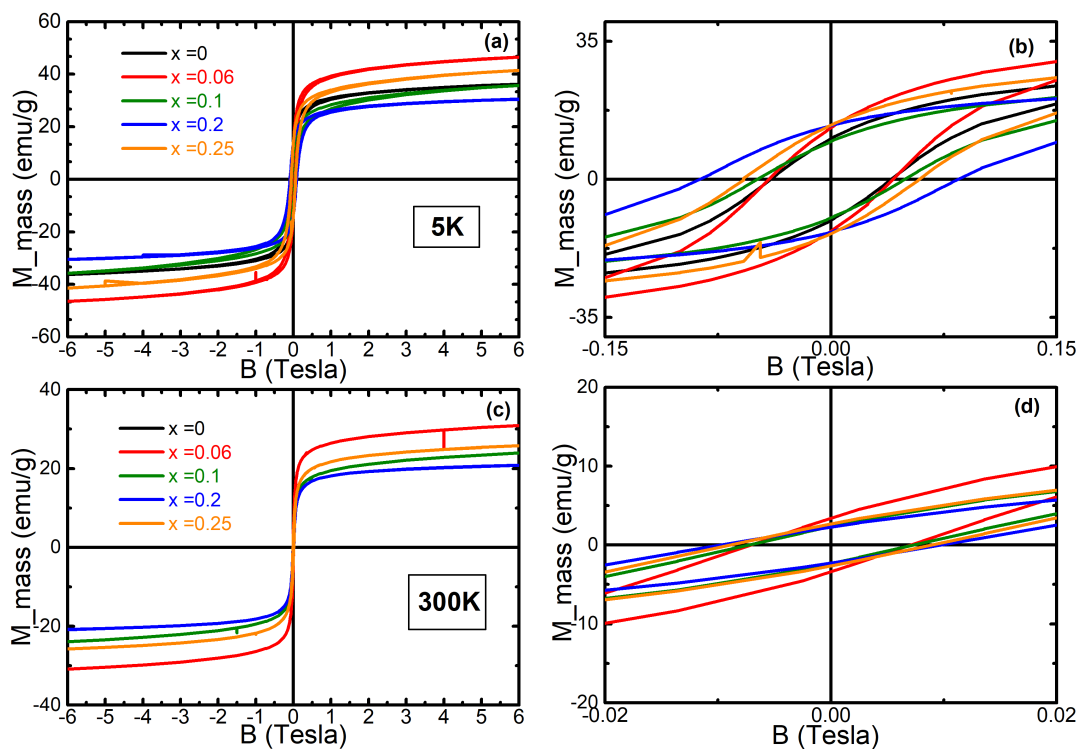
FIGURE 7.16: (a) Magnetization plots for $MnSm_xFe_{2-x}O_4$ with x=0 (black), x=0.06 (red), x=0.1 (green), x=0.2 (blue), and x=0.25 (orange) at 5K (b) Magnetization plotted at the smaller range of applied magnetic field at 5K (c) Magnetization plots for $MnSm_xFe_{2-x}O_4$ at 300K (d) Magnetization plotted at the smaller range of applied magnetic field at 300K

The magnetization plots at the small field region are plotted at 5K and at 300K in the Figure 7.16 (b) and Figure 7.16(d) and show the coercivity is small for all Sm^{3+} doped samples at room temperature. The values of coercivity from the Table 7.5 showed the soft nature of all these Sm^{3+} doped samples. There was only a small increase in the coercivity value with increasing x fraction which could be due to the lattice strain with Sm^{3+} doping and the presence of spin-disordered component within $MnFe_{2-x}Sm_xO_4$ samples. 7.6

2K		
x	Magnetization (M) (emu/g)	Coercivity (H_c) (mT)
0	37	42
0.06	47	45
0.1	36	53
0.2	31	85
0.25	44	68
300K		
0	24	5.4
0.06	31	7
0.1	24	7.1
0.2	21	10
0.25	26	9

TABLE 7.5: Saturation magnetization from the MnSm$_x$Fe$_{2-x}$O4 nanofibers with varying x at lowest temperature (2K) and at room temperature (300K)

The main plots in Figure 7.17 show the temperature dependence magnetization at 6T. These magnetization plots were fitted with the n=1.5 to compare with the un-doped MnFe$_2$O$_4$ nanofibers (MN-620°C). It can be seen that all the x doped MnFe$_{2-x}$Sm$_x$O$_4$ samples have shown a departure in the saturation magnetization at low temperatures from Bloch's temperature dependence. This was very prominent for the x=0.25, where deviation from Bloch's temperature dependence is more prominent with the upturn at a lower temperature. The departure at low temperatures showed the presence of spin-disordered shells in all these samples, which is large for x=0.25. This showed that there was an increase in the spin disorder with increasing x. This could happen due to the presence of excess redundant samarium that gets oxidised and forms secondary phases at the high fraction of x. The fitted parameters of phenomenological equation (2.27) are shown in Table 7.6. It can be seen that the β values for all these samples are comparable to the undoped sample (5.92×10^{-5}) and in range with the bulk (6.33×10^{-5}). The values for spin freezing temperature for the x$\leq$0.25 are also comparable to the T$_F$=43K of the undoped sample for x$\leq$0.2, but T$_F$=32 for x=0.25 is observed. The decreased value at high fractions of x could be due to the fittings from the missing data points that came from the O$_2$ noise.

The upper right insets in Figure 7.17 showed the ZFC-FC curves for the x doped MnFe$_{2-x}$Sm$_x$O$_4$ samples. Similar to the undoped MnFe$_2$O$_4$ nanofibers (MN-620°C) at x=0, there was no evidence of superparamagnetism at low fractions of x=0.06-0.1
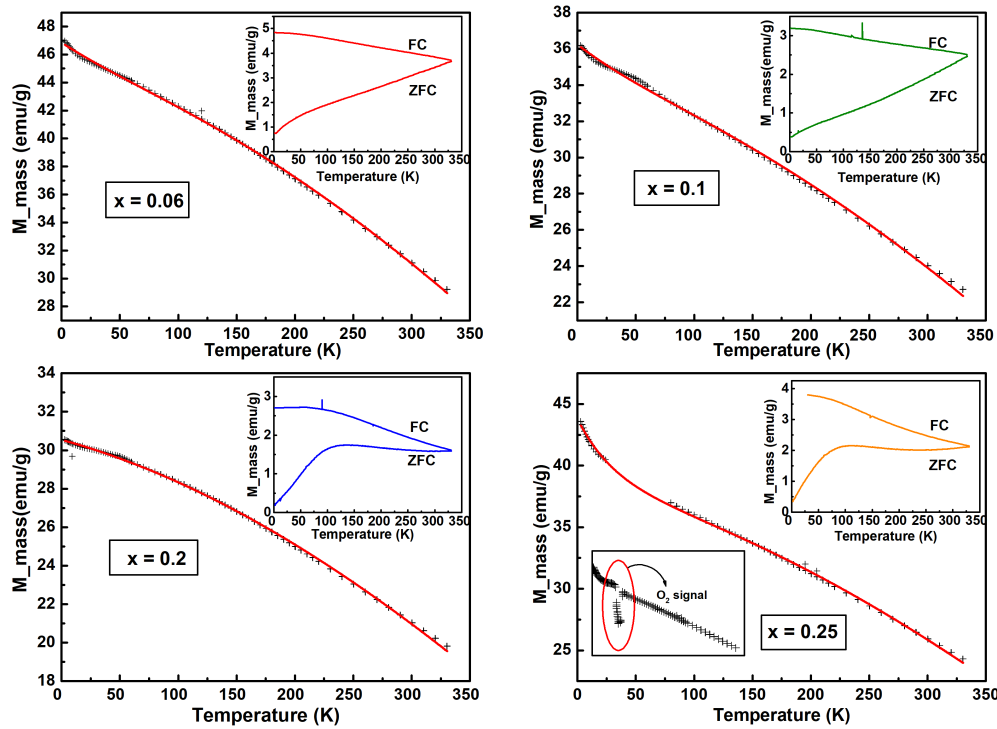
FIGURE 7.17: Temperature dependent magnetization plots fitted with the phenomenological equation with n=1.5 for (a) x= 0.06. Upper right inset: ZFC-FC curve for x=0.06 at 6 mT. (b) x= 0.1. Upper right inset: ZFC-FC plot for x= 0.1 at 6 mT. (c) x= 0.2. Upper right inset: ZFC-FC plot for x= 0.2 at 6 mT. (d) x= 0.25. Upper right inset: ZFC-FC plot for x= 0.25 at 6 mT. Lower left inset: Plot showing the signal from some O_2 phase at low temperature[195]

Sample	$M_{s,c}$(6T, 0K) (emu/g)	$M_{s,d}$(6T,0K) (emu/g)	n	β(K$^{3/2}$)	T_f(K)
x=0.06	44	2	1.5	5.8×10^{-5}	48
x=0.1	34	2	1.5	6.7×10^{-5}	49
x=0.2	33	0.5	1.5	5.1×10^{-5}	45
x=0.25	38	6	1.5	6×10^{-5}	32

TABLE 7.6: Magnetization parameters from the phenomenological equation with n=1.5

due to the presence of more large sized nanocrystals in these nanofibers from the TEM images 7.7. The average crystallite sizes from the XRD (15-16 nm) were also large to be superparamagnetic for these nanofibers. When x was further increased to x≤0.25, the FC-ZFC curve have shown a shift towards superparamagnetic behavior with the T_B= 105 K for x=0.2, and 90K for x=0.25, and both curves overlapped above the room temperature. This is in agreement with the TEM images for both these x≤0.25 nanofibers in Figure 7.8 which showed the formation of both smaller nanoparticles with large nanocrystals. These large nanocrystals were the reason for this residual coercivity from the FC-ZFC plots and also dominate the Scherrer sizes given from the XRD spectra.

7.4 Summary

In this chapter, Sm^{3+} doped $MnFe_{2-x}Sm_xO_4$ nanofibers were prepared to study their structural and magnetic properties at an increasing fraction of x from x=0.06 to x=0.25. All of these samples were synthesized by using the previously developed method for $MnFe_2O_4$ nanofibers (MN-620°C) in chapter 6, which is used as undoped reference material (x=0) to compare with the x doped $MnFe_{2-x}Sm_xO_4$ nanofibers. These nanofibers have shown the formation of thin width $MnFe_{2-x}Sm_xO_4$ nanofibers at all fractions. EDS analysis for all these samples has shown the formation of manganese-rich material where the atomic percentage varied between 38-40 %. Similar to x=0, the formation of both variable-sized nanoparticles was observed at low fractions (x=0.06, x=0.1). This was different at high fractions of x=0.2-0.25, where the formation of more smaller-sized nanoparticles was seen.

STEM maps showed the uniform distribution for samarium at all fractions of x and even there was no sedimentation of samarium at the highest fraction of x=0.25 within these nanofibers. All these samples $MnFe_{1-x}Sm_xO_4$ were indexed to the FCC cubic phase of $MnFe_2O_4$ with no impurity peaks for samples x=0.06-0.2 in the XRD pattern but impurity peaks from some secondary phases of Sm^{3+} were observed for x=0.25. The Scherrer size was increased and lattice parameters were decreased with increasing x. This could happen due to the very complex nature of factors including the redistribution of cations to compensate the lattice strain, points defects in the crystal lattice, and change in spin configurations.

The magnetic analysis showed that there was a slight increase in the magnetic moment from x=0 to x=0.06, which could happen in a result of the redistribution of cations at octahedral and tetrahedral sites at low fractions. When x is increased from x= 0.1 to x=0.2, magnetic moment decreases due to the incorporation of Sm^{3+} ions in the crystal lattice that affects/breaks the exchange pathways between metal cations, or the shift from high spin metal cations to low spin metal cations to compensate the crystal strain. However, a detailed analysis comprising XPS, Mössbauer spectroscopy, and X-ray synchrotron spectroscopy measurements are further required to fully understand this behavior. Further increase in x=0.25 again increases the magnetic moment which is attributed to the formation of secondary phases due to the segregation of samarium ions. Similar to x=0, at low fractions, x=0.06-0.1, no evidence of superparamagnetic behavior was observed for $MnFe_{2-x}Sm_xO_4$ nanofibers, but increasing x to x=0.2-0.25 have shown a shift towards superparamagnetic behavior. This showed that increasing x=0.2-0.25 resulted in the formation of small-sized nanoparticles that were small enough to be superparamagnetic, but the residual coercivity in ZFC-FC curves is attributed to the range in particle sizes. All these samples have shown low coercivity highlighting the soft nature of these x doped $MnFe_{2-x}Sm_xO_4$ nanofibers.

7.5   Future work

1. Further studies including the XPS analysis and Mössbauer spectroscopy to investigate the presence of cations at octahedral and tetrahedral sites.

2. X-ray synchrotron spectroscopy measurements to understand the point defects in the crystal structure within samples.

3. Preparation and characterization of $MnFe_2O_4$ nanofibers doped with the rare earth ions having high magnetic moments (Er^{3+}, Dy^{3+}, Gd^{3+}) to improve their magnetic properties.

4. Preparation of other soft metal ferrite nanofibers ($NiFe_2O_4$, $MnZnFe_2O_4$) and doping them with various rare earth ions to study their structural and magnetic properties.

Preface

The next chapter first describes a brief summary of wireless charging and the importance of prepared nanofibers from chapter 2. Next, it describes the key results obtained from the results in chapters 4-7. In the end, it highlights the proposed objectives and successfully achieved outcomes from this study.

Chapter 8

Conclusions

This thesis reports the exploration and fabrication of electrospun magnetic nanofibers in thin nanodimensions for their potential applications in wireless charging systems. The main objectives of this study was to prepare nanomaterials and analyze their structural, and magnetic properties in comparison to their bulk counterparts. The main magnetic materials of interest for this research were bimetallic $Ni_{1-x}Fe_x$, semiconducting $MnFe_2O_4$, and $MnFe_{2-x}Sm_xO_4$. An electrospinning method was used to prepare these metallic and semiconducting magnetic nanofibrous sheets that are thermally processed at optimised temperature profiles to achieve the desired products. These nanofibers were studied in greater detail to comprehend their structural and magnetic properties at various parameters.

Bimetallic $Ni_{1-x}Fe_x$ nanofibrous sheets at varying x from x~0.1 to x~0.5 were prepared for the first time and their structural and magnetic properties were studied. The synthesis of $Ni_{1-x}Fe_x$ nanofibers at low fractions of x was interesting as bulk material shows high permeability at x=0.18-0.25 but it shows high saturation moment at x~0.5. This intriguing behavior provides a range in x to explore the synthesis of electrospun $Ni_{1-x}Fe_x$ nanofibers. Bulk $MnFe_2O_4$ is a well-known soft-magnetic material for inductive applications. $MnFe_2O_4$ nanofibrous thin sheets were made for their potential reduction in eddy-current losses and for flux-guiding applications in thin nanodimensions. The effect of rare earth ion Sm^{3+} doping in $MnFe_{2-x}Sm_xO_4$ nanofibers were also studied to see how it can affect the structural characteristics and the magnetic response when x was varied. This was important as it has not been reported before in the previous literature. It was expected that it can change the magnetic properties by changing the occupancy of ions at the tetrahedral and octahedral sites in $MnFe_2O_4$.

Chapter 4 presented the comprehensive results from the electrospun $Ni_{1-x}Fe_x$ nanofibers at varying fractions of x starting from the low fraction from x~0.1 to x~0.2. Both electrospun nanofiber sheets were thermally processed by using a three-step temperature profile in the presence of an inert atmosphere followed by a reduction in the presence of 5% H_2/95% Ar gas at high temperature (620°C). The thermal degradation studies (TGA/DSC) on both samples supported the thermal processing profiles used to process the nanofibers to obtain the final product. The nanofiber sheets showed thin widths and contained $Ni_{1-x}Fe_x$ nanoparticles for both fractions

of x. A prominent bimodal particle size distribution was observed at x~0.1 with the presence of large surfaced $Ni_{1-x}Fe_x$ nanoparticles (35 nm) and smaller embedded nanoparticles (5 nm) within the nanofibers due to the high diffusivities of both ions at the surface. The fraction of large nanoparticles was significantly reduced when x was increased to x~0.2, where a skewed particle size distribution was observed towards larger nanopartciles (10-18 nm) with larger fractions of small-sized nanoparticles (5 nm). This could happen due to the presence of a more favorable fraction of x that can lead to the formation of more nucleation centers at minimal enthalpy change. Both fractions of $Ni_{1-x}Fe_x$ nanofibers have shown the FCC crystalline phase of $Ni_{1-x}Fe_x$ and some residual PVP fragments peaks in the XRD data. The saturation magnetization was increased from 46% to 72% of the bulk value with increasing x. A small spin-disordered component (2%) that could be from the spin-disordered shell was observed for both fractions of x. An exchange bias was observed at x~0.2 due to the interface interactions between the spin-disordered shell and magnetically ordered core. The differential susceptibility was increased from 6 to 11 by increasing x from x~0.1 to x~0.2. No evidence of superparamagnetism was found in these nanofibers due to the fraction of large-sized nanoparticles that dominated the ZFC-FC curves.

Chapter 5 reported the fabrication of electrospun x~0.5 nanofibers made by an alternative method. The effect of different solvents was studied for the preparation of x~0.5 nanofibers; first by using 100% DMF and others by using a mixture of solvents methanol: DMF (20%:80% and 50%:50%). DMF-based nanofibers showed thinner nanofibers when compared to the x~0.1 and x~0.2 nanofibers. The reason for such behavior is attributed to the more compatible Hansen's solubility parameters by using DMF than methanol as a solvent. These nanofibers contained predominantly small 5 nm nanoparticles, and some slightly larger nanoparticles (8-13 nm) were also present. Similar to x~0.1 and x~0.2, these x~0.5 nanofibers were indexed to FCC crystal structure of $Ni_{1-x}Fe_x$ but only one residual carbon peak from the polymer PVP fragment was observed in their XRD data. This suggested that the degradation pathway differs in a different solvent when DMF was used for x~0.5 than methanol which is used for x~0.1-0.2. The saturation magnetization at this fraction of x~0.5 was increased to 82% of the total bulk value. These nanofibers showed superparamagnetic behaviour with the blocking temperature, T_B=~125K. There was a remarkable increase in the differential susceptibility to 18 with increasing x~0.5. 20%:80% methanol: DMF solvent-based nanofibers showed thin nanofibers containing large $Ni_{1-x}Fe_x$ nanoparticles. Unlike DMF-based nanofibers, large polycrystalline nanoparticles (30-40 nm) were present in these nanofibers. The $Ni_{1-x}Fe_x$ nanoparticles in these nanofibers were indexed to the FCC crystal phase but the peaks from the PVP fragments were similar to what obtained for x~0.1 and x~0.2 nanofibers. This suggested that a small fraction of methanol can affect the degradation pathway for the PVP degradation at high temperatures. The high field magnetization for this sample was decreased to only 24% of the bulk sample which

showed that the methanol is not suitable for the formation of high-quality $Ni_{1-x}Fe_x$ nanofibers at x∼0.5. The method with 50%:50% methanol: DMF did not produce any isolated nanofibers, and therefore no results were produced for this mixture. This study showed that only 100% DMF gives the high-quality reproducible nanofibers.

Chapter 6 presented the results from the electrospun $MnFe_2O_4$ nanofibers. These nanofibers were thermally processed in different atmospheres, and the ideal processing environment was heating the samples first in presence of argon and then turning off argon gas at high temperatures to allow leak-in air for oxidation of the samples. This step was important as argon was found insufficiently oxidizing due to less oxygen, and the air was too oxidizing due to the high percentage of oxygen. The two best temperature profiles were selected to produce $MnFe_2O_4$ nanofibers, i.e. 700° (MN-700°C) and 620°C (MN-700°C). MN-700°C nanofibers showed the presence of large polycrystalline nanoparticles on the surface but there were also some single crystal rods in the sample. MN-620°C nanofibers contained small $MnFe_2O_4$ nanoparticles in the nanofibers as well as large single crystals. Both samples were indexed to the FCC phase of the $MnFe_2O_4$. The high field saturation magnetization was decreased to 57% for MN-700°C and 46% for MN-620°C when compared to the bulk. This could happen due to the anti-site disorder in the $MnFe_2O_4$ nanoparticles. There was no evidence of superparamagnetism in these nanofibers due to the presence of larger nanocrystals in these nanofibers. A sample processed at 620°C showed the complete formation of single crystal nanorods and the high field saturation magnetization for this sample was increased to 76% of the bulk. This could happen due to the variability of oxygen partial pressure during the thermal processing of $MnFe_2O_4$ nanofibers. This result was very interesting as it can lead to the potential fabrication of single crystal nanorods that may be suitable for flux-guiding applications.

Chapter 7 presented the results from a study of Sm^{3+} doped $MnFe_{2-x}Sm_xO_4$ nanofibers prepared at 620°C with increasing fractions of x from 0.06-0.25. All samples showed the formation of thin nanofibers containing $MnFe_{2-x}Sm_xO_4$ nanoparticles. The increase in x promoted the nucleation of smaller-sized nanoparticles within nanofibers. All samples x≤0.2 showed the successful incorporation of Sm^{3+} in the crystal lattice of $MnFe_2O_4$ but some impurity peaks were observed at x=0.25. There was a systematic decrease in the lattice parameters with increasing x that may be due to the Sm^{3+} induced redistribution of magnetic ions within lattice parameters to compensate for the lattice strain. Another reason could be point defects arising from the O^{2-}/Fe^{2+} vacancies in the crystal lattice due to the charge balancing. The saturation magnetization was increased to 56% at x=0.06 but decreased with further increasing x≤0.2. This could be due to the broken or changed exchange interaction pathways between magnetic ions. It increased further with increasing x=0.25, which could be due to the contribution from the secondary phases from excess Sm^{3+} ion. Superparamagnetism was observed for the high fractions of x=0.2-0.25 due to the formation of smaller nanoparticles with the blocking temperatures, T_B=90-105. This

chapter showed that the Sm^{3+} incorporation can alter the structural properties and cause an enhancement in saturation magnetization at low values of x, and superparamagnetism at larger values of x.

In the introduction, the three main objectives of this study were stated to prepare metallic and semiconductor nanofibers in thin nanodimensions that can potentially be used in wireless charging applications. The first objective was to develop thin sheets of bimetallic $Ni_{1-x}Fe_x$ nanofibers by an electrospinning method and to study their structural and magnetic properties at increasing x~0.1-0.5. This was achieved by the fabrication of $Ni_{1-x}Fe_x$ nanofibers with a modified synthesis method at x=0.1-0.2. An alternative method was developed that produced good quality isolated x~0.5 nanofiber sheets. The differential susceptibility was significantly increased from 6 to 18 for these nanofibers with increasing x from x~0.1 to x~0.5. These results were very encouraging for their potential applications in wireless charging. The second objective was to prepare semiconducting $MnFe_2O_4$ nanofibers and study their structural and magnetic properties. This was achieved where $MnFe_2O_4$ nanofibers were made with different morphologies. The third objective was to synthesize the Sm^{3+} doped $MnFe_{2-x}Sm_xO_4$ nanofibers. It was achieved with the successful incorporation of Sm^{3+} ion in the crystal lattice of $MnFe_2O_4$. This work contains a solid foundation for future studies and investigations related to metallic and nonmetallic materials prepared by the electrospinning method.

Preface

The next chapter explains the potential future direction of this work for further studies.

Chapter 9

Future outlook

The data and discussions throughout this work is encouraging to further study these materials properties regarding the modifications in structural properties and to improve the magnetic properties for the power transfer applications in wireless charging. Some directions of the future work are summarized below.

The $Ni_{1-x}Fe_x$ nanofibers prepared in this work have shown encouraging results with increasing x both for improving the physical properties as well as the magnetic properties. It will be interesting to study the effects of further increasing x to the higher fractions of iron. This is because the bulk $Ni_{1-x}Fe_x$ shows a transition from FCC to BCC transition with x≤0.6 with a high magnetic moment. Therefore, it is remarkably interesting to study; if the structural properties changes at x≥0.6 or the magnetic properties can be tuned further with increasing x. Another important study would be the formation of smaller nanoparticles within these nanofibers to achieve superparamagnetism at high fractions of x as was found at increasing x∼0.5. The superparamagnetic nanoparticles with reasonable susceptibility and decreased coercivity can have potential real-world applications in inductive power systems.

The formation of single crystal $MnFe_2O_4$ nanorods in this study is interesting that warrants further experimental and theoretical analysis. This work has shown a possibility to achieve high purity $MnFe_2O_4$ nanorods, that provided a foundation for another study including a series of experiments at different partial pressure Oxygen/inert gas mixtures. The optimization of oxygen content can lead to reproducible $MnFe_2O_4$ nanorods by the developed method in this study which could lead to high susceptibility due to the shape anisotropy of a nanorod. Another important study would be the exploration of the temperature optimization effects on the nanoparticle's nucleation as well as on the magnetic properties of the samples. The aim would be to develop a temperature profile that can lead to the formation of superparamagnetic nanoparticles with high susceptibilities.

The introduction of Sm^{3+} in the $MnFe_{2-x}Sm_xO_4$ at increasing x=0.06-0.25 established a basis to produce the future nanofibers by using the developed method.

However, the change in the structural and magnetic properties in the crystal lattice by the successful inclusion of Sm^{3+} ions requires undertaking measurements to further understand the crystal structure and the magnetic properties. For example, Mössbauer spectroscopy can be interesting to study the formation of high-spin or low-spin $MnFe_{2-x}Sm_xO_4$ and the anti-site disorder at octahedral and tetrahedral sites. X-ray synchrotron would be effective to study the point defects, i.e., O^{2-} or Fe^{2+} vacancies at Sm^{3+} doping due at Sm^{3+} doping. XPS can also provide information about the oxidation states of Mn^{2+} and Fe^{3+} ions to deduce their locations in the crystal lattice. Another important study would be the inclusion of large ionic radii ions with high magnetic moment ions (RE), i.e., Eu^{3+}, Gd^{3+}, Dy^{3+} in $MnFe_{2-x}RE_xO_4$ nanofibers at various fractions of x to observe the effects in the structural and magnetic properties by using the developed synthesis method.

Appendix A

List of Publications

The list of publications including both published and to be published work during the course of this research is given as follows.

1. Nawaz T, Williams GV, Coles MP, Edgar A, Chong SV. Synthesis of orientated $Ni_{0.89}Fe_{0.11}$/polymer nanofibres with a bimodal nanoparticle size distribution by electrospinning and thermal processing. Materials Today Communications. 2022 Mar 1;30:103120.

2. Nawaz T, Williams GV, Coles MP, Edgar A, Chong SV. Ferromagnetic $Ni_{0.78}Fe_{0.22}$ polymer nanofibers with a sub-11 nm bimodal particle size distribution. draft completed for submission.

3. Nawaz T, Williams GV, Coles MP, Chong SV. Synthesis of novel bimetallic $Ni_{0.5}Fe_{0.5}$ nanofibers with high permeability and small magnetic crystalline anisotropy for potential applications in small electronic devices. draft in progress.

4. Nawaz T, Williams GV, Coles MP, Chong SV. Effect of temperature on the morphology and magnetic properties of electrospun manganese ferrite nanofibers containing graphitic carbon. draft in progress.

5. Nawaz T, Williams GV, Coles MP, Chong SV. A study of Sm^{3+} (x) doping on the morphology and magnetic properties of electrospun $MnFe_{2-x}Sm_xO_4$ nanofibers at an increasing fraction of x=0.06-0.25. draft in progress.

Bibliography

[1] M.G.S. Pearce, G.A. Covic, and J.T. Boys. "Robust ferrite-less double D topology for roadway IPT applications". In: *IEEE Transactions on Power Electronics* 34.7 (2018), pp. 6062–6075.

[2] G.A. Covic and J.T. Boys. "Modern trends in inductive power transfer for transportation applications". In: *IEEE Journal of Emerging and Selected topics in power electronics* 1.1 (2013), pp. 28–41.

[3] R.M. Bozorth. "The permalloy problem". In: *Reviews of Modern Physics* 25.1 (1953), p. 42.

[4] C. Zet and C. Fosalau. "Magnetic nanowire based sensors". In: *Digest Journal of Nanomaterials and Biostructures* 7.1 (2012), pp. 299–306.

[5] V.S. Bhugra, F.R. Hughson, G.V.M. Williams, S.V. Chong, and T. Nann. "Electrospun, oriented, ferromagnetic Ni1-xFex nanofibers". In: *Frontiers in chemistry* 8 (2020), p. 47.

[6] Grant VM Williams, John Kennedy, Peter P Murmu, Sergey Rubanov, and Shen V Chong. "The effect of different Fe concentrations on the structural and magnetic properties of near surface superparamagnetic Ni1- xFex nanoparticles in SiO2 made by dual low energy ion implantation". In: *Journal of Magnetism and Magnetic Materials* 473 (2019), pp. 125–130.

[7] Energy Outlook. "International energy outlook". In: *Outlook* (2010).

[8] A. Jahid, M.S. Hossain, M.K. Hasan Monju, M.F. Rahman, and M. F. Hossain. "Techno-economic and energy efficiency analysis of optimal power supply solutions for green cellular base stations". In: *IEEE Access* 8 (2020), pp. 43776–43795.

[9] Z.A. Arfeen, A.B. Khairuddin, A. Munir, M.K. Azam, M. Faisal, and M.S.B. Arif. "En route of electric vehicles with the vehicle to grid technique in distribution networks: Status and technological review". In: *Energy Storage* 2.2 (2020), e115.

[10] M. Taiebat and M. Xu. "Synergies of four emerging technologies for accelerated adoption of electric vehicles: Shared mobility, wireless charging, vehicle-to-grid, and vehicle automation". In: *Journal of Cleaner Production* 230 (2019), pp. 794–797.

[11] Y.and Abbas U D. Alkawsi G.and Baashar, A.A. Alkahtani, and S.K. Tiong. "Review of renewable energy-based charging infrastructure for electric vehicles". In: *Applied Sciences* 11.9 (2021), p. 3847.

[12] A. Geetha, S. Usha, T. Thentral, C. Subramani, J. Santha Kumar, and C.S. Boopathi. "Wireless Power Transfer for Electric Vehicles with Better Ground Clearance". In: *Proceedings of International Conference on Power Electronics and Renewable Energy Systems*. Springer. 2022, pp. 165–171.

[13] Paoli, L. and Gu, T.l. *Electric Cars Fend off Supply Challenges to More Than Double Global Sales*.

[14] M. Guarnieri. "Looking back to electric cars". In: *2012 Third IEEE HISTory of ELectro-technology CONference (HISTELCON)*. IEEE. 2012, pp. 1–6.

[15] M. Kubański. "Prospects for the use of electric vehicles in public transport on the example of the city of czechowice-dziedzice". In: *Transportation Research Procedia* 44 (2020), pp. 110–114.

[16] A. Dik, S. Omer, and R. Boukhanouf. "Electric Vehicles: V2G for Rapid, Safe, and Green EV Penetration". In: *Energies* 15.3 (2022), p. 803.

[17] A. Triviño, J.M. González-González, and J.A. Aguado. "Wireless power transfer technologies applied to electric vehicles: A review". In: *Energies* 14.6 (2021), p. 1547.

[18] Srdjan Lukic and Zeljko Pantic. "Cutting the cord: Static and dynamic inductive wireless charging of electric vehicles". In: *IEEE Electrification Magazine* 1.1 (2013), pp. 57–64.

[19] I. D'Adamo and P. Rosa. "A structured literature review on obsolete electric vehicles management practices". In: *Sustainability* 11.23 (2019), p. 6876.

[20] L. Fricke. "The Long-term Problem with Electric Vehicle Batteries: A Policy Recommendation to Encourage Advancement for Scalable Recycling Practices". In: *Seattle Journal of Technology, Environmental & Innovation Law* 12.1 (2022), p. 2.

[21] J. Dai and D.C. Ludois. "A survey of wireless power transfer and a critical comparison of inductive and capacitive coupling for small gap applications". In: *IEEE Transactions on Power Electronics* 30.11 (2015), pp. 6017–6029.

[22] Z. Bi, L. Song, R. De Kleine, C.C. Mi, and G.A. Keoleian. "Plug-in vs. wireless charging: Life cycle energy and greenhouse gas emissions for an electric bus system". In: *Applied Energy* 146 (2015), pp. 11–19.

[23] S. Li and C.C. Mi. "Wireless power transfer for electric vehicle applications". In: *IEEE journal of emerging and selected topics in power electronics* 3.1 (2014), pp. 4–17.

[24]   N. Mohamed, F. Aymen, M. Alqarni, R.A. Turky, B. Alamri, Z.M. Ali, and S.H.A. Aleem. "A new wireless charging system for electric vehicles using two receiver coils". In: *Ain Shams Engineering Journal* 13.2 (2022), p. 101569.

[25]   S. Jeong and D. Jang Y.J.and Kum. "Economic analysis of the dynamic charging electric vehicle". In: *IEEE Transactions on Power Electronics* 30.11 (2015), pp. 6368–6377.

[26]   D. Stoppels. "Developments in soft magnetic power ferrites". In: *Journal of Magnetism and Magnetic Materials* 160 (1996), pp. 323–328.

[27]   K.W. Whites. "1 - Magnetostatics". In: *The Electrical Engineering Handbook*. Ed. by WAI-KAI CHEN. Burlington: Academic Press, 2005, pp. 479–497. ISBN: 978-0-12-170960-0.

[28]   E.A. Atekwana, F.M. Mewafy, G. Abdel Aal, D.D. Werkema Jr, A. Revil, and L.D. Slater. "High-resolution magnetic susceptibility measurements for investigating magnetic mineral formation during microbial mediated iron reduction". In: *Journal of Geophysical Research: Biogeosciences* 119.1 (2014), pp. 80–94.

[29]   CG. Stefanita. "Traditional Magnetism". In: *Magnetism: Basics and Applications*. Berlin, Heidelberg: Springer Berlin Heidelberg, 2012, pp. 1–38. ISBN: 978-3-642-22977-0.

[30]   B.D. Cullity and C.D. Graham. *Introduction to Magnetic Materials*. John Wiley Sons, Ltd, 2011. ISBN: 9781118211496.

[31]   F. Parodi. "19 - Physics and Chemistry of Microwave Processing". In: *Comprehensive Polymer Science and Supplements*. Ed. by A. Geoffrey and B. John C. Amsterdam: Pergamon, 1989, pp. 669–728. ISBN: 978-0-08-096701-1.

[32]   R.K. Kotnala and Jyoti Shah. "Chapter 4 - Ferrite Materials: Nano to Spintronics Regime". In: ed. by K.H.J. Buschow. Vol. 23. Handbook of Magnetic Materials. Elsevier, 2015, pp. 291–379.

[33]   H.R. Khan. "Ferromagnetism". In: *Encyclopedia of Physical Science and Technology (Third Edition)*. Ed. by Robert A. Meyers. Third Edition. New York: Academic Press, 2003, pp. 759–768. ISBN: 978-0-12-227410-7.

[34]   Vahak Marghussian. "4 - Magnetic Properties of Nano-Glass Ceramics". In: *Nano-Glass Ceramics*. Ed. by Vahak M. Oxford: William Andrew Publishing, 2015, pp. 181–223. ISBN: 978-0-323-35386-1.

[35]   H.W.F. Sung and C. Rudowicz. "Physics behind the magnetic hysteresis loop—a survey of misconceptions in magnetism literature". In: *Journal of magnetism and magnetic materials* 260.1-2 (2003), pp. 250–260.

[36] MH. Phan, J. Alonso, H. Khurshid, P. Lampen-Kelley, S. Chandra, K. Sto-jak Repa, Z. Nemati, R. Das, Ó. Iglesias, and H. Srikanth. "Exchange bias effects in iron oxide-based nanoparticle systems". In: *Nanomaterials* 6.11 (2016), p. 221.

[37] D. Fritsch. "Electronic and optical properties of spinel zinc ferrite: ab initio hybrid functional calculations". In: *Journal of Physics: Condensed Matter* 30.9 (2018), p. 095502.

[38] V. Zviagin, M. Grundmann, and R. Schmidt-Grund. "Impact of defects on magnetic properties of spinel zinc ferrite thin films". In: *physica status solidi (b)* 257.7 (2020), p. 1900630.

[39] J.H. Shim, S. Lee, J.H. Park, Y.H. Han S.J.and Jeong, and Y.W. Cho. "Coexistence of ferrimagnetic and antiferromagnetic ordering in Fe-inverted zinc ferrite investigated by NMR". In: *Physical review B* 73.6 (2006), p. 064404.

[40] H. Štěpánková, B. Sedlák, V. Chlan, P. Novák, and Z. Šimša. "Fe_{57} NMR and spin structure of manganese ferrite". In: *Physical Review B* 77.9 (2008), p. 092416.

[41] D. Serantes D.and Baldomir. "Superparamagnetism and monte carlo simulations". In: *arXiv preprint arXiv:1106.3438* (2011).

[42] Pawel G., Chandrima B., Michal M., Olav H., Anjan B., and Maciej K. "Chapter Two - The influence of the internal domain wall structure on spin wave band structure in periodic magnetic stripe domain patterns". In: ed. by Robert E. Camley and Robert L. Stamps. Vol. 72. Solid State Physics. Academic Press, 2021, pp. 29–82.

[43] RL Stamps. "Mechanisms for exchange bias". In: *Journal of Physics D: Applied Physics* 33.23 (2000), R247.

[44] R.C. O'handley. *Modern magnetic materials: principles and applications*. Wiley, 2000.

[45] F. Bloch. "Zur theorie des ferromagnetismus". In: *Zeitschrift für Physik* 61.3-4 (1930), pp. 206–219.

[46] C Vázquez-Vázquez, MA López-Quintela, MC Buján-Núñez, and J Rivas. "Finite size and surface effects on the magnetic properties of cobalt ferrite nanoparticles". In: *Journal of Nanoparticle Research* 13.4 (2011), pp. 1663–1676.

[47] H.R. Kirchmayr. "Permanent magnets and hard magnetic materials". In: *Journal of Physics D: Applied Physics* 29.11 (1996), p. 2763.

[48] K. Akihisa I.and Fanli. "Soft Magnetic Materials". In: *Encyclopedia of Smart Materials*. Ed. by Abdul-Ghani Olabi. Oxford: Elsevier, 2022, pp. 10–23. ISBN: 978-0-12-815733-6.

[49] J.M. Silveyra, E. Ferrara, D.L. Huber, and T.C. Monson. "Soft magnetic materials for a sustainable and electrified world". In: *Science* 362.6413 (2018), eaao0195.

[50] O. Gutfleisch, M.A. Willard, E. Brück, C.H. Chen, S.G. Sankar, and J.g. Liu. "Magnetic materials and devices for the 21st century: stronger, lighter, and more energy efficient". In: *Advanced materials* 23.7 (2011), pp. 821–842.

[51] P. Jing, M. Liu, Y. Pu, Y. Cui, Z. Wang, J. Wang, and Q. Liu. "Dependence of phase configurations, microstructures and magnetic properties of iron-nickel (Fe-Ni) alloy nanoribbons on deoxidization temperature in hydrogen". In: *Scientific reports* 6.1 (2016), pp. 1–9.

[52] G.W. Qin, W.L. Pei, Y.P. Ren, Y. Shimada, Y. Endo, M. Yamaguchi, S. Okamoto, and O. Kitakami. "Ni80Fe20 permalloy nanoparticles: wet chemical preparation, size control and their dynamic permeability characteristics when composited with Fe micron particles". In: *Journal of magnetism and magnetic materials* 321.24 (2009), pp. 4057–4062.

[53] K. Zipare, J. Dhumal, S. Bandgar, V. Mathe, and G. Shahane. "Superparamagnetic manganese ferrite nanoparticles: synthesis and magnetic properties". In: *Journal of Nanoscience and Nanoengineering* 1.3 (2015), pp. 178–182.

[54] S.F. Moustafa and W.M. Daoush. "Synthesis of nano-sized Fe–Ni powder by chemical process for magnetic applications". In: *Journal of materials processing technology* 181.1-3 (2007), pp. 59–63.

[55] K. Koh, J. Park, J. Park, X. Zhu, and L. Lin. "Core-shell magnetic nanoparticles for on-chip RF inductors". In: *2013 IEEE 26th International Conference on Micro Electro Mechanical Systems (MEMS)*. IEEE. 2013, pp. 465–468.

[56] D. Kuang, S. Wang, L. Hou, H. Luo, L. Deng, M. Song, J. He, and H. Huang. "Facile synthesis and influences of Fe/Ni ratio on the microwave absorption performance of ultra-small FeNi-C core-shell nanoparticles". In: *Materials Research Bulletin* 126 (2020), p. 110837.

[57] KL. Wu, R. Yu, and XW. Wei. "Monodispersed FeNi$_2$ alloy nanostructures: solvothermal synthesis, magnetic properties and size-dependent catalytic activity". In: *CrystEngComm* 14.22 (2012), pp. 7626–7632.

[58] D.G. Muratov, A.A. Vasilev, M.N. Efimov, G.P. Karpacheva, E.L. Dzidziguri, and P.A. Chernavskiy. "Metal-carbon nanocomposites FeNi/C: production, phase composition, magnetic properties". In: *Inorganic Materials: Applied Research* 10.3 (2019), pp. 666–672.

[59] T. Prakash, G.V.M. Williams, J. Kennedy, P.P. Murmu, J. Leveneur, S.V. Chong, and S. Rubanov. "Synthesis and structural, magnetic and magnetotransport properties of permalloy powders containing nanoparticles prepared by arc discharge". In: *Journal of alloys and compounds* 608 (2014), pp. 153–157.

[60]   G. Wang, D. Zhao, Y. Ma, Z. Zhang, H. Che, J. Mu, Xi. Zhang, and Z. Zhang. "Synthesis and characterization of polymer-coated manganese ferrite nanoparticles as controlled drug delivery". In: *Applied Surface Science* 428 (2018), pp. 258–263.

[61]   E. Mazarío, A. Mayoral, E. Salas, N. Menéndez, P. Herrasti, and J. Sánchez-Marcos. "Synthesis and characterization of manganese ferrite nanoparticles obtained by electrochemical/chemical method". In: *Materials & Design* 111 (2016), pp. 646–650.

[62]   S. Faraji, G. Dini, and M. Zahraei. "Polyethylene glycol-coated manganese-ferrite nanoparticles as contrast agents for magnetic resonance imaging". In: *Journal of Magnetism and Magnetic Materials* 475 (2019), pp. 137–145.

[63]   Pranav P Naik and Snehal S Hasolkar. "Consequence of B-site substitution of rare earth (Gd^{+3}) on electrical properties of manganese ferrite nanoparticles". In: *Journal of Materials Science: Materials in Electronics* 31.16 (2020), pp. 13434–13446.

[64]   Muhammad Asif Yousuf, Mirza Mahmood Baig, Najeeb Fuad Al-Khalli, Muhammad Azhar Khan, Mohamed F Aly Aboud, Imran Shakir, and Muhammad Farooq Warsi. "The impact of yttrium cations (Y^{3+}) on structural, spectral and dielectric properties of spinel manganese ferrite nanoparticles". In: *Ceramics International* 45.8 (2019), pp. 10936–10942.

[65]   Mirza Mahmood Baig, Muhammad Asif Yousuf, Muhammad Farooq Warsi, Philips Olaleye Agboola, Muhammad Sher, and Imran Shakir. "Surfactant assisted synthesis of rare earth Dy^{3+} substituted $MnFe_2O_4$ nanoparticles". In: *Ceramics International* 45.14 (2019), pp. 18014–18022.

[66]   Rui Han, Wei Li, Weiwei Pan, Minggang Zhu, Dong Zhou, and Fa-shen Li. "1D magnetic materials of Fe_3O_4 and Fe with high performance of microwave absorption fabricated by electrospinning method". In: *Scientific reports* 4.1 (2014), pp. 1–5.

[67]   M. Bayat, H. Yang, F.K. Ko, D. Michelson, and A. Mei. "Electromagnetic interference shielding effectiveness of hybrid multifunctional Fe_3O_4/carbon nanofiber composite". In: *Polymer* 55.3 (2014), pp. 936–943.

[68]   X. Huang, J. Zhang, M. Lai, and T. Sang. "Preparation and microwave absorption mechanisms of the NiZn ferrite nanofibers". In: *Journal of Alloys and Compounds* 627 (2015), pp. 367–373.

[69]   J. Füzer, S. Dobák, P. Kollár, Y. Osadchuk, M. Strečková, M. Fáberová, R. Bureš, P. Kurek, and M. Vojtko. "Analysis of magnetic losses and complex permeability in novel soft magnetic composite with ferrite nanofibers". In: *IEEE Transactions on Magnetics* 54.12 (2018), pp. 1–6.

[70] X.G. Li, A. Chiba, and S. Takahashi. "Preparation and magnetic properties of ultrafine particles of Fe Ni alloys". In: *Journal of Magnetism and Magnetic Materials* 170.3 (1997), pp. 339–345.

[71] Y.W. Ju, J.H. Park, H.R. Jung, S.J. Cho, and W.J. Lee. "Electrospun MnFe2O4 nanofibers: preparation and morphology". In: *Composites Science and Technology* 68.7-8 (2008), pp. 1704–1709.

[72] Y. Ren, H. Zhang, H. An, Y. Zhao, J. Feng, L. Xue, T. Luan, and Z. Fan. "Catalytic ozonation of di-n-butyl phthalate degradation using manganese ferrite/reduced graphene oxide nanofiber as catalyst in the water". In: *Journal of colloid and interface science* 526 (2018), pp. 347–355.

[73] T.K.A. Nguyen, E.k.o.P. Kuncoro, and R.A. Doong. "Manganese ferrite decorated N-doped polyacrylonitrile-based carbon nanofiber for the enhanced capacitive deionization". In: *Electrochimica Acta* 401 (2022), p. 139488.

[74] S. Khilari, S. Pandit, J.L. Varanasi, D. Das, and D. Pradhan. "Bifunctional manganese ferrite/polyaniline hybrid as electrode material for enhanced energy recovery in microbial fuel cell". In: *ACS Applied Materials & Interfaces* 7.37 (2015), pp. 20657–20666.

[75] U. Kurtan, D. Dursun, H. Aydın, Muhammet S. Toprak, A. Baykal, and A. Bozkurt. "Influence of calcination rate on morphologies and magnetic properties of MnFe$_2$O$_4$ nanofibers". In: *Ceramics International* 42.16 (2016), pp. 18189–18195.

[76] P. Kidkhunthod, S. Nilmoung, S. Mahakot, S. Rodporn, S. Phumying, and S. Maensiri. "A structural study and magnetic properties of electrospun carbon/manganese ferrite (C/MnFe$_2$O$_4$) composite nanofibers". In: *Journal of Magnetism and Magnetic Materials* 401 (2016), pp. 436–442.

[77] J.F. Cooley. *Apparatus for electrically dispersing fluids.* US Patent 692,631. 1902.

[78] J. Doshi and D.H. Reneker. "Electrospinning process and applications of electrospun fibers". In: *Journal of electrostatics* 35.2-3 (1995), pp. 151–160.

[79] G.I. Taylor. "Electrically driven jets". In: *Proceedings of the Royal Society of London. A. Mathematical and Physical Sciences* 313.1515 (1969), pp. 453–475.

[80] Xi. Hu, S. Liu, G. Zhou, Yubin Huang, Z. Xie, and Xi. Jing. "Electrospinning of polymeric nanofibers for drug delivery applications". In: *Journal of controlled release* 185 (2014), pp. 12–21.

[81] Y. Wang, T. Yokota, and T. Someya. "Electrospun nanofiber-based soft electronics". In: *NPG Asia Materials* 13.1 (2021), pp. 1–22.

[82] J.B. Ballengee and P.N. Pintauro. "Composite fuel cell membranes from dual-nanofiber electrospun mats". In: *Macromolecules* 44.18 (2011), pp. 7307–7314.

[83] J. Nath, K. Sharma, S. Kumar, V. Sharma, V. Kumar, and R. Sehgal. *Electrospun Nanofibers for Wastewater Treatment.* Springer, 2021, pp. 87–117.

[84] A.M. Al-Enizi, M.M. Zagho, and A.A. Elzatahry. "Polymer-based electrospun nanofibers for biomedical applications". In: *Nanomaterials* 8.4 (2018), p. 259.

[85] W.E. Teo and S. Ramakrishna. "A review on electrospinning design and nanofibre assemblies". In: *Nanotechnology* 17.14 (2006), R89.

[86] W. Gilbert. "De Magnete Magnetcisque Corporibus, et de Magno Magnete Tellure (On the Magnet, Magnetick Bodies also, and on the Great Magnet the Earth; a new Physiology, demonstrated by many arguments & Experiments)". In: *Translated 1893 from Latin to English by Paul FleuryMottelay* (1991).

[87] CM. Wu, HG. Chiou, SL. Lin, and JM. Lin. "Effects of electrostatic polarity and the types of electrical charging on electrospinning behavior". In: *Journal of Applied Polymer Science* 126.S2 (2012), E89–E97.

[88] P.X. Ma and R. Zhang. "Synthetic nano-scale fibrous extracellular matrix". In: *Journal of Biomedical Materials Research: An Official Journal of The Society for Biomaterials, The Japanese Society for Biomaterials, and The Australian Society for Biomaterials* 46.1 (1999), pp. 60–72.

[89] D. Liu, S.D. Feyter, M. Cotlet, UM. Wiesler, T. Weil, A. Herrmann, K. Müllen, and F.C. De Schryver. "Fluorescent self-assembled polyphenylene dendrimer nanofibers". In: *Macromolecules* 36.22 (2003), pp. 8489–8498.

[90] S. Grimm, R. Giesa, K. Sklarek, A. Langner, U. Gosele, HW Schmidt, and M. Steinhart. "Nondestructive replication of self-ordered nanoporous alumina membranes via cross-linked polyacrylate nanofiber arrays". In: *Nano letters* 8.7 (2008), pp. 1954–1959.

[91] V. Beachley and Xu. Wen. "Polymer nanofibrous structures: Fabrication, biofunctionalization, and cell interactions". In: *Progress in polymer science* 35.7 (2010), pp. 868–892.

[92] Z. Li and C. Wang. "Effects of working parameters on electrospinning". In: *One-dimensional nanostructures*. Springer, 2013, pp. 15–28.

[93] N. Bhardwaj and S.C. Kundu. "Electrospinning: a fascinating fiber fabrication technique". In: *Biotechnology advances* 28.3 (2010), pp. 325–347.

[94] C.M. Hansen. "The universality of the solubility parameter". In: *Industrial & engineering chemistry product research and development* 8.1 (1969), pp. 2–11.

[95] S.A.C.M. Hansen. *Hansen Solubility Parameters in Practice*. Hansen-Solubility. ISBN: 9780955122026.

[96] K. Nasouri, A.M. Shoushtari, and M.R.M. Mojtahedi. "Thermodynamic studies on polyvinylpyrrolidone solution systems used for fabrication of electrospun nanostructures: Effects of the solvent". In: *Advances in Polymer Technology* 34.3 (2015).

[97]   S. De Vrieze, T. Van Camp, A. Nelvig, B. Hagström, P. Westbroek, and K. De Clerck. "The effect of temperature and humidity on electrospinning". In: *Journal of materials science* 44.5 (2009), pp. 1357–1362.

[98]   K.D. Vernon-Parry. "Scanning electron microscopy: an introduction". In: *III-Vs Review* 13.4 (2000), pp. 40–44.

[99]   K. Akhtar, S.A. Khan, S.B. Khan, and A.M. Asiri. "Scanning electron microscopy: principle and applications in nanomaterials characterization". In: *Handbook of materials characterization*. Springer, 2018, pp. 113–145.

[100] Xi. Wan, W. Wang, J. Liu, and T. Tong. "Estimating the sample mean and standard deviation from the sample size, median, range and/or interquartile range". In: *BMC medical research methodology* 14.1 (2014), pp. 1–13.

[101] J.M. Zuo and J.C. Spence. *Advanced transmission electron microscopy*. Springer, 2017.

[102] Q. Fan. "A new method of calculating interplanar spacing: the position-factor method". In: *Journal of Applied Crystallography* 45.6 (2012), pp. 1303–1308.

[103] J.I.l Langford and A.J.C. Wilson. "Scherrer after sixty years: a survey and some new results in the determination of crystallite size". In: *Journal of applied crystallography* 11.2 (1978), pp. 102–113.

[104] A. Chauhan and P. Chauhan. "Powder XRD technique and its applications in science and technology". In: *J Anal Bioanal Tech* 5.5 (2014), pp. 1–5.

[105] A.L. Patterson. "The Scherrer formula for X-ray particle size determination". In: *Physical review* 56.10 (1939), p. 978.

[106] A.W. Coats and J.P. Redfern. "Thermogravimetric analysis. A review". In: *Analyst* 88.1053 (1963), pp. 906–924.

[107] J.D. Menczel and R.B. Prime. *Thermal Analysis of Polymers: Fundamentals and Applications*. Wiley, 2009. ISBN: 9780471769170.

[108] E. Kita. "DC magnetoelectric effect measurements by a SQUID magnetometer". In: *Ferroelectrics* 162.1 (1994), pp. 397–400.

[109] M. van Schilfgaarde, I.A. Abrikosov, and B. Johansson. "Origin of the Invar effect in iron–nickel alloys". In: *Nature* 400.6739 (1999), pp. 46–49.

[110] E. Kaniukov, A. Shumskaya, D. Yakimchuk, A. Kozlovskiy, I. Korolkov, M. Ibragimova, M. Zdorovets, K. Kadyrzhanov, V. Rusakov, M. Fadeev, E. Lobko, K. Saunina, and L. Nikolaevich. "FeNi nanotubes: perspective tool for targeted delivery". In: *Applied Nanoscience* 9.5 (2019), pp. 835–844.

[111] W. Hong, S. Lee, H.J. Chang, E.S. Lee, and Y. Cho. "Multifunctional magnetic nanowires: a novel breakthrough for ultrasensitive detection and isolation of rare cancer cells from non-metastatic early breast cancer patients using small volumes of blood". In: *Biomaterials* 106 (2016), pp. 78–86.

[112] Y.P. Ivanov, A. Alfadhel, M. Alnassar, J.E. Perez, M. Vazquez, A. Chuvilin, and J. Kosel. "Tunable magnetic nanowires for biomedical and harsh environment applications". In: *Scientific reports* 6.1 (2016), pp. 1–10.

[113] F. Guo, K. Cheng, K. Ye, G. Wang, and D. Cao. "Preparation of nickel-cobalt nanowire arrays anode electro-catalyst and its application in direct urea/hydrogen peroxide fuel cell". In: *Electrochimica Acta* 199 (2016), pp. 290–296.

[114] Y. Li, M. Yuan, H. Liu, and G. Sun. "In situ synthesis of CoFe2O4 nanocrystals decorated in mesoporous carbon nanofibers with enhanced electromagnetic performance". In: *Journal of Alloys and Compounds* 826 (2020), p. 154147.

[115] P.V. Morais, P.H. Suman, R.A. Silva, and M.O. Orlandi. "High gas sensor performance of WO3 nanofibers prepared by electrospinning". In: *Journal of Alloys and Compounds* 864 (2021), p. 158745.

[116] L.F. Yin, D.H. Wei, N. Lei, L.H. Zhou, C.S. Tian, G.S. Dong, X.F. Jin, L.P. Guo, Q.J. Jia, and R.Q. Wu. "Magnetocrystalline anisotropy in permalloy revisited". In: *Physical review letters* 97.6 (2006), p. 067203.

[117] P. Melnikov, V.A. Nascimento, I.V. Arkhangelsky, L.Z. Zanoni Consolo, and L.C.S. De Oliveira. "Thermal decomposition mechanism of iron (III) nitrate and characterization of intermediate products by the technique of computerized modeling". In: *Journal of Thermal Analysis and Calorimetry* 115.1 (2014), pp. 145–151.

[118] J.C. De Jesus, I. González, A. Quevedo, and T. Puerta. "Thermal decomposition of nickel acetate tetrahydrate: an integrated study by TGA, QMS and XPS techniques". In: *Journal of Molecular Catalysis A: Chemical* 228.1-2 (2005), pp. 283–291.

[119] Y.K. Du, P. Yang, Z.G. Mou, N.P. Hua, and L. Jiang. "Thermal decomposition behaviors of PVP coated on platinum nanoparticles". In: *Journal of applied polymer science* 99.1 (2006), pp. 23–26.

[120] D.T. Turner and A. Schwartz. "The glass transition temperature of poly (N-vinyl pyrrolidone) by differential scanning calorimetry". In: *Polymer* 26.5 (1985), pp. 757–762.

[121] B. Glaubitz, S. Buschhorn, F. Brüssing, R. Abrudan, and H. Zabel. "Development of magnetic moments in Fe1- xNix-alloys". In: *Journal of Physics: Condensed Matter* 23.25 (2011), p. 254210.

[122] E.M. Abdelrazek, A.M. Abdelghany, S.I. Badr, and M.A. Morsi. "Structural, optical, morphological and thermal properties of PEO/PVP blend containing different concentrations of biosynthesized Au nanoparticles". In: *Journal of materials research and technology* 7.4 (2018), pp. 419–431.

[123] A. Baldan. "Review progress in Ostwald ripening theories and their applications to nickel-base superalloys Part I: Ostwald ripening theories". In: *Journal of materials science* 37.11 (2002), pp. 2171–2202.

[124] H. Wang, J. Li, Xi. Kou, and L. Zhang. "Synthesis and characterizations of size-controlled FeNi$_3$ nanoplatelets". In: *Journal of crystal growth* 310.12 (2008), pp. 3072–3076.

[125] N.A.M. Barakat, B. Kim, and H.Y. Kim. "Production of smooth and pure nickel metal nanofibers by the electrospinning technique: nanofibers possess splendid magnetic properties". In: *The Journal of Physical Chemistry C* 113.2 (2009), pp. 531–536.

[126] R.L. Edwards. "The magnetic properties of evaporated nickel and iron films". In: *Physical Review* 29.2 (1927), p. 321.

[127] C.R. Lin, M.H. Hsieh, Y.J. Siao, and C.C. Wang. "Preparation and magnetic properties of monodisperse permalloy hollow spheres". In: *Journal of Applied Physics* 103.7 (2008), p. 07D522.

[128] Yan Liu, Yanxiu Chi, Shiyao Shan, Jun Yin, Jin Luo, and Chuan-Jian Zhong. "Characterization of magnetic NiFe nanoparticles with controlled bimetallic composition". In: *Journal of alloys and compounds* 587 (2014), pp. 260–266.

[129] S. Larumbe, C. Gomez-Polo, J.I. Pérez-Landazábal, and J.M. Pastor. "Effect of a SiO$_2$ coating on the magnetic properties of Fe$_3$O$_4$ nanoparticles". In: *Journal of Physics: Condensed Matter* 24.26 (2012), p. 266007.

[130] CM Srivastava and R Aiyar. "Spin wave stiffness constants in some ferrimagnetics". In: *Journal of Physics C: Solid State Physics* 20.8 (1987), p. 1119.

[131] C. Peniche, D. Zaldívar, M. Pazos, S. Páz, A. Bulay, and J.S. Román. "Study of the thermal degradation of poly (N-vinyl-2-pyrrolidone) by thermogravimetry–FTIR". In: *Journal of applied polymer science* 50.3 (1993), pp. 485–493.

[132] LJ Swartzendruber, VP Itkin, and CB Alcock. "The Fe-Ni (iron-nickel) system". In: *Journal of phase equilibria* 12.3 (1991), pp. 288–312.

[133] I.M. Alibe, K.A. Matori, H.j.A. Sidek, Y. Yaakob, U. Rashid, M.H.M. Alibe A. M.and Zaid, S. Nasir, and M.M. Nasir. "Effects of polyvinylpyrrolidone on structural and optical properties of willemite semiconductor nanoparticles by polymer thermal treatment method". In: *Journal of Thermal Analysis and Calorimetry* 136.6 (2019), pp. 2249–2268.

[134] Yuanzhi Chen, Xiaohua Luo, Guang-Hui Yue, Xuetao Luo, and Dong-Liang Peng. "Synthesis of iron–nickel nanoparticles via a nonaqueous organometallic route". In: *Materials Chemistry and Physics* 113.1 (2009), pp. 412–416.

[135] W. El Hotaby, H.H.A. Sherif, B.A. Hemdan, W.A. Khalil, and S.K.H. Khalil. "Assessment of in situ-Prepared Polyvinylpyrrolidone-Silver Nanocomposite for Antimicrobial Applications." In: *Acta Physica Polonica, A.* 131.6 (2017).

[136] M.A.A. Mohamed. "Facile directing agent-free synthesis and magnetism of nanocrystalline Fe–Ni alloy with tunable shape". In: *Materials Science and Engineering: B* 190 (2014), pp. 7–12.

[137] Ihab M Obaidat, Chiranjib Nayek, and Kaustuv Manna. "Investigating the role of shell thickness and field cooling on saturation magnetization and its temperature dependence in Fe3O4/γ-Fe2O3 core/shell nanoparticles". In: *Applied Sciences* 7.12 (2017), p. 1269.

[138] Peter Vang Hendriksen, Søren Linderoth, and P-A Lindgård. "Finite-size modifications of the magnetic properties of clusters". In: *Physical Review B* 48.10 (1993), p. 7259.

[139] L.l. Linderoth S.and Balcells, A. Labarta, J. Tejada, P.V. Hendriksen, and S.A. Sethi. "Magnetization and Mössbauer studies of ultrafine Fe-C particles". In: *Journal of magnetism and magnetic materials* 124.3 (1993), pp. 269–276.

[140] N.T. Lan and T.D. Duong N.P.and Hien. "Influences of cobalt substitution and size effects on magnetic properties of coprecipitated Co–Fe ferrite nanoparticles". In: *Journal of Alloys and Compounds* 509.19 (2011), pp. 5919–5925.

[141] D. Zhang, K.J. Klabunde, C.M. Sorensen, and G.C. Hadjipanayis. "Magnetization temperature dependence in iron nanoparticles". In: *Physical Review B* 58.21 (1998), p. 14167.

[142] Xavier Batlle, N Pérez, P Guardia, O Iglesias, A Labarta, F Bartolomé, LM García, J Bartolomé, AG Roca, MP Morales, et al. "Magnetic nanoparticles with bulklike properties". In: *Journal of Applied Physics* 109.7 (2011), 07B524.

[143] R.K. Zheng, G.H. Wen, K.K. Fung, and X.X. Zhang. "Giant exchange bias and the vertical shifts of hysteresis loops in γ-Fe 2 O 3-coated Fe nanoparticles". In: *Journal of applied physics* 95.9 (2004), pp. 5244–5246.

[144] Y. Shen, Y. Wei, J. Ma, Y. Zhang, B. Ji, J. Tang, L. Zhang, P. Yan, and Xu. Du. "Self-cleaning functionalized FeNi/NiFe$_2$O$_4$/NiO/C nanofibers with enhanced microwave absorption performance". In: *Ceramics International* 46.9 (2020), pp. 13397–13406.

[145] H. Chen, Xi. Huang, L.J. Zhou, G.D. Li, M. Fan, and Xi. Zou. "Electrospinning synthesis of bimetallic nickel–iron oxide/carbon composite nanofibers for efficient water oxidation electrocatalysis". In: *ChemCatChem* 8.5 (2016), pp. 992–1000.

[146] K.A. Gebru and C. Das. "Effects of solubility parameter differences among PEG, PVP and CA on the preparation of ultrafiltration membranes: Impacts of solvents and additives on morphology, permeability and fouling performances". In: *Chinese Journal of Chemical Engineering* 25.7 (2017), pp. 911–923.

[147] A. Guittoum, A. Layadi, A. Bourzami, H. Tafat, N. Souami, S. Boutarfaia, and D. Lacour. "X-ray diffraction, microstructure, Mössbauer and magnetization studies of nanostructured Fe$_{50}$Ni$_{50}$ alloy prepared by mechanical alloying". In: *Journal of Magnetism and Magnetic Materials* 320.7 (2008), pp. 1385–1392.

[148] A. Djekoun, A. Otmani, B. Bouzabata, L. Bechiri, N. Randrianantoandro, and J.M. Greneche. "Synthesis and characterization of high-energy ball milled nanostructured $Fe_{50}Ni_{50}$". In: *Catalysis today* 113.3-4 (2006), pp. 235–239.

[149] C. Iacovita, G.F. Stiufiuc, R. Dudric, N. Vedeanu, R. Tetean, R.I. Stiufiuc, and C.M. Lucaciu. "Saturation of specific absorption rate for soft and hard spinel ferrite nanoparticles synthesized by polyol process". In: *Magnetochemistry* 6.2 (2020), p. 23.

[150] S. Vitta, A. Khuntia, G. Ravikumar, and D. Bahadur. "Electrical and magnetic properties of nanocrystalline $Fe_{100-x}Ni_x$ alloys". In: *Journal of magnetism and magnetic materials* 320.3-4 (2008), pp. 182–189.

[151] B.E. Argyle, S.H. Charap, and E.W. Pugh. "Deviations from $T^{3/2}$ Law for Magnetization of Ferrometals: Ni, Fe, and Fe^{+3}% Si". In: *Physical Review* 132.5 (1963), p. 2051.

[152] T. Nawaz, G.V.M. Williams, M.P. Coles, A. Edgar, and S.V. Chong. "Synthesis of orientated $Ni_{0.89}Fe_{0.11}$/polymer nanofibres with a bimodal nanoparticle size distribution by electrospinning and thermal processing". In: *Materials Today Communications* 30 (2022), p. 103120.

[153] E. Tronc, A. Ezzir, R. Cherkaoui, C. Chanéac, M. Noguès, H. Kachkachi, D. Fiorani, A.M. Testa, J.M. Greneche, and J.P. Jolivet. "Surface-related properties of γ-Fe_2O_3 nanoparticles". In: *Journal of Magnetism and Magnetic Materials* 221.1-2 (2000), pp. 63–79.

[154] D.A. Garanin and H. Kachkachi. "Surface contribution to the anisotropy of magnetic nanoparticles". In: *Physical review letters* 90.6 (2003), p. 065504.

[155] Z. Nedelkoski, D. Kepaptsoglou, L. Lari, T. Wen, R.A. Booth, S.D. Oberdick, P.L. Galindo, Q.M. Ramasse, R.F.L. Evans, S. Majetich, and V.K. Lazaroy. "Origin of reduced magnetization and domain formation in small magnetite nanoparticles". In: *Scientific reports* 7.1 (2017), pp. 1–8.

[156] R.H. Kodama. "Magnetic nanoparticles". In: *Journal of magnetism and magnetic materials* 200.1-3 (1999), pp. 359–372.

[157] B. Molina-Concha, R.D. Zysler, and H. Romero. "Anomalous magnetization enhancement and frustration in the internal magnetic order on (Fe0. 69Co0. 31) B0. 4 nanoparticles". In: *Applied Sciences* 2.2 (2012), pp. 315–326.

[158] S. Ahmad, S. Ali, I. Ullah, M.S. Zobaer, A. Albakri, and T. Muhammad. "Synthesis and characterization of manganese ferrite from low grade manganese ore through solid state reaction route". In: *Scientific Reports* 11.1 (2021), pp. 1–9.

[159] K. Ahalya, N. Suriyanarayanan, and S. Sangeetha. "Effect of pH and annealing temperatures on structural, magnetic, electrical, dielectric and adsorption properties of manganese ferrite nano particles". In: *Materials science in semiconductor processing* 27 (2014), pp. 672–681.

[160] K.M. Batoo. "Study of dielectric and impedance properties of Mn ferrites". In: *Physica B: Condensed Matter* 406.3 (2011), pp. 382–387.

[161] M. Schaefer, G. Dietzmann, and H. Wirth. "Magnetic losses in ferrites and nanocrystalline ribbons for power applications". In: *Journal of magnetism and magnetic materials* 101.1-3 (1991), pp. 95–96.

[162] M.N. Ashiq, S. Saleem, M.A. Malana, and Anis-Ur-Rehman. "Physical, electrical and magnetic properties of nanocrystalline Zr–Ni doped Mn-ferrite synthesized by the co-precipitation method". In: *Journal of Alloys and Compounds* 486.1-2 (2009), pp. 640–644.

[163] M.A. Yousuf, S. Jabeen, M.N. Shahi, M.A. Khan, I. Shakir, and M.F. Warsi. "Magnetic and electrical properties of yttrium substituted manganese ferrite nanoparticles prepared via micro-emulsion route". In: *Results in Physics* 16 (2020), p. 102973.

[164] Xu. Zuo, B. Barbiellini, and C. Vittoria. "Calculation of exchange constants in manganese ferrite ($MnFe_2O_4$)". In: *Journal of magnetism and magnetic materials* 272 (2004), pp. 306–311.

[165] C. Simon, A. Blösser, M. Eckardt, H. Kurz, B. Weber, M. Zobel, and R. Marschall. "Magnetic properties and structural analysis on spinel $MnFe_2O_4$ nanoparticles prepared via non-aqueous microwave synthesis". In: *Zeitschrift für anorganische und allgemeine Chemie* 647.22 (2021), pp. 2061–2072.

[166] S. S. Shinde. "Crystal Structure and Magnetic Interactions of Ferrites". In: 2015.

[167] G.D. Tang, Z.Z. Li, L Ma, W.H. Qi, L.Q. Wu, X.S. Ge, G.H. Wu, and F.X. Hu. "Three models of magnetic ordering in typical magnetic materials". In: *Physics Reports* 758 (2018), pp. 1–56.

[168] K. Islam, M. Haque, A. Kumar, A. Hoq, F. Hyder, and S.M. Hoque. "Manganese ferrite nanoparticles ($MnFe_2O_4$): Size dependence for hyperthermia and negative/positive contrast enhancement in MRI". In: *Nanomaterials* 10.11 (2020), p. 2297.

[169] J.A. Peters. "Relaxivity of manganese ferrite nanoparticles". In: *Progress in Nuclear Magnetic Resonance Spectroscopy* 120 (2020), pp. 72–94.

[170] M. Li, Y. Xiong, Xi. Liu, Xi. Bo, Y. Zhang, Ce. Han, and L. Guo. "Facile synthesis of electrospun MFe_2O_4 (M= Co, Ni, Cu, Mn) spinel nanofibers with excellent electrocatalytic properties for oxygen evolution and hydrogen peroxide reduction". In: *Nanoscale* 7.19 (2015), pp. 8920–8930.

[171] W.I. Hayes, P. Joseph, M.Z. Mughal, and P. Papakonstantinou. "Production of reduced graphene oxide via hydrothermal reduction in an aqueous sulphuric acid suspension and its electrochemical behaviour". In: *Journal of solid state electrochemistry* 19.2 (2015), pp. 361–380.

[172] K.D. Esmeryan, C.E. Castano, A.H. Bressler, C.P. Fergusson, and R. Moham-madi. "Single-step flame synthesis of carbon nanoparticles with tunable structure and chemical reactivity". In: *RSC advances* 6.66 (2016), pp. 61620–61629.

[173] N.F. Syabaniah, N. Syarif, D. Rohendi, M. Wandasari, and W.D. Rengga. "The Light Transmittance and Electrical Conductivity Properties of Gelam Wood Carbon Nanosheet and Its Derivatives". In: *IJFAC (Indonesian Journal of Fundamental and Applied Chemistry)* 4.3 (2019), pp. 126–131.

[174] W. Zhu, X. Meng, Y. Zhan, H. Li, J. Ma, J. Liu, C. Zhai, W. Zhang, X. Fang, and T. Ding. "Carbonization temperature controlled thermal conductivity of graphitic carbon nanoparticles and their polymer composites". In: *AIP Advances* 8.5 (2018), p. 055332.

[175] B. Aslibeiki, P. Kameli, and H. Salamati. "The effect of dipole-dipole interactions on coercivity, anisotropy constant, and blocking temperature of MnFe2O4 nanoparticles". In: *Journal of Applied Physics* 119.6 (2016), p. 063901.

[176] Z.X. Tang, C.M. Sorensen, K.J. Klabunde, and G.C. Hadjipanayis. "Size-dependent Curie temperature in nanoscale $MnFe_2O_4$ particles". In: *Physical Review Letters* 67.25 (1991), p. 3602.

[177] R. Aquino, J. Depeyrot, M.H. Sousa, F.A. Tourinho, E. Dubois, and R. Perzynski. "Magnetization temperature dependence and freezing of surface spins in magnetic fluids based on ferrite nanoparticles". In: *Physical Review B* 72.18 (2005), p. 184435.

[178] J. Wang, Q. Chen, B. Hou, and Z. Peng. "Synthesis and magnetic properties of single-crystals of $MnFe_2O_4$ nanorods". In: *European Journal of Inorganic Chemistry* 2004.6 (2004), pp. 1165–1168.

[179] K. Tanbir, M.P. Ghosh, R.K. Singh, M. Kar, and S. Mukherjee. "Effect of doping different rare earth ions on microstructural, optical, and magnetic properties of nickel–cobalt ferrite nanoparticles". In: *Journal of Materials Science: Materials in Electronics* 31.1 (2020), pp. 435–443.

[180] M.L. Kahn and Z.J. Zhang. "Synthesis and magnetic properties of $CoFe_2O_4$ spinel ferrite nanoparticles doped with lanthanide ions". In: *Applied Physics Letters* 78.23 (2001), pp. 3651–3653.

[181] X. Zhou, Y. Zhou, L. Zhou, J. Wei, J. Wu, and D. Yao. "Effect of Gd and La doping on the structure, optical and magnetic properties of NiZnCo ferrites". In: *Ceramics International* 45.5 (2019), pp. 6236–6242.

[182] M.A. Ahmed, E. Ateia, and S.I. El-Dek. "Spectroscopic analysis of ferrite doped with different rare earth elements". In: *Vibrational spectroscopy* 30.1 (2002), pp. 69–75.

[183] M.A. Ahmed, E. Ateia, and S.I. El-Dek. "Rare earth doping effect on the structural and electrical properties of Mg–Ti ferrite". In: *Materials letters* 57.26-27 (2003), pp. 4256–4266.

[184] G.V. Bazuev, O.I. Gyrdasova, S.I. Novikov, and A.Yu. Kuznetsov. "Synthesis, structure, and magnetic properties of rare-earth-doped $Ni_{0.75}Zn_{0.25}Fe_2O_4$ nickel zinc ferrite". In: *Inorganic Materials* 52.9 (2016), pp. 932–938.

[185] S. Ikram, J. Jacob, K. Mehboob, K. Mahmood, N. Amin, M.I. Arshad, and M. Ajaz un Nabi. "Role of rare earth metal ions doping on structural, electrical, magnetic, and dielectric behavior of spinel ferrites: A comparative study". In: *Journal of Superconductivity and Novel Magnetism* 34.7 (2021), pp. 1833–1842.

[186] M.M. Baig, S. Zulfiqar, M.A. Yousuf, M. Touqeer, S. Ullah, P. Agboola, M.F. Warsi, and I. Shakir. "Structural and photocatalytic properties of new rare earth La^{3+} substituted $MnFe_2O_4$ ferrite nanoparticles". In: *Ceramics International* 46.14 (2020), pp. 23208–23217.

[187] M.N. Akhtar, H.A. Siddiqa, M.S. Nazir, and M.A. Khan. "Preparations and tailoring of structural, magnetic properties of rare earths (REs) doped nanoferrites for microwave high-frequency applications". In: *Ceramics International* 46.17 (2020), pp. 26521–26529.

[188] M.M.N. Ansari, S. Khan, and N. Ahmad. "Effect of R3+ (R= Pr, Nd, Eu and Gd) substitution on the structural, electrical, magnetic and optical properties of Mn-ferrite nanoparticles". In: *Journal of Magnetism and Magnetic Materials* 465 (2018), pp. 81–87.

[189] R.D. Shannon. "Revised effective ionic radii and systematic studies of interatomic distances in halides and chalcogenides". In: *Acta crystallographica section A: crystal physics, diffraction, theoretical and general crystallography* 32.5 (1976), pp. 751–767.

[190] M. Yehia, S.M. Ismail, and A. Hashhash. "Structural and magnetic studies of rare-earth substituted nickel ferrites". In: *Journal of Superconductivity and Novel Magnetism* 27.3 (2014), pp. 771–774.

[191] P. Samoila, C. Cojocaru, L. Sacarescu, P.P. Dorneanu, AA. Domocos, and A. Rotaru. "Remarkable catalytic properties of rare-earth doped nickel ferrites synthesized by sol-gel auto-combustion with maleic acid as fuel for CWPO of dyes". In: *Applied Catalysis B: Environmental* 202 (2017), pp. 21–32.

[192] P.K. Mondal, M.A. Hossain, M.N.I. Khan, and S.S. Sikder. "Structural, magnetic and transport properties of samarium (Sm) doped Cu-Zn ferrites". In: *International Journal of Physical Sciences* 14.3 (2019), pp. 21–29.

[193] M.H. Abdellatif, G.M. El-Komy, and A.A. Azab. "Magnetic characterization of rare earth doped spinel ferrite". In: *Journal of Magnetism and Magnetic Materials* 442 (2017), pp. 445–452.

[194] V.J. Angadi, B. Rudraswamy, K. Sadhana, S.R. Murthy, and K. Praveena. "Effect of Sm^{3+}–Gd^{3+} on structural, electrical and magnetic properties of Mn–Zn ferrites synthesized via combustion route". In: *Journal of Alloys and Compounds* 656 (2016), pp. 5–12.

[195]   Y.A. Freiman, H.J. Jodl, and Y. Crespo. "Solid oxygen revisited". In: *Physics Reports* 743 (2018), pp. 1–55.